



Provided by the author(s) and University of Galway in accordance with publisher policies. Please cite the published version when available.

Title	Fretting wear-fatigue study for tribologically-induced damage in simple and complex geometries
Author(s)	Zhang, Teng
Publication Date	2013-02-22
Item record	http://hdl.handle.net/10379/5100

Downloaded 2024-04-26T06:02:35Z

Some rights reserved. For more information, please see the item record link above.





**Fretting Wear-Fatigue Study for Tribologically-
Induced Damage in Simple and Complex Geometries**

Teng Zhang

**Thesis submitted to National University of Ireland,
Galway for the degree of Doctor of Philosophy**

November, 2012

Abstract

This thesis presents the development of a computational and experimental methodology for predicting fretting wear-fatigue interaction in simple and complex geometries, specifically targeting the taper-lock assembly in modular hip implants.

Nonlinear continuum damage mechanics is first coupled with fretting fatigue analysis. This method shows similar results to the critical plane Smith-Watson-Topper (*SWT*) approach, which can also capture the dependence of fretting fatigue life on slip amplitude. An energy-based wear approach combined with the critical plane *SWT*, together with a non-linear kinematic hardening model for cyclic plasticity, is implemented for Hertzian round-on-flat and rounded punch-on-flat fretting configurations. The effect of contact geometry on fretting performance is addressed and a plastic ratchetting failure is shown to be a possible failure mechanism in partial slip cases, competitive with fatigue damage accumulation.

Tribological and profilometry tests are carried out on two hip implant candidate material combinations, namely CoCr/forged Ti-6Al-4V and CoCr/DLMS Ti-6Al-4V. A scanning electron microscope (SEM) based technique for surface wear measurement is developed. Both coefficient of friction and energy wear coefficient for DLMS Ti-6Al-4V are found to be lower than for forged Ti-6Al-4V.

A fretting wear-fatigue analysis methodology for the taper-lock assembly in modular hip implants is developed and presented. A global model is built for fretting analysis, assuming a flat-on-flat contact. Wear evolution is predicted on the stem surfaces for both material combinations, with CoCr/DLMS Ti-6Al-4V giving superior wear performance. A

micro-scale sub-model for frictional contact and wear-fatigue analysis is developed. Surface undulations (for enhanced frictional locking effects) on the stem and femoral head play an important role in fretting fatigue life. The inclusion of undulations in fretting wear-fatigue simulations will avoid non-conservative design. It is also found that to simulate wear in the micro-scale models can avoid over-conservative designs. Therefore, the combination of fretting wear-fatigue modelling with rough surface profile is a key to accurate fretting performance prediction. The predicted service time, which is comparable with the published test results, shows that the hip joint modelled here meets the National Health Service (UK) requirement.

Publications

Zhang, T., McHugh, P.E. & Leen, S.B. Computational study on the effect of contact geometry on fretting behaviour. *Wear*, 271, 1462-1480 (2011).

Zhang, T., McHugh, P. E. & Leen, S. B. Finite element implementation of multiaxial continuum damage mechanics for plain and fretting fatigue. *International Journal of Fatigue*, 44, 260–272 (2012).

Zhang, T., Harrison, N.M., McDonnell, P.F., McHugh, P.E. & Leen, S.B. Tribological behaviour of Ti-6Al-4V for the stem-head joint in prosthetic hip implants. *Tribology International* (In press)

Zhang, T., Harrison, N.M., McDonnell, P.F., McHugh, P.E. & Leen, S.B. Multi-scale fretting of forged and DMLS Ti-6Al-4V taper joint in modular hip implant. *Tribology International* (In preparation)

Acknowledgements

First and foremost, I would like to thank my supervisors, Prof. Sean Leen and Prof. Peter McHugh. I wish to express my sincere gratitude to Prof. Leen who offered me invaluable guidance, support and inspiration. His enthusiasm and encouragement will continue helping me in the future. I also wish to express my deep gratitude to Prof. McHugh who has always guided me and advised me so kindly. His knowledge and suggestions helped me tremendously. They have made my PhD a very pleasant and enjoyable experience.

I would also like to thank Dr Noel Harrison and Dr Pat McDonnell for their great support in hip implants modelling and testing, Dr Jian Ding for his helpful discussions, Mr. Bonaventure Kennedy for kindly manufacturing CoCr test specimens and Dr. Éadaoin Timmins for the help on SEM testing.

Also I would like to thank my colleagues in NUI Galway - Claire, Evelyn, Ciaran, James, Oliver, Caoimhe, Richard, Neil, Heather, Tadhg and everyone else. Their humour and kindness have made the process a valuable experience, a memory full of happiness.

I also would like to thank my parents who have been always supporting me and caring for me. The love they give me encourages me all the time.

Contents

Abstract.....	I
Publications.....	III
Acknowledgements.....	IV
Chapter 1 Introduction	1
1. 1 Overview	1
1. 2 Background and application for fretting.....	1
1.2.1 General	1
1.2.2 Aeroengine	2
1.2.3 Flexible riser.....	5
1.2.4 Prosthetic implants.....	8
1.2.5 Steel rope wires	11
1. 3 Aims	12
1. 4 Scope of thesis	13
Chapter 2 Literature Review	16
2. 1 Introduction	16
2.2 Contact mechanics.....	16
2.2.1 General	16
2.2.2 Sphere on flat contact	17
2.2.3 Cylinder on flat contact	19
2.2.4 Rounded punch on flat contact	23
2.3 Tribology	27
2.3.1 General	27
2.3.2 Friction.....	27
2.3.3 Wear	28
2.3.4 Archard wear equation.....	28
2.3.5 Energy wear approach.....	29
2.4 Metal fatigue.....	30
2.4.1 General	30
2.4.2 Fatigue mechanisms	30
2.4.3 Stress/strain fatigue approach	32
2.4.4 Fatigue stress criteria.....	36
2.4.5 Damage models	38
2.4.6 Fracture mechanics.....	47

2.5 Fretting.....	52
2.5.1 General	52
2.5.2 Fretting wear modelling	55
2.5.3 Fretting fatigue modelling	56
2.5.4 Surface damage parameters on fretting	57
2.5.5 Ratchtting failure mode.....	59
2.5.6 Fretting in hip joint implant.....	61
2.6 Summary	64
Chapter 3 Continuum Damage Mechanics for Fatigue and Fretting Fatigue	66
3.1 Overview	66
3.2 Fatigue model	66
3.2.1 Continuum damage fatigue model.....	66
3.2.2 Critical plane SWT model.....	67
3.2.3 Material data	68
3.3 Computational methodology.....	71
3.3.1 Fatigue damage computation.....	71
3.3.2 FE modelling of fatigue and fretting fatigue tests	73
3.4 Results and discussion	80
3.4.1 Plain fatigue results	80
3.4.2 Fretting fatigue results	89
3.5 Conclusions	96
Chapter 4 Finite Element Methodology for Fretting Wear-Fatigue Interaction	98
4.1 Overview	98
4.2 Constitutive model.....	99
4.3 Wear model	101
4.4 Fatigue model	106
4.4.1 Critical plane SWT fatigue damage model.....	106
4.4.2 Wear-fatigue damage algorithm	108
4.5 Ratchetting failure model	111
4.6 Summary	112
Chapter 5 An Investigation on the Effect of Contact Geometry on Fretting Wear-Fatigue Performance	113
5.1 Overview	113
5.2 Computational methodology.....	116
5.2.1 FE modelling	116
5.2.2 Loading histories.....	120

5.2.3 Tribological data	123
5.3 Results and discussion	124
5.3.1 Validation of unworn FE modelling methodology	124
5.3.2 Validation of FE energy-based wear simulation	130
5.3.3 Validation of FE critical-plane SWT fatigue life prediction simulation	134
5.3.4 Wear predictions for RF2 and RPF geometries.....	135
5.3.5 Cyclic plasticity and ratchetting for RF2 and RPF geometries	139
5.3.6 Critical-plane SWT evolution for RF2 and RPF geometries.....	143
5.3.7 Competition between ratchetting and fatigue.....	149
5.4 Conclusions	153
Chapter 6 Tribological Characterisation of Hip Implant Materials	157
6.1 Introduction	157
6.2 Material properties.....	157
6.3 Test method	158
6.3.1 Test description	158
6.3.2 3D stem neck-femoral head contact simulation	160
6.3.3 Tibological test.....	161
6.3.4 Profilometry test.....	163
6.3.5 Wear coefficient and hardness test.....	164
6.4 Results and discussion	164
6.4.1 3D stem-head contact modelling results.....	164
6.4.2 Pin design.....	169
6.4.3 Tribological tests results	170
6.4.4 Profilometry tests results	173
6.6 Sample tribological tests for other materials	178
6.7 Material grain size.....	179
6.8 Summary	179
Chapter 7 Fretting Wear-Fatigue of Taper-Lock Coupling in a Prosthetic Hip Implant.....	180
7.1 Overview	180
7.2 Numerical modelling of fretting wear and fatigue for hip implant	180
7.2.1 2D axisymmetric FE global model for fretting wear and fatigue in hip implants	180
7.2.2 Material data	183
7.2.3 2D FE submodel for fretting wear and fatigue in hip implants	183
7.3 Results and discussion	186
7.3.1 Analytical validation of 2D axisymmetric model	186
7.3.2 FE wear and fatigue results for global model.....	188

7.3.3 FE wear and fatigue results for submodel	194
7.3.4 Discussion	200
7.4 Conclusions	202
Chapter 8 Conclusions and Future Work	204
8.1 Conclusions	204
8.2 Future work.....	206
8.2.1 Tribological parameter improvement	206
8.2.2 Simulation of real pressure armour layers in flexible risers	207
8.2.3 Combining wear-fatigue methodology.....	207
8.2.4 Fretting wear-fatigue tests in hip implants	208
8.2.5 Design of hip implants	209
Appendix A1 NLCD model derivations	210
Appendix A2 SWT Fortran program and wear-fatigue interpolation program	233
Appendix A3 Abaqus subroutine for energy wear approach.....	244
References.....	247

Chapter 1

Introduction

1. 1 Overview

The subject of contact mechanics is generally considered to have started in 1882 (Johnson, 1985) with the publication by Heinrich Hertz of his paper *On the contact of elastic solids*. His interest in this problem was aroused by experiments on optical interference between glass lenses. Significant engineering developments in contact mechanics were achieved in the railway industry, in marine reduction gears and in the rolling contact bearing industry in the early 20th century.

Nowadays, wear and fatigue are familiar phenomena in industry. The economic implications of wear and fatigue are severe. It has been reported (Glaeser, 1981) that billions of dollars could be saved if the wear and fatigue life of components could be increased.

1. 2 Background and application for fretting

1.2.1 General

Fretting is, generally, in macroscopic scale engineering applications, defined as a surface damage phenomenon associated with small amplitude (under tens of μms), oscillatory motion which may occur between two nominally clamped contacting surfaces (Varenberg et al., 2004, Waterhouse, 1992). It is generally accepted that the transition from fretting to reciprocating sliding is in the range from 50 to 300 μm (Vingsbo et al. 1988), regardless of the normal load. Fretting has also been observed and studied in nano-scale (Varenberg et al., 2005). In the past, fretting (wear) was usually called fretting corrosion because oxidation is

normally accompanied with the fretting process, e.g. the fretting corrosion product of steel is normally reddish brown (while the pure corroded steel is normally gray) (Fitch, 1992). Under fretting motion, the resulting fretting wear and fretting fatigue can have significant implications for the fretted components. This phenomenon has been observed in many areas, as described in subsequent sections.

1.2.2 Aeroengine

High bypass ratio turbofan engines are normally adopted for civil use because of good fuel efficiency and low noise. As illustrated in Fig. 1.1, when the engine is in operation, bypass air flows around the jet core without mixing with the fuel and burning. The ratio of the bypass air to the amount of air flowing through the core is the bypass ratio. The study by the Intergovernmental Panel for Climate Change (Penner et al, 2000) suggests that a 25% increase in propulsive efficiency could be achieved by increasing the bypass ratio from around/under 10 (for modern transport engines) to above 30 (for unducted propulsors resembling large, swept propellers).

One economic way to increase the bypass ratio, which will not increase the engine weight, is to reduce the core diameter. However, this will generate increased stresses in the transmission components, which already experience wide variations in torque, axial load and rotating bending moments between take-off, cruise and landing. Spline couplings are frequently employed in the transmission shafts in turbofan engines due to their high torque transmission capacity and ability to accommodate misalignment and relative movements (Dudley 1957). However, as a result of being subjected to cyclic loading and small amplitude relative motion in the contacting regions, spline couplings are susceptible to fretting fatigue and fretting wear (Leen et al. 2002). As shown in Fig. 1.2 for a scaled aeroengine spline

coupling, fretting fatigue cracks and wear damage have been observed in these couplings. To prevent fretting failure in spline couplings and to deliver better design for increased bypass ratios in turbofans, it is necessary to comprehensively understand the fretting phenomenon in such components.

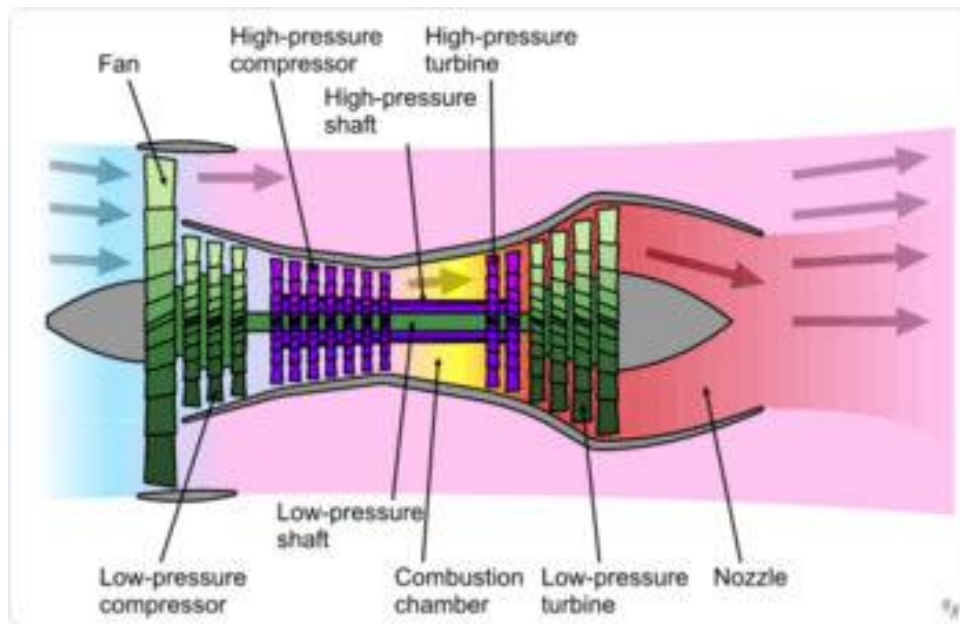


Fig. 1.1. Schematic diagram of a high-bypass turbofan engine

Another common location of fretting damage in turbofan engines is in the dovetail blade and disc assembly which is mounted on a circular rotor, as shown in Fig. 1.3. Fretting in this kind of joint has been recognized as one of the costliest sources of in-service damage related to high cycle fatigue in the US Air Force [Nicholas T. Critical issues in high cycle fatigue. *Int J Fatigue* 1999;21(S):221–31.].

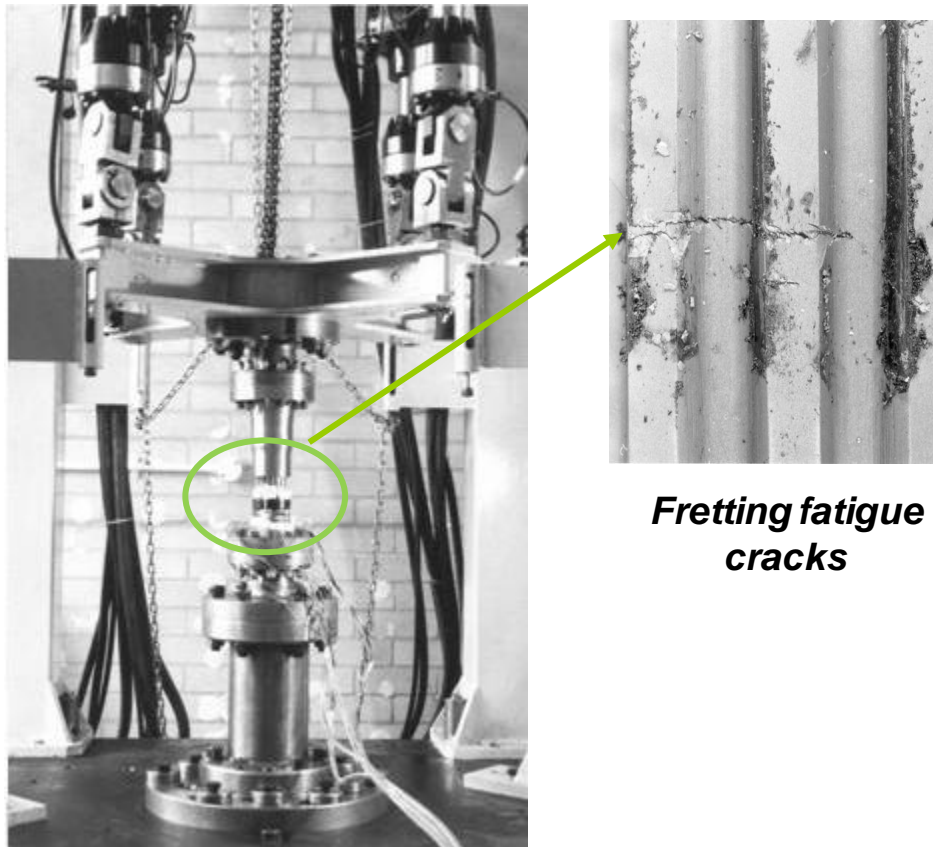


Fig. 1.2. Fretting damage on spline couplings (Leen et al. 2002)

Another common location of fretting damage in turbofan engines is in the dovetail blade and disc assembly which is mounted on a circular rotor, as shown in Fig. 1.3. Fretting in this kind of joint has been recognized as one of the costliest sources of in-service damage related to high cycle fatigue in the US Air Force (Nicholas T., 1999)

Many researchers and companies like Rolls-Royce and Pratt & Whitney have made great efforts in the research and development of fretting phenomenon in aero-engines. Apart from the aerospace industry, many other real-life service components also have the potential to experience fretting damage:

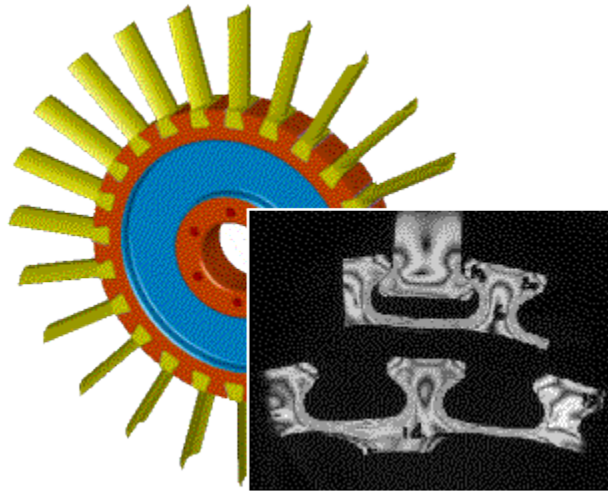


Fig. 1.3. Dovetail blade and disc assembly in aeroengine compressor (from <http://www.mie.utoronto.ca>)

1.2.3 Flexible riser

Although many countries in the world have met their obligations to reduce CO₂ emissions in order to tackle climate change, within the time scale for sufficient supply of clean energy to take place, fossil fuels like oil and gas will still be used. Due to the convenience of petroleum detection and extraction, the onshore oil industry has been developed for decades. However, oil depletion is inevitable, e.g. by 2004, 48 states of the U.S.A. were producing less than half the oil they did in 1970 (Appenzeller, T., 2004). Also, war and instability in certain regions (i.e. Middle East) lead to fluctuations in oil production and therefore greatly affects the global economy.

Continuous development in the offshore oil and gas industry is taking place for decades as significant quantities of resources have been found in areas such as the outer continental shelf and sedimentary basins, i.e. the U.S. Bureau of Ocean Energy Management, Regulation and Enforcement estimates that 60% of the total oil (86 billion barrels) and 40% of the total

natural gas (420 trillion cubic feet) in remaining undiscovered fields in the United States are contained in the area of the Gulf of Mexico. Other notable offshore fields today are found in the North Sea, the Santa Barbara basin, Nova Scotia, South China Sea, etc.

One specific example application which has motivated the present work is the pressure armour layer of a marine flexible riser which has been used for years in the offshore industry. Companies like MCS Kenny, NKT Flexibles and Technip would like to know the contacting phenomena in such layers, in order to estimate the life and performance of the risers. This unbonded riser structure increases considerably the resistance to pressure, tension and torsion. As illustrated in Fig. 1.4, a marine flexible riser is a pipe composed of several layers including spirally wound steel layers and thermoplastic material layers. With the relative motion between the adjacent layers, it is designed to allow large deflections under combined torque, axial and bending loads. Due to the dynamic environment for such risers, subjected to combined conditions of waves, current and movement of the floating body to which is connected the riser, the life expectancy of the product may depend not just on the quality of the material (resistant to sea water and oil, aging), but also on the wear resistance and fatigue performance of the contacting/moving components. When the relative motion is small enough, potential fretting wear and fatigue may occur in the steel layers - especially in the groove and nub contact regions in the pressure armour layer, which has an interlocking contact arrangement, as illustrated in Fig. 1.5 and 1.6. A Hertzian round on flat (Fig. 1.5a) contact geometry is commonly assumed for this groove-nub contact due to the ready availability of the contact (normal and tangential) analytical solutions for this geometry. In reality the contact geometry is closer to a round punch on flat (Fig. 1.5b). One aim of this work is to consider the problem of predicting the comparative fretting performance of these two contrasting contact geometries, under a specified normal load, with a specified tangential

displacement cycle, for a given material combination and within a specified geometrical space envelope. The objective is to understand which geometry is better in terms of both wear and fatigue/cracking performance, particularly when wear-induced evolution of contact geometry is accounted for.

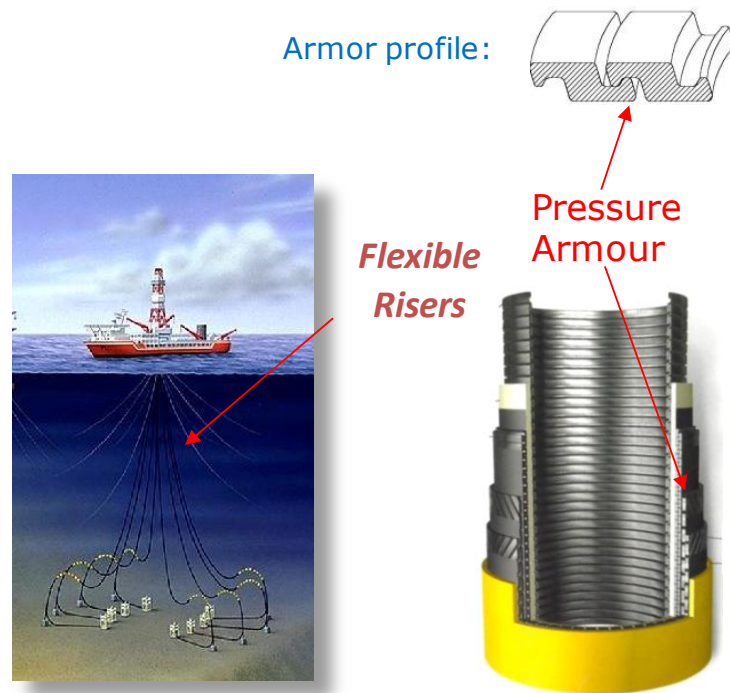
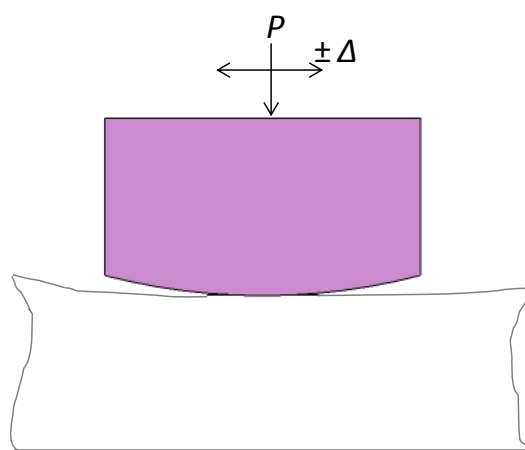
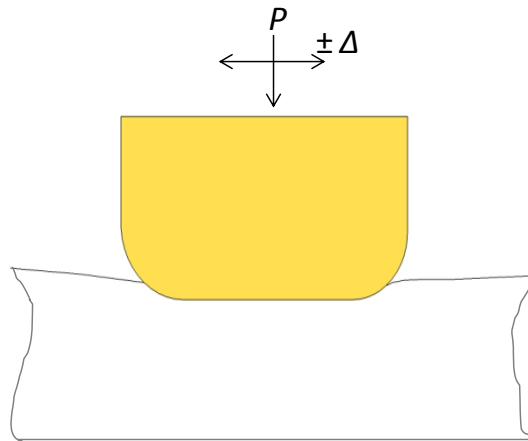


Fig. 1.4. Flexible riser and pressure armour layer. (From MCS Kenny)



(a)



(b)

Fig. 1.5. Schematic of (a) Hertzian cylinder on flat contact and (b) rounded punch on flat contact.

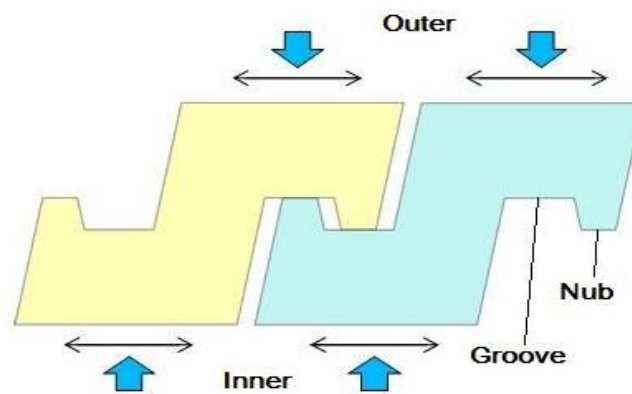


Fig. 1.6. Schematic of pressure armour layer contact.

1.2.4 Prosthetic implants

Globally, the medical technology industry is estimated to be worth between €173 billion and €196 billion. In Ireland, the medical device sector is thriving and has grown to become a significant contributor to the Irish economy. There are now over 160 medical technology companies in Ireland, exporting €6.8b worth of products annually and employing over 24,000 people.

In the world, the orthopaedic implants sector holds a specifically important market position, e.g. U.S. demand for orthopaedic implants will increase 8.9 percent annually to nearly \$22 billion in 2012, predicted by 'Orthopedic Implants US Industry Study with Forecasts for 2012 & 2017'. In the Irish medical devices industry, orthopaedic implants are also among the most important products. This may be attributed to the following reasons:

- joint diseases account for half of all chronic conditions for elderly people;
- fractures related to osteoporosis have dramatically increased in the past 10 years, especially in women over 50 years old;
- a significant number of people are injured or disabled every year by road accidents;
- active usage of the joints occurs in people who are frequently doing fairly extreme sports, e.g. marathons.

As the knee or the hip loses function due to the above reasons, joint replacement becomes necessary.

Although fretting occurs in orthopaedic implants, such as hip joints, it hasn't yet received adequate attention. As illustrated in Fig. 1.7, a prosthetic hip implant normally contains a long stem implanted in the femur and a spherical femoral head that articulates with the acetabulum. Typically, for a modular head, a cylindrical taper coupling is employed between the stem neck and the head. The candidate materials for the stem and acetabular cup are normally Co-Cr, Ti-6Al-4V (Ti64) alloys and 316L stainless steel since they have good mechanical properties and biocompatibility. Two different manufacturing methods of Ti64 alloy hip stems are available, forged and direct metal laser sintered (DMLS). The stem-head coupling is susceptible to fretting fatigue and fretting wear (corrosion) due to the potential for

oscillatory small amplitude displacements, under the combined effects of the clamping pressure due to the taper-lock with superimposed ambulatory (cyclic) loading, exacerbated by the *in vivo* environmental conditions. The development of a scientific approach for fretting life prediction in such couplings is particularly important for new candidate materials and manufacturing methods. At the same time, the fretting wear debris (metal particles and ion release) can cause a local inflammatory reaction in the bone tissues/cells, which is one of the reasons leading to osteolysis, and eventually resulting in aseptic loosening, or, cause other problems, e.g. pseudotumors, which may have potential danger to the host and caused by metal sensitivity. In this case, it is necessary for the patient to have a hip joint replacement with an increased size implant. For example, partly due to the above reason, a worldwide recall was required for hip implants involving the DePuy ASR AX acetabular system, launched in 2004; 3,516 Irish patients had this device fitted, according to RTE news.

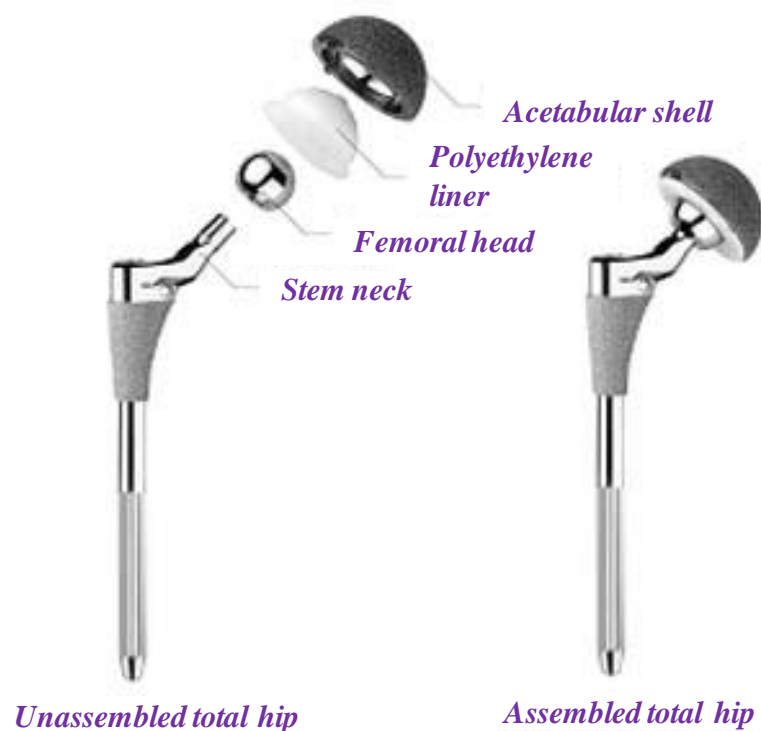


Fig. 1.7. A total hip joint prosthesis adopting a modular stem (from www.zimmer.com)

To deal with the aseptic loosening problem, to select the correct material and to manufacture a robust hip implant product, it is necessary to comprehensively understand and be able to predict the fretting wear performance of the candidate materials (Ti-6Al-4V, Co-28Cr-6Mo, etc.) for such couplings under realistic operating condition. One objective of this work is to predict fretting and wear behaviour at the head-neck contact of a hip implant, based on both experiments and computational simulation.

1.2.5 Steel rope wires

Steel wire ropes have great ability to support large axial loads with comparatively small bending or torsional stiffness (Wang et al., 2012). Due to the combination of high strength and flexibility, they have been successfully employed in a many industries, i.e., mines, lifts, bridges, barges, tyres, etc. (Waterhouse et al., 1971)

Wire ropes are normally composed of wires wound into bundles called strands, which are then wound into the final rope (Cruzado et al., 2011) as shown in Fig. 1.8. In service, tensile loading on the rope is applied and released periodically, and certain positions of the rope run over the sheave constantly. This results in sudden tensile loading or bending in the rope and thus large stress concentration on the contacting surfaces of the adjacent wires occurs. Also the loading condition leads to small amplitude oscillatory motion between the contacting wires. Therefore despite the excellent mechanical performance of the rope, it is susceptible to internal fretting damage (McColl et al., 1995; Harris et al., 1993; Attia, 1992). Typical positions which are especially important for fretting are between the outermost wires of strands and core or between the outermost wires of adjacent strands (Cruzado et al., 2011).

The endurance and life of the wire rope are extremely important for the safety of people in industry, e.g., miners, lift users, etc. Therefore the study of fretting in wire ropes is essential.

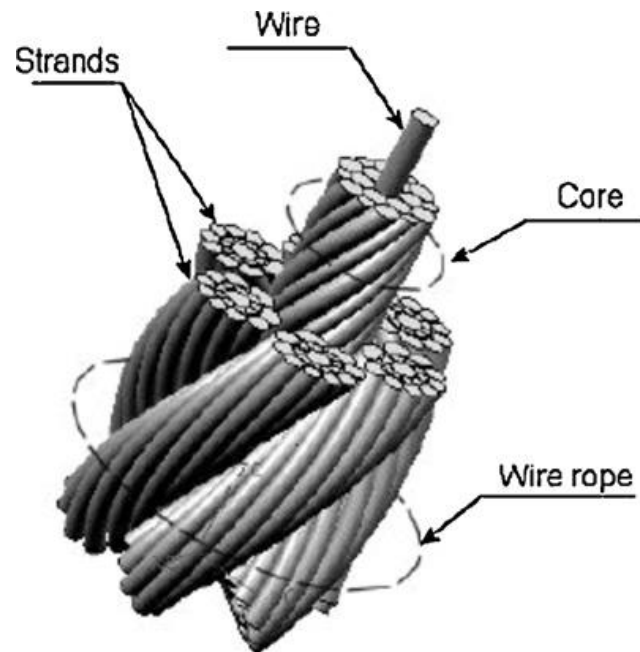


Fig. 1.8. Schematic of wire rope (Cruzado et al., 2011)

1.3 Aims

The aim of this work is the development and validation of methodologies for fretting fatigue, wear and wear-fatigue interaction in simple and complex engineering contacts, with particular application to taper-lock assemblies in modular hip implants. The objectives should be expressed in terms of the following:

Computational developments:

- Continuum damage mechanics for fatigue damage in fretting
- Energy-based wear simulation technique with plasticity

- Wear-fatigue interaction predictive tool

Experimental:

- Tribological characterisation of DMLS Ti64 and more conventional Ti64 for hip implant applications

Applications:

- Effect of contact geometry, in terms of wear-fatigue evolution, for marine riser nub-groove contact and other applications
- Macro-scale and micro-scale fretting wear-fatigue analysis of taper-lock assembly in prosthetic hip implants.

1. 4 Scope of thesis

The scope of this thesis is shown in Fig.1.9.

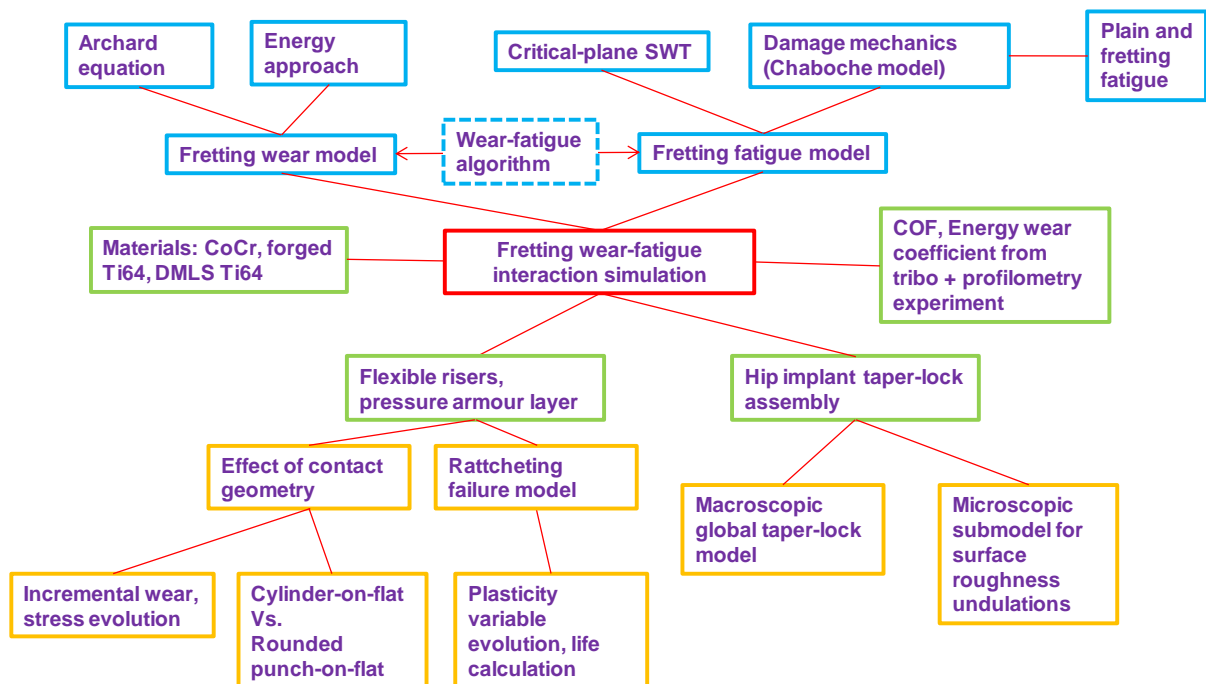


Fig. 1.9 Methodology map

Chapter 2 presents relevant knowledge about fretting in the literature. Contact mechanics, tribology and especially wear are introduced. Fatigue of metals is discussed and different approaches to estimate fatigue lives are presented. The combined methodology of wear and fatigue to solve fretting problems is reviewed.

Chapter 3 describes the three-dimensional finite element implementation of a continuum damage mechanics formulation for multiaxial plain fatigue and fretting fatigue, incorporating elastic modulus reduction due to fatigue damage. The implementation is validated against theoretical and published experimental results for uniaxial and notched multiaxial fatigue under different combinations of mean and alternating stresses for Ti-6Al-4V. An automatic incrementation scheme is developed for efficient computation of damage accumulation and hence stress re-distribution. The method is also implemented in two-dimensional, plane strain for fretting fatigue and is shown to successfully capture the effect of contact slip on fatigue life for a round-on-flat fretting geometry. Comparisons are also made with a critical-plane multiaxial fatigue approach for fretting and very good agreement is achieved.

Chapter 4 describes a combined finite element (FE) modelling based methodology for fretting wear-fatigue interaction. The energy wear approach (Fouvry et al. 2003) is adopted to calculate wear depth through a UMESHMOTION subroutine and the critical plane Smith-Watson-Topper (SWT) (Smith et al. 1970) method in conjunction with the Miner - Palmgren rule (Palmgren, 1924) is adopted to predict multiaxial fretting crack nucleation. A non-linear kinematic hardening plasticity formulation is employed to model the Bauschinger effect which is a complex phenomenon observed in the cyclic behaviour of polycrystalline metals and single crystals. Fretting lives are also predicted based on the ratchetting failure as a competitive mechanism to fatigue cracking.

Chapter 5 presents experimental testing of a number of mechanical and biomedical engineering materials. Ti-6Al-4V is used in aeroengine and prosthetic hip implant applications. 316L stainless steel is a typical material used in flexible risers and is also implemented in hip implants. Co-28Cr-6Mo is a typical candidate material for hip implants. Two different manufacturing methods of Ti64 alloy hip stems are considered here, forged and direct metal laser sintered. Representative tribological tests and profilometry analysis are carried out to investigate the tribological behaviour and wear resistance of the material combinations under realistic loading conditions.

Chapter 6 presents a study combined methodology described in Chapter 4 to two different contact arrangements: round on flat (RF) and round punch on flat (RPF). This is a first step towards understanding and predicting fretting in flexible risers and other complex contacts. It adopts a finite element (FE) methodology to compare the significance of the round on flat (Hertzian assumption) to that of a round punch on flat, in terms of fretting performance.

Chapter 7 presents application of the combined fretting wear-fatigue methodology described in Chapter 4 to a real prosthetic hip implant. 2D axisymmetric modelling of the head-neck contact is employed to predict wear-fatigue interaction for the hip implant. Fretting wear-fatigue performance for stems made from forged Ti64 and DMLS Ti64 is compared. A macro-micro model of the head-neck contacting surfaces is built to investigate the effect of machining undulations on fretting wear-fatigue performance.

Chapter 8 outlines the conclusion of this work and overall discussions are given. Recommendations for future work are also made.

Chapter 2

Literature Review

2.1 Introduction

Fretting occurs when two contacting bodies experience small amplitude oscillatory motion. It is observed in many mechanical assemblies such as keyway-shaft couplings, shrink-fitted couplings, dovetail blade-disc assemblies, hip joint implants, etc. To comprehensively study fretting, a variety of studies need to be carried out. This literature review will first discuss the existing knowledge of contact mechanics and then tribology, especially wear, will be reviewed. An overview of fatigue of metals is also given. Later it will focus on the computational fretting wear and fatigue problem and the corresponding applications.

2.2 Contact mechanics

2.2.1 General

The subject of contact mechanics is said to have started in 1882 with the publication by Heinrich Hertz of his classic paper *On the contact of elastic solids* (Johnson, 1985). The Hertz theory considers the normally loaded solids as non-conforming bodies. The assumptions made in the theory are as follows (Johnson, 1985):

1. The surfaces are continuous and non-conforming
2. The strains are small so that the solids remain in the elastic regime
3. Each solid can be considered as an elastic half-space (the contact width should be much smaller than the contact radius and the lateral dimension of the solid)

4. The surfaces are frictionless

Solutions for sphere on flat and cylinder on flat contacts (Hertzian geometries) are given in the Hertz theory. The flat punch with rounded corners on flat contact has been examined by Jäger (Jäger, 2002) and Ciavarella and co-workers (Ciavarella et al. 2003, Ciavarella et al. 1998).

2.2.2 Sphere on flat contact

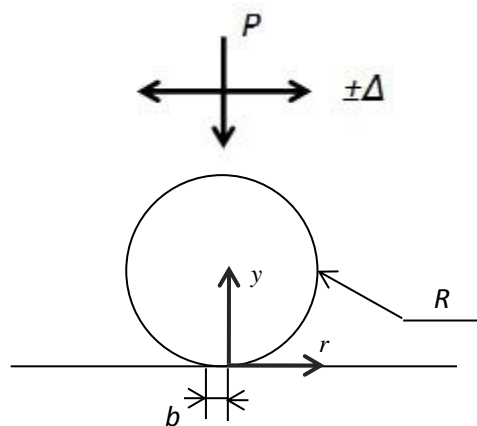


Fig. 2.1 Sphere on flat contact

Fig. 2.1 shows the contact between a sphere and a flat surface. A normal load P and an applied stroke of $\pm\Delta$ is applied to the sphere specimen. $Q(t)$ is the measured tangential force with an amplitude of Q_{max} .

Consider the normal load only state. The contact area will be circular, having a radius b .

When experiencing a tangential load parallel to the flat surface, the sphere will tend to slide. When $Q_{max} \geq \mu P$, Amonton's law of friction specifies the tangential traction at a certain distance r to the contacting centre.

If Q_{max} is less than μP , partial slip occurs and in the central of the contact region, a stick zone exists. The method of solution to the problem of partial slip was first presented by

Cattaneo (1938) and independently by Mindlin (1949). The stick zone has a circular shape and the stick radius is given in Johnson, 1985.

Typical distributions of contact pressure and shear traction under gross slip conditions for the sphere on flat are shown in Fig. 2.2.

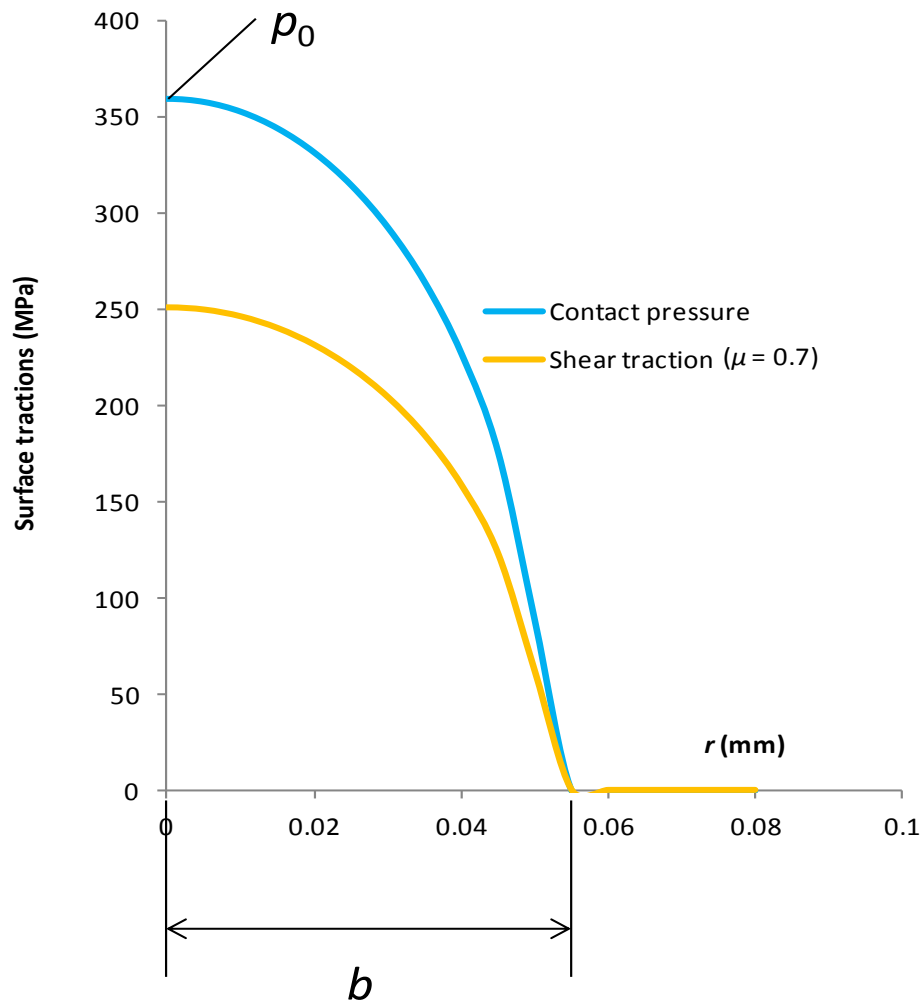


Fig. 2.2 Typical distributions of contact pressure and shear tractions ($\mu = 0.7$) for sphere on flat in gross slip.

The complete stress field for a general point on the contact surface has been found by Hamilton and Goodman, (1966), Hamilton, (1983), Sackfield and Hills, (1983), Hills, Nowell and Sackfield, (1993).

2.2.3 Cylinder on flat contact

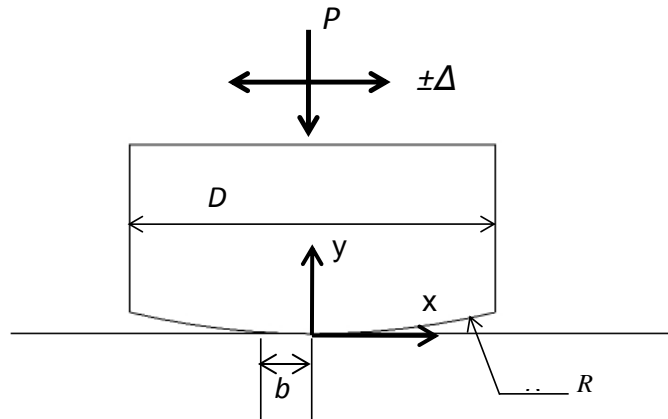


Fig. 2.3 Cylinder on flat contact

The solution for stress, strain and slip fields of this contact is well known, therefore this arrangement is widely used for fretting studies. As shown in Fig.2.3, a normal load P and a stroke of $\pm\Delta$ (resulting in an alternating tangential force $Q(t)$ of amplitude Q_{max}) are applied to the cylinder specimen.

Consider the normal load only state. The contact pressure distribution is given by the Hertzian solution (Johnson, 1985)

The normal stresses due to the normal load along the y -axis can be derived (Johnson, 1985). When the tangential load is introduced, relative slip occurs between the two contacting surfaces. In gross slip situations, Q_{max} is increased to its limiting value μP , at which point the cylindrical body slides. The tangential traction is given by:

$$q(x) = \mu p_0 (1 - x^2 / b^2)^{1/2} \quad (2.1)$$

The shear stress τ_{xy} can be expressed as:

$$\tau_{xy} = (\tau_{xy})_p + (\tau_{xy})_q \quad (2.2)$$

where the suffixes p and q refer to stress components due to the normal pressure and tangential traction acting separately. The shear stress components are given by (Hills and Nowell, 1994).

If Q_{max} is less than μP , partial slip occurs and in the centre of the contact region, a stick zone exists (Fig. 2.4). The shear traction in this condition has been presented by Johnson, (1985).

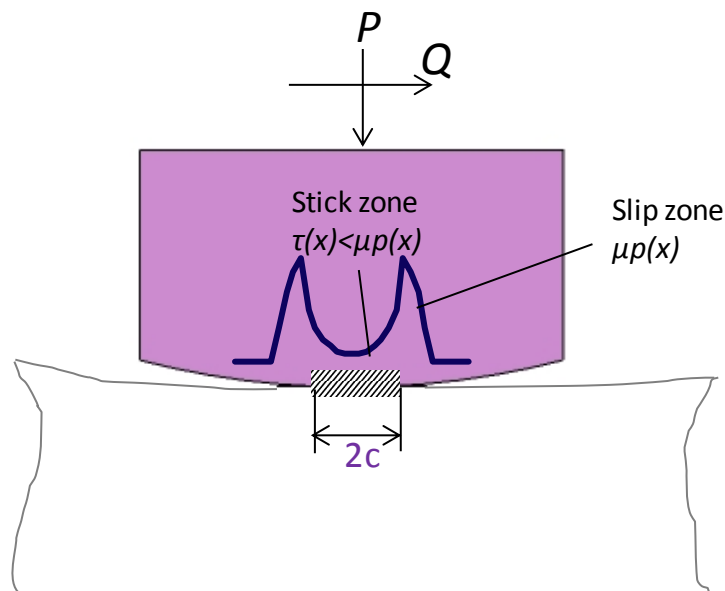


Fig. 2.4 Schematic of partial slip condition for cylinder on flat contact

Typical distributions of contact pressure and shear traction in the gross and partial slip conditions for the cylinder on flat contact are shown in Fig. 2.5.

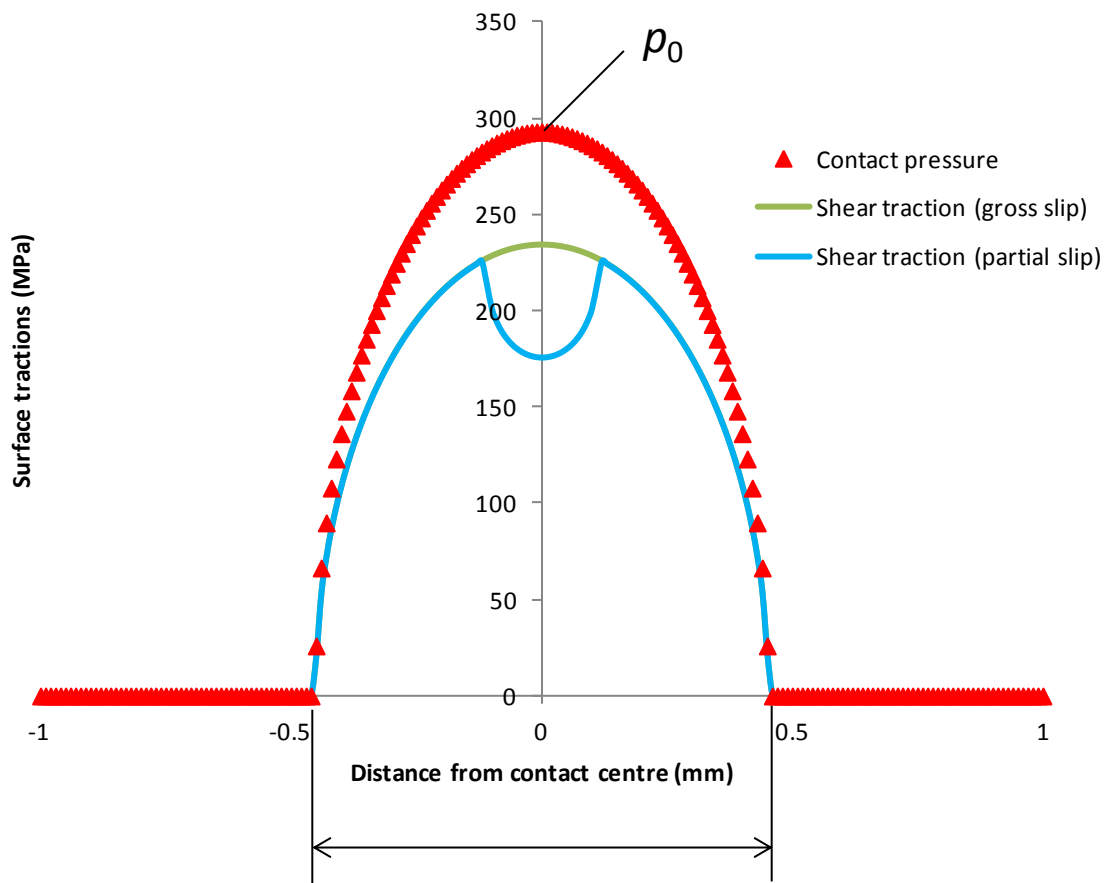


Fig. 2.5 Typical distributions of contact pressure and shear tractions for cylinder on flat.

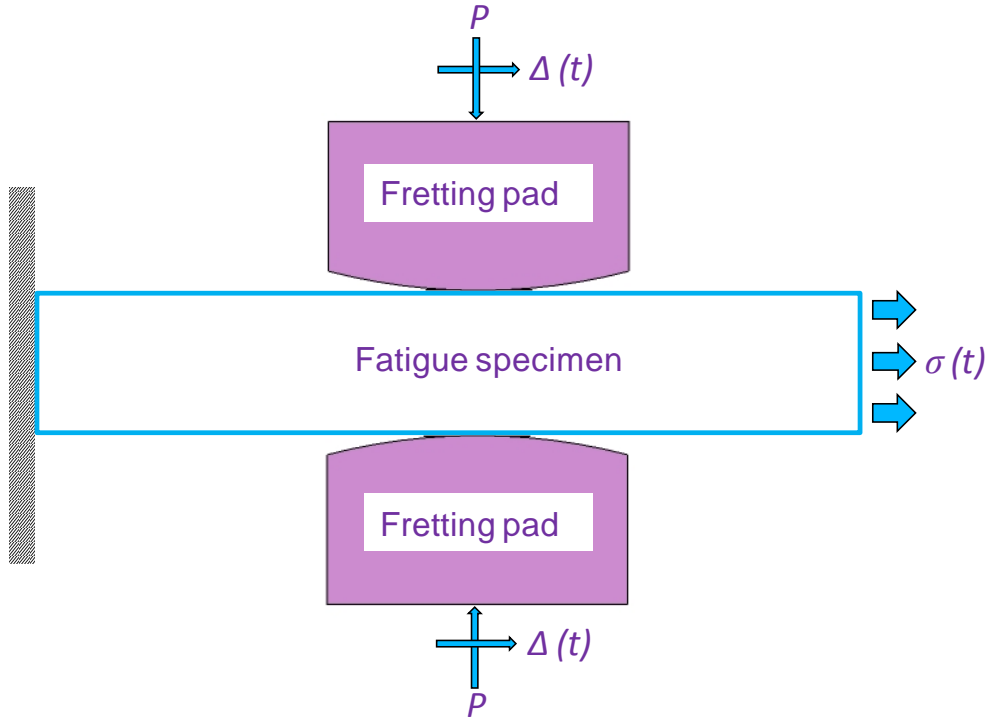


Fig. 2.6 Cylinder on flat fretting contact with substrate loading

Fretting fatigue normally takes place in the presence of bulk stresses within one or both of the contacting bodies (Hills, 1994), due to loadings other than the contact itself. Hills et al. (1988) employed an arrangement shown in Fig. 2.6 to represent a typical fretting fatigue situation with a substrate load. Under such conditions, the shear traction distribution shifts to one side by an eccentricity of e , as predicted by Hills and Nowell (1994), resulting in a modified distribution given by:

$$q(x) = \mu p_0 \sqrt{1 - (x/b)^2} + q'(x) \quad (2.3)$$

where

$$q'(x) = 0 \quad (2.4)$$

in the slip zone and

$$q'(x) = -\mu p_0 \frac{c}{b} \sqrt{1 - ((x - e)/c)^2} \quad (2.5)$$

in the stick zone.

The eccentricity is given by:

$$e = \frac{\sigma b}{4\mu p_0} \quad (2.6)$$

where σ is the substrate load, c is the stick zone half width, μ is coefficient of friction, P is the normal load and Q is the tangential load.

Fig. 2.7 shows the theoretical distribution of shear traction from Eq. 2.5.

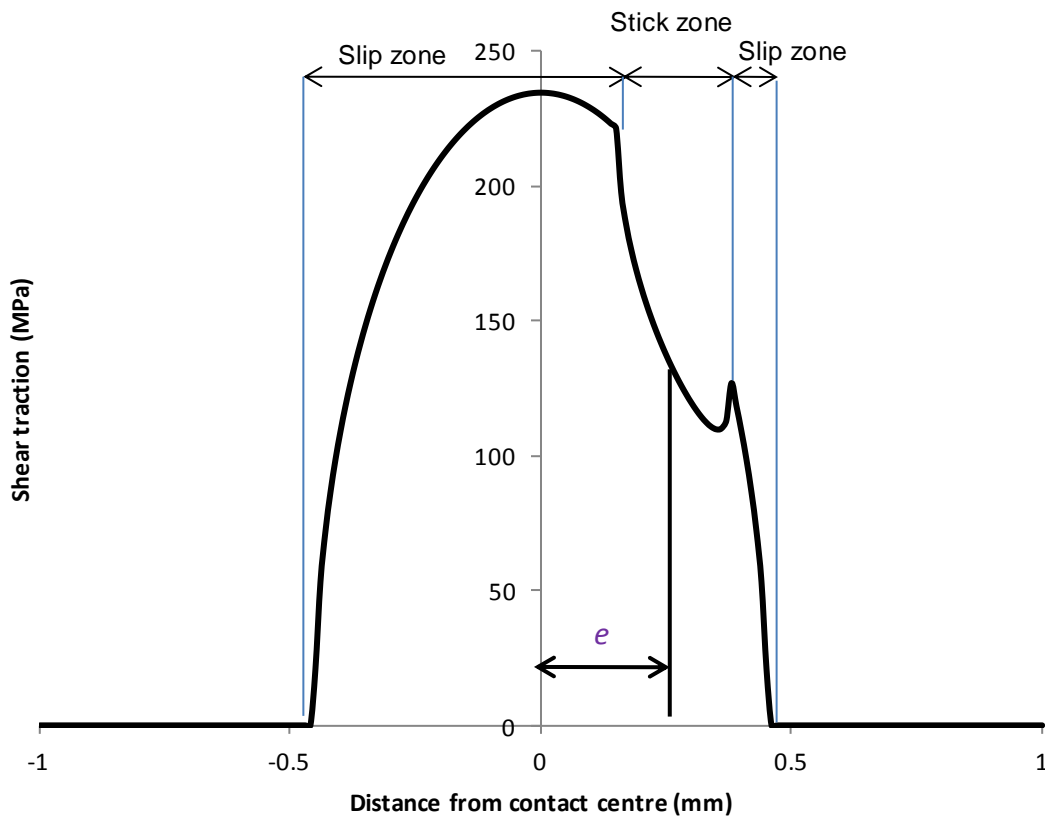


Fig. 2.7 Typical shear traction distribution of cylinder on flat by theoretical calculations (Hills et al. 1994)

2.2.4 Rounded punch on flat contact

Clements et al. (2008) shows drawings of the pressure armour layer interlocking contact profiles in a flexible riser. However, in reality it is difficult to be certain that it is a cylinder on flat contact or a punch on flat with rounded edges (or even sharp edges). Therefore it is important to study the contact performance of other geometries, too. As shown

in Fig. 2.8, a normal load P and an applied stroke $\pm\Delta$ (resulting in an alternating tangential force $Q(t)$ of amplitude Q_{max}) are applied to the rounded punch.

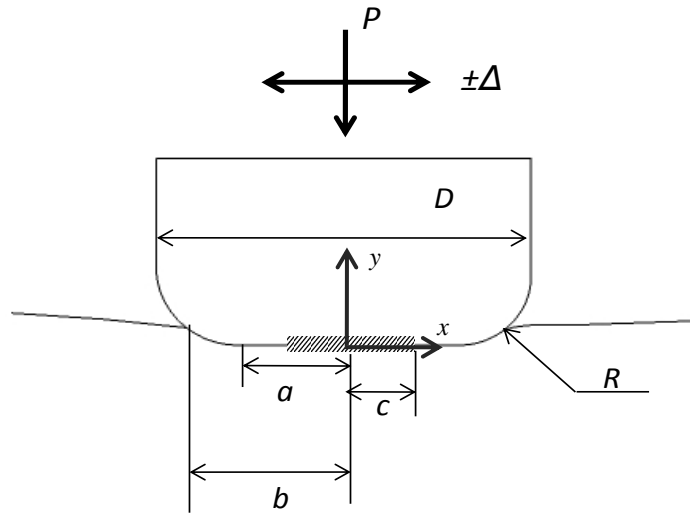


Fig. 2.8 Rounded punch on flat contact

Ciavarella et al. (1998, 2003) and Jager (2002) have described the analytical solutions for this contact. Considering the normal load only state, the contact half width b is implicitly given by:

$$\frac{PAR}{b^2} = \frac{\pi}{2} - \frac{a}{b} \sqrt{1 - \left(\frac{a}{b}\right)^2} - \arcsin\left(\frac{a}{b}\right) \quad (2.7)$$

where

$$A = \frac{\kappa_1 + 1}{4G_1} + \frac{\kappa_2 + 1}{4G_2} \quad (2.8)$$

$$\kappa_1 = \begin{cases} 3 - 4\nu_1 & \text{for plane strain} \\ \frac{3 - \nu_1}{1 + \nu_1} & \text{for plane stress} \end{cases} \quad (2.9)$$

The symbols G_1 and ν_1 denote the shear modulus and Poisson's ratio of body 1, respectively, and the index 2 characterizes values of body 2. The formula for κ_2 can be obtained after substitution of the index 1 with 2 in Eq. 2.9.

Letting

$$x = b \sin \phi \tag{2.10}$$

$$a = b \sin \phi_0$$

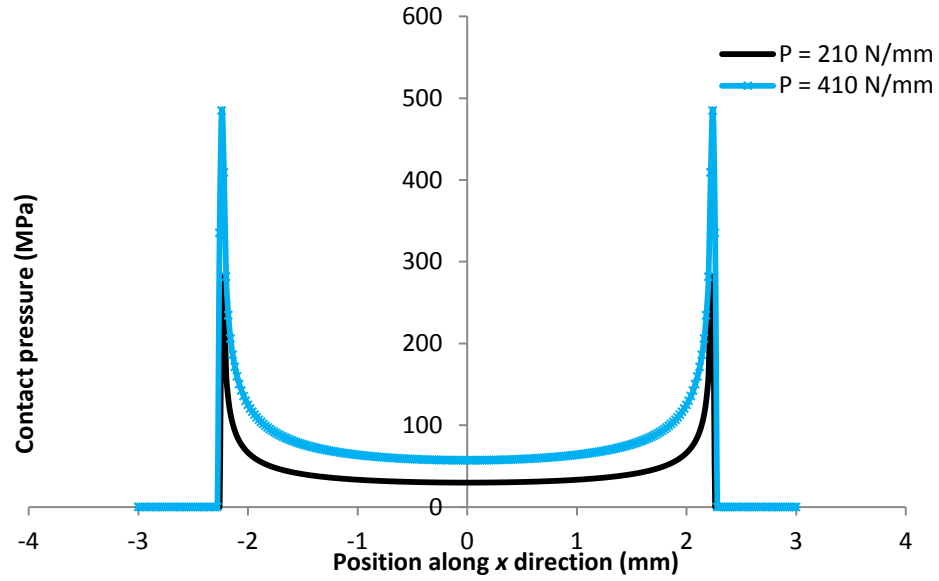
then the contact pressure $p(\phi)$ is given by:

$$\frac{2\pi R}{aE^*} p(\phi) = -(\pi - 2\phi_0) \frac{\cos \phi}{\sin \phi_0} - \frac{\sin \phi}{\sin \phi_0} \ln \left| \frac{\sin(\phi + \phi_0)}{\sin(\phi - \phi_0)} \right| - \ln \left| \tan \frac{\phi - \phi_0}{2} \tan \frac{\phi_0}{2} \right| \tag{2.12}$$

The calculation of b needs a non-linear solution. The resulting distribution, upon solution of Eq. 2.12, of the contact pressure is shown in Fig. 2.9. As the normal load increases, contact area (b) increases and the overall pressure increases. The accurate contact pressure calculation needs small x increment (Δx). Convergence of peak contact pressure can be achieved if Δx small enough. The location of peak contact pressure is normally between a and b . In this case (Fig. 2.9), it is at ± 2.235 mm.

When a tangential load is introduced, if Q_{max} is smaller than the limiting value μP , partial slip occurs. Also here, a stick zone exists and c is the stick zone half width. The value of c is given by:

$$\frac{|Q(t)|}{\mu P} = 1 - \left(\frac{c}{b}\right)^2 \frac{\pi/2 - (a/c)\sqrt{1 - (a/c)^2} - \arcsin(a/c)}{\pi/2 - (a/b)\sqrt{1 - (a/b)^2} - \arcsin(a/b)} \tag{2.13}$$



(a)

Fig. 2.9 Contact pressure distributions of rounded punch on flat contact for two loading conditions.

It is important to note that the above analytical solution is only applicable when $a \leq c \leq b$, which is actually quite restrictive, i.e. once the stick zone width is smaller than the flat area length, this method is no longer applicable (Ciavarella and Macina, 2003).

The maximum tensile stress typically occurs at the trailing edge of a sliding contact. High values of the maximum tensile stress increase the possibility of crack propagation from surface defects (Koji, 2000), or lead to secondary fractures near pre-existing flaws (Wang et al., 2003). The maximum tensile stress in the rounded punch on flat is calculated as (Ciavarella and Macina, 2003):

$$\sigma_{xx}(b,0) = 2\mu \frac{(b-a)}{AR} - 2 \frac{\mu}{\pi AR} w(c) \quad (2.14)$$

where $w(c)$ is:

$$w(c) = -4\sqrt{b^2 - c^2} \arccos \sqrt{\frac{a+c}{2c}} + 2(b-a) \arcsin \sqrt{\frac{(b+c)(c-a)}{2c(b-a)}} + 2(a+b) \arcsin \sqrt{\frac{(b-c)(c-a)}{2c(a+b)}} \quad (2.15)$$

Substantial amount of work on RPF has also been done by Dini et al. 2004, 2005 and 2006; Hils and Dini 2006; Nowell et al. 2006, etc. Experimental tests have been carried out on RPF configuration, e.g. Bramhall, 1973; Cattaneo, 1938; Nowell, 1988.

2.3 Tribology

2.3.1 General

Tribology is the science and technology of interacting bodies in relative motion (Hutchings, 1992); it broadly includes the study of friction, wear and lubrication. This work is mainly concerned with friction and wear.

2.3.2 Friction

Friction is defined as the resistance encountered by one surface when moving over another. Two important classes of relative motion are sliding and rolling.

Lenoardo da Vinci (1499) first described two empirical Laws of Sliding Friction:

1. The friction force is proportional to the normal load;
2. The friction force is independent of the apparent area of contact.

The two laws are found to be true for most metals and many other materials except for polymers. A third law attributed to Coulomb (1785) states:

3. The friction force is independent of the sliding velocity.

A common observation is that to initiate sliding the initial tangential force is greater than the sliding tangential force, which means the coefficient of static friction is greater than

the coefficient of dynamic friction. However once steady-state sliding is achieved, it is found for most situations that the coefficient of friction is independent of the sliding velocity over a large range.

2.3.3 Wear

When two surfaces are in contact and sliding over each other, the accumulation of particle detachment, 'wear', can be observed for one or both of the surfaces. Wear can be mainly divided into six categories: adhesion, abrasion, fatigue, erosion, corrosion and electrical arc. (Bhushan & Gupta, 1991). Adhesive wear often relates to the galling tendency in which wear debris and material compounds transfer from one surface to another. In many engineering applications, surfaces slide over each other associated with the presence of hard particles. The resulting wear in this condition is called abrasive wear (Hutchings, 1992). Godet and co-workers (Godet, 1984) argued that mechanisms such as adhesion and abrasion are only particle detachment mechanisms whereas a real wear process should be governed by both particle detachment and elimination of wear particles. They referred to the process whereby particles transport from inside the contact to outside as 'third-body flow'. The effect of this debris layer against wear is taken into account.

2.3.4 Archard wear equation

The classical Archard wear equation for sliding wear (Archard, 1953) is based on the theory of asperity contact and has been validated against pin-on-ring sliding tests for a series of materials (Archard et al., 1956). It is given by:

$$\frac{V}{S} = K \frac{P}{H} \quad (2.16)$$

where V is the wear volume, S is the sliding distance, K is the dimensionless wear coefficient, P is the normal load and H is the hardness of the material. The Archard wear equation links

the loss of material volume to the product of the sliding distance by the normal load. It describes the severity of wear by means of the wear coefficient K .

For engineering applications the quantity K/H is often more useful. This is called the dimensional wear coefficient (k). In fretting wear, it has been found that, for this approach, the dimensional wear coefficient is dependent on load and stroke, e.g. see McColl et al., 2004.

2.3.5 Energy wear approach

An alternative wear prediction method, referred to as the energy wear approach, which has been proposed by Fouvry and co-workers, e.g. Fouvry et al., 2003, considers the interfacial shear work as the significant wear parameter controlling wear volume calculation. This approach has benefits over the Archard-based approach in that a single wear coefficient can be used across a range of fretting load-stroke combinations, i.e. energy wear coefficient α 'unifies' wear prediction across a wide range of stroke, from 846 μm to 1.38 mm in Magaziner et al., 2008 and from 50 μm to 100 μm in Liskiewicz et al., 2005, specifically including both partial slip and gross slip regimes. The energy wear approach can be represented by the following equation:

$$V = \alpha \sum E \quad (2.17)$$

where α is the dimensional wear coefficient and $\sum E$ is the accumulated dissipated frictional energy. The concept of the energy wear coefficient is that a value independent of load and stroke be identified from tests across a range of loads and strokes (Fig. 2.10); this is not typically possible with the Archard approach. Nonetheless, it can be shown that in the gross slip regime, the two approaches (in terms of predictions) are the same for an appropriate choice of Archard and energy wear coefficients, i.e. $\alpha/\mu = K/H$, certainly in terms of

predicted wear scar dimensions. However, in the partial slip regime, when $Q < \mu P$, the two approaches will not give the same results unless K/H is modified. This will be discussed more in Chapter 6.

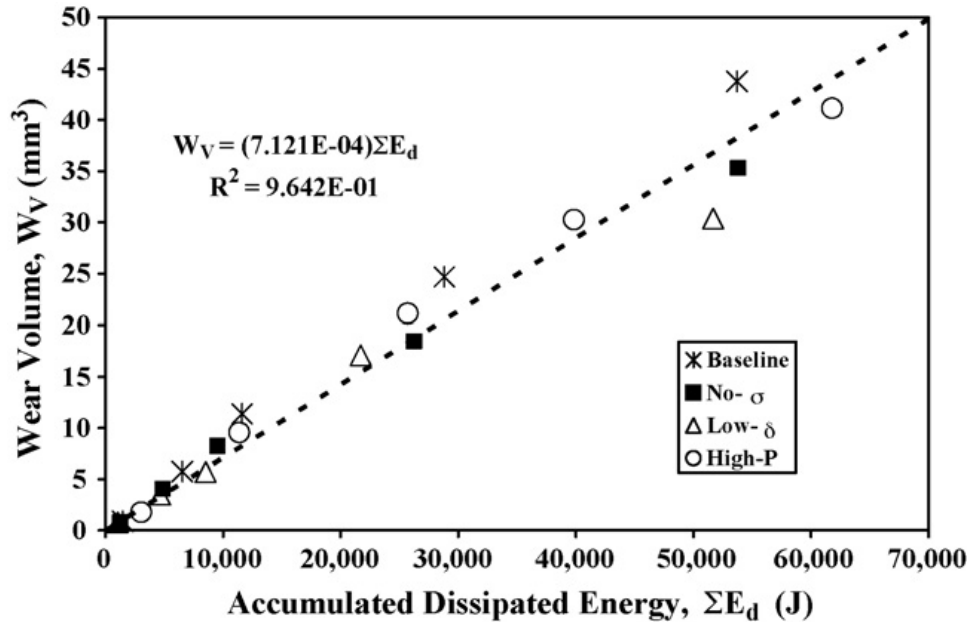


Fig. 2.10 Variation of wear volume with total dissipated energy for a number of load conditions and stroke amplitudes (Magaziner et al. 2008)

2.4 Metal fatigue

2.4.1 General

When a component or a whole structure experiences cyclic external loading, fatigue may occur leading to fracture, even without noticeable damage throughout the majority of the loading cycles (Klesnil et al. 1992). Development of this branch of technology has been significant in the past century. Schütz, 1996 described the history of fatigue study in detail.

2.4.2 Fatigue mechanisms

In nature, most structural metals are polycrystalline and contain numerous crystals or grains. Each grain has its own mechanical properties, ordering direction, and directional

properties. Slip in grains has been observed under both monotonic and cyclic loading but with different slip profiles (Stephens et al., 2000). Using electron microscopy, Forsyth, 1969 showed that both slip band intrusions and extrusions occurred on the metal surface when it experienced cyclic loading. Slip band intrusions result in micro-scale stress concentrations, which may cause the cracks to develop. It has been shown in Kennedy, (1963) that increased intensification of slip lines as a function of load cycles occurs for pure polycrystalline nickel. More slip lines occur and thicken as the number of cycles increases. After electropolishing, most of the slip bands can be eliminated. However, a few slip bands remain, which are called 'persistent slip bands'. Moreover, it has been found that fatigue cracks grow from these persistent slip bands (Forsyth, 1969). Fatigue cracks initiate in local slip bands followed by the two stages of fatigue crack growth: stage I and stage II (Forsyth, 1969). In stage I, the micro fatigue cracks tend to grow in a plane of maximum shear stress range. In stage II, as the cycle number increases, the fatigue cracks tend to grow along planes of maximum tensile stress range. Finally, fracture occurs. Grain size has strong relationships with fatigue cracks. Typical identified nucleated crack lengths in fretting tests on Ti-6Al-4V, specifically designed to capture crack nucleation, were of the same order as the grain size (20–50 μm). Therefore the use of crystal plasticity (CP) within a fretting model is sometimes a logical step for modelling of crack initiation in fretting. Also, volume averaging is normally carried out to deal with stress gradient.

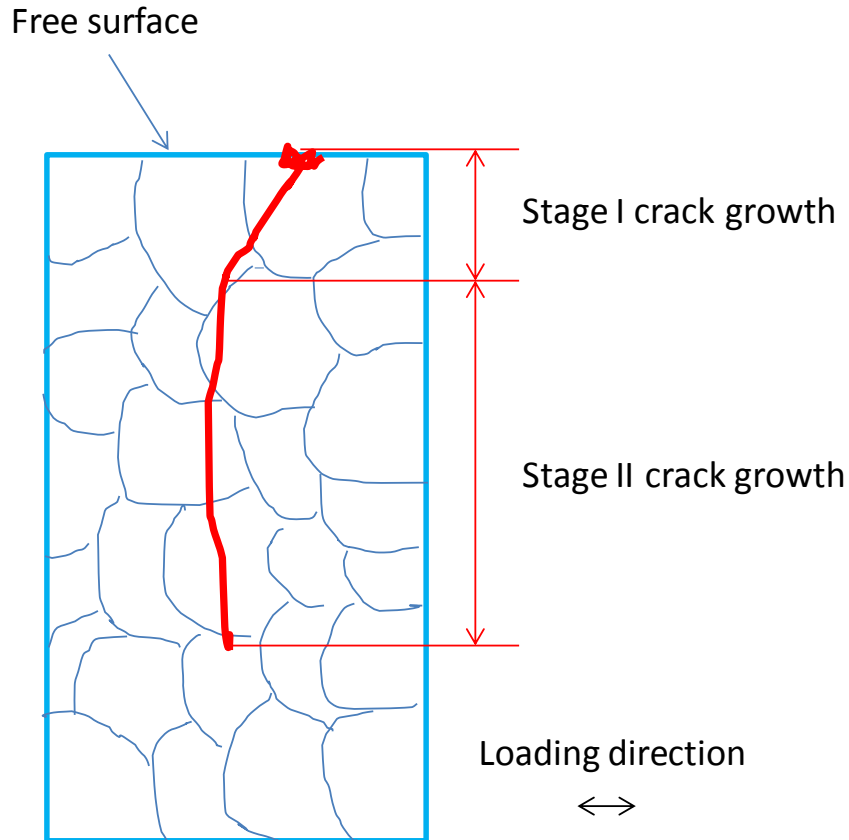


Fig. 2.11 The two stages of fatigue crack growth.

2.4.3 Stress/strain fatigue approach

During the 1850s and 1860s Wöhler performed many fatigue tests which are considered to be the first systematic investigation of fatigue (Wöhler, 1858 and Wöhler, 1860). He presented the stress versus life ($S-N$) diagrams (Wöhler, 1870) and pointed out how stress amplitude affects fatigue life. Goodman, (1899, 1962) proposed a simplified theory concerning the effect of mean stress. Later Gerber, (1874), Soderberg, (1930) and Morrow (1960) proposed different relationships between the mean stress and the alternating stress at a given fatigue failure lifetime, as shown in Fig. 2.12. Among the four curves, Soderberg, (1930) gives the most conservative relationship.

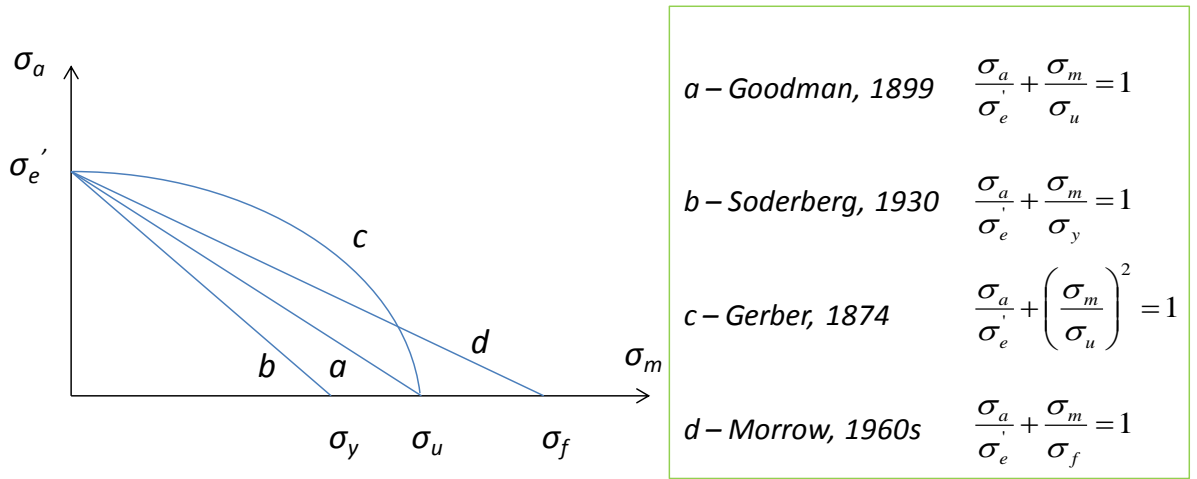


Fig. 2.12 Relationship between mean stress and alternating stress for a given fatigue failure lifetime by different researchers. (σ_y - yield stress; σ_u - ultimate tensile stress; σ_f - true fracture stress; σ_e' - effective alternating stress at failure for a lifetime of N_f cycles; σ_a - alternating stress; σ_m - mean stress)

Basquin, (1910) developed the stress-life approach by finding out the log-log relationship between stress amplitude and life in high cycle fatigue (HCF):

$$\frac{E\Delta\epsilon_e}{2} = \sigma_f' (2N_f)^f \quad (2.18)$$

where $E\Delta\epsilon_e/2$ is the maximum normal stress amplitude in the elastic range of the material, σ_f' and f are the (Basquin) fatigue strength coefficient and exponent (HCF constants), and E is the Young's modulus.

When experiencing high amplitudes of cyclic plastic stresses and strain, low cycle fatigue (LCF) takes place. The relationship between the plastic strain amplitude and the number of cycles to failure is given by the Coffin-Manson equation (Zahavi et al., 1996):

$$\frac{\Delta\epsilon_p}{2} = \epsilon_f' (2N_f)^g \quad (2.19)$$

where $\Delta\varepsilon_p/2$ is the maximum normal strain amplitude in the plastic range of the material, ε_f' and g are the (Coffin-Manson) fatigue ductility coefficient and exponent (LCF constants).

Total fatigue damage have been evaluated using various combinations of parameters, known as fatigue indicator parameters, FIPs. Fatigue life can be calculated using the values of FIPs. One well known FIP is the Smith-Watson-Topper (SWT) parameter proposed by Smith et al. (Smith et al., 1970). It considers both elastic (HCF) and plastic (LCF) strain components and takes into account the mean stress effect by multiplying the Basquin's formulation for the maximum normal stress σ_{\max} by the total strain-life equation.

Total strain can be related to life through the following equation which is the summation of Basquin's equation and the Coffin-Manson equation:

$$\frac{\Delta\varepsilon}{2} = \frac{\Delta\varepsilon_e}{2} + \frac{\Delta\varepsilon_p}{2} = \frac{\sigma_f'}{E} (2N_f)^f + \varepsilon_f' (2N_f)^g \quad (2.20)$$

where $\Delta\varepsilon$ is the total strain range. The SWT parameter is then given by:

$$SWT = \sigma_{\max} \frac{\Delta\varepsilon}{2} = \frac{(\sigma_f')^2}{E} (2N_f)^{2f} + \sigma_f' \varepsilon_f' (2N_f)^{f+g} \quad (2.21)$$

SWT parameter and Equations 2.18 and 2.19 were developed for uniaxial fatigue cases where the largest principal stress is much greater than the other principal stresses. For most engineering applications fatigue is a multiaxial problem. Many efforts have been made to develop a scientific approach for multiaxial fatigue. Brown & Miller, (1973) first suggested the combined use of maximum shear strain range and tensile strain normal to the plane of maximum shear. Evolved from Brown & Miller's work, the critical plane approach has been developed and widely used (Kallmeyer et al., 2002). It is based on the physical observation that fatigue cracks initiate and grow on certain planes within a material, where the crack growth and orientation depends on the normal stresses and/or shear stresses and strains on

these planes (Socie, 1987). The planes on which most fatigue damage occurs are called 'critical planes'. Combined with FIPs, i.e. the SWT parameter, the critical plane approach can provide solutions to multiaxial fatigue problems.

Fatemi and Socie (1988) further developed the critical plane approach by using normal stress instead of tensile strain normal to the plane of maximum shear. This is due to the existence of non-proportional loading or out-of-phase loading in many engineering applications. Under proportional loading conditions, the principal stresses are proportional to each other, hence the angle of principal axes remain constant during all the fatigue cycles. Non-proportional (out-of-phase) loading has often been found to be more damaging than the equivalent proportional loading in the low cycle region by a number of researchers (Garud, 1981, Zamrik et al., 1973, Kanazawa et al., 1977). While under non-proportional loading, the principal axes rotate and the material experiences extra cyclic hardening, thus more damage occurs in this situation. The use of normal stress instead of strain in the parameter accounts for the additional cyclic hardening thus overcomes the problem for non-proportional loading conditions (Fatemi and Socie, 1988).

For a shear dominated failure, the Fatemi-Socie (FS) parameter is often adopted. It has been used in fretting analyses, e.g. Hirsch et al., 2011:

$$FS = \frac{\Delta\gamma}{2} (1 + k\sigma_{\max}) = \frac{\tau'_f}{G} (2N_f)^f + \gamma'_f (2N_f)^g \quad (2.22)$$

where $\Delta\gamma$ is the shear strain range over one cycle and k is a fitting parameter. G is the shear modulus, τ'_f is the fatigue shear stress and γ'_f is the fatigue shear strain coefficient.

Materials behaviour and/or loading conditions result in different failure modes, i.e. shear and tensile. Therefore the choice of FIP depends on materials and loading conditions. Fatemi and Soice (1988) have proposed the use of one of two multiaxial FIPs, one for shear

cracking failure modes and one for tensile cracking failure modes. Such parameters should take account of both crack initiation and propagation. For shear cracking failure modes, e.g. the FS parameter, the parameter should include shear strain amplitude for crack initiation, and maximum normal stress on the plane of maximum shear strain amplitude for crack propagation. For tensile cracking, e.g. the SWT parameter, the parameter should include maximum principal strain amplitude for initiation, and maximum normal stress on the plane of maximum principal strain amplitude for propagation.

2.4.4 Fatigue stress criteria

The stresses that result in fatigue failure present a more complex problem than the static failure, since the principle stresses and their directions may fluctuate constantly in each cycle in an arbitrary way. Sines, (1959) showed that the relation between the effect of the static stress and the permissible amplitude of alternating stress was linear. Verified by a series of experimental data, the Sines criterion considers that the permissible alternation of the octahedral shear stress for a constant life is a linear function of the mean hydrostatic stress. Mathematically it is expressed as:

$$\frac{1}{3} \left\{ (\sigma_{1a} - \sigma_{2a})^2 + (\sigma_{2a} - \sigma_{3a})^2 + (\sigma_{1a} - \sigma_{3a})^2 \right\}^{\frac{1}{2}} \leq A - \eta \sigma_{H,mean} \quad (2.23)$$

where σ_{1a} , σ_{2a} , σ_{3a} are the principal stress amplitudes and A , η are material constants for the specific cyclic lifetime. $\sigma_{H,mean}$ is the mean hydrostatic stress defined by:

$$\sigma_{H,mean} = \frac{1}{6} [\max(\text{tr}(\boldsymbol{\sigma})) + \min(\text{tr}(\boldsymbol{\sigma}))] \quad (2.24)$$

with $\text{tr}(\boldsymbol{\sigma}) = \sigma_{11} + \sigma_{22} + \sigma_{33}$. The 'max' and 'min' are selected over a fatigue loading cycle.

Another way to describe the Sines criteria is by the octahedral shear stress amplitude which is expressed by:

$$A_H = \frac{1}{2} \left\{ (\sigma_{1a} - \sigma_{2a})^2 + (\sigma_{2a} - \sigma_{3a})^2 + (\sigma_{1a} - \sigma_{3a})^2 \right\}^{\frac{1}{2}} \quad (2.25)$$

$$= \frac{1}{2} \left[\frac{3}{2} (S_{ij,max} - S_{ij,min}) \bullet (S_{ij,max} - S_{ij,min}) \right]^{1/2}$$

where $S_{ij,max}$ and $S_{ij,min}$ are the maximum and the minimum values of the deviatoric stress tensor ij components during one loading cycle.

The Sines fatigue limit criterion in this model is formulated by:

$$A_H^* = \sigma_{10} (1 - 3b_1 \sigma_{H,mean}) \quad (2.26)$$

where σ_{10} is the fatigue limit at the fully reversed loading condition and b_1 is a material constant.

Fig. 2.13 shows schematic constant life contours in 2D principal stress space for different hydrostatic mean stress levels, according to the multiaxial version of the Sines criterion. It assumes that if the stress state is within a given level curve corresponding to a particular value of life, a fatigue life greater than that value of life is obtained. It is also observed that for a given desired cyclic lifetime (e.g 10^5), from the tensile mean stress condition to the compressive mean stress condition, the size of the ellipse increases; also, for a given stress range, lower life is obtained when increasing hydrostatic mean stress and higher life is obtained when reducing hydrostatic mean stress.

Alternatively, for example, the Crossland criterion can be adopted, which is formulated by:

$$A_H^* = \sigma_{10} \frac{1 - 3b_1 \sigma_{H,max}}{1 - b \sigma_{10}} \quad (2.27)$$

where $\sigma_{H,max}$ is the maximum hydrostatic stress, expressed by:

$$\sigma_{H,max} = \frac{1}{3} \max(tr(\boldsymbol{\sigma})) \quad (2.28)$$

By comparing the two criteria for 'silal' cast iron and Cr-Va steel under reversed tension-torsion, (Lemaitre and Chaboche, 1990) shows that the selection of one or the other of the two criteria depends on the material.

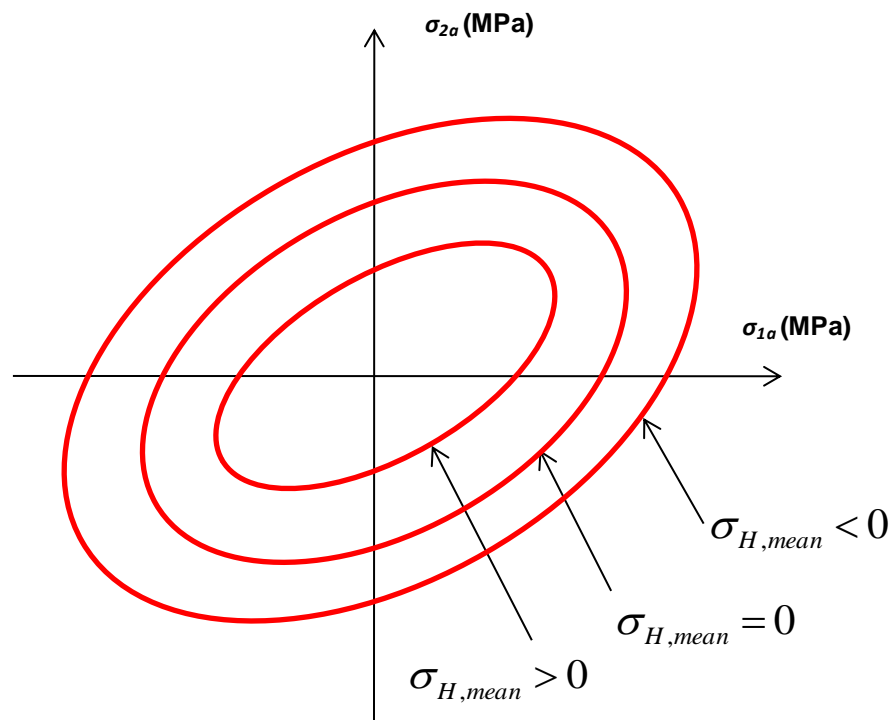


Fig. 2.13. Schematic constant life contours in 2D principal stress space for different hydrostatic mean stress levels according to the multiaxial version of the Sines criterion, for the specific cyclic life time.

2.4.5 Damage models

Fatigue damage can be considered as the damage accumulation from each fatigue cycle. Cyclic damage can be calculated using a variety of methods, for example, the use of FIPs, such as the SWT and the FS parameters, discussed above. The most common damage

accumulation rule is the linear damage rule first formulated by Miner in 1945 based on a suggestion by Palmgren in 1924. It has been extensively used in fatigue design as follows:

$$W = \sum_{i=1}^N \frac{n_i}{N_{fi}} \quad (2.29)$$

where N is the number of different load cycles experienced, n_i is the number of cycles experienced at fatigue loading level i , and N_{fi} is the predicted number of cycles to failure from a stress/strain fatigue life approach at loading cycle i . The occurrence of $W = 1$ indicates predicted location, orientation and number of cycles for crack nucleation. This Miner-Palmgren damage rule assumes the accumulated damage is independent of the load levels thus damage is linearly accumulated. However, in reality, the rate of damage accumulation may be a function of the load amplitude such that at low load levels most of the life is involved in crack nucleation, while at high load levels most of the life is spent in crack growth (Stephens et al., 2000). For example, Fig. 2.14 shows the schematic of actual fatigue damage fraction versus cycle ratio at three stress levels and the one by linear damage rule. Evidently at point A in Fig. 2.14, the accumulation of damage D is quite different; thus the produced damage fraction is dependent on the stress level. To remedy the deficiency of the linear Palmgren-Miner law, researchers have proposed non-linear cumulative fatigue damage rules, e.g. Marco and Starkey, (1954). However, though many non-linear damage rules have been developed, due to the complicating factors encountered during complex loading levels, the Palmgren-Miner rule is still the most widely used approach to predict fatigue life of nucleation and in many cases the total life to fracture.

Damage laws are normally based on the fundamentals of material microstructures. Zhang et al. 2009 and McDowell et al. 2010 investigate the microstructure-sensitive model

for fretting/fatigue purposes. Dick et al. 2006 and Goh et al. 2003 introduce crystal plasticity to fretting.

A large part of fatigue life is related to the process of microcrack nucleation and development until some macroscopic crack initiates; partly because of this, damage evolution is often quite non-linear, as shown in Fig. 2.14. Damage mechanics (Lemaitre and Chaboche, 1990) is a continuum approach which describes the material degradation throughout fatigue

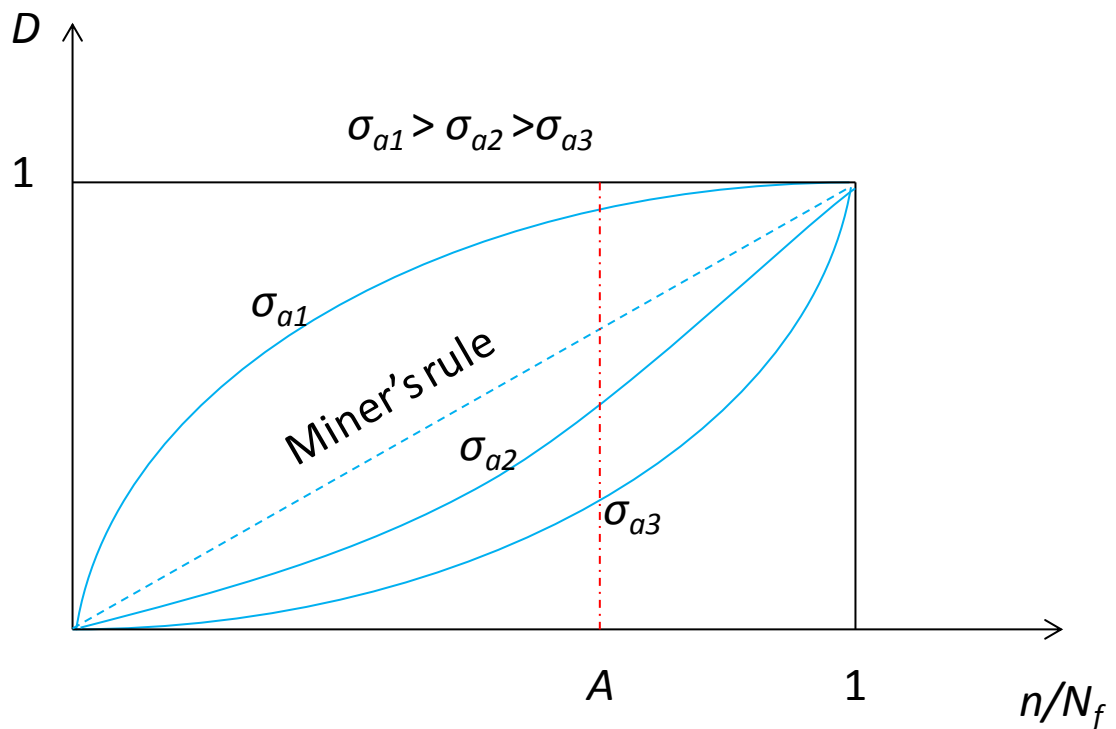


Fig. 2.14 Schematic of fatigue damage fraction versus cycle ratio.

loading cycles. After the stage that some macroscopic crack initiates, crack propagation becomes more rapid and fracture mechanics can be adopted. While fracture mechanics is based on the analysis of existing cracks, cumulative damage theories predict the evolution of internal damage before macrocracks become visible. Based on remaining life and continuum damage concepts (Chaboche et al., 1988), Lemaitre and Chaboche, (1990) proposed a non-linear continuous damage (NLCD) model for uniaxial fatigue. However, the measurements

obtained from changes in the mechanical response suggest that it is necessary to take into account damage evolution using the concept of effective stress. Therefore a combined damage formula was proposed (Chaboche et al., 1988). Since the applied loads are often multiaxial and have complex histories in one loading cycle, the NLCD model was extended to 3D (Lemaitre and Chaboche, 1990). The NLCD model has been applied in engineering simulations. For example, Kim and co-workers (2007) studied creep-fatigue-interacted lifetime based on continuum damage mechanics for the Ni-based superalloy. Marmi and co-workers (2009) applied the continuum fatigue damage model as a post-processor to the finite element (FE) analysis of tensile samples with and without notches, where reasonable agreement was shown between the FE results and experimental data. Fretting fatigue cracks may remain hidden under the contacting bodies until growth. The use of the NLCD model represents a potentially powerful method for predicting the evolution of fretting fatigue damage. Damage mechanics has not previously been applied to fretting fatigue and therefore this represents a limitation in fatigue life prediction method for fretting problems.

LeMaitre and Chaboche (1990) have presented some fundamental concepts in damage mechanics. As illustrated in Fig. 2.15, the mechanical measurement of local damage relative to the direction \vec{n} , for example in a cylinder on flat contact arrangement, is given by:

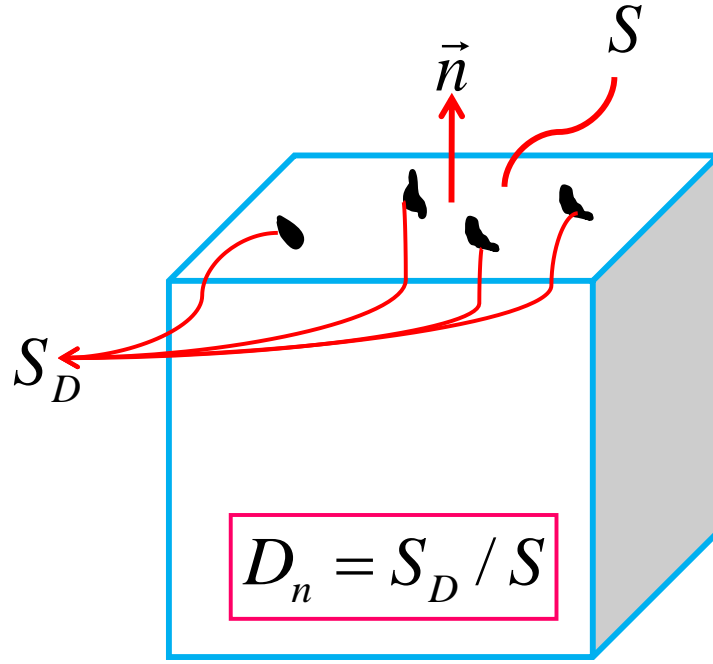


Fig. 2.15 Damaged element illustration.

$$D_n = S_D / S \quad (2.30)$$

where S_D is the total area of the defect traces and S is the area of a section of the volume element identified by its normal \vec{n} .

Assuming isotropic damage evolution for the material, the damage tensor \mathbf{D} is reduced to a scalar variable $\mathbf{D} = D \cdot \mathbf{I}$: where \mathbf{I} is the second-order identity tensor. In a uniaxial model, based on remaining life and continuum damage concepts, one way to introduce fatigue damage growth can be illustrated as this form:

$$\frac{dD}{dN} = D^\alpha \cdot \left[\frac{\sigma_{\max} - \bar{\sigma}}{M(\bar{\sigma})} \right]^\beta \quad (2.31)$$

where N is the number of cycles, σ_{\max} is the maximum stress during one loading cycle, $\bar{\sigma}$ is the mean stress during one loading cycle, β is a material constant and $M(\bar{\sigma})$ is a function which depends on $\bar{\sigma}$, given as:

$$M(\bar{\sigma}) = M_0(1 - b_2\bar{\sigma}) \quad (2.32)$$

where M_0 and b_2 are constants determined from Woehler's curves from fatigue tests, possibly as functions of temperature. α depends on σ_{\max} and $\bar{\sigma}$:

$$\alpha = 1 - a \left\langle \frac{\sigma_{\max} - \sigma_l(\bar{\sigma})}{\sigma_u - \sigma_{\max}} \right\rangle \quad (2.33)$$

where σ_u is the ultimate tensile stress and a is a material parameter determined from fatigue tests. The fatigue limit $\sigma_l(\bar{\sigma})$ is satisfactorily represented by Goodman's linear relation, and depends on the mean stress as follows:

$$\sigma_l(\bar{\sigma}) = \sigma_{l_0} + \bar{\sigma}(1 - b_1\sigma_{l_0}) \quad (2.34)$$

where σ_{l_0} is the fatigue limit at the fully reversed loading condition and b_1 is a material constant.

The elastic damage law has been justified on thermodynamical grounds in (Lemaitre and Chaboche, 1990). The effective area of resistance is $\tilde{S} = S - S_D = S(1 - D)$; thus by definition, the effective stress $\tilde{\sigma}$ is given by:

$$\tilde{\sigma} = \sigma S / \tilde{S} = \sigma / (1 - D) = E \varepsilon_e \quad (2.35)$$

where ε_e is the strain measured from the damaged material. Alternatively, the damaged material law can be written as:

$$\sigma = E(1 - D)\varepsilon_e = \tilde{E}\varepsilon_e \quad (2.36)$$

where \tilde{E} can be interpreted as the elastic modulus of the damaged material (Lemaitre and Chaboche, 1990) and thus damage becomes:

$$D = 1 - \tilde{E} / E \quad (2.37)$$

In engineering, damage measurement can be achieved by using the above equation. However, the measurement of very small strains to calculate \tilde{E} can be difficult.

To use the concept of \tilde{E} to represent the damaged material which contains fatigue-induced defects or cavities can be adopted and thus material stiffness reduces throughout the loading cycles. It is worth noting that in fretting fatigue, due to contact loading-induced compressive stresses during a significant portion of the fretting cycle, micro-crack closure occurs over a significant portion of the fretting cycle. Hence, the use of modulus reduction for damage modelling may over-estimate the effects of local cracking.

It has been shown in (Chaboche et al., 1988) that Eq. 2.51 is not sufficient to achieve non-linear accumulation and evolution of damage. As pointed out by (Lemaitre and Chaboche, 1990), damage evolution equations of the form of Eq. 2.51, in which the loading and damage D are separable variables, always leads to linear accumulation. However, this only works well when there is little variation in the amplitude and mean values of stress. Hence, to achieve non-linear accumulation (i.e. for different stress levels, mean and amplitude) and non-linear evolution (see also Marco and Starkey, 1954), it is necessary to use a more sophisticated damage evolution equation with non-separable D and loading, by replacing D in Eq. 2.51 by $[1-(1-D)^{\beta+1}]$ (Chaboche et al., 1988), so that the damage rate equation becomes:

$$\dot{D} = \frac{dD}{dN} = [1 - (1 - D)^{\beta+1}]^{\alpha} \cdot \left[\frac{\sigma_{\max} - \bar{\sigma}}{M_0 (1 - b_2 \bar{\sigma})(1 - D)} \right]^{\beta} \quad (2.38)$$

Comparisons between Equation 2.51 and 2.58 have been made. Fig. 2.16 shows the damage evolution curve based on Equation 2.51 and 2.58, accumulated in a custom-written Fortran program. Evidently the modified damage rate equation is much more non-linear compared with Equation 2.51.

The number of cycles to failure for an assumed constant stress condition is obtained by integrating the above between $D = 0$ and $D = 1$ ($D = 1$ for $N = N_F$), leading to:

$$N_F = \frac{1}{1 + \beta} \cdot \frac{1}{aM_0^{-\beta}} \frac{\langle \sigma_u - \sigma_{\max} \rangle}{\langle \sigma_{\max} - \sigma_l(\bar{\sigma}) \rangle} \cdot \left[\frac{\sigma_a}{1 - b_2 \bar{\sigma}} \right]^{-\beta} \quad (2.39)$$

where σ_a is the constant stress amplitude during one loading cycle.

Fig. 2.16 shows $S-N$ data predicted by the integrated theory (Eq. 2.59) for different R ratios for uniaxial condition for Ti-6Al-4V.

The stress and strain in real engineering problems are normally multiaxial; therefore the NLCD model needs to be extended to 3D (Chaboche et al., 1988), to give damage evolution:

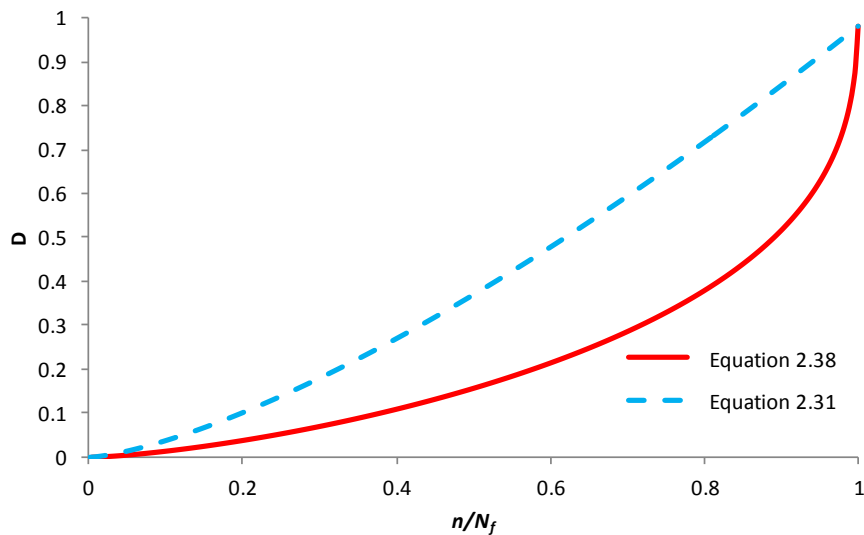


Fig. 2.15 Damage evolution estimated by Equation 2.38 and 2.31 in Fortran program, for $\bar{\sigma} = 400$ MPa and $\sigma_{\max} = 800$ MPa for Ti-6Al-4V.

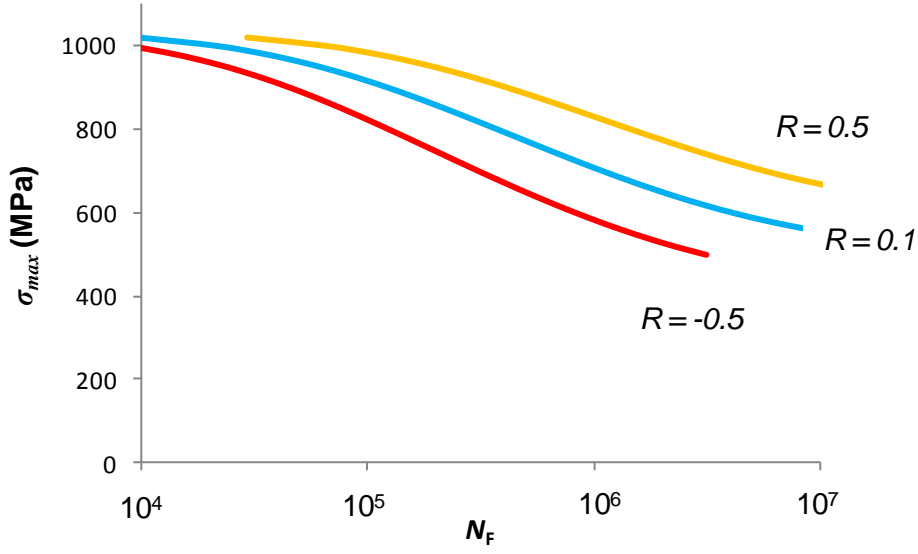


Fig. 2.16. S - N data predicted by integrated theory (Eq. 2.39) for different R ratios for Ti-6Al-4V.

$$\dot{D} = \frac{dD}{dN} = \left[1 - (1-D)^{\beta+1} \right]^{\alpha} \cdot \left[\frac{A_{II}}{M_0 (1 - 3b_2 \sigma_{H,mean}) (1-D)} \right]^{\beta} \quad (2.40)$$

where A_{II} is the amplitude of octahedral shear stress. The parameter α is given by:

$$\alpha = 1 - a \left\langle \frac{A_{II} - A_{II}^*}{\sigma_u - \sigma_{e,max}} \right\rangle \quad (2.41)$$

where $\sigma_{e,max}$ is the maximum equivalent stress which is calculated by maximising the von Mises stress over a loading cycle, A_{II}^* is the fatigue limit criteria as described in section 2.4.3.

By integration of Eq. 2.60 between $D = 0$ and $D = 1$ ($D = 1$ for $N = N_F$) for an assumed constant loading, the number of cycles to failure for a multiaxial loading case is given by:

$$N_F = \frac{1}{1 + \beta} \cdot \frac{1}{a M_0^{-\beta}} \frac{\langle \sigma_u - \sigma_{e,max} \rangle}{\langle A_{II} - A_{II}^* \rangle} \cdot \left[\frac{A_{II}}{1 - 3b_2 \bar{\sigma}} \right]^{-\beta} \quad (2.42)$$

The calculation of multiaxial stresses (e.g. A_{II} and $\sigma_{e,max}$) is normally complicated and needs the help of FE simulations, especially for the cases where large stress gradient exists. With the multiaxial stresses calculated, Eq. 2.42 can be used to predict fatigue lives for a constant stress condition.

Other models can also be adopted to simulate damage. For example, the cohesive zone model (CZM) is a general model which can deal with the nonlinear zone ahead of the crack tip—due to plasticity or microcracking in many materials. Particularly with the use of XFEM, crack propagation can be simulated in FE, based on linear fracture mechanics.

2.4.6 Fracture mechanics

Fracture mechanics is the field of study which concerns crack propagation in materials. It is first developed during World War I by English aeronautical engineer, A. A. Griffith, to explain the failure of brittle materials. He showed that the product of the nominal stress, σ , the square root of the crack length, l , and the material properties governed crack extension for brittle materials. This product was shown to be related to the energy release rate, G (Stephens et al. 2000). From a thermodynamic point of view, Griffith (1921) stated that a crack would grow in a stable fashion if the energy released by an increment in growth was equal to the energy required for the creation of two new surfaces. Irwin (1957) later made modifications to Griffith's theory by applying it to metals (ductile) with small plastic deformation at the crack tip and used the stress intensity factor (SIF) K to quantify the crack tip driving force. Fig. 2.17 defines the different stages of crack propagation in terms of SIF range at the crack tip and crack growth rate, due to fatigue loading.

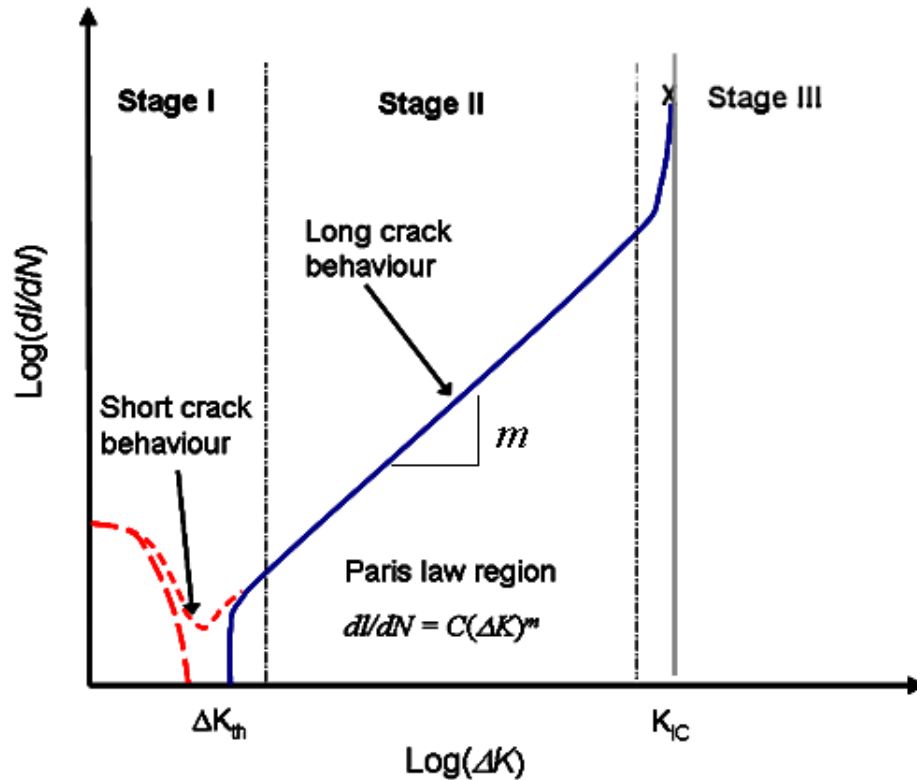


Fig. 2.17. Schematic of typical crack growth behaviour. (Madge, 2008)

Irwin also observed that if the size of the plastic zone around a crack is small compared to the size of the crack, the energy required to grow the crack will not be critically dependent on the state of stress at the crack tip (Erdogan, 2000). Therefore, a purely elastic solution could be used to calculate the amount of energy available for fracture. Linear elastic fracture mechanics (LEFM) uses the stress intensity factor K to characterise the crack tip stress field. Analytical SIFs are available for a range of different ideal geometries, they are generally in the form:

$$K = Y\sigma\sqrt{\pi l} \tag{2.43}$$

where Y is a dimensionless geometric parameter and σ is the nominal stress. In practical geometries closed form of Y is difficult to obtain but approximation can be made from Y values for idealised geometries (e.g. Rooke et al., 1976, and Sih et al., 1962).

The Paris-Erdogan law (Paris et al., 1963) describes the log-linear property of the majority of the curve shown in Fig. 2.17, known as ‘Stage II’ growth. It is proposed that the crack growth in this region is given as:

$$\frac{dl}{dN} = C(\Delta K)^m \quad (2.44)$$

where ΔK is the SIF range due to the cyclic fatigue loading. C and m are characterized material data from experiments.

To furnish a wider application regime, Donahue et al (1972) proposes that at low ΔK values a threshold ΔK_{th} exists in many materials and below which no growth occurs, given by:

$$\frac{dl}{dN} = C(\Delta K - \Delta K_{th})^m \quad (2.45)$$

Similarly, Klesnil & Lucas (1972) proposed another equation as below to describe this:

$$\frac{dl}{dN} = C(\Delta K^m - \Delta K_{th}^m) \quad (2.46)$$

Mean stress influences the crack growth behaviour, as shown in Fig. 2.18. A commonly used equation depicting mean stress effects in regions II and III is the Forman equation (Forman et al. 1967):

$$\frac{dl}{dN} = \frac{C'(\Delta K)^{m'}}{(1-R)K_c - \Delta K} \quad (2.47)$$

where C' and m' are empirical material fatigue crack growth rate constants, R is the stress ratio and K_c is the applicable fracture toughness for the material and thickness.

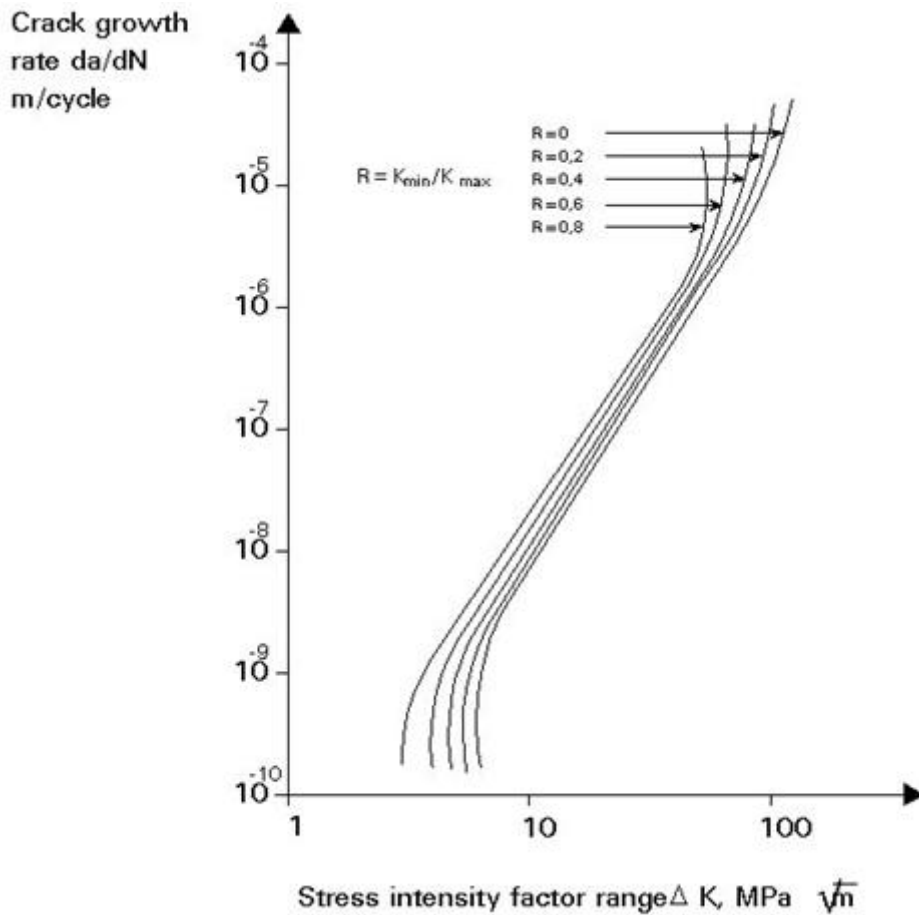


Fig. 2.18. Schematic mean stress influence on fatigue crack growth rates. (Stephens et al. 2000)

Limitations exist for LEFM. The LEFM approach works well for conditions with small-scale crack tip yielding. This is controlled primarily by the plastic zone size to crack length ratio and the magnitude of the operating stress (Stephens et al., 2000). When operating stress levels are too high with resulting excessive plasticity or when cracks are small in comparison to either the plastic zone or microstructural dimensions, LEFM assumptions are violated. For the former, elastic-plastic fracture mechanics (EPFM) can be concerned. For the latter, researchers have suggested crack growth laws for the short-crack problem. El-Haddad et al (1979) proposes an empirical modification to the Paris-Erdogan law given in equation 2.44 to

correct for short crack behaviour. It is observed that at very short lengths a crack will grow at a rate equivalent to a crack that is some constant l_0 longer than the physical crack:

$$\Delta K = Y\Delta\sigma\sqrt{\pi(l+l_0)} \quad (2.48)$$

where l_0 is an intrinsic crack length and generally considered to be an empirical fitting parameter. It is found that l_0 corresponds to the ‘critical crack size’ from threshold fatigue behaviour (Kitagawa & Takahashi, 1976) and is defined as follows:

$$l_0 = \frac{1}{\pi} \left(\frac{\Delta K_{th}}{\sigma_e} \right)^2 \quad (2.49)$$

A number of researchers have applied fracture mechanics to fretting fatigue problems. Hattori et al (2003) adopted the stress-singularity parameters at the contact edge to estimate crack locations and used a range of stress-intensity factor definitions to predict the propagation behaviour. Yuan et al (2009) used known fracture parameters to assess incomplete fretting contact problems and found that the fretting failure is affected by both loading condition and friction pad geometry. M. Mirzajanzadeh et al. (2011) studied the effect of interference fit on the stress intensity factor and its influence on the fretting fatigue crack behaviour. Nowell et al. (2006) reviewed the developments on multiaxial initiation criteria to fretting problem, size effects on fretting and notch fatigue, and methods of crack initiation using asymptotic analysis together with short crack arrest concepts. Madge et al (2008) predicted the effects of fretting wear on crack nucleation and propagation under fretting fatigue conditions using a global-sub modelling finite element approach, with El-Haddad crack growth and including multiaxial effects with mean stress effects also modelled. The resulting predicted lives were successfully compared to test data across a range of slip amplitude. Furthermore, it is predicted that wear under gross sliding conditions significantly retards crack propagation rate whereas under partial slip conditions it increases crack

propagation rates across the slip zone. However, the overall distinction between nucleation and propagation aspects of life can be neglected under certain conditions (Madge et al., 2008). Therefore in this thesis, only nucleation life is calculated and propagation is not taken into account.

2.5 Fretting

2.5.1 General

Fretting occurs when two contacting bodies experience small amplitude oscillatory motion. It is observed in many mechanical assemblies such as keyway-shaft couplings, shrink-fitted couplings, dovetail blade-disc assemblies, hip joint implants, etc.

Many parameters affect fretting behaviour. Collins and Macro (1964) cited fifty variables which affect fretting. Primary variables that can directly affect fretting behaviour are classified as normal load, coefficient of friction, and slip amplitude (Dobromirksi, 1992). Even within these fretting can be divided into three regimes (Vingsbo et al. 1988) by slip amplitude, namely gross slip regime (GSR), partial slip regime (PSR) and mixed slip regime (MSR). A typical fretting map is shown in Fig. 2.19. Historically fretting is categorised as occurring when the relative motion is less than 300 μm , where above it is categorised as reciprocating sliding. Generally fretting can result in fretting wear and under certain conditions, especially in PSR and MSR, fretting fatigue occurs. Using 'fretting map' approaches, Vingsbo et al. (1988) have shown that the fretting damage evolution is strongly dependent on the slip amplitude. Fig. 2.20 shows that in the stick region little effect of wear exists and high fretting fatigue life is often obtained since no relative motion occurs. As slip amplitude increases, the partial slip state occurs. In this regime wear rate is typically low but fretting fatigue life reduces significantly. In the gross sliding regime, fretting wear becomes

dominating while fretting fatigue life rapidly recovers to the level seen in the stick regime. Fouvry et al (2004) comprehensively describe the characteristics of gross sliding and partial slip. In detail, gross sliding dissipates larger frictional energy and generates more wear volume than partial slip; however, partial slip is susceptible to cracking, with the specific damage positions reported to be within the slip band and near the trailing edge of contact - so called the stick-slip interface (Araujo et al., 2002; Fridrici et al., 2005).

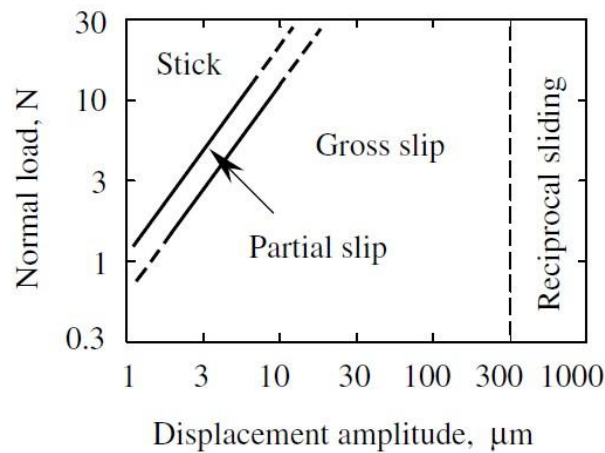


Fig. 2.19 A typical fretting map (Vingsbo et al. 1988)

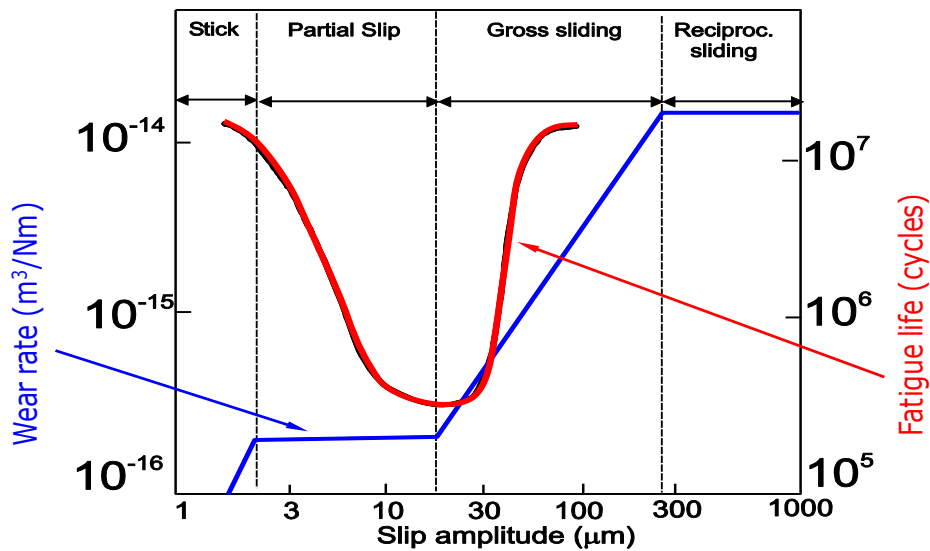


Fig. 2.20 The effect of slip amplitude on fretting wear rate and fretting fatigue life. (After Vingsbo & Soderberg, 1988)

A significant amount of effort has been expended on research into fretting wear and fatigue problems. Based on the assumptions such as idealised material response and half space geometries, early work by Cattaneo (1938) and Mindlin (1949) on the combined normal and tangential loading of a Hertzian geometry, specifically presenting an analytical solutions for the partial slip case, has proved invaluable in the analysis and design of (Hertzian) engineering contacts with respect to contact failure and fretting fatigue. More recently, a rounded punch-on-flat contact problem has also been studied (Ciavarella et al. 1998 and Ciavarella et al. 2003) and analytical solutions have been developed. However, for complicated geometries of real mechanical components, due to their complexity in both geometry and loading conditions, analytical solutions are not sufficient to solve the problem. Experiments are always a good way to investigate the case; however, it is normally economically viable. With the increasing performance of powerful computers, it is possible to simulate fretting in real-life components numerically. Boundary elements have been adopted in a few applications (e.g. McFarlane et al, 1999; Zografos and Dini, 2009) but finite elements have gained greater popularity. In terms of numerical simulations of engineering components that experience fretting, the main concern has been given to gas turbine blade/disc dovetail joints (e.g. Papinkos, 1998), railway axles (e.g. Ekberg, 2004) riveted panels (e.g. Szolwinski, 2000) and spline couplings (e.g. Leen et al, 2003). Also, the extended finite element method (XFEM) is a numerical technique that extends the classical finite element method (FEM) approach by enriching the solution space for solutions to differential equations with discontinuous functions. It was developed in 1999 by Ted Belytschko and co-workers (Moës et al. 1999) to model the propagation of various discontinuities.

2.5.2 Fretting wear modelling

Fretting wear can be treated as a micro-structural fatigue mechanism and is usually associated with material degradation, particle detachment, tribological transformation, etc. A significant amount of effort has been expended on research into fretting wear problems. McColl and co-workers (McColl et al. 2004, Ding et al. 2004) developed an experimentally-validated FE based incremental method for fretting wear simulation (via material removal). The method was applied to a Hertzian geometry to predict the wear-induced evolution of contact geometry and the associated effect on contact surface and sub-surface contact variables, such as contact pressure, slip and stresses. Key fretting phenomena due to material removal were predicted, such as the effect of slip amplitude on evolution of multiaxial contact stresses and multiaxial fatigue indicator parameters, such as the *SWT* parameter. More recently, Mohd Tobi et al. (2009) highlighted the evolution of plastic strain and the effects of incremental plasticity during fretting wear, using linear and nonlinear kinematic hardening models respectively. Contact geometry plays an important role in fretting wear. Madge et al. (2007, 2008) combined the Archard wear simulation method with an FE-based, multiaxial fatigue prediction to successfully predict the effect of fretting wear on fretting fatigue life in the elastic conditions, with experimental validation against Hertzian round on flat (RF) and rounded punch on flat (RPF) fretting fatigue (with substrate fatigue loading) configurations for Ti-6Al-4V.

In fretting wear simulation, wear coefficient calculation is normally based on experimental tests. For the Archard wear coefficient, it is a function of wear volume, stroke and normal load. For different slip regimes such as gross sliding or partial slip and different loads, the Archard wear coefficient is found to vary. Madge (2007) and Ding (2009) have extrapolated the Archard wear coefficient based on experiments (Magaziner et al., 2004) and

modified it with the cycle jumping factor numerically. As for the energy wear coefficient, it is associated with the frictional energy; hence the coefficient inherently include the effect of shear status so that a single wear coefficient can be used across a range of fretting load-stroke combinations (Magaziner et al., 2008), specifically including partial slip, gross slip and arguably reciprocating sliding regimes. The experimental work on Ti-6Al-4V in Magaziner et al. (2008) concludes that from fretting to reciprocating sliding conditions, wear volume is linearly proportional to the dissipated energy; thus, the wear coefficient remains as a constant. However, Magaziner et al. (2008) also implies that for harder material and/or much smaller slip amplitude conditions, the energy wear coefficient could be dependent upon the relative slip amplitude and contact load (Fridrici et al, 2001).

2.5.3 Fretting fatigue modelling

Fatigue damage parameters such as *SWT* and *FS* have been introduced in the previous section. Of course, the stress state associated with fretting leads to a multiaxial fatigue problem. One approach adopted to predict fretting fatigue life from fretting-induced stresses was the critical plane approach, e.g. Szolwinski and Farris (1996). This method searches for the maximum of a fatigue damage parameter (e.g. *SWT*, *FS*, etc.) over a number of different planes and predicts life based on the most damaging plane. Combining critical plane approach with fatigue damage parameters, a number of researchers have successfully analysed fretting fatigue, e.g. Araujo & Nowell, 2002; Sum et al, 2005; Fridrici et al, 2004. Specifically, Araujo & Nowell, (2002) observed a contact size effect in fretting fatigue life in experiments on A14%Cu and Ti-6Al-4V, where it was shown that under nominally similar stress conditions, the fretting fatigue life increases as the contact width decreases. When contact width is below a certain value, infinite life is obtained. This is consistent with the previous concept established by (Stieler, 1954; Peterson, 1959 and Neuber, 1958) that, crack

initiation depends on the volume of material stressed and on the stress gradient. Araujo & Nowell, (2002) also finds that only by implementing a volume averaging process on the fatigue damage parameter (SWT and FS) it can provide a qualitative explanation of the contact size effect observed in the tests. The length-scale of the process volume was found to be comparable with the size of the material microstructure. Sum et al, (2005) modelled an experimental spline coupling geometry under complex loading conditions using elastic-plastic material behaviour with regard to fretting performance. Partial slip was predicted under large bending moments and the predicted location of the stick-slip interface was consistent with fretting fatigue crack positions in the experimental tests. The work of Sum et al, (2005) also shows that detailed, careful non-linear finite element modelling has the ability to capture the size effect in fretting. This is due to that FE simulation averaging the stress field over an elemental volume, which is similar to the method explained in Araujo & Nowell, (2002).

A large part of fretting fatigue life is related to the process of microcrack nucleation and development until some macroscopic crack initiates. After this stage fretting fatigue crack propagation becomes more rapid and fracture mechanics can be adopted. The existence of cracks has local consequences such as steep stress gradients which can be directly addressed if crack growth is explicitly modelled by fracture mechanics. A number of researchers have applied fracture mechanics to fretting fatigue problems. This has been described in Section 2.4.5.

2.5.4 Surface damage parameters on fretting

Surface damage on fretting fatigue has been studied by a number of researchers. Based on the study on dovetail joint between blade and disc of a typical gas-turbine, Ruiz et al (1984) proposed two fretting parameters F_1 , F_2 that can affect fretting wear and fretting

fatigue, respectively. These parameters combine mechanical parameters such as relative slip amplitude δ , surface shear traction τ and sub-surface tensile stress parallel to the surface σ , in the form of: $F_1 = \tau \cdot \delta$, $F_2 = \sigma \cdot \tau \cdot \delta$. Specifically, F_2 is attractive because it combines a surface damage ($\tau \delta$) and a sub-surface damage (σ). Ruiz et al. (1984) established a 2D FE model of the dovetail to analyse the stress field and displacement. In addition fretting fatigue experiments are carried out and cracks are observed. Based on the experimental results and FE results, a relationship between F_2 and fretting fatigue life was suggested as $N = N_{40} \sqrt{\frac{k_{40}}{F_2}}$, where where N_{40} and k_{40} are the fatigue life and F_2 parameter obtained for the 4 to 40kN loading range. The F_2 parameter was successful in predicting the crack nucleation position at the contact edge, which corresponded to their experiments.

Many researchers have adopted F_2 in their studies. For example, Kuno et al. (1989) finds the parameter to work well for a different geometry, which was a sphere on plate axisymmetric Hertzian contact. The peak F_2 value was found to be consistent with the location of crack initiation.

However, apparently F_2 is a very simplified parameter and it doesn't account for the transition from on slip regime to another, and the associated somewhat dramatic change in life (Ding et al. 2011). In addition the stress term in F_2 is a uniaxial representation of fatigue damage. This probably is the reason why Ruiz parameter fails to give satisfactory results, e.g. Neu et al. (2000) found that the Ruiz parameter failed to observe that cracks tend to grow initially at an oblique angle and did not account for the local multiaxial state of stress. With regard to this, some researchers have further developed this concept. Vidner and Leidich (2007) presented an enhanced Ruiz fretting fatigue damage parameter (FFDP), with a combined energetic-multiaxial enhancement parameter (eFFDP), where specific frictional

power was assumed to control fretting damage. Sum et al (2007) proposed a similar approach called D_{fret} , which combined SWT with a function of τ and δ . More recently, Ding et al. (2010) proposed two empirical parameters D_{fret1} and D_{fret2} . as shown below:

$$D_{fret1} = \delta_{app}^* \left\langle 1 - \frac{\delta_{app}^*}{\delta_{th}} \right\rangle^r P^m \quad (2.50)$$

where δ_{app}^* is applied displacement amplitude, P is applied normal load, δ_{th} is a threshold limit beyond which wear becomes dominant and there is no crack formation, and r and m are two further tribological constants.

$$D_{fret2} = (1 + C\sigma\delta) \left\langle 1 - \frac{\tau\delta}{(\tau\delta)_{th}} \right\rangle^n \quad (2.51)$$

where $(1 + C\sigma\delta)$ is an empirical estimation of enhanced possibility of crack formation under

the frictional work $\tau\delta \cdot \left\langle 1 - \frac{\tau\delta}{(\tau\delta)_{th}} \right\rangle^n$ is introduced to characterise the effects of fretting wear.

$(\tau\delta)_{th}$ is the threshold limit of $\tau\delta$ beyond which wear becomes more dominant over cracking.

D_{fret1} is shown to correlate test data against fretting fatigue life in terms of the so-called running conditions of contact displacement and normal load. A linear relationship between D_{fret1} and fretting fatigue life is presented so that it provides a reasonably quick and accurate means to estimate fretting fatigue life from running conditions. D_{fret2} is a more complex parameter which is shown to have the ability to capture the effect of relative slip on fretting fatigue life and fretting fatigue contact size effect.

2.5.5 Ratchtting failure mode

Fig. 2.21 shows the history of plastic strain under cyclic loading. It is categorized into three types, namely elastic shakedown, cyclic plasticity and ratchetting. In fretting, cyclic

plastic deformation can be very small but in certain loading conditions, over many cycles, it could accumulate to large values and reach a critical value which cause ductility exhaustion and failure.

Kapoor (1997) studied the role of the plastic ratchetting mechanism in reciprocating sliding contact and predicted delamination wear for metallic materials using ratchetting strain. Ambrico and Begley (2000) presented FE results for a Hertzian fretting test and showed that ratchetting phenomenon was predicted for certain load combinations, specifically when $P > P_y$ (where P is the normal load and P_y is the Hertzian-predicted normal load to first yield). It was also shown in Mohd Tobi et al., (2009), using a linear kinematic hardening (LKH) model, that cyclic plasticity and ratchetting effects play an important role in fretting of Ti-6Al-4V, particularly when wear effects are accounted for. The difference in Mohd Tobi et al., (2009) is that even when $P < P_y$, due to the effects of the evolving contact geometry by wear, a plastic ratchetting phenomenon is predicted as well in certain loading conditions. It is assumed that for a ratchetting failure to occur, the total accumulated strain must reach a critical value ε_c , which is defined as the stress-triaxiality dependant material ductility (Yan et al. 2000). This value depends on material, the local stress triaxiality resulting from geometric constraints and loading condition. The number of cycles to failure by ratchetting N_r can be predicted using the following equations:

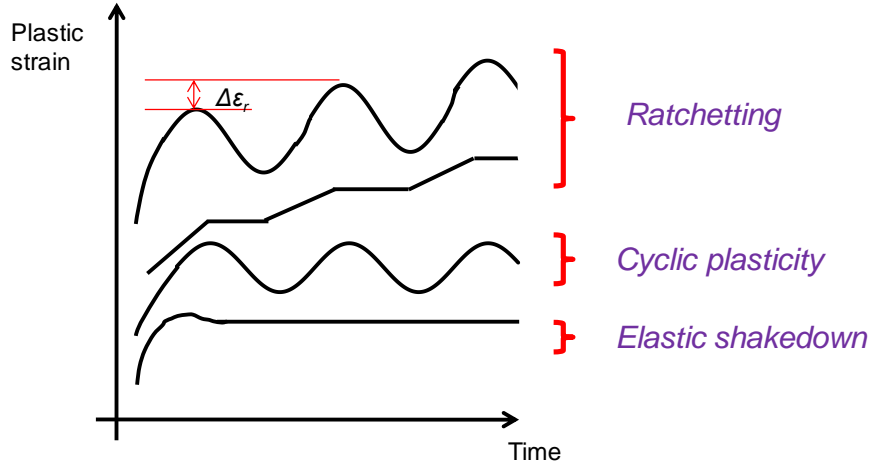


Fig. 2.21 Category of plastic strain history under cyclic loading.

$$\sum_i^{N_r} \Delta \varepsilon_r = \varepsilon_c \quad (2.52)$$

$$\Delta \varepsilon_r = \sqrt{\frac{2}{3} \Delta \varepsilon_{ij}^r \Delta \varepsilon_{ij}^r} \quad (2.53)$$

where $\Delta \varepsilon_r$ is a (uniaxial) equivalent ratchetting strain, corresponding to a multiaxial ratchetting strain condition (See Fig. 2.21). Hence there is a possible competition between failure due to (i) ductility exhaustion via ratchetting and (ii) fatigue failure (low- or high-cycle or combined) as represented here by the critical-plane SWT parameter. Thus, whichever occurs first, viz. ductility exhaustion or critical fatigue damage, determines the mechanism, location and life to crack nucleation.

2.5.6 Fretting in hip joint implant

The use of modular interlocking components is a popular design feature of the prosthetic hip joint implant (Hallab et al., 2004). Fretting behaviour may possibly occur in the hip implant at overall two major locations:

- the modular junction, where the acetabular cup and the stem head are in contact,

- the bone plate contact with screw head (on the femur), as illustrated in Fig. 2.22.

The resulting fretting wear debris is recognized as a key reason for failure of total joint replacements. The clinical significance of fretting wear debris has been addressed in a number of studies, e.g. Barrack et al. (1994), Collier et al. (1992), McKellop et al. (2001). Metal debris released from fretting wear can create a local inflammatory reaction in the tissue and eventually contribute to onset of necrosis or osteolysis (Dumbleton et al., 2002). Furthermore, the fretting wear debris created by a femoral stem or cup may migrate to the ball-socket interface, resulting in third-body abrasive wear of the bearing surfaces (Hop et al., 1997).

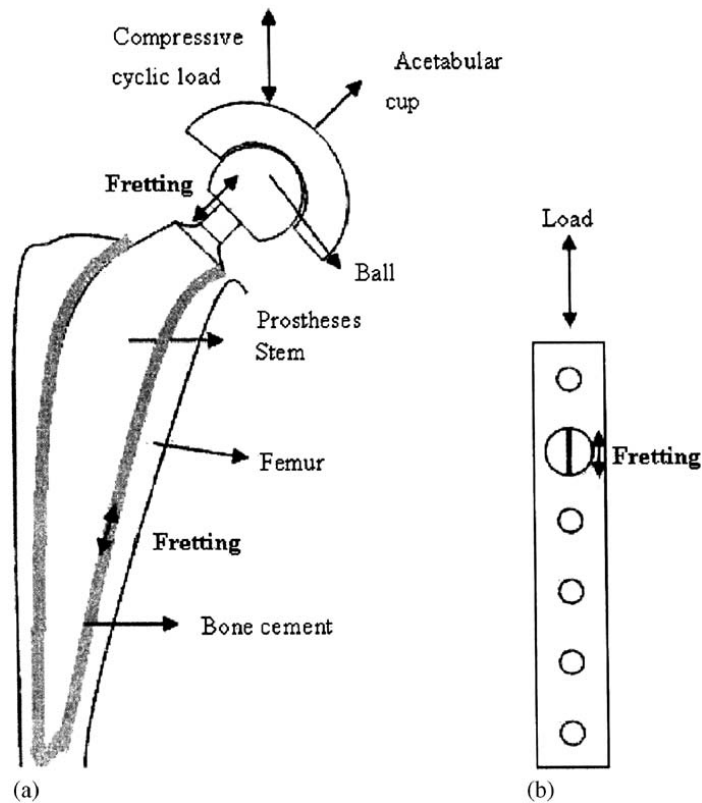


Fig. 2.22 (a) hip joint and (b) bone plate. (Aravind et al. 2007)

To study fretting in hip joint implants, the detailed loading conditions need to be investigated. Duda et al. (1997) developed a 3D model to improve the understanding of

femoral loading by taking into account all thigh muscles, as well as body weight and contact forces at the hip, based on previous work of Brand et al. (1986), Patriarco et al. (1981), etc. The study describes the internal load state acting at different levels along the human femur during various phases of the gait cycle.

Different materials have been used as prosthetic hip joint components. Experimental work has been carried out to investigate various aspects of fretting in hip joint implant. Duisabeau et al. (2004) performed fretting tests in ambient air, as well as in Ringer's solution, with Ti-6Al-4V representing the stem material and 316L stainless steel representing the cup material. The results demonstrate that introducing a corrosive lubricant leads to modification of the fretting regime. Therefore environmental condition is suggested to be another parameter which affects the fretting map. Furthermore, Duisabeau et al. (2004) investigated a hip joint adopting AISI 316L SS as the femoral head and Ti-6Al-4V as the stem neck. It was shown that the 316L SS head exhibited a better behaviour in regard to emission of particles under both fretting and fretting corrosion conditions than the Ti-6Al-4V neck. Vadiraj et al. (2007) investigated the effect of surface treatments on fretting fatigue damage of biomedical titanium alloys and showed that surface-modified alloys with PVD TiN coating and plasma nitriding are much improved with regard to fretting performance. Ebramzadh et al. (2005) developed an experimental fretting wear simulator that is capable of reproducing in-vivo motion and stresses at the interfaces of total joint replacements, with cyclic displacements from 3 to 1000 microns. Hallob et al. (2004) investigated the differences in the fretting corrosion of metal-metal and ceramic-metal modular assemblies of total hip replacements. An in-vitro comparison of ceramic (zirconia, ZrO_2) and metal (Co-alloy) femoral-head fretting on Co-alloy stem components is carried out. Greater metal release and potentiodynamic fretting of the metal-metal modular assembly were observed when compared to ceramic-

metal modular assembly. Specifically, decreased susceptibility of the ZrO₂/Co-alloy assembly to fretting can be supported by potentiodynamic studies in which both a smaller average voltage drop and a shorter average recovery time are associated with ZrO₂ femoral heads on Co-alloy stems, as compared to Co-alloy heads.

The author is not aware of any finite element simulation on fretting in hip joint implants, especially at the stem head/acetabular cup interlocking contact.

2.6 Summary

This chapter reviewed a variety of subjects which are necessary for the study of fretting. Discussion of the existing knowledge of contact mechanics and then tribology, especially wear, has been reviewed. An overview of fatigue of metals is also given in terms of fatigue mechanisms and different approaches to calculate fatigue problems (e.g. stress/strain fatigue approach, damage mechanics, and fracture mechanics). The development of computational methods for the fretting wear and fatigue problems and the corresponding applications are discussed in detail (e.g. hip implants).

It has been noted the following has not been properly addressed and thus is investigated in this work in later chapters:

- The implementation of the coupled continuum damage mechanics to fretting
- The development of energy wear approach combining critical plane SWT for fretting with plasticity
- The computational comparative study on the effect of contact geometry for marine riser pressure armour layer
- The experimental assessment of biomedical materials such as CoCr, forged Ti64 and DMLS Ti64

- The computational study of fretting in hip joint hip implants

Chapter 3

Continuum Damage Mechanics for Fatigue and Fretting

Fatigue

3.1 Overview

The three-dimensional finite element implementation of a continuum damage mechanics formulation for multiaxial fatigue is presented in this chapter, incorporating elastic modulus reduction due to fatigue damage. The implementation is validated against theoretical and published experimental results for uniaxial and notched multiaxial fatigue under different combinations of mean and alternating stresses for Ti-6Al-4V. An automatic incrementation scheme is developed for efficient computation of damage accumulation and hence stress redistribution. The method is also implemented in two-dimensional, plane strain for fretting fatigue and is shown to successfully capture the effect of contact slip on fatigue life for a round-on-flat fretting geometry. Comparisons are also made with a critical-plane multiaxial fatigue approach for fretting. The work is a first step towards a more general fatigue damage approach to unify wear and fatigue prediction for fretting.

3.2 Fatigue model

3.2.1 Continuum damage fatigue model

LeMaitre and Chaboche (1990) have presented some fundamental concepts in damage mechanics and later derived the damage model for fatigue calculation. The detailed equations

have been well described in section 2.4.4. Here it adopts the damage model with Sine's criteria (for multiaxial conditions) to simulate plain fatigue and fretting fatigue problems.

For uniaxial conditions the damage rate equation has been shown in Eq. 2.38.

The number of cycles to failure for an assumed constant stress condition is obtained by integrating the above between $D = 0$ and $D = 1$ ($D = 1$ for $N = N_F$), leading to Eq.2.39.

The stress and strain in real engineering problems are normally multiaxial, therefore the NLCD model can be extended to 3D, to give damage evolution in Eq. 2.40.

By integration of Eq. 2.40 between $D = 0$ and $D = 1$ ($D = 1$ for $N = N_F$) for an assumed constant loading, the number of cycles to failure for a multiaxial loading case has been shown in Eq. 2.42.

3.2.2 Critical plane SWT model

A critical plane approach incorporating the Smith-Watson-Topper (Smith et al. 1970) fatigue parameter has also been adopted here, for comparative purposes, to predict multiaxial fatigue, following the methodology established by Sum et al. (2005) and further developed in (Mohd Tobi et al. 2009) for application to fretting crack nucleation. It combines low cycle fatigue and high cycle fatigue and take into account of the effect mean stress. It was shown in Sum et al. (2005) that the FE-implementation of this approach can capture stress gradient effects, e.g. the contact size effect; this is attributed to the built-in volume-averaging nature of the Gaussian sampling technique in the FE method, based on mesh convergence studies. The critical plane approach is based on the physical observations that fatigue cracks initiate and grow within a material on certain planes, where the growth and orientation depends on the normal stresses and strains on these planes. The *SWT* life prediction equation employs a

combined high-cycle fatigue (HCF) and low-cycle fatigue (LCF) equation, and consideration of the peak stress to account for the mean stress effect, as follows:

$$SWT = \sigma_{max} \frac{\Delta\varepsilon}{2} = \frac{\sigma_f'^2}{E} (2N_F)^{2d} + \sigma_f' \varepsilon_f' (2N_F)^{d+f} \quad (3.1)$$

where σ_{max} is the peak normal stress on the critical plane, $\Delta\varepsilon$ is the maximum normal strain amplitude on the same plane, σ_f' and d are the (Basquin) fatigue strength coefficient and exponent (HCF constants), ε_f' and f are the (Coffin-Manson) fatigue ductility coefficient and exponent (LCF constants) and E is Young's modulus.

The FE-implementation of the critical-plane SWT parameter is achieved by transforming the time histories of element centroidal stresses and strain ranges onto planes at 5° intervals over a 180° range using the two-dimensional transformation (Mohr's circle) equations for stress and strain. The maximum normal stress σ_{max} with respect to time, and the corresponding strain range $\Delta\varepsilon$ are determined for each of the 36 planes in each element. $\Delta\varepsilon$ is the difference between the maximum and minimum values of strain normal to the candidate plane over the complete loading cycle. Thus, SWT values are obtained for each candidate plane in each element. These values are then employed to establish the maximum critical plane SWT value with respect to plane orientation in each element, which in turn is used with Eq. 3.1 to furnish a number of cycles to failure, N_F .

3.2.3 Material data

The material studied throughout is Ti-6Al-4V, with a Young's modulus of 116 GPa, Poisson's ratio of 0.34 and yield stress of 940 MPa (Marmi et al. 2009). Macroscopic yielding is not predicted for the loading conditions investigated. The ultimate tensile stress σ_u used is 1040 MPa and the fatigue limit at fully reversed loading condition σ_{10} is taken as 358 MPa.

The material damage constants for Ti-6Al-4V are adopted from (Marmi et al. 2009), as shown in Table 1. σ_{10} and b are similarly obtained from fatigue limit data at different mean stresses ($R = -1$, $R = 0.1$, and $R = 0$). Initial estimates of M_0 , β come from stress-controlled ($R = -1$) fatigue tests stress-life data. b_2 comes from stress-life data at different mean stresses, e.g. ($R = 0$, $R = -1$). The a value is identified from measurements of damage (e.g. modulus degradation) evaluation during fatigue testing (see (Chaboche and Lesne, 1988)), for example, based on the evaluation of stress range in strain-controlled fatigue tests. The specified value of a is not needed in the integrated formula as studied in (Marmi et al. 2009) but it is required in the incremental damage formulation of the present work. Detailed experimental methods to obtain the value of a have been described in (Chaboche and Lesne, 1988). In the present work, based on the known values of $aM_0^{-\beta}$ and β , a is identified numerically, as the value which gives the same life for the incremental method in the 3D unnotched FE model (section 3.3.1) as calculated by the integrated formula (Eq. 3.2). This results in an identified value of 0.75. As shown below, this value also gives excellent agreement for other loading conditions.

In order to make an objective comparison between the performance of the proposed new FE-based incremental damage approach and the previously validated critical plane *SWT* method for fretting fatigue, the σ_f' and d constants of the *SWT* model are identified here by calibration with the fatigue damage model data of Table 3.1. Fig. 3.1 presents the comparison of plain fatigue life across a range of alternating and mean stress levels, as predicted by the critical plane *SWT* model and the integrated NLCD model under the uniaxial conditions. The fitting is not perfect in the compressive mean stress conditions and this needs further work to identify the constants. The identified *SWT* constants are shown in Table 3.2. Here the *SWT* constants correspond to a definition of crack initiation as the development of a 10 μm crack

(Madge et al. 2008), which is consistent with the length scale of integration points depth below the surface in the FE models. Note that ε_f' and f have been taken from (Madge et al. 2008).

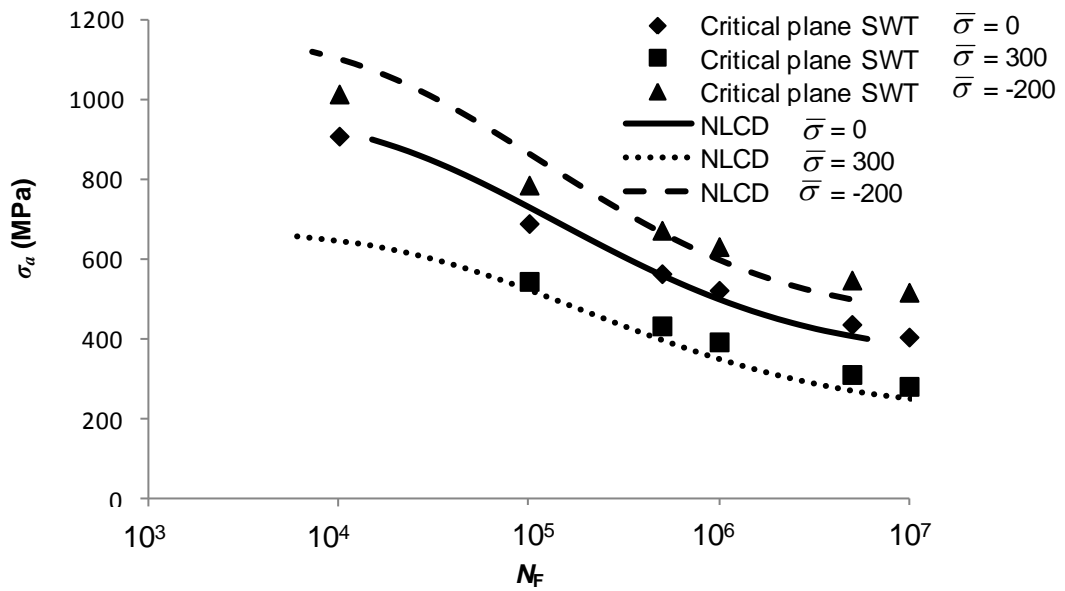


Fig. 3.1 Fatigue life comparison between integrated NLCD and critical plane *SWT* model for uniaxial case.

Table 3.1. Material parameters of the Lemaitre and Chaboche fatigue damage model for Ti-6Al-4V (Marmi et al. 2009).

β	$aM_0^{-\beta}$	b_1	b_2	a
1.79	1.79×10^{-11}	0.0013	0.00055	0.75

Table 3.2. Material parameters of *SWT* model for 10 μm crack nucleation (Madge et al. 2008).

σ_f' (MPa)	d	ε_f'	f
2500	-0.108	0.841	-0.688

3.3 Computational methodology

3.3.1 Fatigue damage computation

User material subroutines (UMATs in Abaqus) are used to define non-standard material constitutive behaviour. For the implementation of the coupled continuum damage theory here, it is necessary to employ a UMAT subroutine where the damage is computed at each integration point, throughout the loading history, for each time increment and accumulated continuously.

Eq. 2.40 is a non-linear equation in D , which requires a numerical solution. It is necessary to assume an initial value of D . In this work, the damage value of first loading cycle is taken to equal $1/N_F$ as in the linear accumulation rule, where N_F is calculated by Eq. 2.42, using the FE-predicted multiaxial stresses of the stabilized cycle.

As illustrated in the flowchart of Fig. 3.2, the subsequent damage at every integration point is accumulated to predict the reduction in Young's modulus $E^{(i)}$, using the following equation:

$$E^{(i+1)} = E^{(i)}(1 - D^{(i+1)}) \quad (3.2)$$

Once the damage at any integration point reaches a value of 1, fatigue crack nucleation is deemed to have occurred at this material point. Since it is too expensive computationally to simulate damage accumulation for every fatigue cycle, a cycle jumping factor ΔN is introduced to Eq. 2.40 to give the following equation for damage increment:

$$\Delta D = [1 - (1 - D)^{\beta+1}]^\alpha \cdot \left[\frac{A_{II}}{M_0 (1 - 3b_2 \sigma_{H,mean})(1 - D)} \right]^\beta \Delta N \quad (3.3)$$

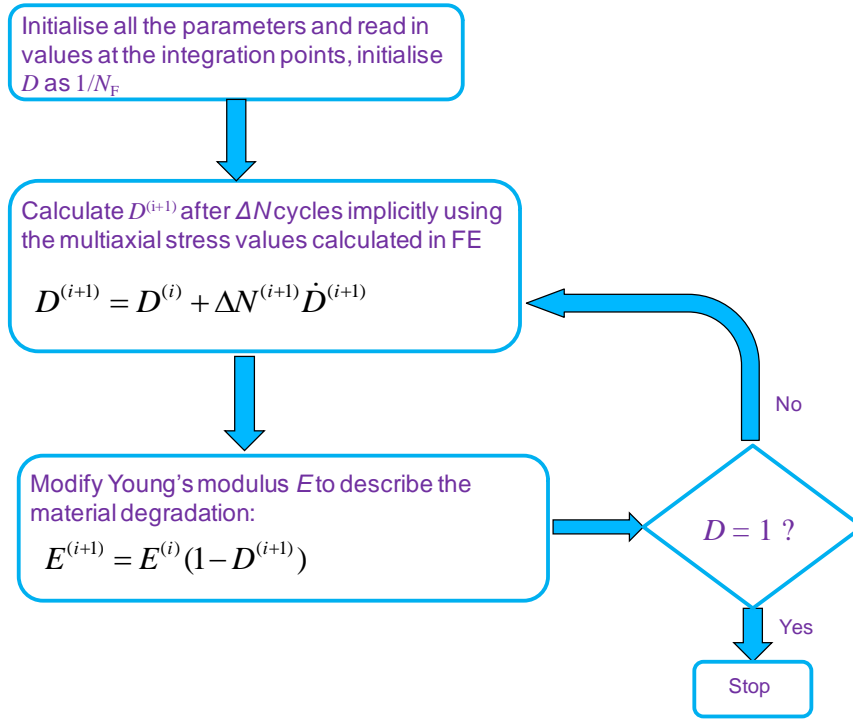


Fig. 3.2. Simplified UMAT subroutine algorithm

It is thus assumed that during each ΔN increment in number of fatigue cycles the multiaxial stress condition remains constant.

Forward difference, central difference and backward difference integration schemes are implemented to compare the accuracy and stability of these integration schemes with respect to the cycle jump size, ΔN .

The forward difference integration scheme is given by:

$$D^{(i+1)} = D^{(i)} + \Delta N^{(i+1)} \dot{D}^{(i)} \quad (3.4)$$

where i is the FE fatigue cycle number. The central difference implementation is given by:

$$D^{(i+1)} = D^{(i)} + \Delta N^{(i+1)} \dot{D}^{(i+1/2)} \quad (3.5)$$

where $\dot{D}^{(i+1/2)}$ is derived as:

$$\dot{D}^{(i+1/2)} = \frac{\dot{D}^{(i)} + \dot{D}^{(i-1)}}{2} + \Delta N^{(i+1)} \ddot{D}^{(i)} \quad (3.6)$$

Finally, the backward difference scheme is implemented as:

$$D^{(i+1)} = D^{(i)} + \Delta N^{(i+1)} \dot{D}^{(i+1)} \quad (3.7)$$

where $\dot{D}^{(i+1)}$ is estimated implicitly by the Newton-Raphson method which has been implemented in the fatigue damage material subroutine. Further details of these integration schemes are given in the Appendix A1.

3.3.2 FE modelling of fatigue and fretting fatigue tests

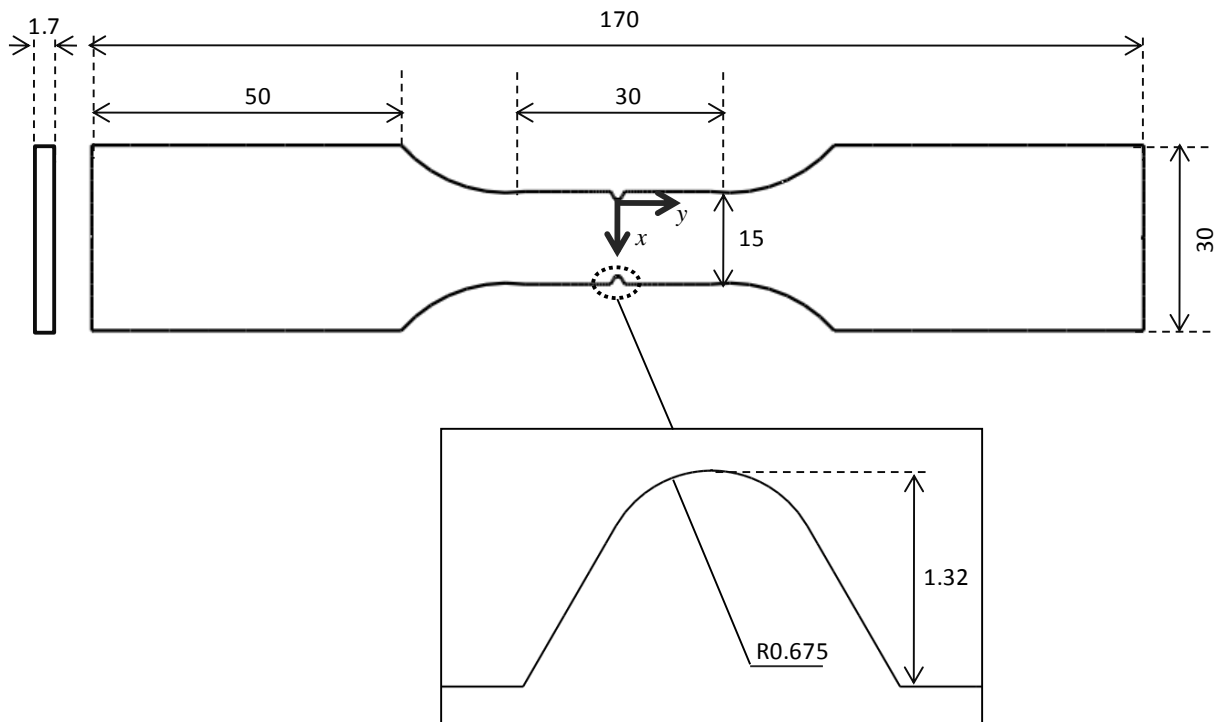


Fig. 3.3. V-notched specimen, all dimensions in mm.

Two fatigue specimens are modelled in FE for the plain fatigue tests, a notched case and an unnotched case. The V-notched specimen is based on the geometry from the MIL-HDBK-5H handbook (1998), as illustrated in Fig. 3.3. This shape of V-notched specimen corresponds to an elastic stress concentration factor K_t of 3.3, where K_t is given by:

$$K_t = \frac{\sigma_{yy,max}}{\sigma_{net}} \quad (3.8)$$

where $\sigma_{yy,max}$ is the maximum opening stress at the notch tip and σ_{net} is the average stress on the reduced section of the specimen. The high cycle fatigue (HCF) tests in (Military Handbook, 1998) adopt a stress ratio R of 0.1, 0.5 and -0.5 ($R = \sigma_{min}/\sigma_{max}$, where σ_{min} and σ_{max} are the minimum and maximum stresses during one loading cycle, respectively) and the same R ratios are analysed in this study.

The general purpose, non-linear, FE code Abaqus is used here. The unnotched specimen is modelled as a thin square sheet giving a homogeneous stress state. The V-notched model is shown in Fig. 3.4; one eighth of the specimen is modelled with symmetry boundary conditions at the plane of symmetry. 8-node linear hexahedral brick elements (C3D8) are used for both models with a highly- refined mesh with a smallest element width of 25 μm in the notch tip region, based on a mesh convergence study. As can be seen in Fig. 3.4, the 25 μm mesh gives relatively satisfactory results in terms of stress value A_{II} . Negligible effect of increased refinement in the thickness direction is found. Therefore a two-layer element model in the thickness direction is adopted. The material constitutive behaviour is defined via a 3D users material (UMAT) subroutine, as described in Section 3.3.1.

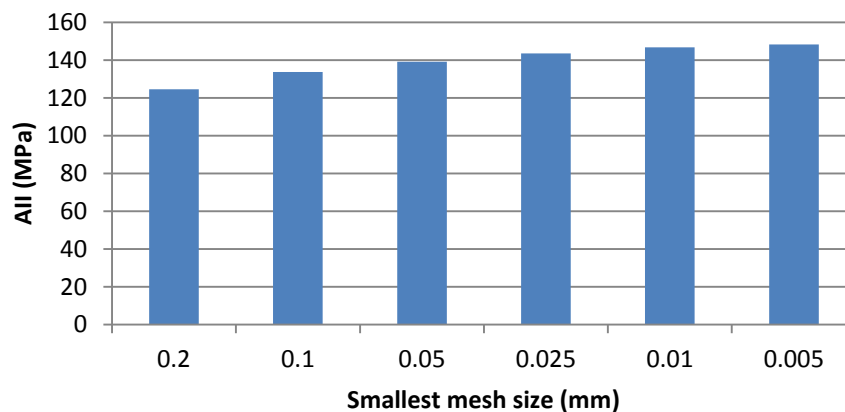


Fig. 3.4 Mesh convergence study

The FE model developed for the analyses of fretting fatigue uses a two-dimensional, plane strain assumption. The round on flat fretting geometry is based on the USAF test configuration of Jin and Mall (2002). As shown in Fig. 3.5, a pair of cylindrical fretting pads (radius R of 50.8mm) are held in contact with a uniaxially loaded specimen with the width w of 6.4 mm and thickness of 3.8 mm. The purpose of the test and model is to comparatively assess the predicted effect of stroke amplitude on fretting fatigue damage behaviour. As depicted in Fig. 3.5, a constant normal load, P , with a value of 208 N/mm, is applied to the fretting pad in the first step; then a cyclic stroke $\Delta(t)$ is applied to the fretting pads while an in-phase cyclic fatigue stress $\sigma(t)$ is loaded on the specimen. The fatigue stress has a maximum value of 550 MPa and a stress ratio R of 0.03. The magnitude of applied stroke is varied from test to test here to study its effect on fatigue damage. Fig. 3.6 shows the FE model of the fretting fatigue configuration. The tangential load and normal load are both applied to the top centre of the fretting pad. The top surface is constrained linearly so that all the surface nodes will move together vertically, in order to preclude the occurrence of a tilting moment.

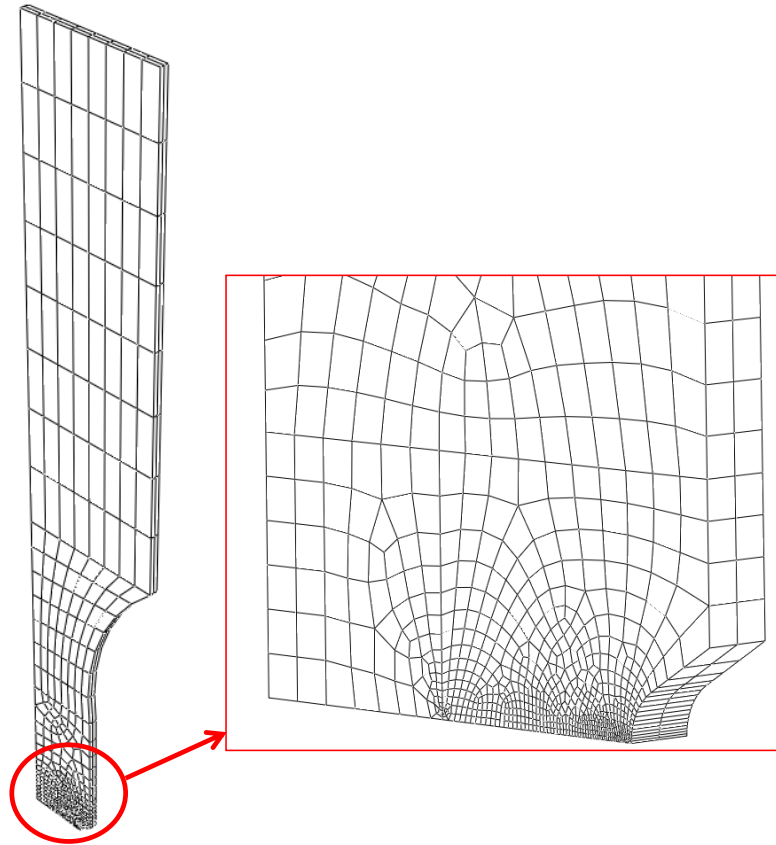


Fig. 3.4. FE mesh of the V-notched specimen

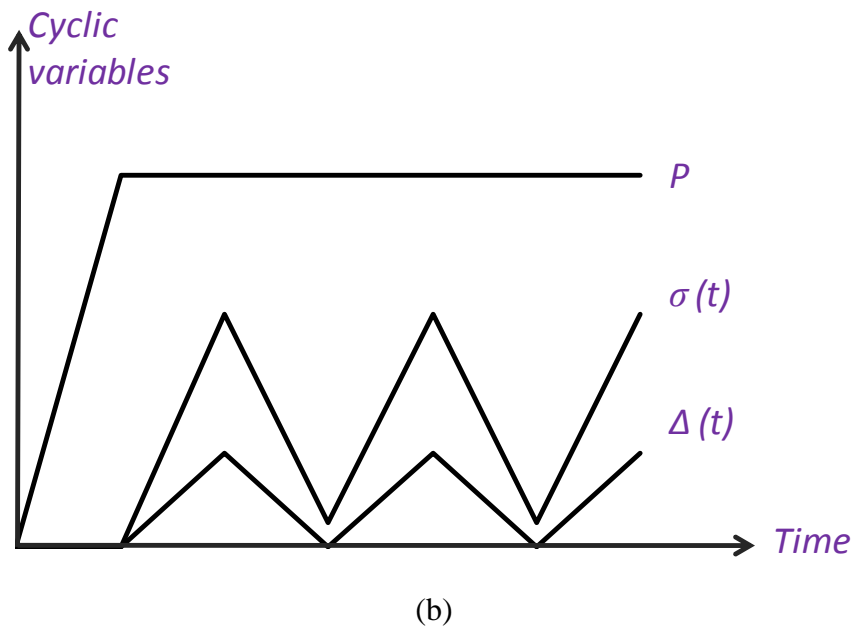
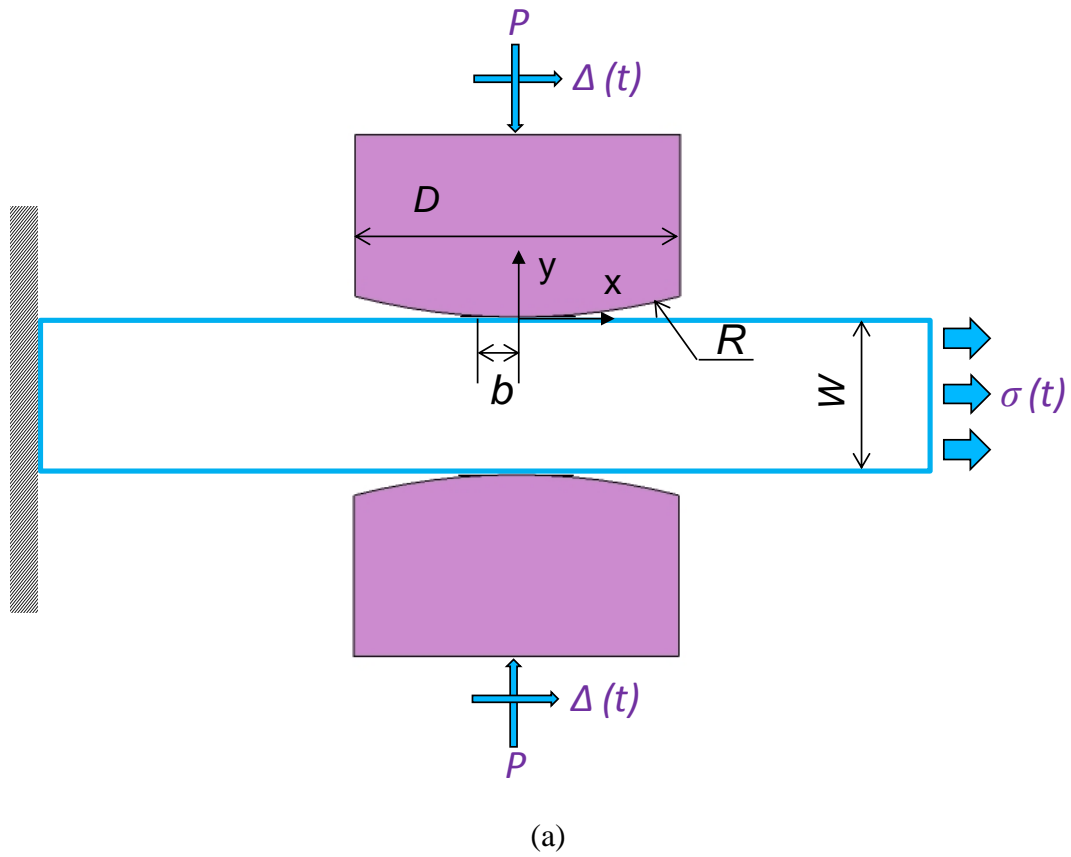


Fig. 3.5. (a) Schematic of the fretting fatigue test configuration of Jin and Mall (2004) (radius $R = 50.8 \text{ mm}$, $D = 9.5 \text{ mm}$, $w = 6.4 \text{ mm}$, contact half width b). (b) Fatigue and fretting load history.

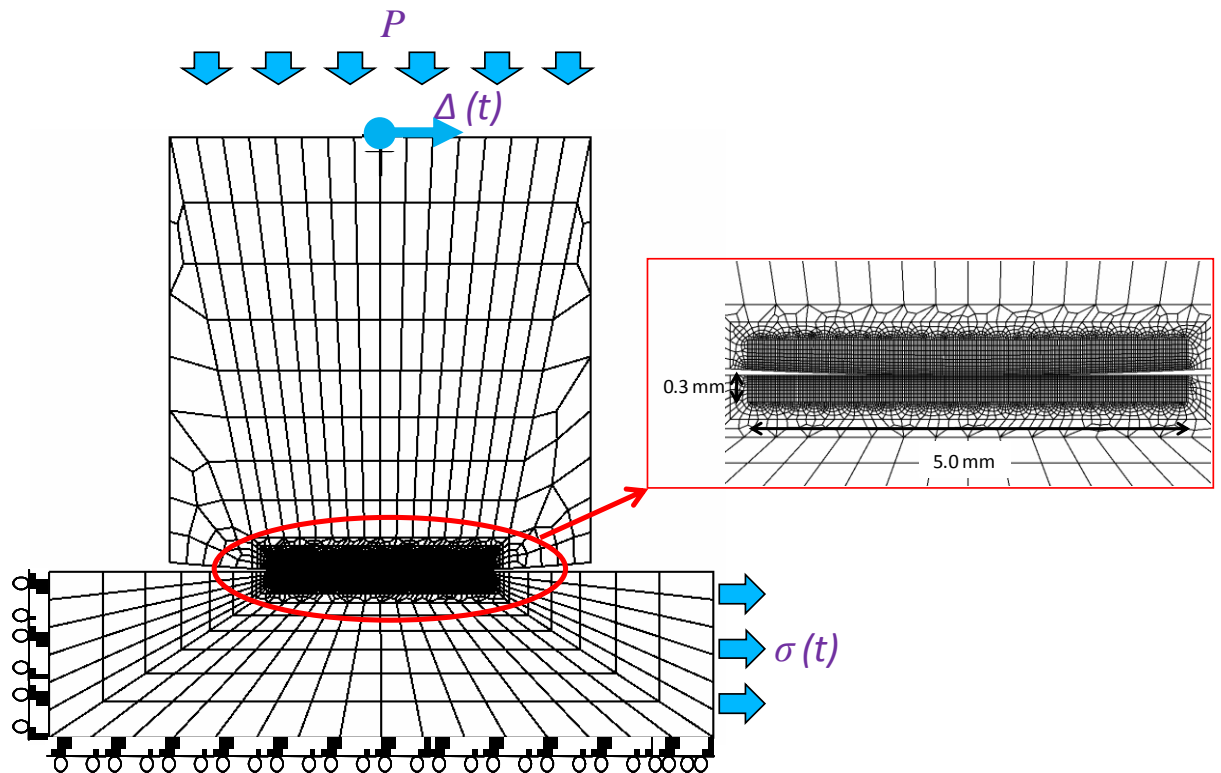


Fig. 3.6. Mesh details of FE model of fretting test

The contact surface interaction is defined via the finite sliding contact pair approach which adopts the master-slave algorithm in Abaqus. The maximum allowable penetration depth (*h-crit*) between the slave and master nodes during the iterative solution process is set to 1 μm . The minimum allowable distance between the initial coordinates of adjacent nodes on the mating contact surface (*ADJUST parameter*) is set to 0.001 μm . Coulomb friction is employed based on the Lagrange multiplier contact algorithm to ensure the exact stick condition when the shear stress is less than the critical shear value according to the Coulomb friction law. These contact parameters have been identified from previous studies, e.g. see McColl et al. 2004. A constant coefficient of friction (COF) (μ) of 0.8 is used throughout the analyses, based on the measured data for the same test configuration (Jin and Mall, 2004).

Detailed mesh refinement studies with respect to the contact surface mesh were carried out to achieve convergence with respect to the surface tractions and sub-surface stresses for both models, using available theoretical solutions for the Hertzian geometry. The comparisons between theoretical and converged FE predictions are presented below. A user material subroutine which adopts the same algorithm as in Section 3.3.1 is used to define the material's mechanical behaviour and calculate fatigue damage accumulation; it is a modified version of the 3D subroutine used above for plain fatigue analyses, to be suitable for the 2D plane strain implementation.

In comparisons between FE modelling and testing of fretting, it is necessary to distinguish between local and global slip. Fig. 3.7 shows this in a schematic. Since FE predicted relative slip is locally computed it is called the local slip δ_{local} ; since the experimental observed slip incorporates the effects of rig compliance and the surface conditions, it is called the global slip δ_{global} (Madge et al., 2007). As shown in Fig. 3.7, node A on the fretting pad and node B on the substrate specimen are originally in contact. With applied forces acting on both the fretting pad and substrate specimen, nodes A and B move to new positions as A' and B' respectively. In FE simulation, the local relative slip for node A is calculated as the distance between A' and B'. In experimental tests, based on the measurement of the extensometer, global relative slip can be calculated. Detailed procedure of the calculation is explained in (Wittkowsky et al. 1999). It has been pointed out by Jin and Mall (2004) that the FE predicted relative slip and the experimental observed slip magnitudes across the range from partial slip to gross slip do not agree. Sabelkin and Mall (2005) concluded that (i) the experimentally observed relative slip was significantly larger than the actual slip at the contact surface and (ii) this is controlled by rig compliance and the COF. In order to estimate the local slip in FE and following the work of (Sabelkin and Mall 2005),

Madge (2007) employed the following relationship between FE and experimental slip (δ_{local} and δ_{global} respectively):

$$\delta_{local} = \delta_{global} \frac{C_{COF}}{C_{rig}} \quad (3.9)$$

where C_{rig} is a constant which accounts for the effect of rig compliance and C_{COF} is a constant which accounts for the effect on compliance of COF. The resulting C_{rig}/C_{COF} adopted here has been determined as 8 based on the data in (Sabelkin and Mall 2005). The ratio is normally geometrically related and not suitable in other conditions.

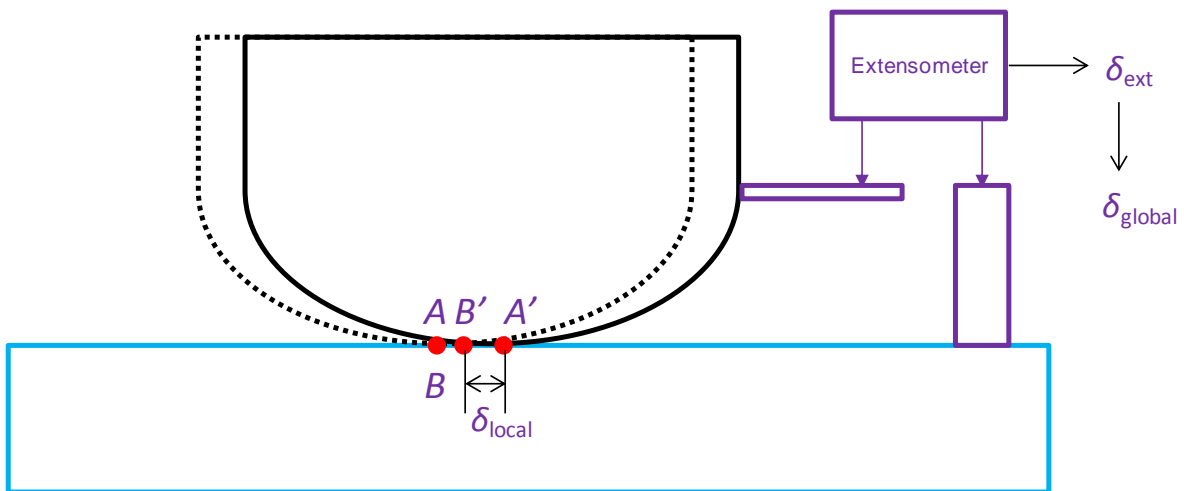


Fig. 3.7. Description of local δ_{local} and δ_{global} .

3.4 Results and discussion

3.4.1 Plain fatigue results

The different schemes are evaluated for the 3D unnotched plain fatigue case. Only the backward difference scheme gives conservative life results as ΔN is increased compared to the uniaxial analytical result (calculated by Eq. 2.39), as illustrated in Fig. 3.8. The other two

schemes predict longer life than the theoretical result as ΔN is increased. From Fig. 3.8, it can be seen that for $\Delta N/N_F < 0.02$ a converged FE life prediction is obtained in comparison with the theoretical solution.

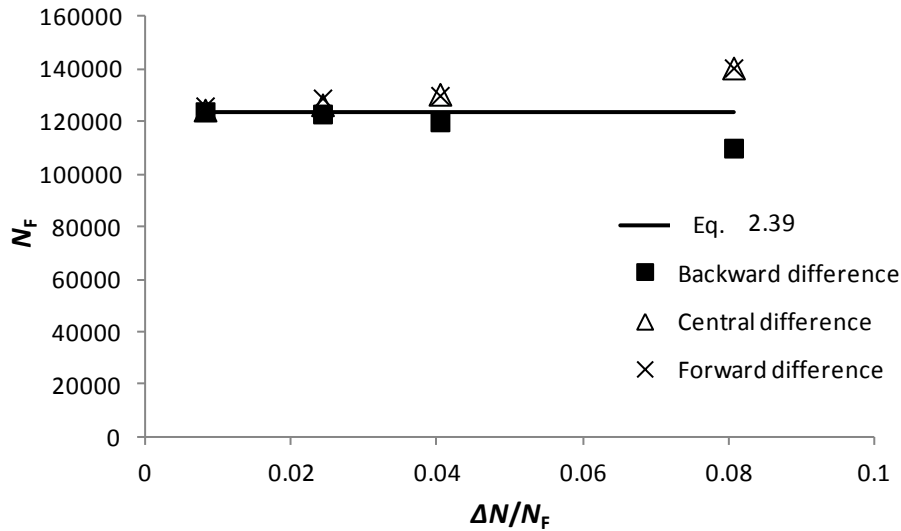


Fig. 3.8. Cycle jumping factor convergence study using different integration schemes for unnotched plain fatigue specimen, with $\sigma_{\max} = 800$ MPa, $R = -0.5$.

Fig. 3.9 shows the calculated damage evolution for the case of $\sigma_{\max} = 800$ MPa, $R = -0.5$. The damage is low initially, but accumulates rapidly as N approaches N_F . Therefore using a constant ΔN is not efficient since it is too expensive for low N and not accurate enough near N_F . Consequently a variable cycle jumping technique is adopted here based on a slope monitoring algorithm, where the *slope* is given by:

$$slope = \frac{D^{i+1} - D^i}{\Delta N} \quad (3.10)$$

For example, Fig. 3.10 shows the cycle jumping factor variation history as employed by the variable ΔN algorithm using the backward difference integration scheme for the same

case as Figs. 3.8 and 3.9. For the initial part of life, generally when $slope < 10^{-8}$, a relatively large ΔN is adopted as it is assumed that over a large number of cycles, stresses remain roughly the same, and generally the resulting $\Delta N/N_F \approx 0.08$. As the cycle number grows, to be more accurate, ΔN is reduced and generally the resulting $\Delta N/N_F \approx 0.04$. Nearly approaching N_F , when damage is accumulated rapidly, an even smaller ΔN is used and generally the resulting $\Delta N/N_F \approx 0.01$. Adopting the variable cycle jumping technique, the predicted N_F is 120,011 for the case shown in Fig. 3.10, which gives an error of just 3.2%, compared to the theoretical life shown in Fig. 3.8. This cycle jumping factor variation scheme is adopted in the later sections.

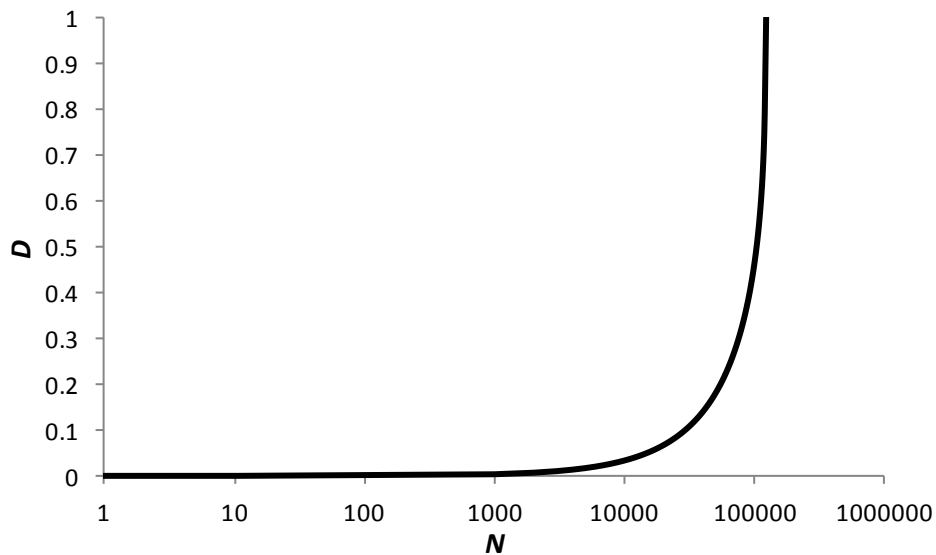


Fig. 3.9. Damage evolution using backward difference integration scheme for unnotched plain fatigue specimen, with $\sigma_{max} = 800$ MPa, $R = -0.5$.

Fig. 3.11 shows a comparison of the FE-predicted $S-N$ data for the unnotched specimen using the 3D incremental damage formulation with the integrated expression of Eq. 2.39. Excellent agreement is obtained by the former for all three R values. Homogeneous damage is predicted since no stress gradient occurs in this uniaxial problem.

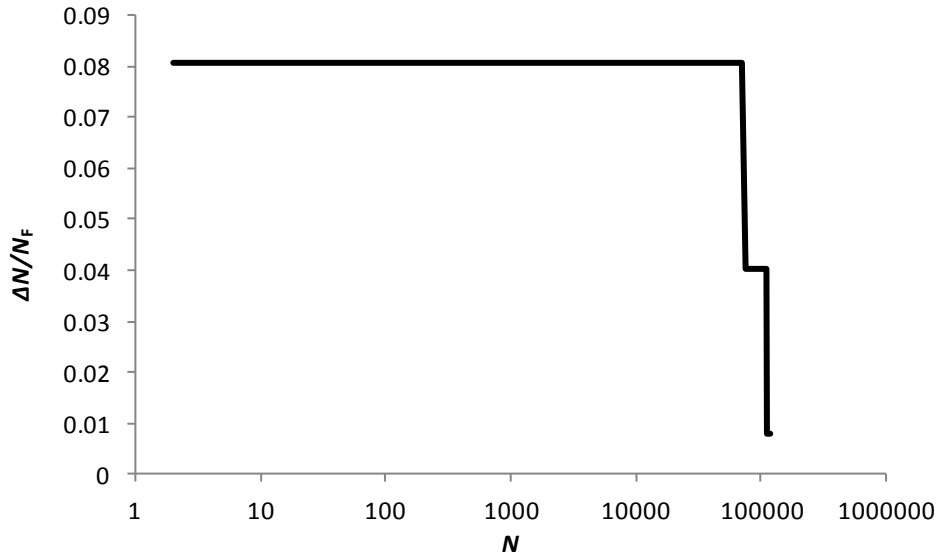


Fig. 3.10. Cycle jumping factor variation history using backward difference integration scheme for unnotched plain fatigue specimen, with $\sigma_{\max} = 800$ MPa, $R = -0.5$.

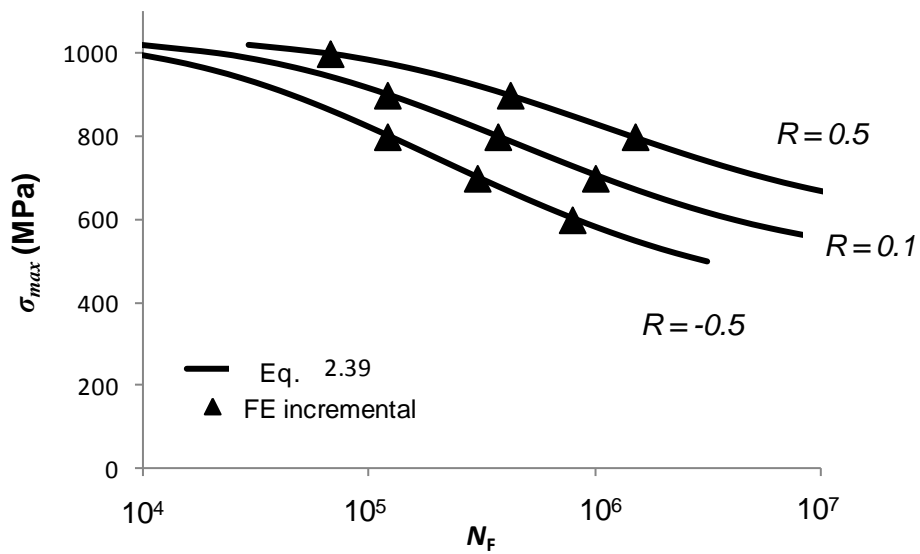
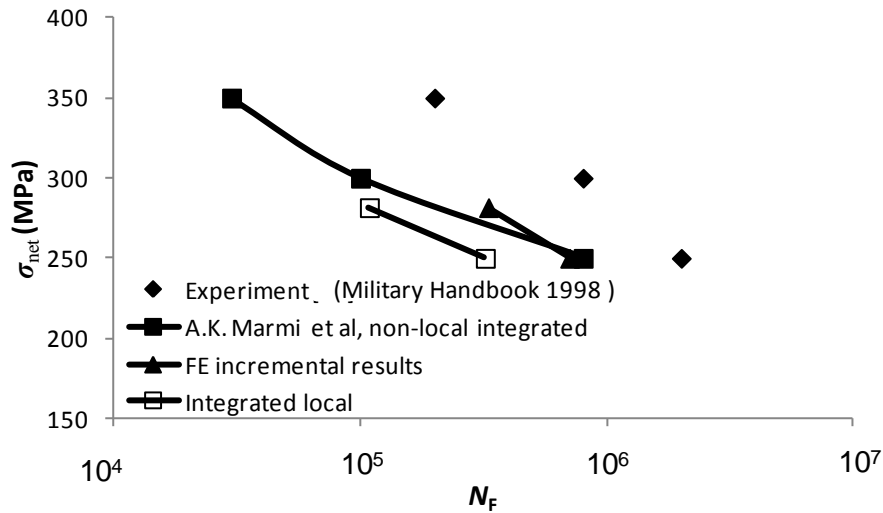
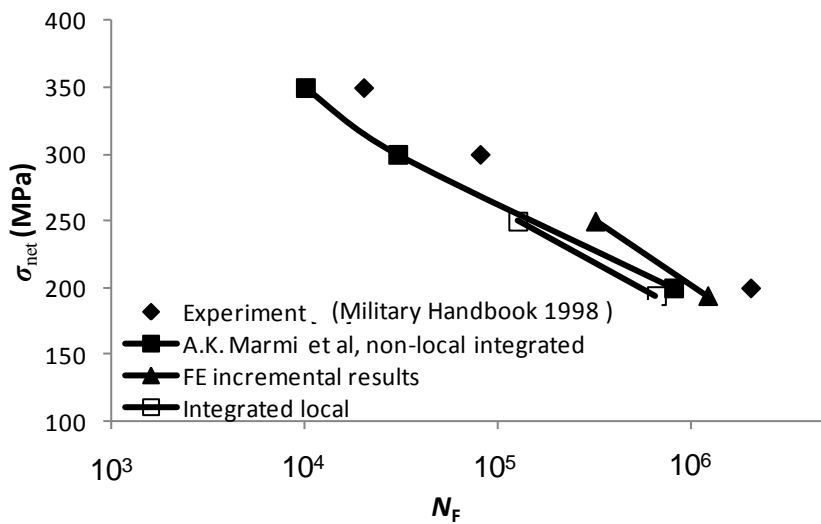


Fig. 3.11. $S-N$ data predicted by FE incremental damage prediction and integrated theory for different R ratios for unnotched case.



(a)



(b)

Fig. 3.12. *S-N* data comparison by different methods for V-notched case for (a) $R = 0.1$, and (b) for $R = -0.5$

Figs. 3.12 (a) and (b) show comparisons between the predicted *S-N* data for the V-notched case of Fig. 3.4, from three different predictive methods and experiments (Military Handbook, 1998), as follows:

- The 'Marmi et al. 2009' predicted results correspond to a non-local method combined with the integrated Lemaitre-Chaboche model (Eq. 2.42) as a postprocessor after FE analysis. The multiaxial stresses are obtained from a stabilized fatigue cycle in FE without coupled damage accumulation.
- The 'integrated local' predictions correspond to a local method combined here with the integrated Lemaitre-Chaboche model (Eq. 2.42), where the multiaxial stresses are obtained from a stabilized fatigue cycle using the FE model of Fig.3.5, without coupled damage accumulation.
- The 'FE incremental results' correspond to predictions based on FE analyses using the FE model of Fig. 3.5, coupled with incremental damage accumulation using the backward difference integration scheme (Eqs. 3.5 and 3.7) and associated material degradation (Eq. 3.2).

Clearly, the integrated local approach predicts conservative lives compared to the 'FE incremental results' and 'Marmi et al' predictions, consistent with the findings in (Marmi et al. 2009). The coupled damage predictions of the new approach developed ('FE incremental results') here overall are seen to give better agreement with the test data, than the two other approaches. The incremental results show significantly superior performance than the 'integrated local' analytical results for both R ratios and significantly better prediction than the 'non-local integrated' for the $R = -0.5$ case. The experimental results presented correspond to macro-cracking, whereas the present results predict micro-cracking. Hence, the difference is attributable to crack propagation in the test data, which is not captured by the model results. Note that, the fatigue damage user material formulation developed, at present, assumes elastic material behaviour. Hence, the 'FE incremental' and 'integrated local' results of Fig. 3.12 are not applied to $\sigma_{net} \geq 284.8$ MPa, above which notch plasticity is predicted.

For the V-notched case, due to the stress concentration being localized at the notch tip, fatigue damage is predicted to localise at the mid-thickness position along the notch tip. This is due to the Poisson effect at the notch tip: along the thickness direction at the notch tip, the straining is expressed as:

$$\varepsilon_{33} = \frac{1}{E}(\sigma_{33} - \nu(\sigma_{11} + \sigma_{22})) \quad (3.11)$$

At the two edges of the notch tip the straining at the thickness direction ε_{33} is significant while at the mid-thickness position, ε_{33} is very small. Therefore a much bigger σ_{33} is localised at the mid-thickness position hence the multiaxial stress is greater at this position, therefore the resulting damage is more severe. The damage initialises, gradually spreads and penetrates. This is illustrated in Fig. 3.13, which shows the FE predicted damage evolution (incremental damage method) for $R = 0.1$, $\sigma_{app} = 116$ MPa ($\sigma_{net} = 282$ MPa). With the incremental evolution of damage, the material is predicted to 'soften' in the associated area, so that stress redistribution occurs, as shown in Fig. 3.13. The x axis of Figs. 3.14(a) to 3.14(c) is shown in Fig. 3.4. The evolution of damage distribution across the notch ligament is shown in Fig. 3.14(a). The damage is predicted to be highly localised at the notch tip, but negligible for $x > 0.1$ mm. The peak damage value (at $x = 0$) accumulates to around 0.56 after $N = 0.63N_F$ and reaches 1 at the notch tip at $N = N_F$. A significant drop in maximum equivalent stress ($\sigma_{e,max}$) is predicted near the notch tip from 900 MPa ($N = 0$) to 500 MPa ($N = N_F$), while the peak value shifts away from the notch tip as N increases (Fig. 3.14(b)). A similar profile of octahedral shear stress amplitude (A_{II}) is shown in Fig. 16(c) but in this case the effect of damage on stress is even more dramatic. An A_{II} value of around 410 MPa at the notch tip reduces to only 50 MPa at $N = N_F$ and the peak A_{II} position shifts inwards across the ligament towards $x = 0.1$ mm. This illustrates material 'softening', due to fatigue damage at the hot

spot, and stress redistribution to the adjacent material. Hence the incremental damage method (Eqs. 3.3 and 3.7), illustrated in Fig. 3.13, in contrast to the integrated formula, local (Eq. 2.40) or non-local for life calculation, is capable of capturing the material degradation, stress redistribution and the resulting effects on fatigue lives, resulting in more accurate life prediction.

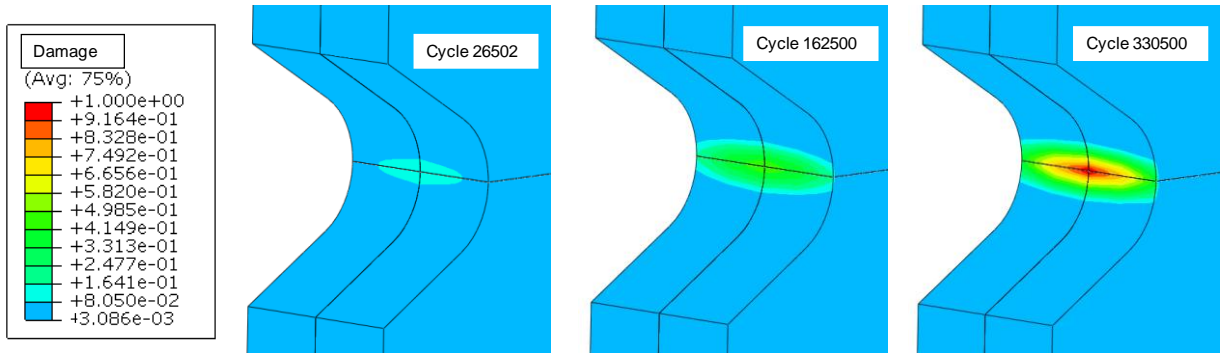
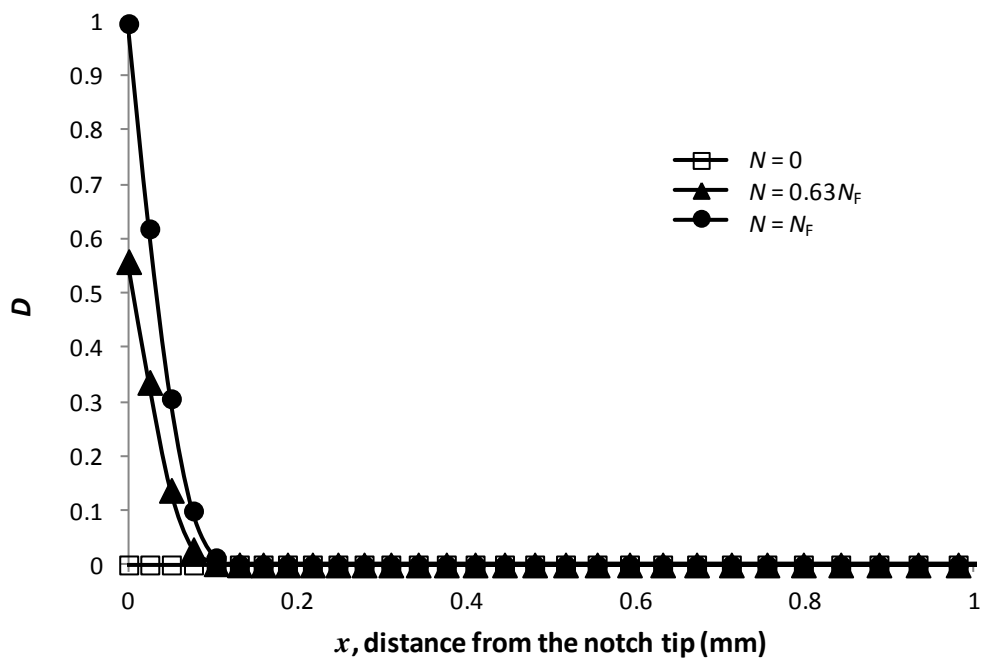
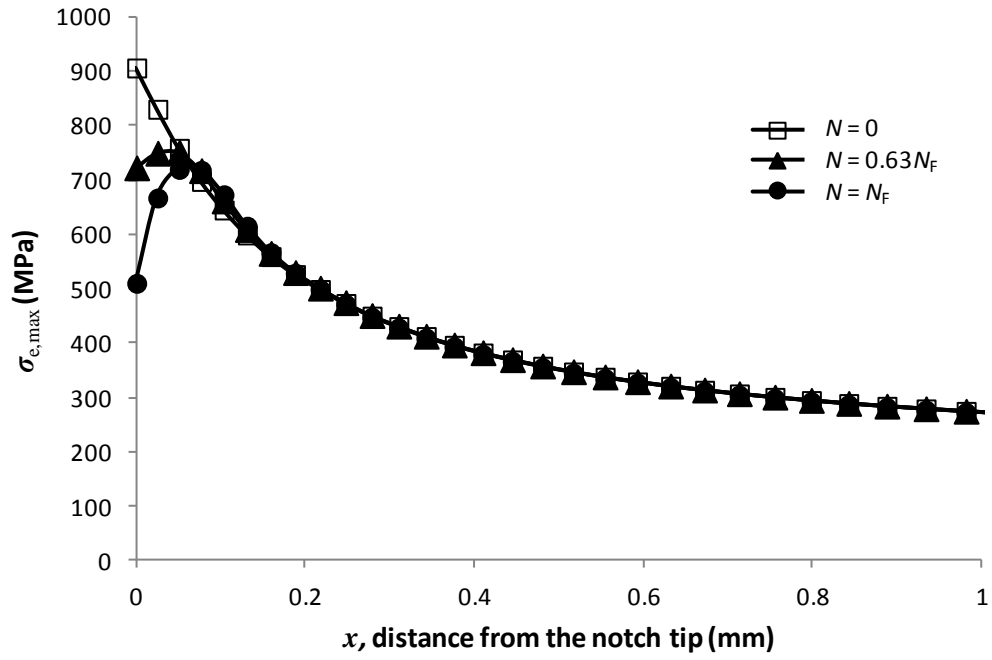


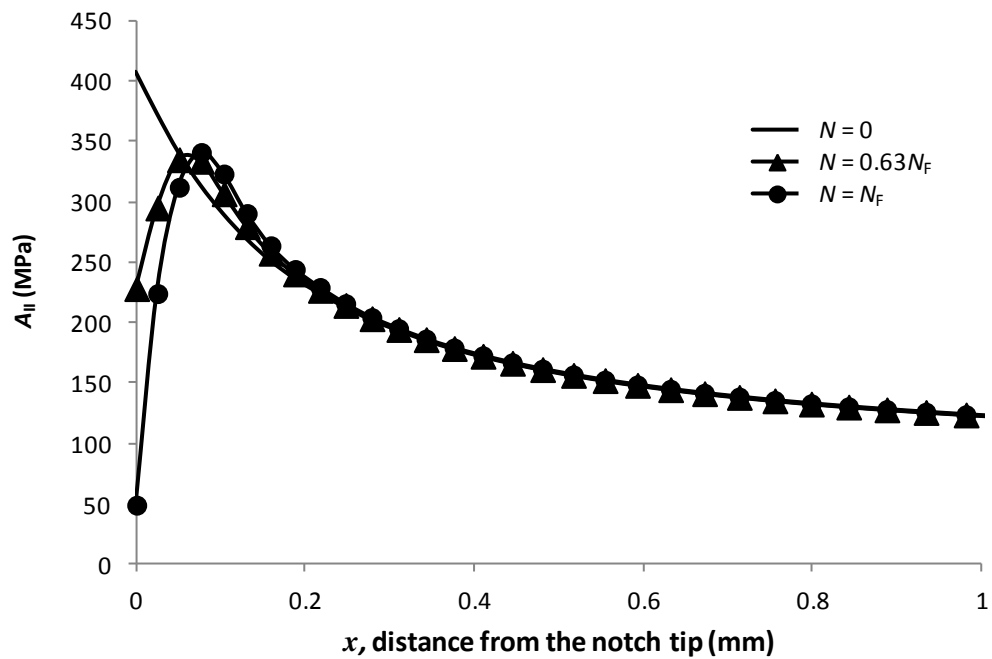
Fig. 3.13. FE predicted evolution of incremental damage distribution for $R = 0.1$, $\sigma_{app} = 116$ MPa ($\sigma_{net} = 282$ MPa), for V-notched case



(a)



(b)



(c)

Fig. 3.14. FE-Predicted evolution of variable distributions across notch ligament, for $R = 0.1$, $\sigma_{app} = 116$ MPa ($\sigma_{net} = 282$ MPa), in V-notched case from the incremental damage method, for (a) damage (b) maximum equivalent stress and (c) octahedral shear stress amplitude.

3.4.2 Fretting fatigue results

Fig. 3.15 shows the theoretical (Johnson, 1985 and Hills and Nowell, 1994) and FE-predicted distributions of shear traction. The model shows excellent agreement with the theory from Hills and Nowell (1994) and successfully predicts the eccentricity ($e = 0.265$ mm) of the centre of the stick zone from the centre of the contact.

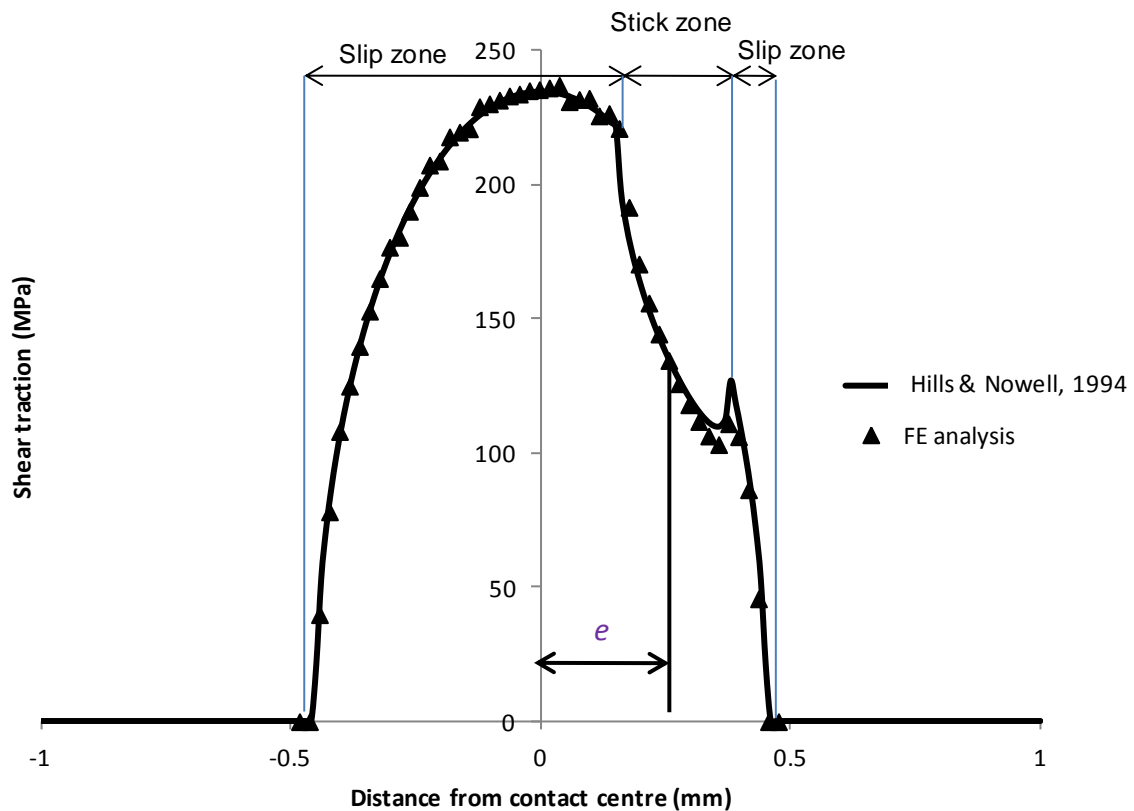


Fig. 3.15. Comparison of FE predicted and theoretical shear traction distributions for $Q = 156$ N/mm ($\Delta = 50$ mm) and $\sigma = 550$ MPa ($e = 0.265$ mm).

A plane strain version of the NLCD model is implemented here in an Abaqus user material subroutine to investigate the capability of the fatigue damage methodology to predict fretting fatigue crack nucleation. In the development of the fretting fatigue damage

methodology, it is of specific interest to predict the effect of material degradation (due to damage) on fretting stresses, in order to assess the performance of previously published methods, such as the critical plane approach.

Fretting can be divided into three regimes by slip amplitude, namely the gross slip regime (GSR), the partial slip regime (PSR) and the mixed slip regime (MSR). Using 'fretting map' approaches, Vingsbo et al. (1988) have shown that the fretting damage evolution is strongly dependent on the slip amplitude. Generally fretting can result in fretting wear and, under certain conditions, especially in PSR and MSR, fretting fatigue can occur. Fretting fatigue life is highly sensitive to slip amplitude, therefore analysis are carried out here to investigate life results under different slip amplitudes, especially below the gross slip threshold, where wear is not significant but fatigue cracks may initiate.

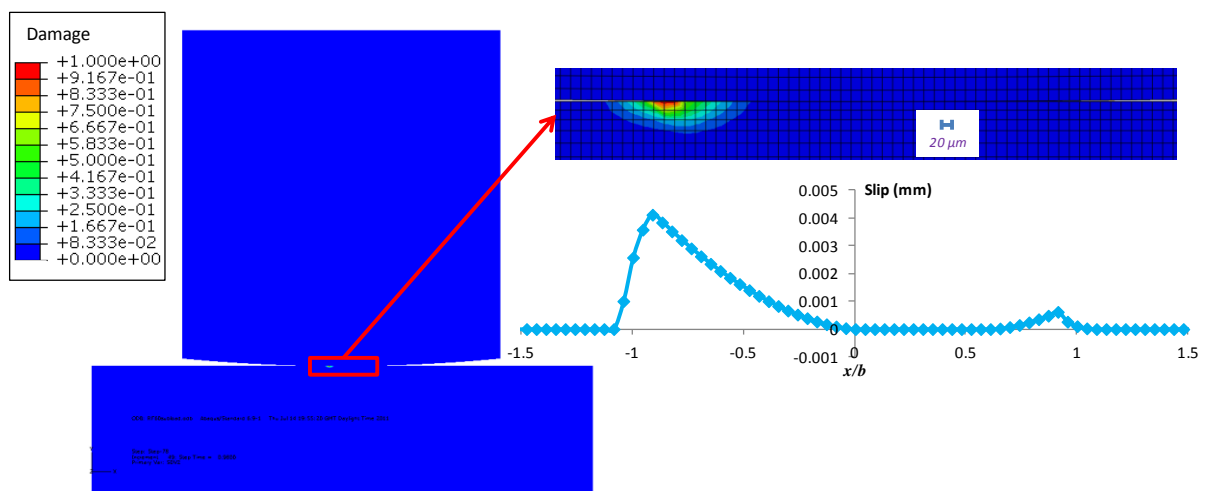
The applied strokes and resulting predicted relative slips are listed in Table 3.3.

Table 3.3. Applied half stroke Δ and resulting FE predicted relative slip amplitudes for the fretting fatigue configuration. (substrate fatigue stress σ has a maximum value of 550 MPa) (p.s. = partial slip; g.s. = gross slip)

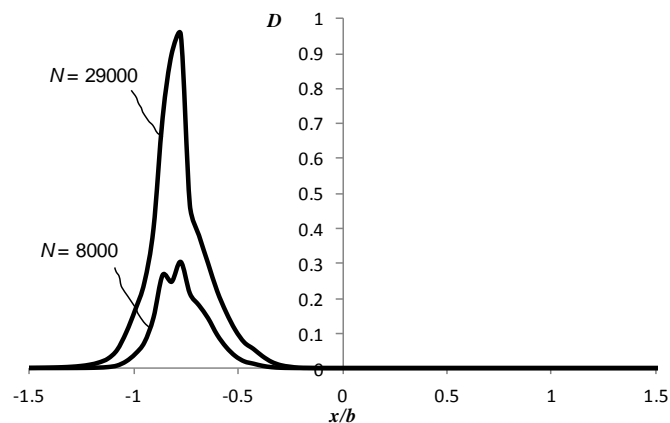
Δ (μm)	30	40	50	60	65	70
δ_{local} (μm)	0.87	1.64	2.67	4.12	6.52	11.47
Slip regime	p.s.	p.s.	p.s.	p.s.	g.s.	g.s.

Figs. 3.16(a) and 3.16(b) show the surface fatigue damage contours (at $N = N_F$), the associated contact slip distribution and the predicted evolution of surface fatigue damage for an applied stroke of $\Delta = 60 \mu\text{m}$. As illustrated in Fig. 3.16(a), localised damage is predicted slightly to the left of the centre of the slip zone, gradually spreading to the adjacent material. In experimental testing, fretting cracks are typically observed across the slip zone as

illustrated in (Araujo, J.A.& Nowell, 2002) (Fridrici et al. 2005). The fatigue damage mechanics predictions of Fig. 3.16(a) are clearly consistent with this measured trend. Fig. 3.16(b) shows the predicted evolution of damage at a depth of 3 μm along the flat specimen surface (where the first layer of integration points under the flat specimen surface are). Damage is predicted to concentrate at $x/b = -0.778$, well inside the trailing edge of contact ($x/b = 1$) which is at $x \approx -0.460$ mm. This is consistent with (Araujo & Nowell, 2002) (Fridrici et al. 2005).



(a)



(b)

Fig. 3.16. FE-predicted (a) contour plot of fretting fatigue damage after 30,000 cycles for fretting fatigue configuration and the corresponding location of maximum damage and (b)

evolution of damage at depth of 3 μm below fatigue specimen surface when $\Delta = 60 \mu\text{m}$ for incremental NLCD method.

Fig. 3.17 shows the FE-predicted distribution of critical-plane SWT along the flat specimen surface. The SWT peak of 5.36 MPa is predicted to occur at $x/b = -0.839$ mm, which is the location of maximum relative slip and which is also near the trailing edge of contact.

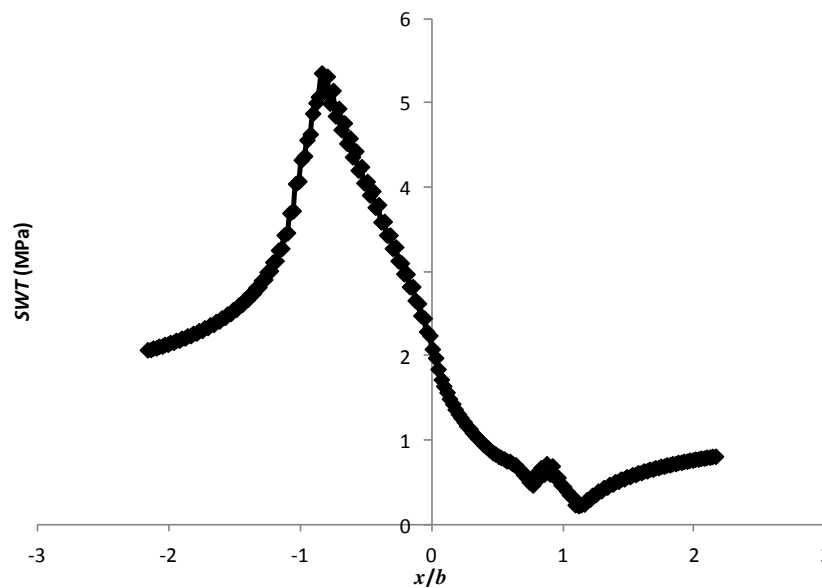


Fig. 3.17. FE-predicted critical plane SWT distribution along the fatigue specimen surface for the fretting fatigue configuration fretting fatigue configuration when $\Delta = 60 \mu\text{m}$.

Fig. 3.18 shows a comparison of predicted and measured (Jin and Mall, 2004) effect on fretting fatigue life of slip amplitude. The predictions are obtained using the FE-based incremental damage (NLCD) method. The NLCD FE result shows excellent agreement with the experimental results and successfully predicts the trend that the fatigue life decreases with increasing relative slip in the partial slip regime, which is consistent with the findings in (Madge, 2007). Specifically, the FE predicted life reduces from about 100,000 cycles to

about 21,000 cycles as the slip is increased from 1.64 μm to 6.52 μm . Above the partial slip-gross slip threshold, the predicted life increases slightly to about 25,000 cycles for a relative slip of 11.47 μm , which is consistent with test data (Jin and Mall, 2004). Table 3.4 shows a comparison of predicted fretting fatigue lives and failure locations from three different methods, namely, (i) the incremental NLCD model, (ii) the integrated NLCD model and (iii) the critical plane *SWT* method. As for the plain fatigue analysis, the integrated NLCD method predicts more conservative lives compared to the incremental NLCD method, due to the omission of material degradation and stress redistribution effects. The data in Table 3.4 and Fig. 3.19 shows that the *SWT* method generally over predicts life compared to the incremental NLCD method and the integrated NLCD method, but overall gives quite similar results as to the incremental NLCD method. From Table 3.4 it can be seen that the incremental NLCD model predicts that crack positions are within the slip band and near the trailing edge of contact, where the material is normally severely damaged as reported by previous findings (Araujo & Nowell, 2002) (Fridrici et al. 2005).

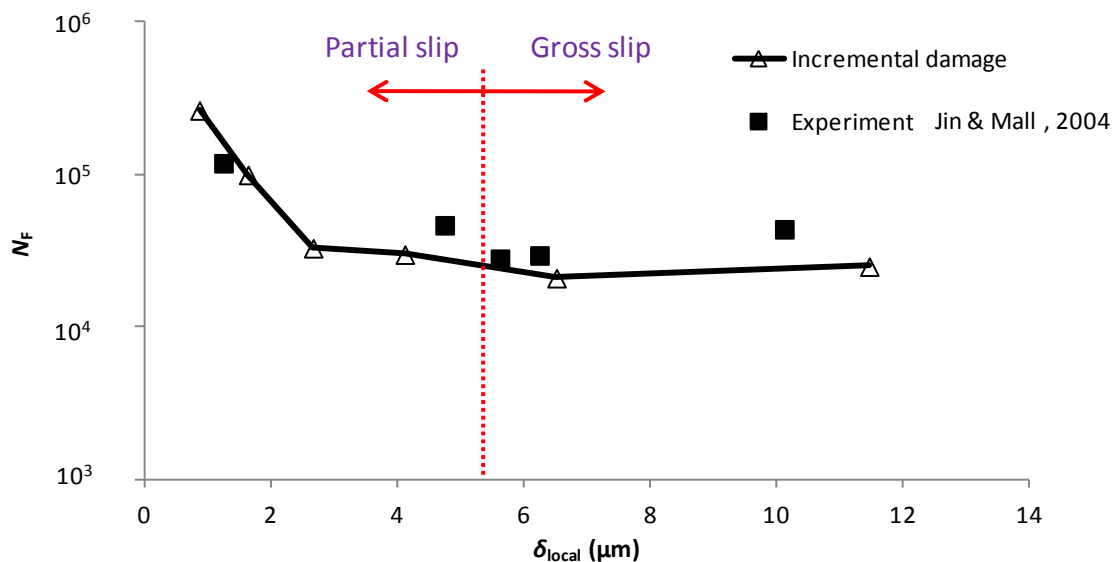


Fig. 3.18. Comparison of FE predicted and experimental fretting fatigue life as a function of slip amplitude.

Table 3.4. Comparison of measured and predicted lives and failure locations (b is the predicted contact half width).

N_F experiment (Jin and Mall 2004)	Predicted N_F			
	Relative slip δ_{local} (μm)	Incremental NLCD	Integrated NLCD	Critical plane SWT
1.19×10^5 ($\delta_{local} = 1.43 \mu\text{m}$)	0.87 (PS)	2.65×10^5 (at $x/b = 0.957$)	1.25×10^5 (at $x/b = 0.957$)	4.47×10^5 (at $x/b = 0.924$)
4.67×10^4 ($\delta_{local} = 5.43 \mu\text{m}$)	1.64 (PS)	1.00×10^5 (at $x/b = -0.913$)	6.46×10^4 (at $x/b = -0.913$)	1.25×10^5 (at $x/b = -0.920$)
2.82×10^4 ($\delta_{local} = 6.43 \mu\text{m}$)	2.67 (PS)	3.30×10^4 (at $x/b = -0.870$)	2.44×10^4 (at $x/b = -0.870$)	4.47×10^4 (at $x/b = -0.833$)
2.96×10^4 ($\delta_{local} = 7.14 \mu\text{m}$)	4.12 (PS)	3.00×10^4 (at $x/b = -0.778$)	2.14×10^4 (at $x/b = -0.778$)	2.95×10^4 (at $x/b = -0.839$)
4.40×10^4 ($\delta_{local} = 11.57 \mu\text{m}$)	6.52 (GS)	2.10×10^4 (at $x/b = -0.783$)	1.81×10^4 (at $x/b = -0.783$)	2.69×10^4 (at $x/b = -0.798$)
	11.47 (GS)	2.50×10^4 (at $x/b = -0.783$)	1.80×10^4 (at $x/b = -0.783$)	2.68×10^4 (at $x/b = -0.798$)

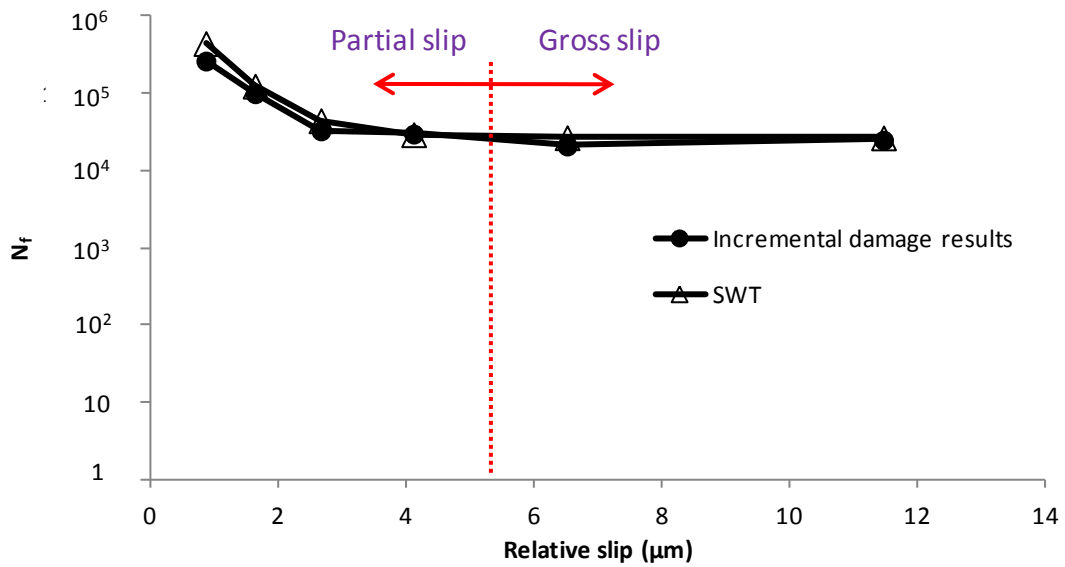


Fig. 3.19. Comparison of incremental NLCD based and SWT based fretting fatigue life as a function of slip amplitude.

Previous work by Mohd Tobi et al (2009) has shown that inclusion of the effects of wear in the model predictions will lead to a significant reduction in partial slip life for low slip for the same contact geometry as used here, albeit without the substrate fatigue load. This provides possible explanation for the non-conservative predictions in the low slip (partial slip) regime in this paper. It should also be noted that a constant COF value has been employed here across all fretting load cases, based on an average value identified from the test measurement (Jin and Mall, 2004; Sabelkin and Mall, 2006). This may lead to an underestimate of fatigue damage for partial slip cases, where high local COF values have been reported to occur (Sabelkin and Mall, 2005). Furthermore, there is insufficient test data available to quantify the key effect of scatter in fatigue; similarly for the predicted results. Even though the test and incremental damage predictions are different for small slips, in reality, for fatigue, these differences are negligible (i.e. 2.65×10^5 compares to 1.19×10^5 and 1.00×10^5 compares to 4.67×10^5) due to being certainly within expected level of experimental scatter. Perhaps of greater significance is the conservative nature of the incremental damage results compared to the critical-plane *SWT* results which have been shown to give excellent correlation to the same test data previously when wear effects were included with *SWT*. Another important factor is the issue of mesh refinement. Even though the present model gave good correlation with the analytical shear traction, it is not easy to validate sub-surface stress predictions. The computational overhead associated with coupled damage calculations precludes exhaustive mesh refinement. Hence it can be anticipated that additional mesh refinement could lead to higher local partial slip stresses and hence further reduced lives. This in turn would lead to more conservative predictions. The failure locations between the integrated and incremental models have no difference here. Essentially, this suggests that the effect of stress redistribution is not sufficient in this work to shift the hot-

spot. This also shows some possible benefits to use an integrated damage model. However, a significant effect for fretting is the effect of wear. Combining this with fatigue damage mechanics is an onerous task analytically and computationally, particularly for complex geometries such as hip joint taper-lock assemblies, as analysed in Chapter 6 and 7 in this thesis. It can be anticipated that wear-induced stress evolution would lead to different trends in terms of predicted crack location.

3.5 Conclusions

A finite element based method coupled with a nonlinear continuum damage model has been developed and validated for uniaxial and multiaxial plain fatigue, unnotched and notched conditions. The method has been applied to a fretting fatigue round on flat case for Ti-6Al-4V with comparisons against published data for the effect of slip on life. Some key findings are:

- Incremental damage accumulation coupled with FE analysis provides an insight into load redistribution in the high stress gradient area and predicts longer life compared with the integrated formula.
- The backward difference integration scheme is shown to be superior to the forward difference, since it predicts more conservative life with increasing cycle jumping factor, though it is significantly more computationally expensive.
- FE analysis of fretting fatigue coupled with the NLCD model predicts a similar trend of life versus slip to the critical plane *SWT* method and experimental results.
- The life is predicted to reduce as slip amplitude increases in the partial slip regime and slightly increases above the partial slip-gross slip threshold. This

shows NLCD model potentially has the ability to capture the key phenomenon in fretting fatigue that life drops then increases from partial slip regime to gross slip regime, as shown before by Jin and Mall, 2004 and Madge et al., (2007), even without simulating wear.

- The predicted cracking positions are across the slip band and, specifically, in the centre of the slip zone, which is consistent with the experimental observations.

This chapter investigated nonlinear continuum damage mechanics and life for plain and fretting fatigue based on NLCD model. It has been shown that NLCD model is capable of capturing the key role of loading conditions and slip regimes on fretting lives and shows excellent agreement with previous test results. The life prediction of NLCD model show good agreement with the critical plane SWT approach. Since the computational expense is normally significantly higher than the critical plane SWT approach (e.g. for one V-notched case with the mesh presented here under $R = 0.1$, NLCD model takes nearly 20 hours while SWT costs 20 minutes as a post-process), the later chapters adopt the latter for studying the effect of contact geometry and hip implant taper-lock analysis.

Chapter 4

Finite Element Methodology for Fretting Wear-Fatigue Interaction

4.1 Overview

Fretting wear has been shown in Madge et al. (2007) to have a significant influence to fretting fatigue lives. In this chapter, a finite element based methodology for fretting wear-fatigue interaction is developed. A non-linear kinematic hardening plasticity formulation is employed to model the Bauschinger effect, which is a complex phenomenon observed in the cyclic behaviour of polycrystalline metals and single crystals. The energy wear approach (Fouvry et al., 2003) is adopted to simulate wear-induced material removal. An adaptive meshing technique implemented in a user subroutine and the critical plane SWT (Smith et al., 1970) method, in conjunction with the Miner - Palmgren rule for cumulative fatigue damage (Palmgren, 1924), is adopted to predict multiaxial fretting crack nucleation. A wear-fatigue damage algorithm is implemented to interpolate the fatigue damage accumulation throughout the fretting cycles, within the adaptive meshing framework of the wear analysis. Fretting lives are also predicted based on wear-induced plastic ratchetting as a competitive mechanism to fretting fatigue failure.

4.2 Constitutive model

The Bauschinger effect is a complex phenomenon observed in the cyclic behaviour of polycrystalline metals and single crystals and it can be explained by anisotropy of the dislocation fields from previous loading, whereby the yield stress in compressive loading is reduced relative to that in a preceding tensile (plastic) half-cycle and similarly reduced in tensile loading relative to that in a preceding compressive half-cycle. The kinematic hardening model is a simplified representation used to model this effect, which assumes that the yield stress range remains constant and equal to $2\sigma_y$, where σ_y is the yield stress, and the reduction in yield stress in the reversed direction is equal to the increment in yield stress in the preceding (opposite) loading direction. The non-linear kinematic hardening model is employed here to model the *Bauschinger* effect. The translation of the centre of the yield surface in kinematic hardening is governed by a tensor \mathbf{x} called the *backstress*, defined for non-linear hardening as follows:

$$d\mathbf{x} = \frac{2}{3} C d\boldsymbol{\varepsilon}^p - \gamma \mathbf{x} dp \quad (4.1)$$

where the plastic strain increment, $d\boldsymbol{\varepsilon}^p$ is calculated via the flow rule, as follows:

$$d\boldsymbol{\varepsilon}^p = d\lambda \frac{\partial f}{\partial \boldsymbol{\sigma}} = \frac{3}{2} dp \frac{\boldsymbol{\sigma}'}{\sigma_e} \quad (4.2)$$

$$f = \sigma_e - \sigma_y = \left(\frac{3}{2} (\boldsymbol{\sigma}' - \mathbf{x}') : (\boldsymbol{\sigma}' - \mathbf{x}') \right)^{\frac{1}{2}} - \sigma_y \quad (4.3)$$

$$dp = \left(\frac{2}{3} d\boldsymbol{\varepsilon}^p : d\boldsymbol{\varepsilon}^p \right)^{\frac{1}{2}} \quad (4.4)$$

where C is a the hardening modulus, f is the von Mises yield function, dp is the increment in effective plastic strain, σ_e is the von Mises equivalent stress, σ' and \mathbf{x}' are the deviatoric stress and backstress tensors, respectively, and σ_y is the yield stress. $d\lambda$ is the plastic multiplier, which, for a von Mises equivalent stress, is equivalent to the increment in effective plastic strain. The same cyclic elastic-plastic constitutive material model is employed for all three geometries, corresponding to published data for Ti-6Al-4V from Benedetti et al. (2004). The elastic material properties used for the cylinder and flat are: Young's modulus of 116 GPa and Poisson's ratio of 0.342. It was shown by Mohd Tobi et al. (2009), using a linear kinematic hardening (LKH) model, that cyclic plasticity and ratchetting effects potentially play an important role in fretting of Ti-6Al-4V, particularly when wear effects are accounted for. A non-linear kinematic hardening (NLKH) formulation is used in the present fretting simulations with wear and fatigue. The NLKH model is superior to the LKH model in the modelling of cyclic plasticity phenomena, specifically ratchetting (Ambrico and Begley, 2000); in particular, the LKH model is known to underestimate ratchetting relative to the NLKH model. The cyclic material response is represented in Abaqus using the elastic-plastic constitutive law proposed by Lemaitre and Chaboche (1990). The cyclic strain-hardening behaviour is given by the following equation:

$$\frac{\Delta\sigma}{2} - k = \frac{C}{\gamma} \tanh\left(\gamma \frac{\Delta\varepsilon_p}{2}\right) \quad (4.5)$$

where k , C , γ are the characteristic coefficients, the values of which are 840 MPa, 8976 MPa, and 102, respectively, taken from Benedetti et al. (2004) for Ti-6Al-4V; k is the cyclic (initial) yield stress, and γ is the rate of decay of the modulus.

The algorithm used in this work integrates the nonlinear isotropic/kinematic hardening model (combined) and provides accurate solutions if the values of γ change moderately in an increment due to temperature and/or field variable dependence. Fig 4.1 shows a comparison of the FE-predicted cyclic stress-strain response and the theoretical formulation of Equation 4.5. The FE results are shown for three discrete values of applied plastic strain range under uniaxial conditions (corresponding to three different strain-controlled analyses), thus validating the FE-implementation of the Ti-6Al-4V cyclic material behaviour.

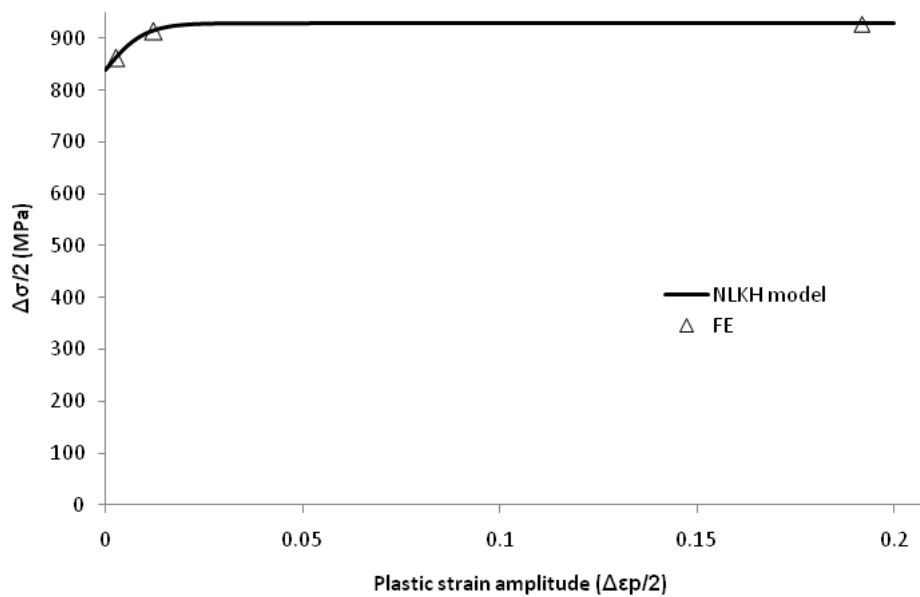


Fig. 4.1. Comparison of FE-predicted cyclic behaviour with NLKH theoretical formulation.

4.3 Wear model

Previous wear simulation work by Leen and co-workers, e.g. (McColl et al., 2004; Madge et al., 2008), was based on the use of a modified Archard approach, based on the classical Archard wear equation for sliding wear (Archard, 1953):

$$\frac{V}{S} = K \frac{P}{H} \quad (4.6)$$

where V is the wear volume, S is the sliding distance, K is the wear coefficient, P is the normal load and H is the hardness of the material. This approach has been implemented in the Abaqus FE code, using both an external Fortran program (McColl et al., 2004) and, more recently, an adaptive meshing subroutine within Abaqus (Ding et al., 2009; Mohd Tobi et al., 2009), and validated for both a high strength CrMoV aeroengine steel (SuperCMV) (McColl et al. 2004) and Ti-6Al-4V alloy (Ding et al. 2009), under a range of load-stroke combinations. However, it has been found that, the measured wear co-efficient is dependent on load and stroke, e.g. see McColl et al. (2004) and Ding et al. (2009). An alternative method, referred to as the energy wear approach, has been proposed by Fouvry and co-workers, e.g. Fouvry et al. (2004), which considers the interfacial shear work as the significant wear parameter controlling wear volume calculation. This approach has been shown to be superior to the Archard-based approach in that a single wear coefficient can be used across a range of fretting load-stroke combinations, specifically including both partial slip and gross slip regimes. The energy wear approach can be represented by the following equation:

$$V = \alpha \sum E \quad (4.7)$$

where α is the wear coefficient and $\sum E$ is the accumulated dissipated energy. The concept of the energy wear coefficient is that a value independent of load and stroke be identified from tests across a range of loads and strokes; this is not typically possible with the Archard approach. It can be shown that in the gross slip regime, the two approaches (in terms of predictions) are the same for an appropriate choice of Archard and energy wear coefficients, i.e. $\alpha/\mu = K/H$, certainly in terms of predicted wear scar dimensions. However, in the partial slip regime, when $Q < \mu P$, the two approaches will not give the same results.

For a 2D model, at time t and position x , the local wear depth can be related to the local accumulated dissipated energy, as follows:

$$h(x,t) = \alpha E(x,t) \quad (4.8)$$

where x is horizontal distance of a contact node from the centre of contact and $E(x,t)$ is the 2D accumulated dissipated energy, given by:

$$E(x,t) = \int_{t=0}^t q(x,t) ds(x,t) \quad (4.9)$$

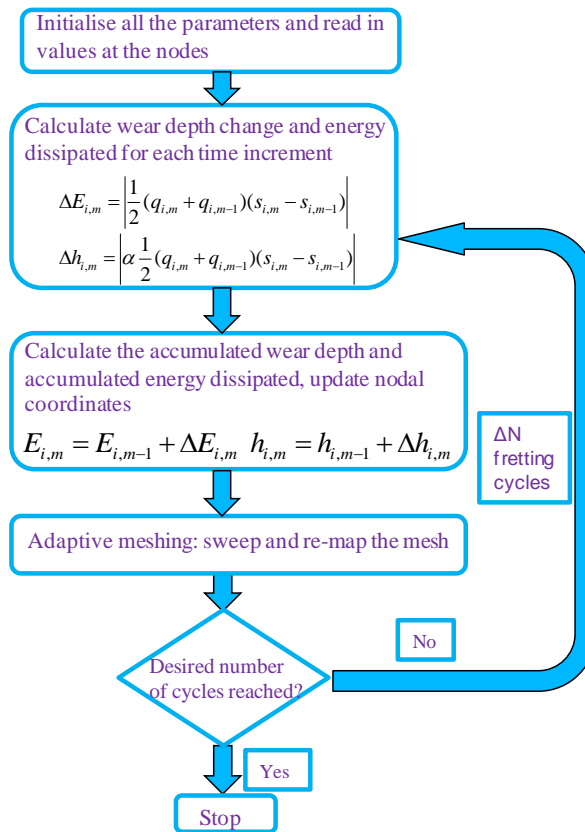
where $q(x,t)$ is the local instantaneous shear traction and $ds(x,t)$ is the local instantaneous incremental relative slip.

In this chapter, following the FE-implementation previously developed for the Archard-based wear simulation method (Madge et al. 2007), the adaptive meshing UMESHMOTION user subroutine within Abaqus is used to incrementally simulate the material removal according to the above equations, as described graphically in the flowchart of Fig. 4.2a. Thus, for a contact node i at the m^{th} increment, Equation 4.7 can be written as:

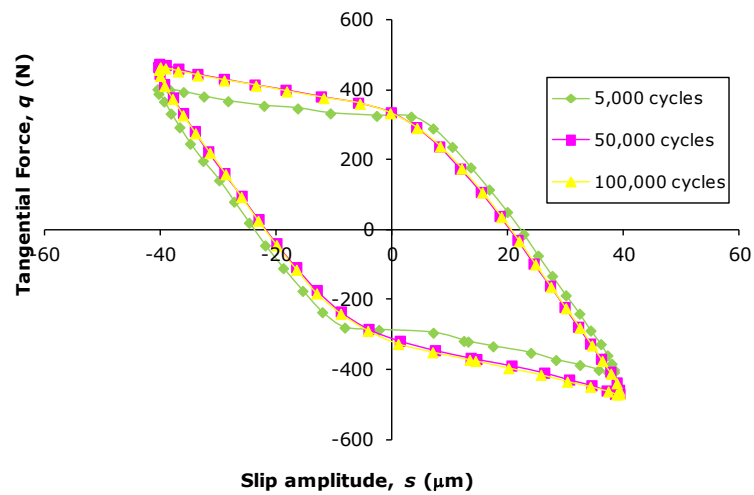
$$\Delta h_{i,m} = \alpha E_{i,m} \quad (4.10)$$

where the incremental dissipated energy $E_{i,m}$ is:

$$E_{i,m} = q_{i,m} \Delta s_{i,m} \quad (4.11)$$



(a)



(b)

Fig. 4.2. (a) Flowchart depicting FE implementation of energy wear methodology. (b) Illustration of energy accumulation by slip and tangential force.

where $q_{i,m}$ and $\Delta s_{i,m}$ are the shear traction and incremental slip, respectively, at node i in the m^{th} increment. Following the cycle-jumping technique used previously in the Archard-based approach (Ding et al., 2009) to efficiently predict the accumulated wear depth and associated evolution of geometry and fretting variables, the total accumulated nodal wear h_i after a N_T fretting cycles is thus:

$$h_i = \sum_{n=1}^{N_T / \Delta N} \sum_{m=1}^{m_{\max}} \Delta h_{i,m} \quad (4.12)$$

where m_{\max} is the maximum increment number within one fretting cycle and ΔN is the increment in fretting cycles (cycle jump) during which the fretting variables are assumed to remain constant. Caution is required to ensure that accuracy is not sacrificed. This is achieved here via ΔN sensitivity studies and comparison with measured wear data from Ding et al. (2009). The adaptive meshing algorithm of Abaqus applies the local wear increment for all surface nodes in two steps. First, the local wear increment is implemented by moving the surface nodes in the local normal direction; this geometry update is implemented as a purely Eulerian analysis. Secondly, the material quantities (variables) are re-mapped to the new positions, by advection from the old location to the new location by solving the advection equations using a second order numerical method called the Lax-Wendroff method, see Fig. 4.3. These two steps cause an equilibrium loss which is corrected by solving the last time increment of the contact problem (Smith and Liu, 1953). The wear analyses simulate up to 300×10^3 cycles using a cycle jump ΔN of 2×10^3 with 100 increments in one simulated tangential fretting cycle.

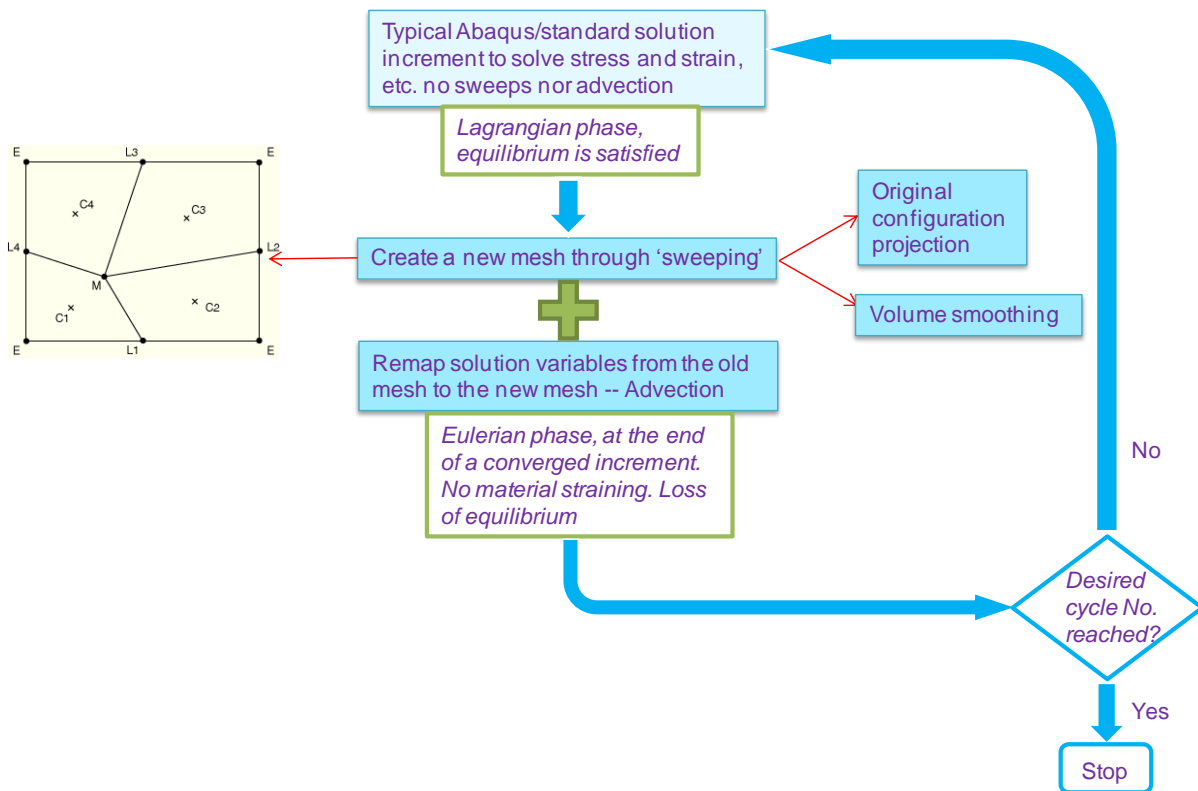


Fig. 4.3 Description of different phases in adaptive meshing.

4.4 Fatigue model

4.4.1 Critical plane SWT fatigue damage model

Many approaches based on local parameters have been proposed in the literature, e.g. the critical distance method (Taylor, 2007) has been developed during recent years and successfully used for fatigue assessment of notched components. A critical plane approach incorporating the Smith-Watson-Topper (Smith et al. 1970) fatigue parameter is used here to predict crack nucleation, following the methodology established by Sum et al. (2005) and further developed in Madge et al. (2008) for application to crack nucleation. This is achieved by back-extrapolation of the fatigue constants, using linear elastic fracture mechanics, to infer the lives corresponding to 10 μm crack lengths, for example, for given stress levels. It was shown by Sum et al. (2005) that the FE-implementation of this approach can capture stress

gradient effects, e.g. the contact size effect; this is attributed to the built-in volume-averaging nature of the Gaussian sampling technique in the FE method. The critical plane approach is based on the physical observations that fatigue cracks initiate and grow within a material on certain planes, where the growth and orientation depends on the normal stresses and strains on these planes. The *SWT* life prediction equation employs a combined high-cycle fatigue (HCF) and low-cycle fatigue (LCF) equation, and consideration of the peak stress to account for the mean stress effect, as follows:

$$SWT = \sigma_{\max} \frac{\Delta \varepsilon}{2} = \frac{\sigma_f'}{E} (2N_f)^{2d} + \sigma_f' \varepsilon_f' (2N_f)^{d+e} \quad (4.13)$$

where σ_{\max} is the peak normal stress on the critical plane, $\Delta \varepsilon$ is the maximum normal strain amplitude on the same plane, σ_f' and d are the (Basquin) fatigue strength coefficient and exponent (HCF constants), ε_f' and e are the (Coffin-Manson) fatigue ductility coefficient and exponent (LCF constants) and E is Young's modulus. The values of these constants corresponding to 10 μm crack nucleation employed here for Ti6Al4V, as obtained from Madge et al. (2008) and Ding et al. (2009) are listed in Table 4.1.

The FE-implementation of the critical-plane *SWT* parameter is achieved by transforming the time histories of element centroidal stresses and strain ranges onto planes at 5° intervals over a 180° range using the two-dimensional transformation (Mohr's circle) equations for stress and strain. The maximum normal stress σ_{\max} with respect to time, and the corresponding strain range $\Delta \varepsilon$ are determined for each of the 36 planes in each element. $\Delta \varepsilon$ is the difference between the maximum and minimum values of strain normal to the candidate plane over the complete loading cycle. Thus, *SWT* values are obtained for each candidate plane in each element. These values are then employed to establish the maximum critical

plane SWT value with respect to plane orientation in each element, which in turn is used with Eq. 4.13 to furnish a number of cycles to failure, N_f .

Table 4.1. SWT constants for Ti-6Al-4V corresponding to 10 μm crack nucleation (from Madge et al. (2008) and Ding et al. (2009))

σ_f' (MPa)	d	ϵ_f'	e
1817.2	-0.0978	0.841	-0.688

One of the difficulties in the case of combined wear-fatigue calculations is the fact that the stress cycles change with evolving contact geometry. Thus, a fatigue damage accumulation methodology is required. The Miner-Palmgren rule is used here to calculate the damage accumulation, as follows:

$$D(N) = \sum_{i=1}^N \frac{\Delta N_i}{N_{fi}} \quad (4.14)$$

where ΔN_i is the number of cycles experienced at loading cycle i (a wear increment) with an associated SWT value of SWT_i and N_{fi} is the predicted number of cycles to failure (via Equation 4.13) for SWT_i . The occurrence of $D(N) = 1$ indicates predicted location, orientation and number of cycles for crack nucleation.

4.4.2 Wear-fatigue damage algorithm

Due to the use of adaptive meshing to represent material removal by wear, the position of the integration points is modified incrementally and is no longer linked uniquely to actual material points throughout the analysis. The integration points follow the mesh sweeping scheme and store mechanical/material information in both Lagrangian and Eulerian phases; the material points are pure Eulerian coordinates which represent material components. As illustrated in Fig. 4.4, due to wear, the position of the integration points (blue crosses) is

pushed down away from the material points (red circles) since the contact surface is modified. However, in fatigue life prediction using critical-plane SWT combining the Miner-Palmgren rule, damage is accumulated at the integration points throughout the fretting wear-fatigue cycles, although some of the damage at those integration points which are near surface could have been 'worn away' together with the material. Therefore it is necessary to compensate the extra fatigue damage accumulated by a modified wear-fatigue damage algorithm. The basic assumption of the algorithm used here is that damage is monitored at the integration points, which are moving through the material. Hence, increments of damage must be interpolated from damage at different material points in different increments. Then, failure is defined to correspond to damage at any one integration point reaching a value of 1.

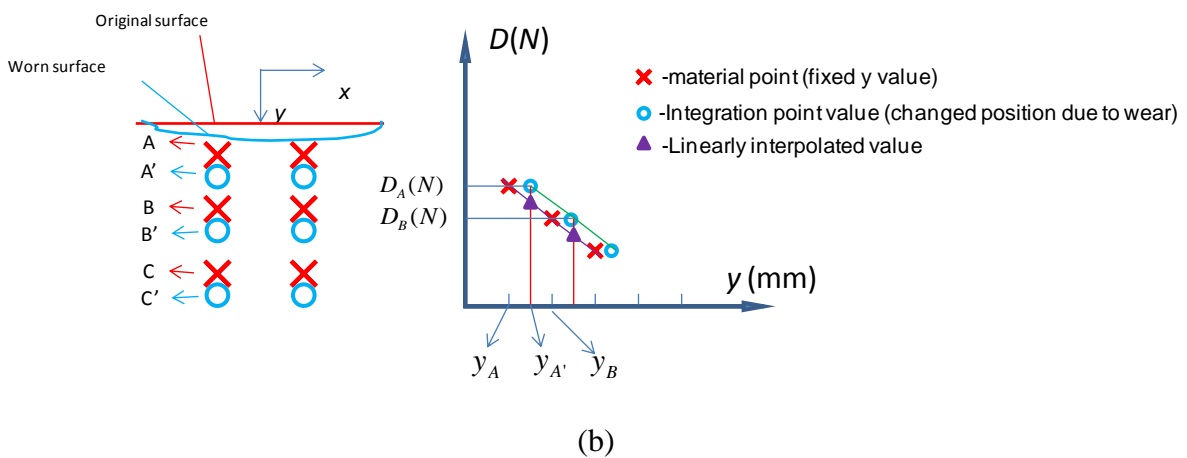
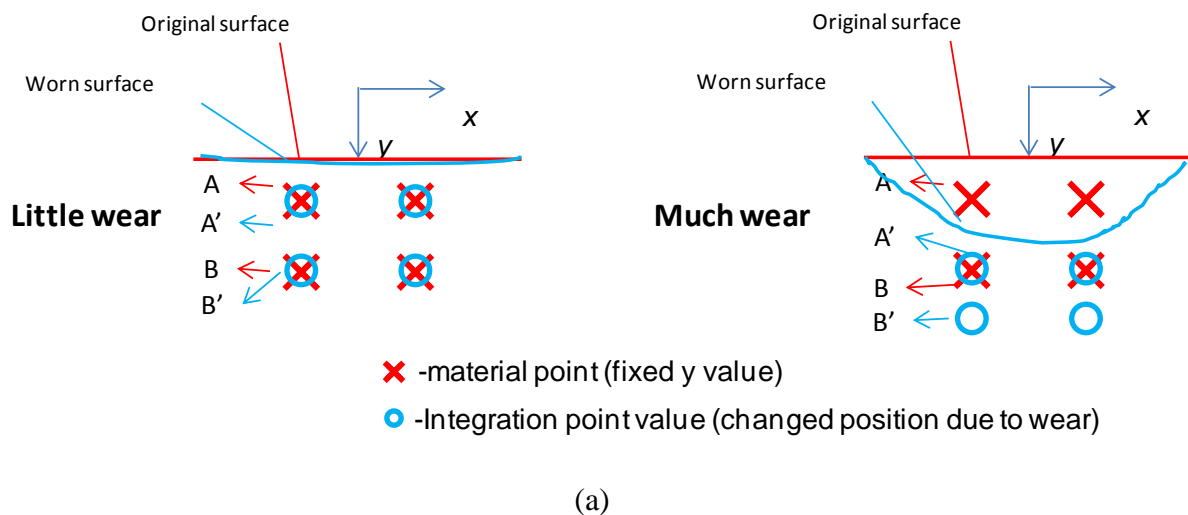


Fig. 4.4. (a) Schematic of two extreme cases of integration points moving due to adaptive meshing and (b) Schematic of fretting wear-fatigue algorithm for general case (where D is the accumulated damage, y is the depth, A, B, C are the material points and A', B', C' are the integration points)

Fig. 4.3a shows two extreme cases which can help understanding the algorithm and Fig. 4.3b shows the general case and the schematic of linear interpolation process. Fig. 4.3(left) shows a case where wear is negligible, in which damage at the integration point A', at N_i th wear increment, can directly represent the damage at material point A. Fig. 4.3(right) shows a case where wear is significant, and the integration point A' happened to move to a position where the second layer of material point B is. In this case damage at integration point A' now should actually represent the damage accumulated at material point B (A has been worn away). For a general case between this two, a linear interpolation scheme is developed. Referring to Fig. 4.3b, in any one wear increment, given integration point A' (originally at A) has moved from y_A to $y_{A'}$ and integration point B' (originally at B) has moved from y_B to $y_{B'}$. From previous increment, the fatigue damage has been accumulated at y_A and y_B . Incremental damage $\Delta N_i/N_{fi}$ and total damage (see Eq. 4.14) are now calculated at the (moving) integration points. So a decision needs to be made to attribute that damage to a location (material point). The decision made here is to associate the total damage with the material point with coordinates corresponding to the original integration point locations, e.g. y_A and y_B . Then it is necessary to refer this damage forward to the material points with coordinates corresponding to the current integration point locations, e.g. $y_{A'}$ and $y_{B'}$. This is achieved here by a simple, linear interpolation scheme, which defines the damage at $y_{A'}$ and $y_{B'}$ as follows:

$$D_{A'} = \frac{D_A - D_B}{y_A - y_B} \cdot (y_{A'} - y_A) + D_A \quad (4.15)$$

Similarly for integration point B', the temporary accumulated damage value is:

$$D_{B'} = \frac{D_B - D_C}{y_B - y_C} \cdot (y_{B'} - y_B) + D_B \quad (4.16)$$

where D_A , D_B are the total damage values at increment N_i , but referred to locations y_A and y_B , and $D_{A'}$, $D_{B'}$ are the total damage values at increment N_i , referred to locations $y_{A'}$ and $y_{B'}$, i.e. the updated (current) integration point locations. Note that D_A , D_B are incrementally accumulated linear damage and assumed to be the pseudo damage at the material points (of the first and second layer, respectively) which may be already worn away. The algorithm checks the interpolated accumulated damage for each increment for each integration points; once damage at a single point reaches 1, fatigue life will be reported. The detailed program is coded in Fortran and listed in the Appendix A2.

4.5 Ratchetting failure model

Plastic ratchetting has been described in detail in Chapter 2. It was also shown in Mohd Tobi et al., (2009), using a linear kinematic hardening (LKH) model, that cyclic plasticity and ratchetting effects play an important role in fretting of Ti-6Al-4V, particularly when wear effects are accounted for. Here combining the non-linear kinematic hardening model, it is assumed here that for a ratchetting failure to occur, the total accumulated strain must reach a critical value ε_c , which is defined as the stress-triaxiality dependant material ductility (Yan et al. 2000). This value depends on the local stress triaxiality resulting from geometric constraints and loading condition. The number of cycles to failure by ratchetting N_r can be predicted using the following equations:

$$\sum_i^{N_r} \Delta \varepsilon_r = \varepsilon_c \quad (4.17)$$

$$\Delta \varepsilon_r = \sqrt{\frac{2}{3} \Delta \varepsilon_{ij}^r \Delta \varepsilon_{ij}^r} \quad (4.18)$$

where $\Delta \varepsilon_r$ is a (uniaxial) equivalent ratchetting strain, corresponding to a multiaxial ratchetting strain condition (See Fig. 2.21). Hence there is a possible competition between failure due to (i) ductility exhaustion via ratchetting and (ii) fatigue failure (low- or high-cycle or combined) as represented here by the critical-plane SWT parameter and, earlier, by the continuum damage mechanics (Sines, 1959) fatigue damage. Thus, whichever occurs first, viz. ductility exhaustion or critical fatigue damage, determines the failure mechanism, location and life for crack nucleation.

4.6 Summary

In the chapter an FE based methodology for fretting wear-fatigue interaction is developed. A fatigue damage accumulation algorithm which accounts for adaptive meshing effects (wear-induced material removal) is presented for accurate prediction of fretting fatigue life. A ratchetting failure model for fretting-induced plasticity is an alternative failure model for fretting fatigue. The methods presented here are implemented in subsequent chapters to study the effect of contact geometry of fretting wear-fatigue performance and as the basis for a predictive tool for wear-fatigue analysis and assessment of hip implant taper-lock couplings.

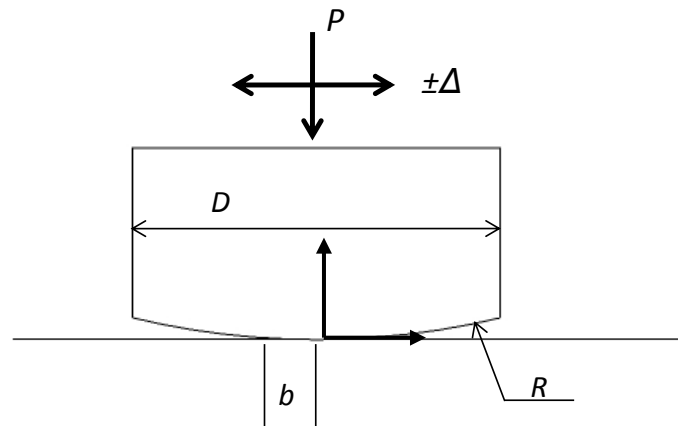
Chapter 5

An Investigation on the Effect of Contact Geometry on Fretting Wear-Fatigue Performance

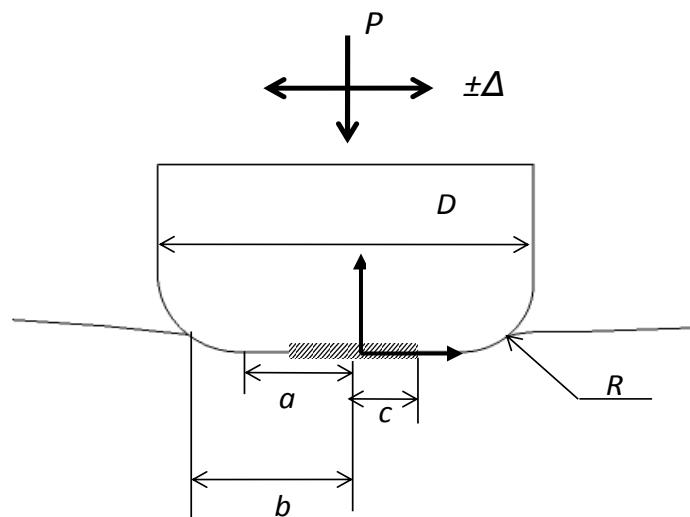
5.1 Overview

A key challenge in the design of engineering couplings and contacting components relates to the development of an understanding of the comparative performance of contrasting contact geometries for a given application, including loading, applied deformations and geometrical space envelope. Fretting is observed in many mechanical assemblies such as keyway-shaft couplings and shrink-fitted couplings. Two specific examples which have motivated the present work are (i) the pressure armour layer of a marine flexible riser, where the groove and nub experience fretting contact damage and (ii) the micro-scale undulations of Ti64 in the taper-lock coupling of the modular hip implant (see Chapter 7). A Hertzian cylinder-on-flat contact geometry is commonly assumed for the groove-nub contact of (i), due to the ready availability of the contact (normal and tangential) analytical solutions for this geometry. In reality the contact geometry is closer to a rounded punch-on-flat. The present work adopts a finite element methodology which has been described in Chapter 4. It is concerned with the problem of predicting the comparative fretting performance of two contrasting contact geometries to transmit a specified normal load, with a specified tangential displacement cycle, for a given material combination and within a specified geometrical space envelope, as illustrated in Fig. 5.1. The geometries adopted here are from Jin & Mall, 2004; one of Hertzian geometry and one with medium rounded corner. One extreme case is the sharp cornered flat on flat contact, which is not concerned here. The objective is to

understand which geometry is better in terms of both wear and fatigue/cracking performance, particularly when wear-induced evolution of contact geometry is accounted for.



(a)



(b)

Fig. 5.1. Schematic of fretting contacts: (a) Round on flat (RF2) (Round radius $R = 50.8 \text{ mm}$, $D = 9.5 \text{ mm}$, half contact width b) and (b) Round punch on flat (RPF) (Radius $R = 2.54 \text{ mm}$, half flat region width $a = 2.25 \text{ mm}$, $D = 9.5 \text{ mm}$, half contact width b).

The pressure armour layer of a marine flexible riser is designed to allow large deflections under combined torque, axial and bending loads, leading to potential fretting contact damage to the groove and nub contact regions, as illustrated in Fig. 5.2. Feret et al. (1987) have presented analytical solutions for the calculation of stresses and slip in structural layers of unbounded flexible pipes, without explicit consideration of (i) the local contact geometry and (ii) wear effects. The present work is a first step towards understanding and predicting fretting in flexible risers and other complex contacts with inclusion of wear effects. An incremental wear simulation method based on the energy approach of Fridrici et al. (2001) and previous work Ding et al. (2009) is adopted. A non-linear kinematic hardening plasticity formulation is employed and a critical-plane, Smith-Watson-Topper approach is used to predict multiaxial fretting crack nucleation. Wear evolution and crack nucleation predictions are validated against existing published data for Ti-6Al-4V (Ding et al., 2009). Under the same fretting variables (normal load, stroke, etc), different contact geometries are shown to result in significant differences in fretting behaviour. In order to assess this difference comparatively, this study describes the prediction of evolution of contact geometry, wear, salient surface and sub-surface fretting variables, including plasticity and fatigue damage parameters across a range of fretting strokes for the two arrangements.

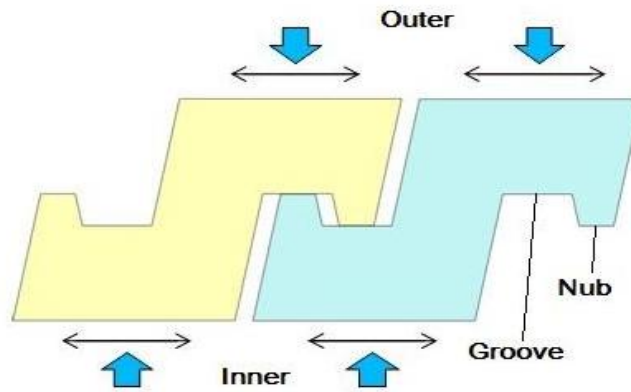


Fig. 5.2. Schematic of pressure armour layer contact.

5.2 Computational methodology

5.2.1 FE modelling

Three FE models are developed for the analyses of this work, as shown in Table 6.1. In all cases a two-dimensional, plane strain assumption has been employed. The general purpose, non-linear FE code Abaqus is used for all of the analyses. The first model, RF1, is based on the geometry of the University of Nottingham fretting test rig and is employed here to validate the energy-based wear prediction methodology against the experimental and (modified Archard method) numerical results of (Ding et al., 2009). The second and third models, RF2 and RPF, are round-on-flat and rounded punch-on-flat fretting geometries, based on the USAF test configuration of Mall and co-workers from (Jin & Mall, 2002). The purpose of the RF2 and RPF models is to comparatively assess the predicted effect of contact geometry on the wear-fatigue-plasticity behaviour, across a range of applied stroke values, as depicted in Fig. 5.1. All three models use the same material, namely Ti-6Al-4V, but different tribological constants are employed in each, as identified from the relevant test data (see Section 5.3.2 for description of this aspect).

Table 5.1. Table of FE models for different fretting geometries studied.

Model	Pad type	Key dimensions	Test rig and source
RF1	Cylindrical pad	Pad radius, 6 mm	University of Nottingham test rig, e.g. Ding et al. (2009)
RF2	Cylindrical pad	Pad radius, 50.8 mm	USAF test rig, e.g. Jin & Mall (2002)
RPF	Rounded punch pad	See Fig 6.1	USAF test rig, e.g. Jin & Mall (2002)

Fig. 5.3 shows a schematic of the University of Nottingham fretting test rig which employs a crossed cylinder on flat arrangement. Fig. 5.4 shows the RF1 FE model, which has a pad radius of 6 mm. 2 dimensional (2D), four noded, quadrilateral, plane strain elements were used due to their reliability in frictional contact analyses (McColl et al., 2004 and ABAQUS user's manuals, 1998). Matched meshes were employed also to prevent contact pressure fluctuations (McColl et al., 2004). The mesh is designed to be highly refined in the contact region (typical element dimension is 10 μm), to capture the complicated variation of the key variables, including contact pressure, relative slip, and sub-surface stresses, and to become gradually more coarse with increasing distance from the contact regions, for computational efficiency. The mesh design process is particularly complicated for wear simulation analyses, due to the need to allow for widening of the contact region (particularly in gross slip cases) and therefore the need for consideration of moving stress concentration locations, e.g. stick-slip interfaces and contact edges are typically predicted to move due to wear-induced material removal.

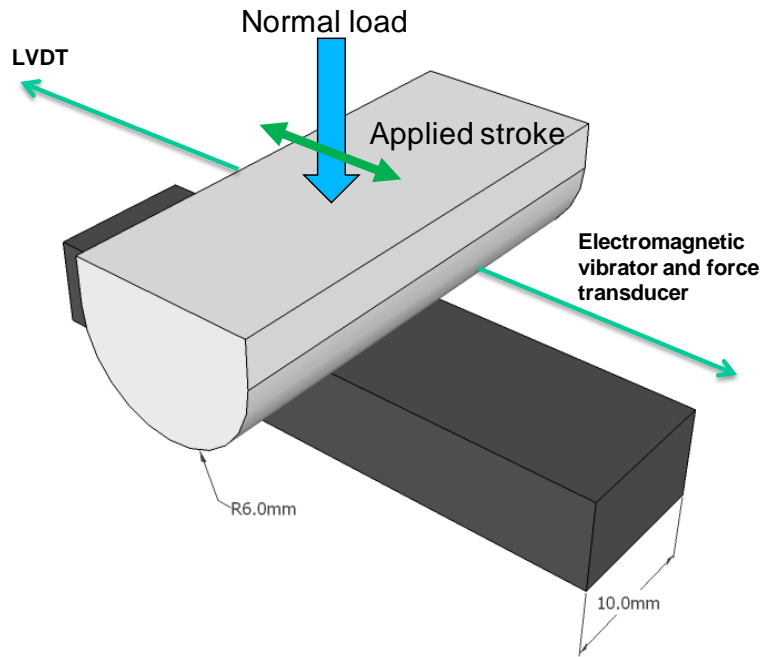


Fig. 5.3. Schematic of fretting test rig for RF1 test 1 and 2.

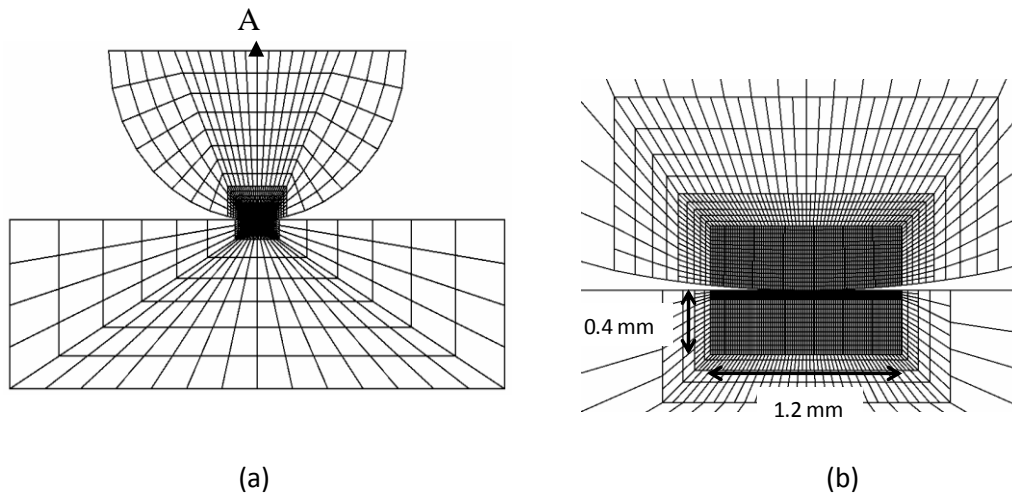


Fig. 5.4. Mesh details of FE model RF1 (a) full model, (b) contact region detail.

Figs. 5.5 and 5.6 show the RF2 and RPF FE models. The pads in these models are assigned the same height and width in order to make a meaningful comparison for the same

nominal geometrical space envelope. The finite element mesh design follows the same methodology and rationale as that of the RF1 model.

The contact surface interaction is defined via the finite sliding contact pair approach which adopts the master-slave algorithm in Abaqus. The maximum allowable penetration depth (*h-crit*) between the slave and master nodes during the iterative solution process is set to 1 μm . The minimum allowable distance between the initial coordinates of adjacent nodes on the mating contact surface (*ADJUST parameter*) is set to 0.001 μm . Coulomb friction is employed based on the Lagrange multiplier contact algorithm to ensure the exact stick condition when the shear stress less than the critical shear value according to the Coulomb friction law. These contact parameters have been identified from previous studies, e.g. see (McColl et al., 2004).

Detailed mesh refinement studies were carried out to achieve convergence with respect to the unworn surface tractions and sub-surface stresses for all three models, using available theoretical solutions for the unworn geometries. The comparisons between theoretical and converged FE predictions for the unworn cases are presented in the results section below.

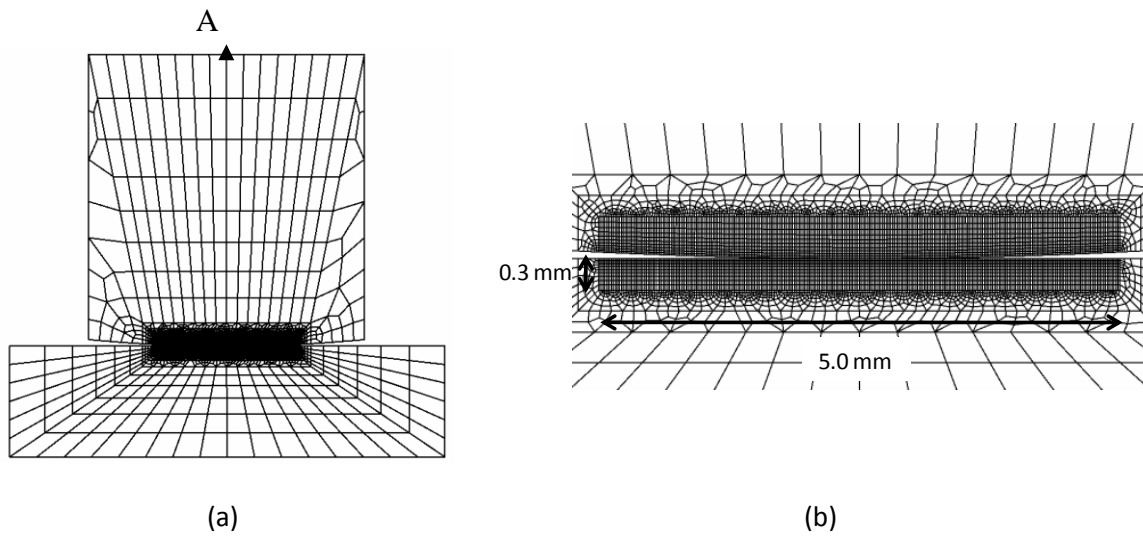


Fig. 5.5. Mesh details of FE model RF2 (a) full model. (b) contact region detail.

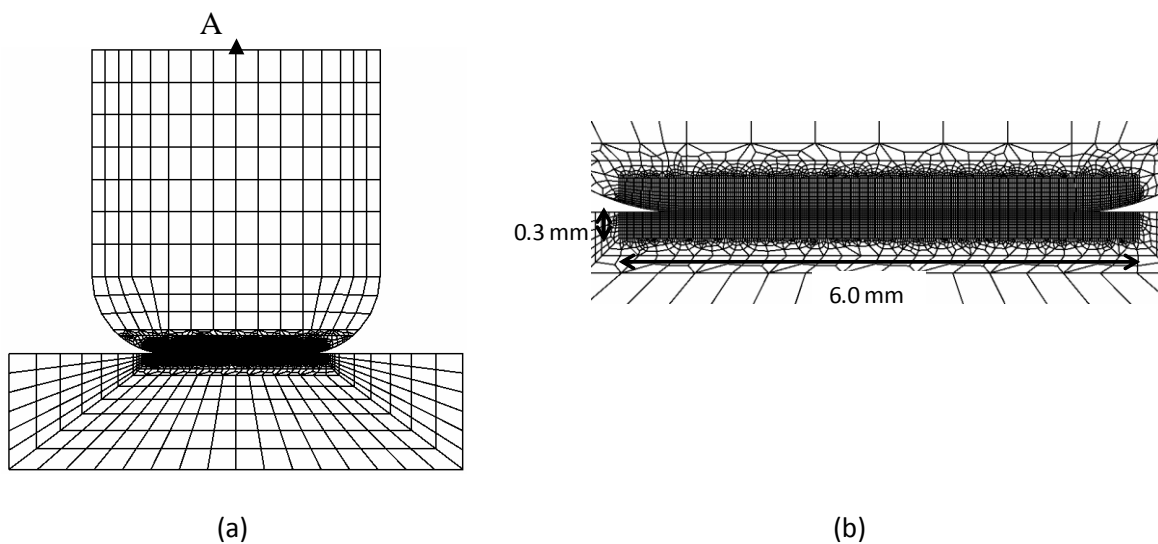


Fig. 5.6. Mesh details of FE model RPF (a) full model. (b) contact region detail.

5.2.2 Loading histories

Fig. 5.7 illustrates the loading history modelled to simulate the fretting cycles. 1 fretting cycle shown in Fig. 5.7 represents ΔN wear cycles, which has been explained in detail in section 4.3. The first step in the analysis is to apply the constant normal load P at point A, on the top of the FE model of the fretting pad (see Figs. 5.4 to 5.6). In the subsequent steps a

periodic cyclic x -direction displacement of amplitude Δ is applied to the cylinder while constraining the bottom half of the flat specimen in the x and y -directions. The displacement amplitude Δ is varied for each simulation to model partial slip through to gross sliding to simulate the experimental results. To ensure uniform horizontal and vertical displacement of nodes on the top surface of the cylinder, linear constraint equations are employed. Due to the compliance effect of the experimental rig, the actual relative contact slips between the contacting components is normally less than the applied stroke 2Δ in the experiment. Therefore the displacement amplitude Δ is based on the relative slip rather than the applied stroke. For the gross sliding condition, the relative slip corresponding to the stroke applied in the experiment is determined from the width across the parallel portions of the hysteresis loop of the experiment. For the partial slip condition, the required displacement is taken as that value which gives the measured maximum tangential force. This again is attributed to the machine compliance and as an estimation, it can be adopted in the FE analysis for fretting analysis.

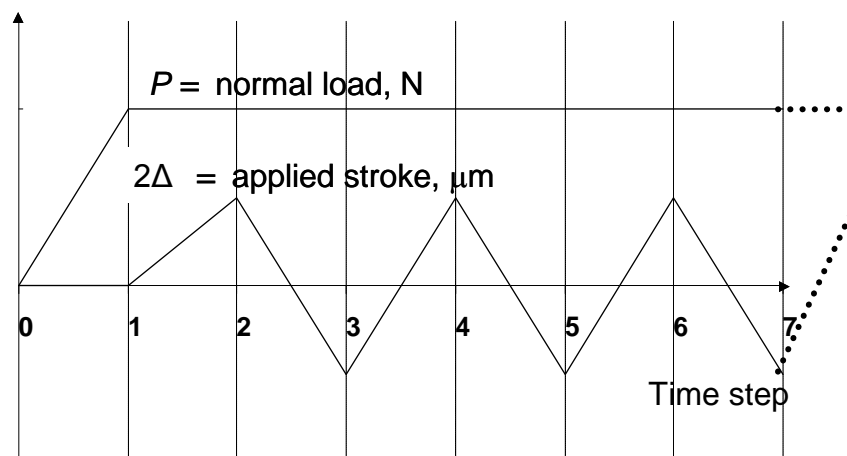


Fig. 5.7. Displacement and load history for fretting experiments and analyses.

Table 5.2 shows the fretting conditions to which the RF1 model is applied. These correspond to two selected test cases from the experimental programme reported in (Ding et al., 2009), Test 1 corresponding to a gross slip condition and Test 2 corresponding to a partial slip case.

Table 5.2. Conditions of fretting tests of cylinder on flat arrangement (RF1).

Test no.	Normal load (N/mm)	Applied half-stroke, Δ (μm)	Slip regime
1	50	40	GS
2	100	22.6	PS

Table 5.3 shows the range of test conditions used for the RF2 and RPF models. The normal load is held fixed at 208 N/mm, following the tests carried out in (Magaziner et al., 2008 and Jin & Mall, 2002) (and also analysed in (Madge et al., 2007), for both geometries and the stroke is varied between 7 μm and 20 μm , thus spanning from the partial slip (PS) regime into the gross slip (GS) regime for both.

Table 5.3. Conditions of fretting analysis of RF2 and RPF arrangements.

Arrangement	Analysis no.	Normal load (N/mm)	Applied half-stroke, Δ (μm)	Slip regime
RF2	3	208	7	PS
	4	208	10	PS
	5	208	14	PS
	6	208	20	GS
RPF	7	208	7	PS
	8	208	10	PS
	9	208	14	GS
	10	208	20	GS

The constitutive model, wear simulation model, fatigue accumulation model and ratchetting failure model adopted have been described in Chapter 4 (Section 4.3 - 4.5).

5.2.3 Tribological data

A coefficient of friction (COF) μ value of 0.9 is used for the RF1 model, based on the experimental measurements from (Ding et al., 2009) from stabilised gross sliding tests. A COF value of 0.8 is used for both RF2 and RPF, based on the test data reported in (Magaziner et al., 2008).

The energy wear coefficient for the RF1 model has been identified from the test programme and data described in (Ding et al., 2009). Specifically, following the method described in (Fouvry et al., 2003), the wear volume corresponding to different numbers of fretting cycles was plotted against accumulated energy, as represented in Equation 4.7 and the slope represents the energy wear coefficient, α . The resulting value for RF1 is 1.12×10^{-8} MPa⁻¹. Furthermore, the formulation of the present paper has been compared with the previous Archard-based formulation from (Ding et al., 2009) for RF1 gross slip conditions and was shown to give identical results (in terms of wear scar depth profile evolution up to 100,000 cycles).

The fretting wear scars and hysteresis loops for the test corresponding to RF2 have been presented in detail in (Magaziner et al., 2008), permitting identification of the energy wear coefficient (α value) for RF2 and RPF, as 7.121×10^{-7} MPa⁻¹ (7.121×10^{-4} mm³/J) (see Table 6.4).

Table 5.4 Energy wear coefficients for different models

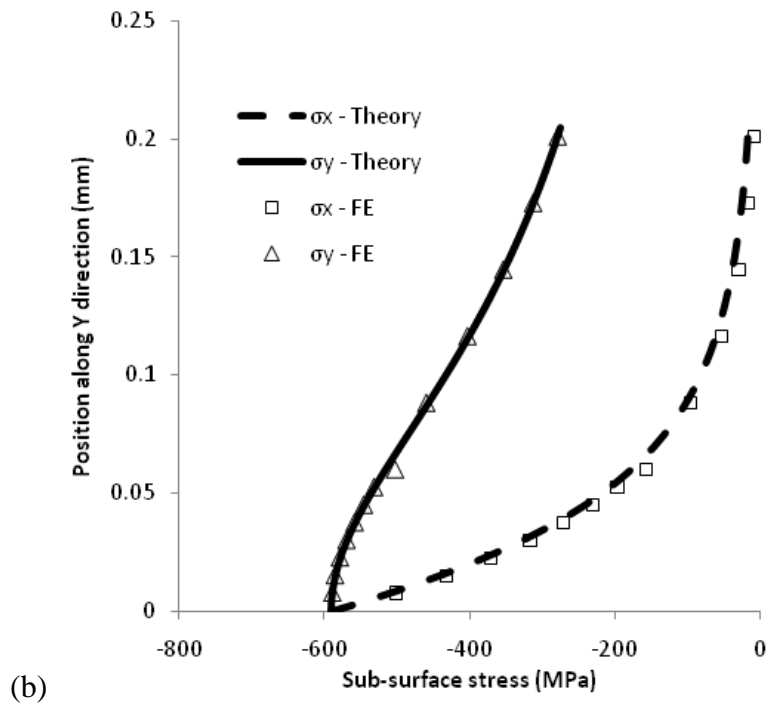
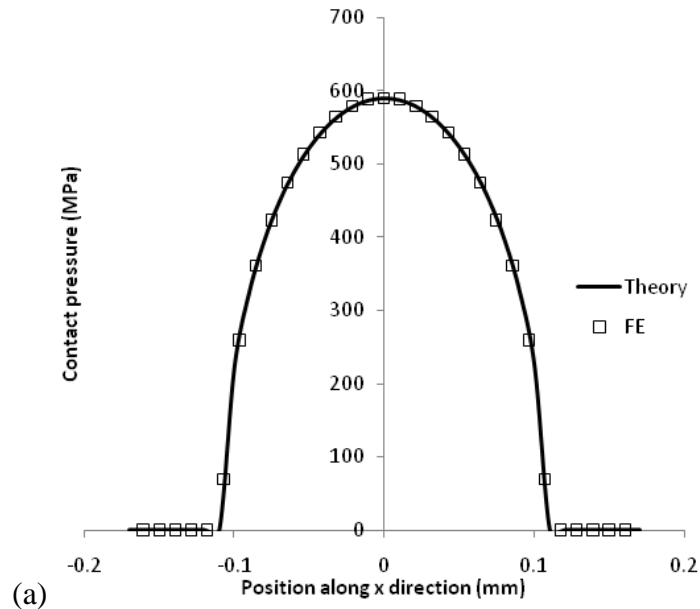
Models	RF1	RF2	RPF
Energy wear coefficient (MPa ⁻¹)	1.120×10^{-8}	7.121×10^{-7}	7.121×10^{-7}

5.3 Results and discussion

5.3.1 Validation of unworn FE modelling methodology

The establishment of a satisfactory (converged) FE mesh is critical to the prediction of accurate stresses, strains and hence plasticity and fatigue parameters in fretting problems. The theoretical solutions for the Hertzian (frictionless) problem have been presented above and these results are employed here to validate the FE model of the cylinder on flat fretting geometry (called RF1 above). Figs. 5.8a and 5.8b show the comparisons of the FE-predicted contact pressure and sub-surface stresses, along the Y (vertical)-axis, using the mesh of RF1 (Fig. 5.4), with the Hertzian (frictionless) solution from (Johnson, 1985), for normal loading only. Clearly, the FE model gives excellent agreement for the frictionless case. Fig. 5.8c shows a comparison of the FE-predicted and theoretical frictional shear stress distribution (from (Johnson, 1985)), under a sliding tangential load combined with normal loading, at a depth of 20 μm along the horizontal surface (parallel to the free surface of the flat specimen). The FE frictional solution is in excellent agreement with the theoretical solution. The mesh for the USAF round on flat fretting geometry, RF2 (see Fig. 5.5), gave the same quality of agreement with the theoretical solution. The development of a theoretical solution for the nearly-complete problem of a rounded punch on flat contact problem under combined normal and tangential loading is a more recent development (Ciavarella et al., 1998) and indeed, as highlighted above, the most recent solutions, as presented in (Ciavarella et al., 2003), are only applicable within certain geometrical limitations, specifically, $a \leq c \leq b$, viz. the stick-zone semi-width must lie between the flat semi-width and the contact semi-width. This is actually a narrow range of allowable geometries. The benefit of the FE modelling approach is that it does not have such limitations, provided due account is taken of large deformation and finite

sliding effects. Another limitation of the findings presented in (Ciavarella et al., 2003) is that no closed-form solution for stress distributions was presented; only single point expressions for trailing edge stress were presented. Clearly, the FE solution provides an approximate distribution of stress.



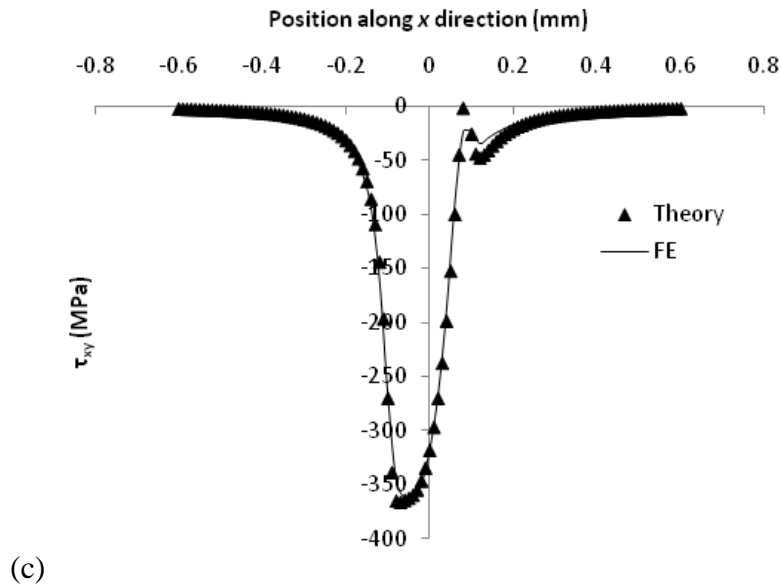


Fig. 5.8. Comparisons of RFI FE prediction and analytical solution under a normal load of 100 N/mm: (a) distribution of contact pressure; (b) sub-surface stress along Y-axis; and (c) Distribution of shear stress τ_{xy} at depth $y = 20 \mu\text{m}$ for combined normal and tangential loading ($\mu = 0.6$).

Figs. 5.9 to 5.12 show comparisons of key FE-predicted fretting and contact variables with the corresponding theoretical results from (Ciavarella et al., 2003) for the RPF model. A key challenge in the present work is to develop a sufficiently refined mesh to capture the severe stress gradients associated with the nearly-complete contact edges, on the one hand, and yet remain computationally efficient in terms of minimising the run-times required for wear simulations over large numbers of fretting cycles. Significant effort was therefore expended in the development of such a suitable mesh (Fig. 5.6). Fig. 5.9 shows that the predicted contact pressure distribution under normal loading for the final RPF mesh is in close agreement with the theoretical result; for example, the maximum difference is 13% at

the peak pressure location (edge of contact). The slight discrepancy is attributed due to the FE mesh having necessarily employed a large deformation assumption for accurate resolution of the contact tractions, whereas the theoretical solution is based on a small deformation assumption.

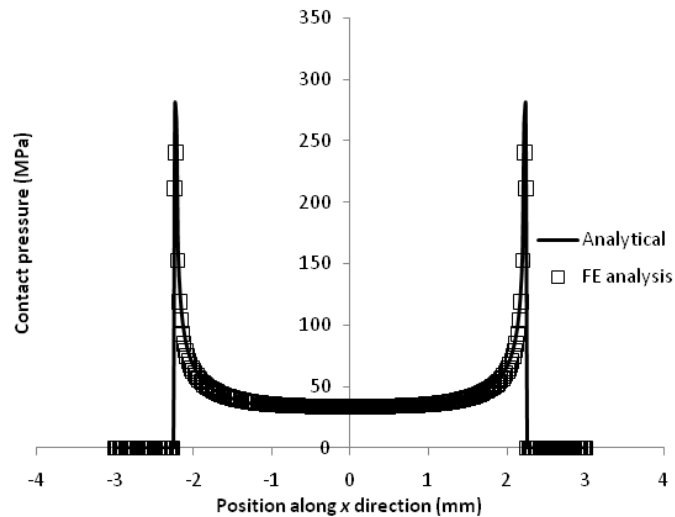


Fig. 5.9. Comparison of distribution of contact pressure between FE prediction and analytical solution, for RPF under a normal load of 208 N/mm.

Fig. 5.10 shows a comparison of the FE and theoretical predictions for contact semi-width across a range of normal loads, again showing excellent agreement between the two methods, with the difference increasing with increasing load and deformation. Under tangential loading $Q/\mu P = 0.5$ for the RPF model with a COF (μ) of 0.8, a partial slip and a stick zone develop and a trailing-edge tensile stress peak develops also, leading under cyclic tangential loading to fretting cracking. Therefore, the accurate prediction of these trailing edge stresses is critical to fretting damage prediction. Fig. 5.11 shows a comparison of FE-predicted and theoretical stick zone semi-width, c , as a function of pad geometry parameter a/b , illustrating convergence of the predicted results for large values of a/b , viz. $a/b > 0.95$; again, the small deformation assumption appears to be questionable for $a/b < 0.95$. Small a/b

is associated with large load conditions (for example, when $a/b = 0.8$, $P = 16253 \text{ N/mm}$ and $Q = 4063 \text{ N/mm}$), and in these conditions the theory is limited relative to the FE. (The theory assumes that: the strains are very small compared with each body and the relative radii of curvature of the surface.) The a/b ratios of the present paper are above 0.95. Fig. 6.12 shows a comparison of the FE-predicted distribution of tangential (σ_x) stress with the theoretically-predicted trailing edge tensile stress peak (from Equation 2.34); the FE model agrees with the latter to within 11%.

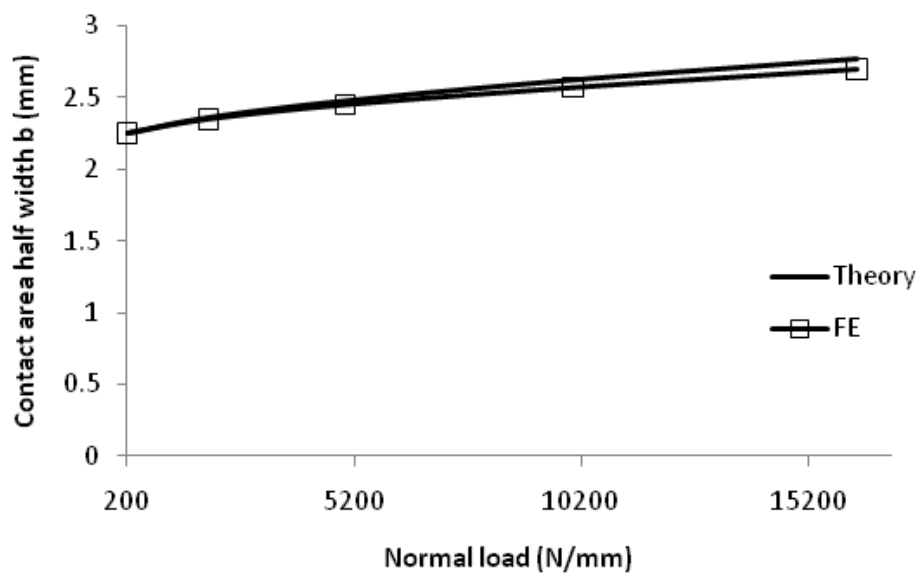


Fig. 5.10. Comparison of contact area half width between FE prediction and analytical solution, across a range of normal loads for RPF.

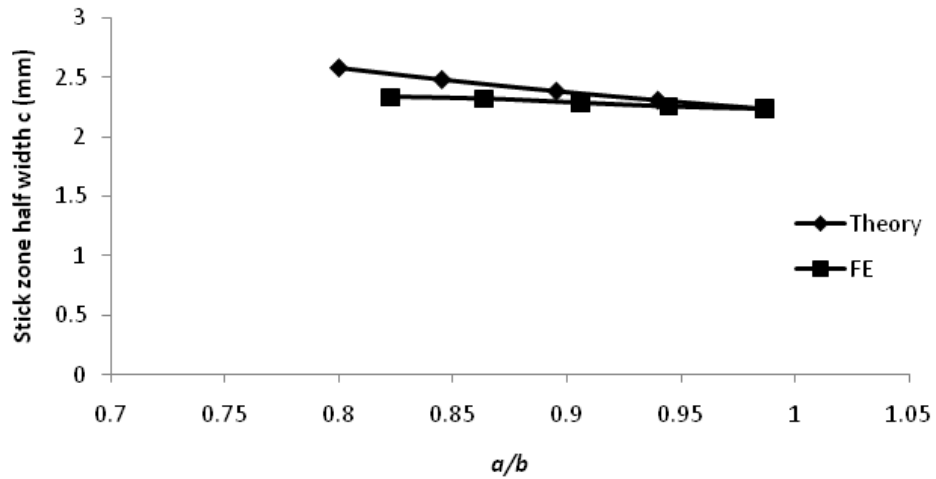


Fig. 5.11. Comparison of stick zone half width between FE prediction and analytical solution, for RPF, across a range of a/b values, under $Q/\mu P = 0.5$ for RPF.

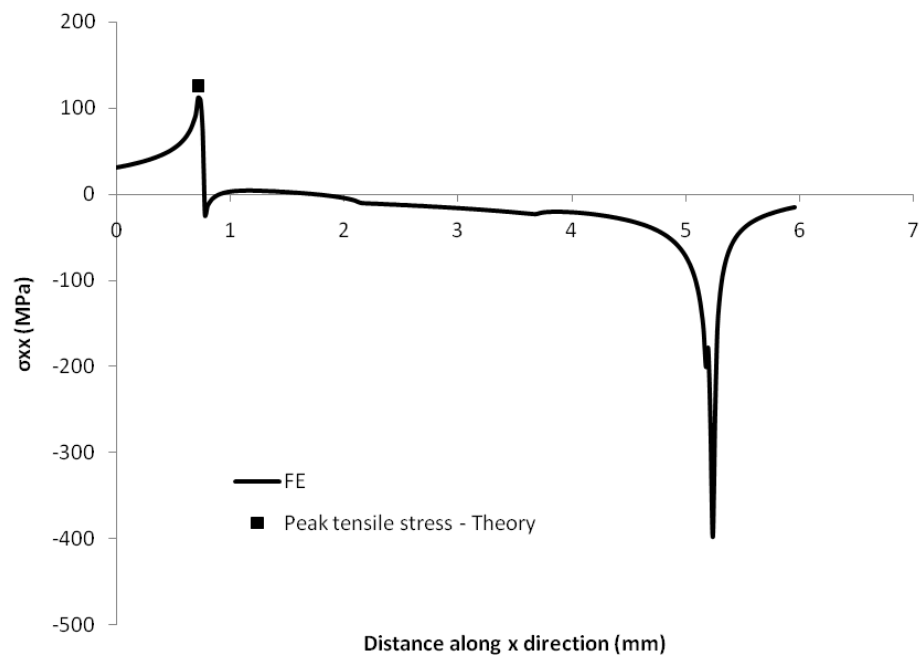
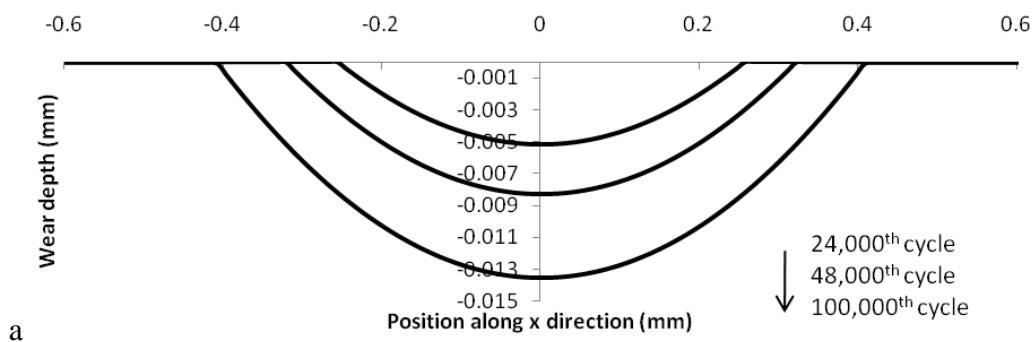


Fig. 5.12. Comparison of peak tensile stress between FE prediction and analytical solution, under a normal load of 208 N/mm and a half-stroke of 7 μm for RPF, with $\mu = 0.8$.

5.3.2 Validation of FE energy-based wear simulation

Having established successful performance of the unworn FE models for both the round on flat and rounded punch on flat fretting configurations, the next logical step is to validate the performance of the wear simulation methodology. One aspect of this validation is to examine the performance of the energy-based wear simulation method against previous Archard-based implementations, e.g. (Ding et al., 2009); a second aspect is to compare the energy-based wear predictions with measured test data. Fig. 5.13a shows the FE-predicted wear scar evolution in the RF1 cylinder on flat arrangement for the gross slip case of Table 5.22 for 100,000 cycles. These results are almost identical to the Archard-based simulation results of (Ding et al., 2009). The wear scar is predicted to have a U-shape and the scar width and depth increase as the number of cycles increases. Fig. 5.13b shows the predicted evolution of contact pressure with fretting cycles, for the instant of zero tangential displacement in each of the selected cycles up to 100,000 cycles. Clearly, the contact pressure peak is predicted to drop dramatically within the first 24,000 cycles from more than 400 MPa to about 100 MPa and thereafter decays more slowly. Concomitantly, the pressure distribution becomes more uniform with increasing cycles. These results are consistent with previously published gross slip wear simulation predictions (McColl et al., 2004 and Ding et al., 2009).



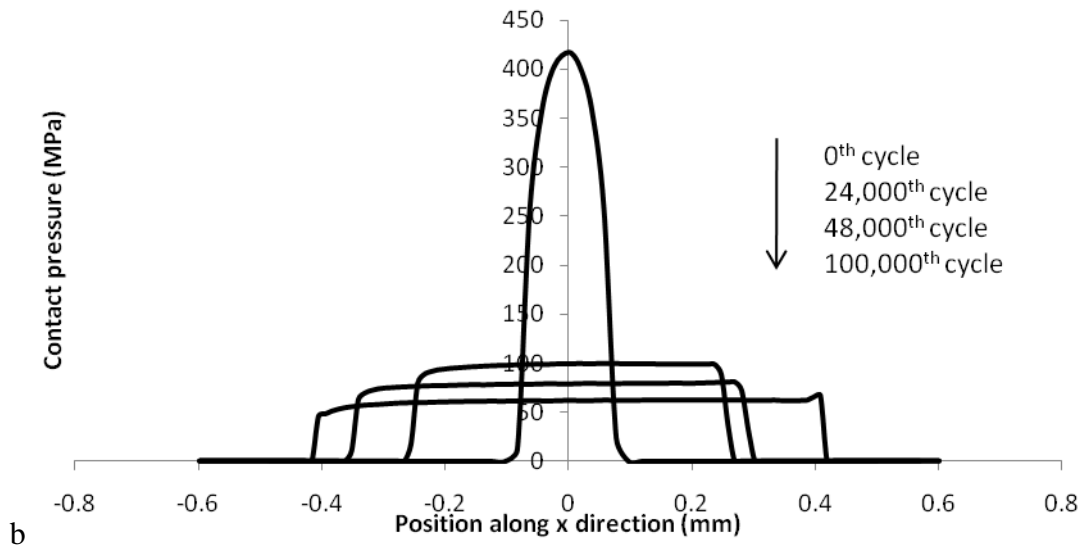


Fig. 5.13. Predicted evolutions of (a) wear profile and (b) contact pressure distribution for Test 1, RF1 GS.

Figs. 5.14a and 5.14b show corresponding FE-predicted results for the partial slip case (Test 2 of Table 5.2) for the RF1 round on flat geometry. These results are consistent qualitatively with the partial slip predictions of Mohd Tobi et al. (2009), but those of Mohd Tobi et al. (2009) are closer to the experiment values due to having matched the Archard wear coefficient directly to the experimental data. The following key points can be noted from Figs 5.14a and 5.14b:

- the wear scar is predicted to increase in width with increasing cycles, but more slowly than the gross slip case, and the stick zone is predicted to decrease in size, due to plasticity at the stick-slip interface leading to increased slip and hence wear at this interface.
- the contact pressure distribution is initially Hertzian with a peak at the centre of contact; with wear, the contact pressure in the slip zones reduces gradually to an almost

negligible value, causing a pressure distribution more akin to that of a rounded punch on flat with peak values of about 770 MPa at the stick zone edges after 300,000 cycles.

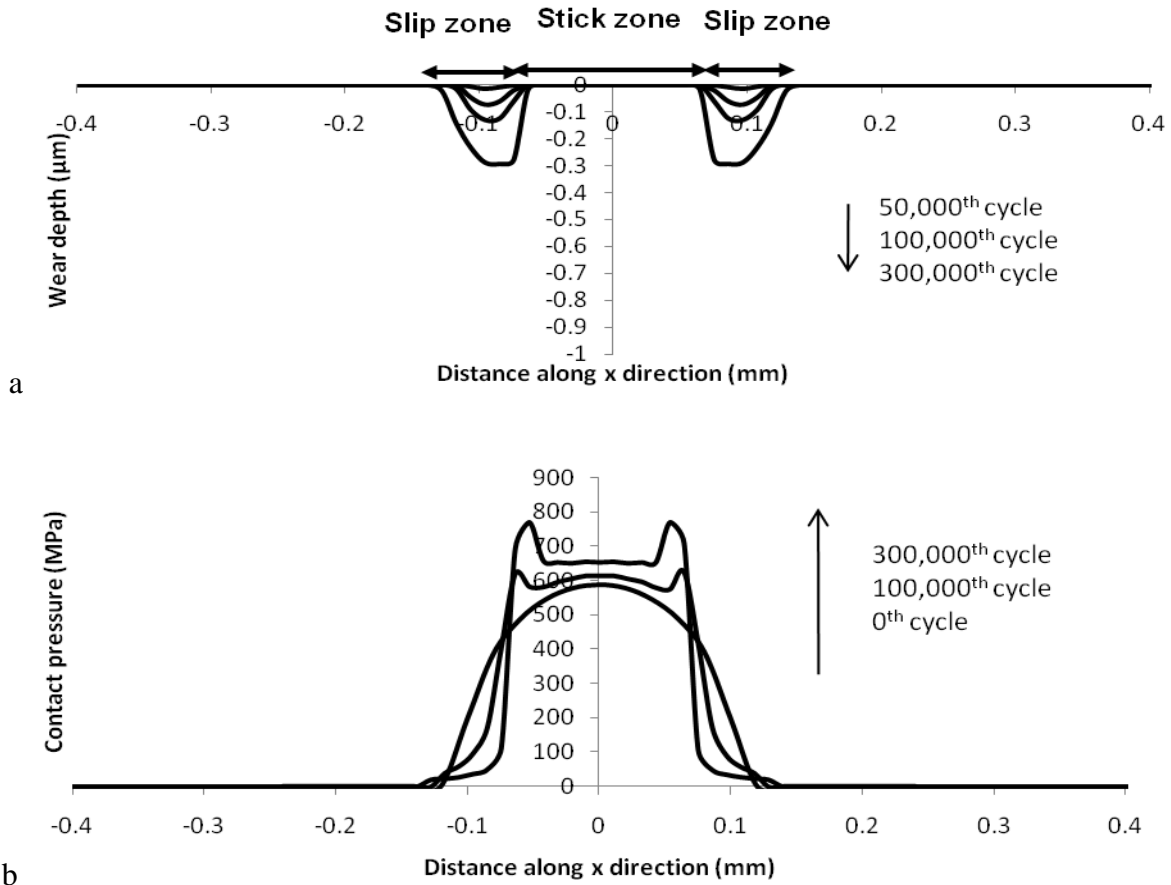


Fig. 5.14. Predicted evolutions of (a) wear profile and (b) contact pressure distribution for Test 2, RF1 PS.

Figs. 5.15 and 5.16 show comparisons of the FE-predicted wear scars with measured 2D profiles from the experimental wear scars, for the partial and gross slip tests of Table 5.2. Table 5.5 shows a tabulated comparison of some of the key data from these figures. The predicted scar width is good for the gross slip case and although the maximum measured depth is about twice the predicted value, the wear volumes are consistent and measurements effectively fluctuate about the numerical prediction. For the partial slip case, the maximum

wear depth is significantly under-predicted by a factor of about 10 relative to the measured value although the stick zone width and the scar width are in reasonably good agreement.

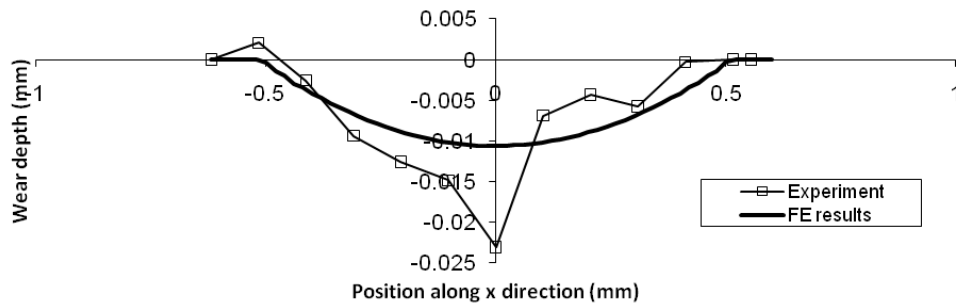


Fig. 5.15. Wear scar comparison between FE (100,000 cycles) and experiment (100,000 cycles) for gross slip case for RF1 Test 1.

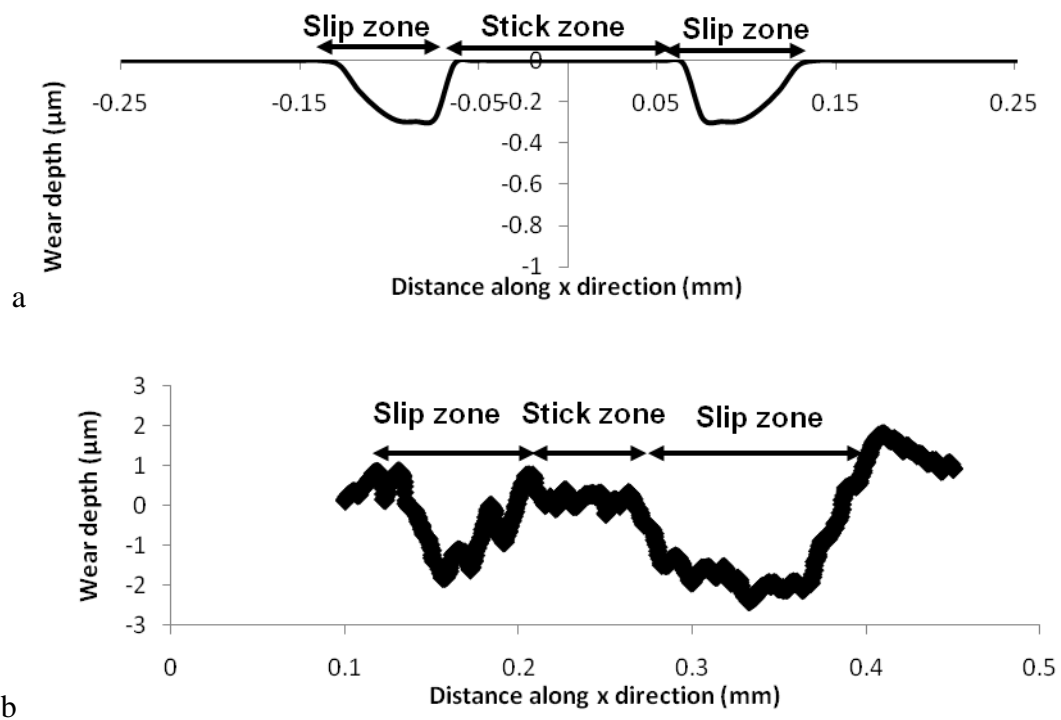


Fig. 5.16. Qualitative wear scar comparison between (a) FE (300,000 cycles) and (b) experiment (300,000 cycles) for partial slip case for RF1 Test 2.

Table 5.5. Wear scar comparison between FE analysis and experiment (a). Gross slip case. (b). Partial slip case

(a)			
Method	Max wear depth (μm)		Wear scar width (mm)
FE	10.8		1.0
Experiment	22.6		1.1

(b)			
Method	Stick zone width (μm)	Max wear depth (μm)	Scar width (mm)
FE	106	0.29	0.26
Experiment	76	2.39	0.25

5.3.3 Validation of FE critical-plane SWT fatigue life prediction simulation

The fretting fatigue life validation is also carried out. Comparison of cycles to crack nucleation and position between FE simulations and experiments (Ding et al., 2009) is shown in Table 5.6 and very good agreement has been achieved. For the gross slip case, no cracking is predicted (infinite life), and none was observed in tests after 3×10^5 cycles. For the partial slip case, the predicted crack locations is $0.479a_0$ which is within zone of measured cracks; cracking is predicted at 0.15×10^5 cycles and tests showed cracking within 10^5 cycles. This is excellent agreement.

Table 5.6. Comparison of fretting fatigue lives between experiment and FE SWT prediction

Slip regime	Normal load (N)	Half-stroke (μm)	Experiment (Ding et al., 2009)		FE SWT life prediction	
			Crack location (x/a_0)	Cycles to nucleation	Crack location (x/a_0)	Cycles to nucleation
Gross slip	500	40	N/A	$> 3 \times 10^5$	N/A	∞
Partial slip	1000	22.6	~ 0.4 to ~ 0.9	$< 1 \times 10^5$	0.479	0.15×10^4

5.3.4 Wear predictions for RF2 and RPF geometries

A key objective of the present chapter is to provide a comparative assessment of the predicted fretting performance of two contrasting contact geometries under the same normal load but across a range of applied displacements. Table 5.3 summarises the range of half-strokes adopted for this comparative study. Note that the normal load employed is 208 N/mm, which is a small fraction of the normal yield load for the RF2 geometry of 5536 N/mm; thus the RF2 tests are well within the elastic domain under normal loading. The FE analyses confirm that the RPF normal load is also well within the elastic domain. Figs. 5.17 to 5.19 show sample results from the predicted fretting wear behaviour of the RF2 and RPF geometries and Table 5.7 provides a quantitative comparison of the key wear scar data for both cases. Fig. 5.17 shows the evolutions of the RF2 worn flat surface across the range of Δ values. Fig. 5.18 shows corresponding evolutions for the RPF gross slip cases. Fig. 5.19a shows the evolution of contact pressure for the RF2 14 μm half-stroke case, which shows a typical partial slip pressure evolution profile as described before in Fig. 5.14b. Fig. 5.19b shows the dramatic effect of wear under 14 μm half-stroke condition (note it is gross slip condition) for the RPF geometry, with the edge-of-contact (EOC) peak pressures removed completely and a new more uniform pressure distribution exhibiting certain features of the (worn) Hertzian type distribution with localised peaks on the right hand side. It should be noted that with wear, particularly due to the cycle jumping technique, whereby the material removal for ΔN cycle is applied incrementally during the tangential loading cycle, it is inevitable that the instantaneous pressure distributions for $N > 0$ will be non-symmetric. This

is true for both the RF2 case, although less pronounced, and more obviously the RPF case (Fig. 5.19b). Some other key points to be noted from these results are as follows:

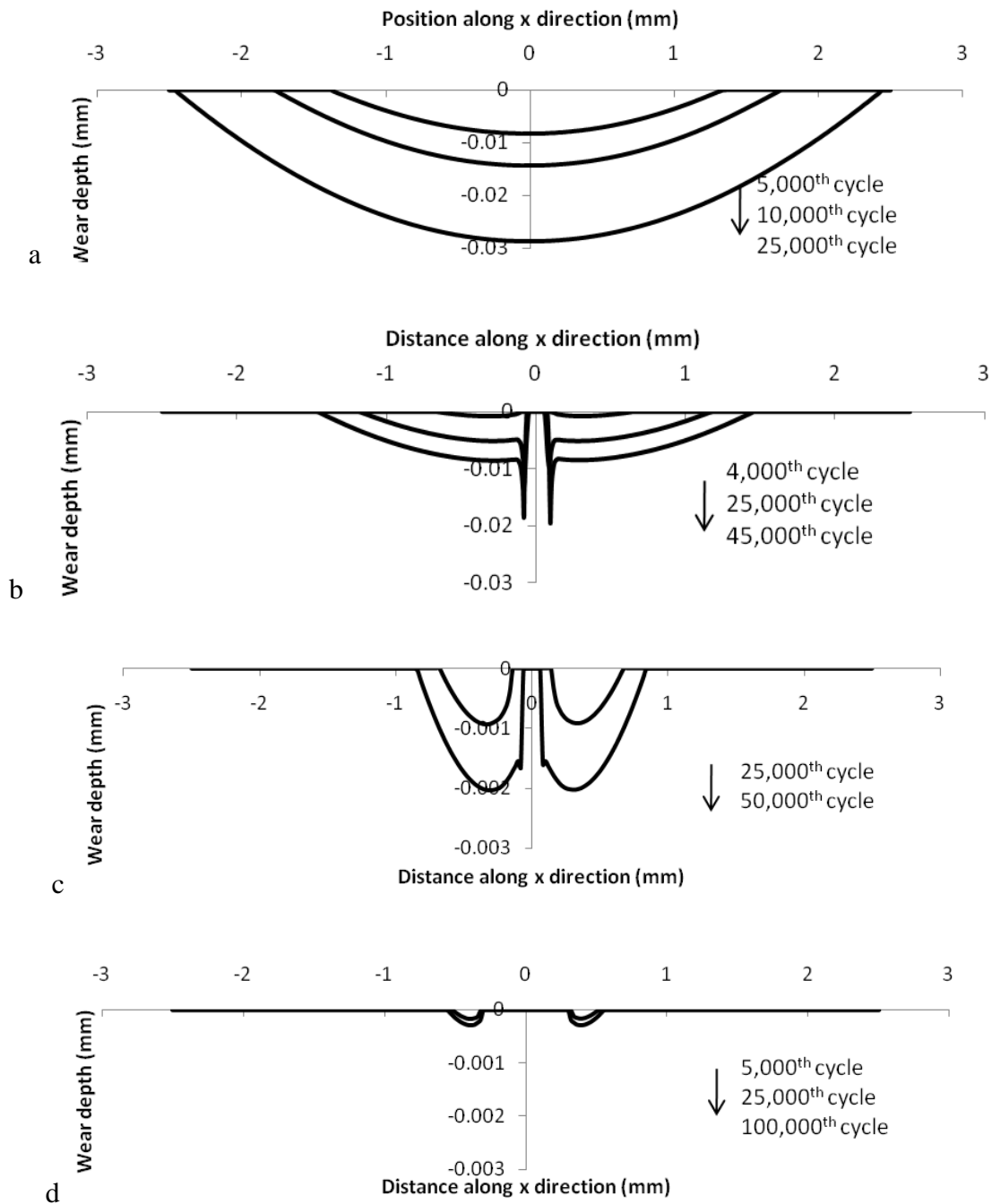
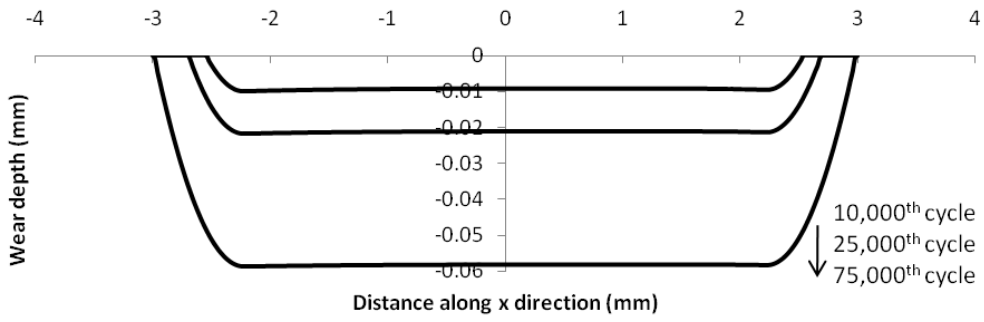
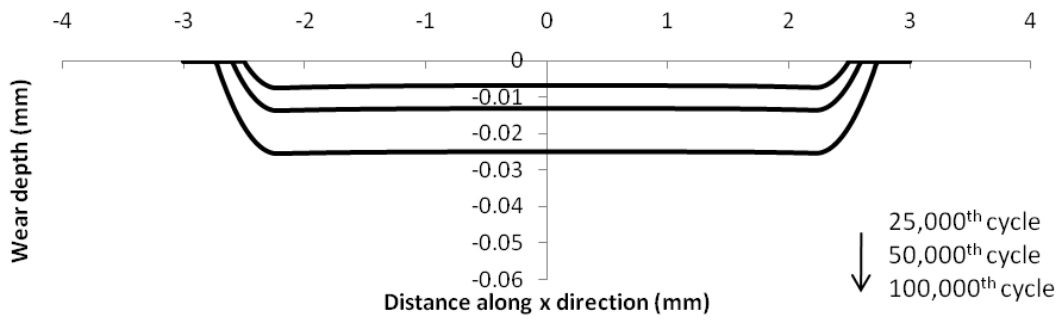


Fig. 5.17. Predicted evolutions of wear profile for RF2 : (a) 20 μm half-stroke, Analysis 6, (b) 14 μm half-stroke, Analysis 5, (c) 10 μm half-stroke, Analysis 4, (d) 7 μm half-stroke, Analysis 3.



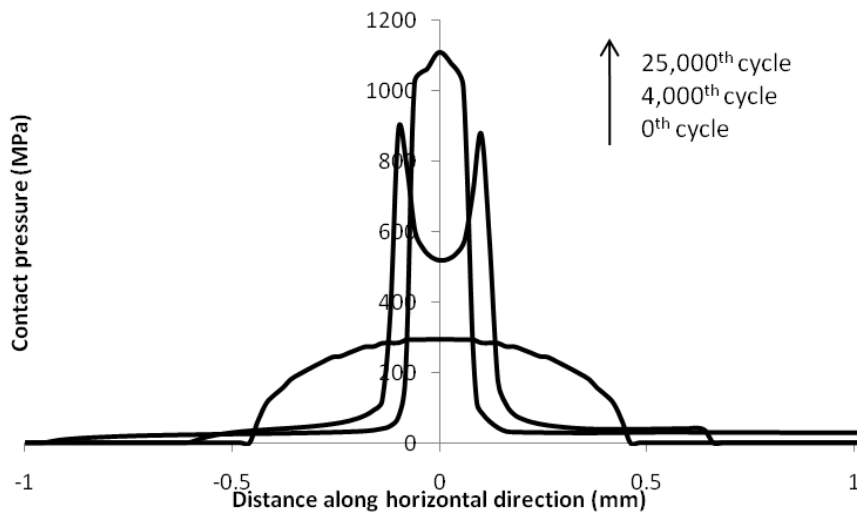
(a)



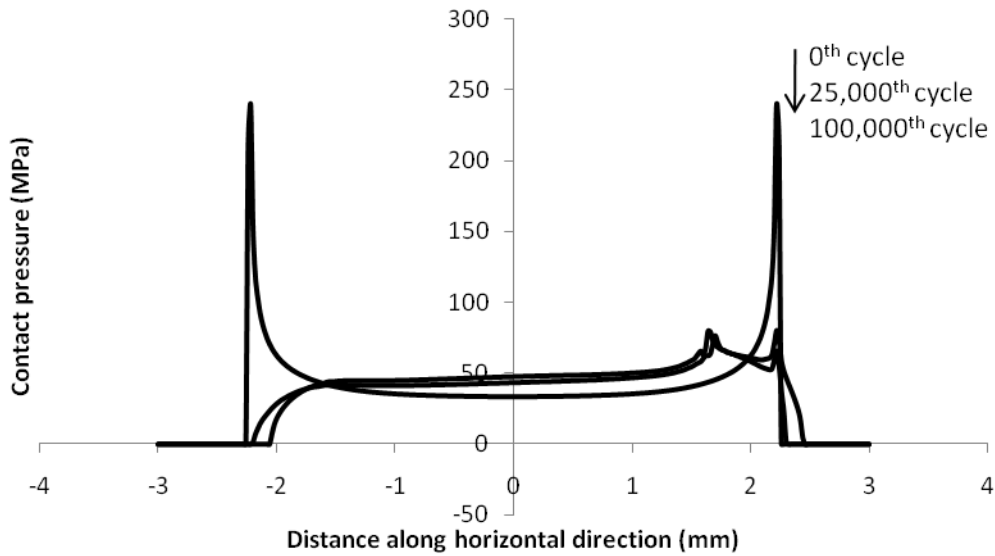
(b)

Fig. 5.18. Predicted evolutions of wear profile for RPF : (a) 20 μm half-stroke, Analysis 10,

(b) 14 μm half-stroke, Analysis 9.



(a) Contact pressure evolution for RF2, 14 μm half-stroke.



(b) Contact pressure evolution for RPF, 14 μm half-stroke.

Fig. 5.19. Predicted evolutions of contact pressure for RP2 and RPF for 14 μm half-stroke.

Table 5.7. Wear scar comparison between RF2 and RF under a range of half-strokes at the 25,000th cycle

Half-stroke (μm)	Scar width (mm)		Max scar depth (μm)		Wear scar area (mm^2)	
	RF2	RPF	RF2	RPF	RF2	RPF
7	1.04	n/a	0.3	n/a	n/a	
10	1.28	n/a	0.9	n/a	n/a	
14	2.36	4.96	9.7	7.4	0.008	0.033
20	4.88	5.36	28.6	21.7	0.093	0.108

1. The FE predictions indicated no stabilised partial slip solution for the RPF, consistent with the theoretical findings of Ciavarella et al., (1998), and therefore the wear simulation method predicted no wear for these cases
2. As a result, the initial contact pressure profile is predicted to persist with two peaks at the EOC positions.

3. Due to the larger initial contact width, the predicted RPF (GS) wear scars are much more uniform than the RF2 scars.
4. The GSR threshold (Δ_{th}) is calculated to be 15 μm for the RF2 model and 12 μm for the RPF model.
5. Partial slip wear is predicted for the RF2 model but the reduction of applied displacement leads to a dramatic reduction in wear volume and wear scar dimensions; for example, reducing the half-stroke from 20 μm (GS) to 10 μm (PS), leads to a predicted reduction in maximum wear depth (after 25,000 cycles) of a factor of about 30. However, even in partial slip at 14 μm half-stroke, for RF2, a significant maximum (localised at stick-slip interface) wear depth of about 20 μm is predicted after 45,000 cycles. It is also worth noting the prediction of extra deep wear pits at the stick-slip interface in Fig. 5.17b, due to the occurrence of localised plasticity, which is discussed in more detail in Section 5.3.5.
6. The predicted reduction in maximum scar depth with reducing half-stroke, from 20 μm (GS) to 14 μm (GS), for the RPF case is similar to that of RF2 (about 65% reduction), but of course there is a much more dramatic reduction to zero wear for RPF with further reduction in half-stroke below Δ_{th} , due to the transition to zero-slip or 'stick'. Identification of Δ_{th} is therefore an important step in fretting wear characterisation, particularly for the rounded punch on flat fretting geometry and presumably also, by extension, for the general punch on flat fretting geometry.

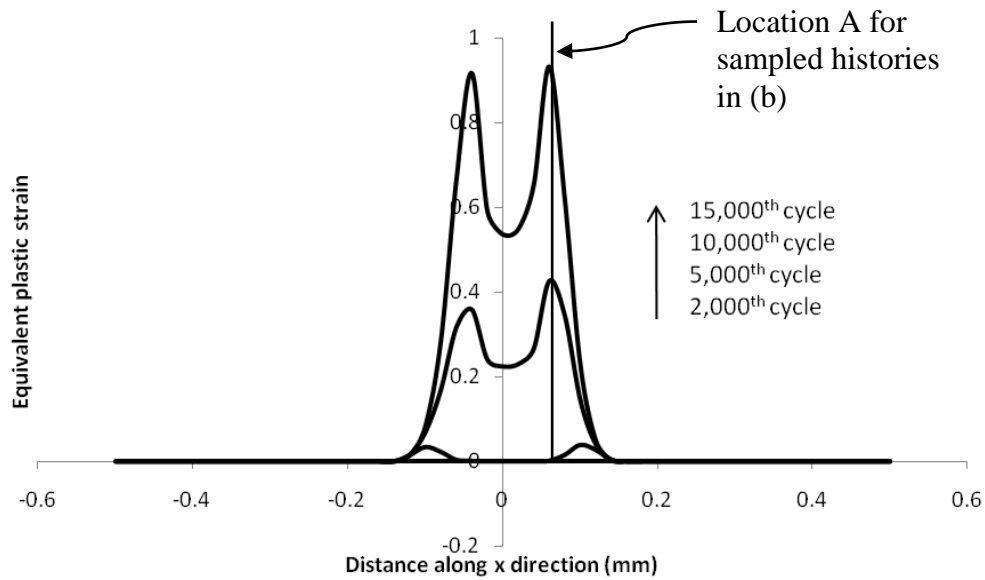
5.3.5 Cyclic plasticity and ratchetting for RF2 and RPF geometries

It is shown in Mohd Tobi et al., (2009) for the same Ti-6Al-4V material as studied here, using a LKH material model, that for partial slip, the cyclic plasticity effects lead, on the one

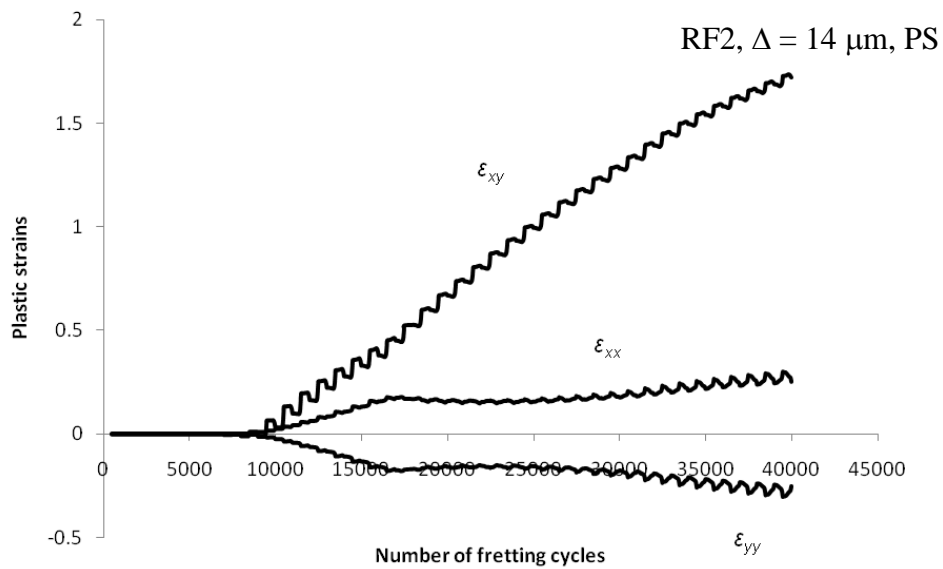
hand, to ratchetting phenomena at the evolving stick-slip interface region, with associated plastic damage accumulation, which interacts with fatigue damage accumulation and, on the other hand, to accentuation of critical-plane *SWT* values predicting rapid crack nucleation, as observed experimentally, and multiple cracking locations, as also observed experimentally. Although the predictions of Mohd Tobi et al., (2009) demonstrated, for the first time, a wear-induced cyclic plasticity phenomenon, whereby an ostensibly elastic initial (unworn) Hertzian contact problem is predicted to develop significant cyclic plasticity and ratchetting behaviour at the evolving stick-slip interface, the predicted accumulated plastic strains remained short of the ductility exhaustion limit. The predicted ratchetting rate was observed to gradually decrease towards a steady-state value of ratchet strain below the failure strain of the material. Thus it was not possible, with the LKH model, to predict partial slip cracking due to ratchetting for these cases. Hence, the present work has adopted a NLKH model which, as mentioned above, has been shown to represent cyclic plasticity phenomena more realistically.

Figs. 5.20 and 5.21 present the results of the comparative contact geometry study in the context of wear-induced plasticity. Firstly, no plasticity was predicted for the RPF geometry and, secondly, only the 10 μm and 14 μm half-stroke RF2 cases gave plasticity. Fig. 5.20a shows that for the 14 μm case, which is very close to the Δ_{th} value of 12 μm for RF2, a substantial and rapid accumulation of equivalent plastic strain (p) is predicted at the (evolving) stick-slip interface, starting within the first 2000 cycles and reaching a peak accumulated value of about 90% after 15,000 cycles at $x = -0.06$ mm. Fig. 5.20b shows the wear-induced evolution of the individual plastic strain components at this location, demonstrating the development of shear-driven plasticity at about 8000 cycles (at this location), leading to an almost uniform ratchetting rate. As described by Mohd Tobi et al., (2009), this behaviour is

dissimilar to conventional ratchetting, where a constant cyclic load and hence stress/strain typically exists, in that it is primarily driven by the predicted cyclically-increasing contact pressure at the stick-slip interface.



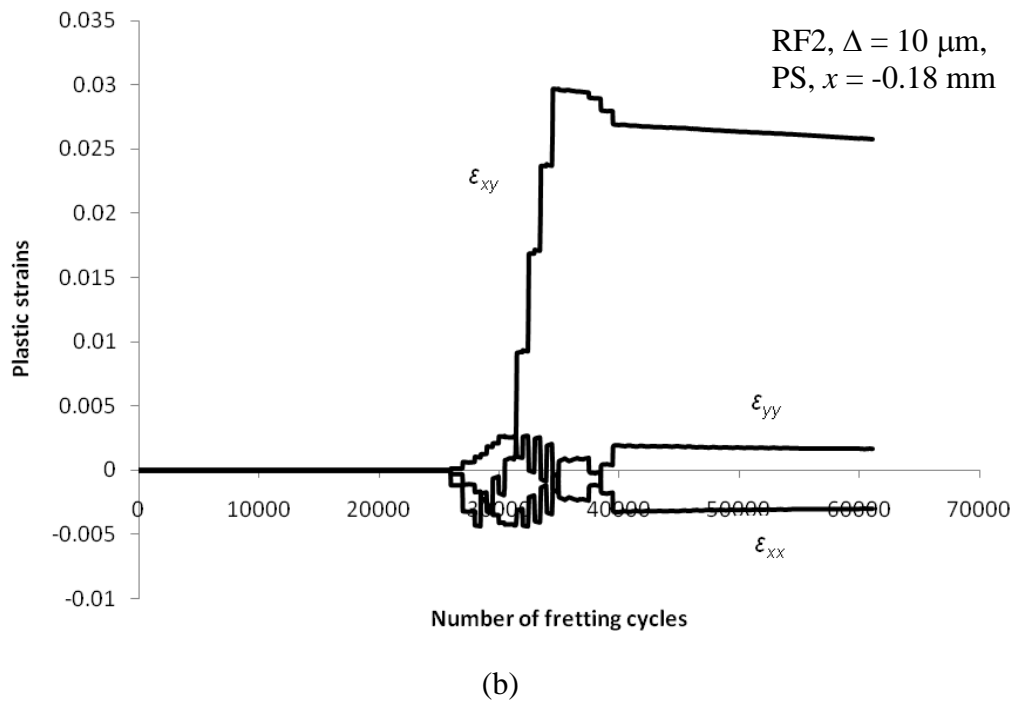
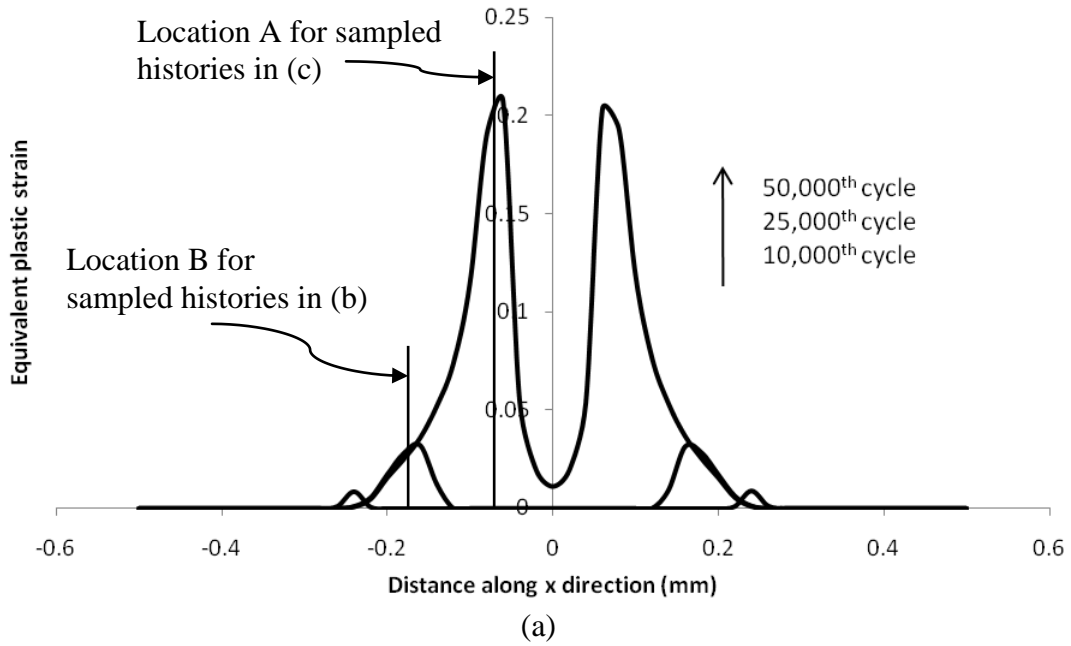
(a)

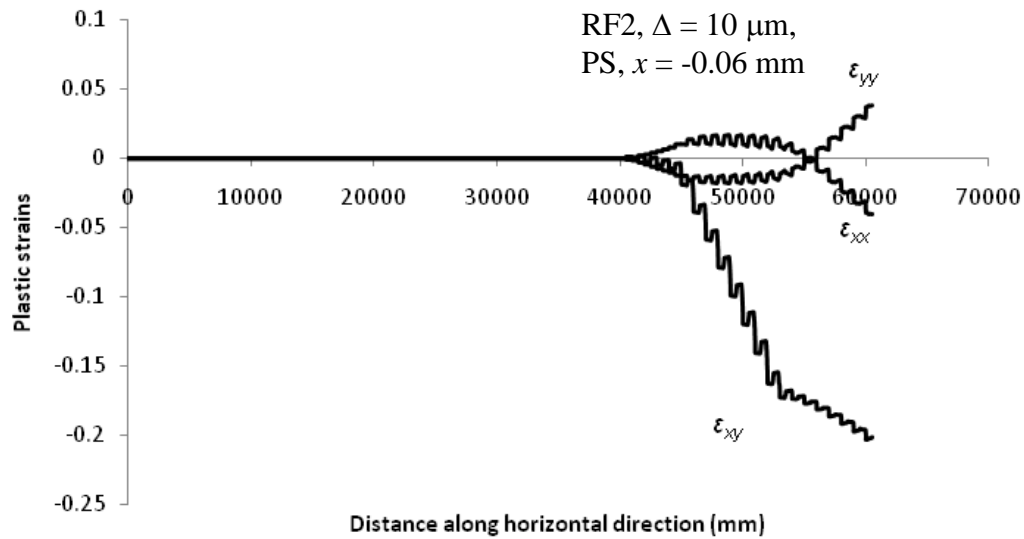


(b)

Fig. 5.20. (a) Predicted evolution of accumulated equivalent plastic strain distribution and (b) plastic strain histories at $x = 0.06$ mm [Point A in (a), initially in stick zone and after 15,000 cycles at the stick-slip interface] in RF2 for $\Delta = 14$ μm

Figs. 5.21a and 5.21b show a similar, but less detrimental, ratchetting behaviour for the 10 μm condition, with lower overall resulting p (Fig. 5.21a) and a greater number of cycles before the onset of plasticity.





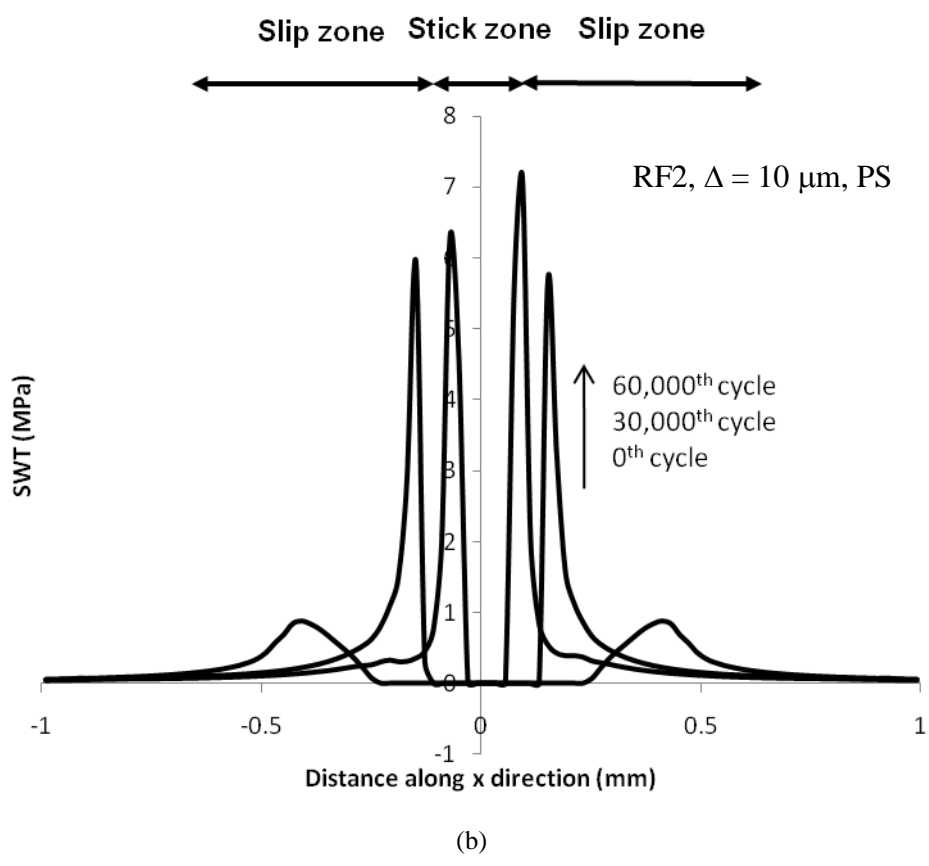
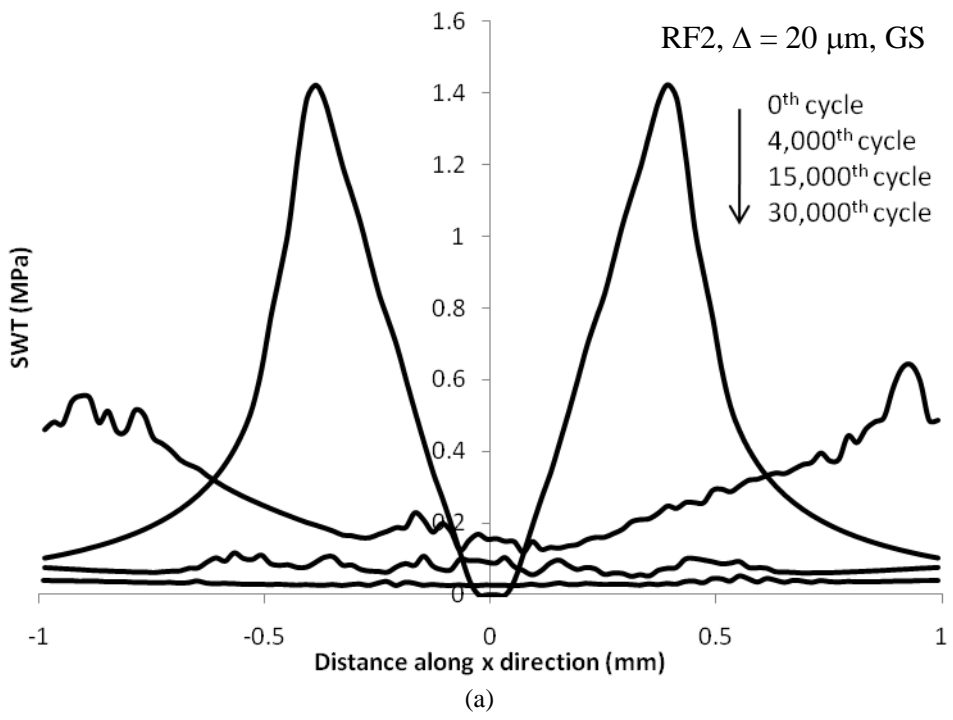
(c)

Fig. 5.21. Predicted plastic strain evolutions in RF2 for $\Delta = 10 \mu\text{m}$: (a) accumulated equivalent plastic strain distribution, (b) plastic strain components at $x = -0.182 \text{ mm}$ [point B in (a), initially in stick zone, after 50,000 cycle in slip zone] and (c) plastic strain histories at $x = -0.063 \text{ mm}$ [point A in (a), initially in stick zone, after 50,000 cycles in slip-stick interface].

5.3.6 Critical-plane SWT evolution for RF2 and RPF geometries

Figs. 5.22 to 5.24 illustrate some key detailed aspects of the critical-plane *SWT* crack nucleation predictions from the round on flat (RF2) and rounded punch on flat (RPF) analyses. Figs. 5.22a and 5.22b show the predicted wear-induced evolution of critical-plane *SWT* distribution for $20 \mu\text{m}$ and $10 \mu\text{m}$ half-strokes in the round on flat; Figs. 5.22c and 5.22d show the corresponding predictions for the rounded punch on flat. The results show that, in general, the *SWT* levels in the rounded punch on flat are significantly lower than those in the round on flat. For the round on flat, as presented previously, e.g. see Ding et al., (2009), for similar geometries, material removal due to wear is predicted to have a profound effect on the *SWT* distributions, leading to an (i) attenuation (about 60%) and outward movement of peak *SWT* value (at EOC) with increasing cycles for gross slip cases (Fig. 5.22a), due to stress re-distribution caused by wear scar widening and (ii) accentuation (about 875%) and inward

movement (towards the evolving stick-slip interface) of peak SWT value with increasing cycles for partial slip cases (Fig. 5.22b). These effects are compounded, in the present analyses, for the round on flat partial slip condition, by cyclic plasticity phenomena. Thus a competitive relationship is predicted between fatigue damage accumulation and ratchetting failure. The RPF initial peak *SWT* values are only between about 18% (10 μm) and 7% (20 μm) of the corresponding RF2 values. However, the wear-induced attenuation in peak *SWT* values is less significant for the RPF cases, viz. between 0% (10 μm) and 20% (20 μm). It is worth noting that the initial (unworn) critical-plane *SWT* value for the round on flat is about 50% higher for the 20 μm (GS) case than for the 10 μm (PS) case, whereas for the rounded punch on flat the initial value of the 10 μm case is significantly higher than that of the 20 μm case. In other words, for the round on flat, the initial fatigue parameter is higher for higher strokes, whereas for the rounded punch on flat, it is higher for lower strokes. The former is a straightforward effect of increasing shear traction with increasing PS stroke. However, for the RPF case, the transition from stick across the contact to slip, leads to a redistribution of shear stress away from the localised peak value at the leading EOC causing a small increase across a large portion of the contact width. Thus, due to the very highly localised EOC stresses, when $\Delta < \Delta_{\text{th}}$ the predicted EOC slip is zero, so that the peak localised EOC stress converts directly into a peak localised EOC *SWT* value (of Figure 5.22d). In contrast, when $\Delta > \Delta_{\text{th}}$, the leading EOC shear stress peak is predicted to significantly diminish, resulting in a 30% smaller predicted *SWT* peak for the 20 μm case than for the 10 μm case.



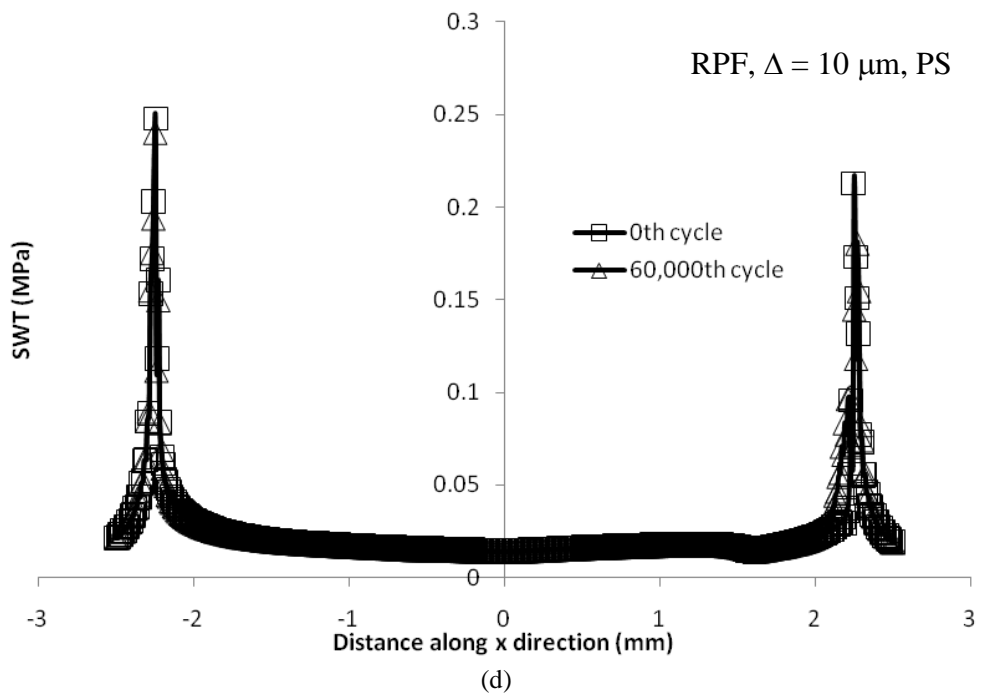
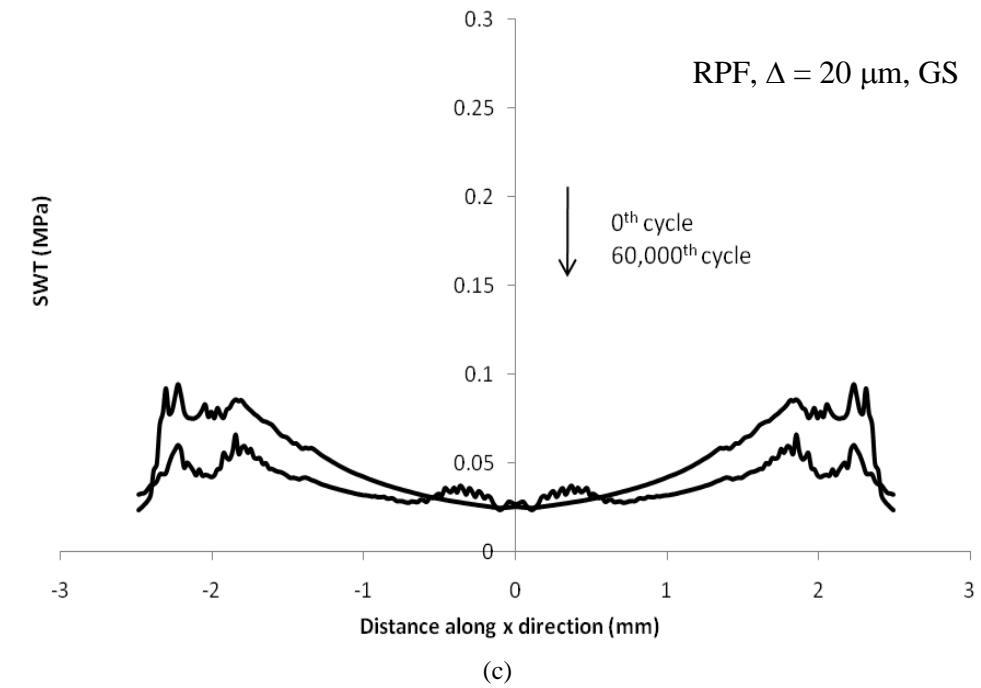


Fig. 5.22. Predicted evolutions of critical-plane SWT for: (a) RF2, 20 μm half-stroke (b) RF2, 10 μm half-stroke (c) RPF, 20 μm half-stroke (d) RPF, 10 μm half-stroke.

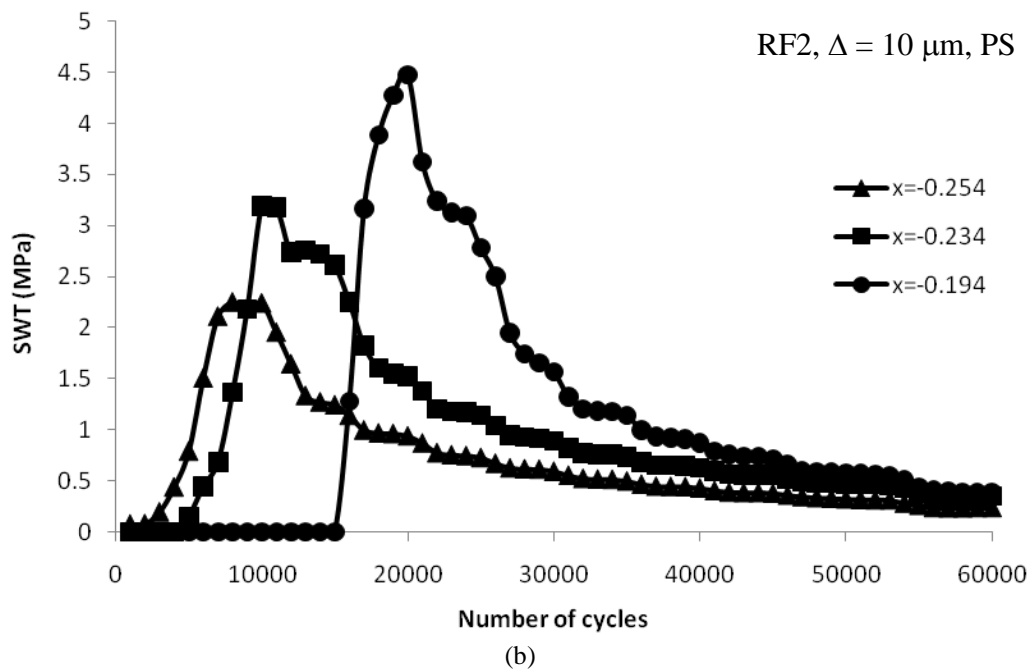
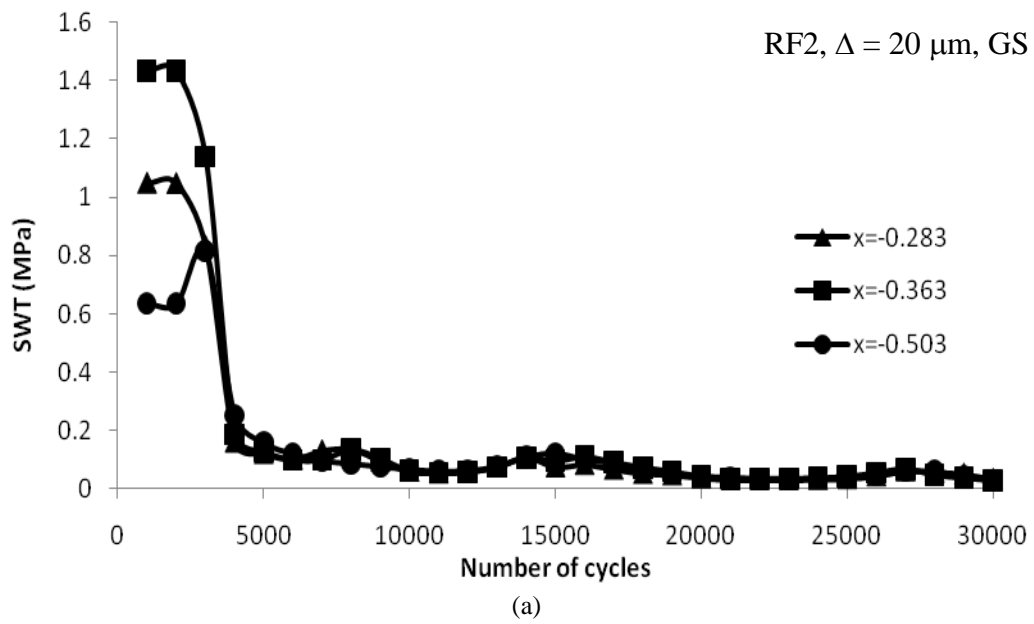
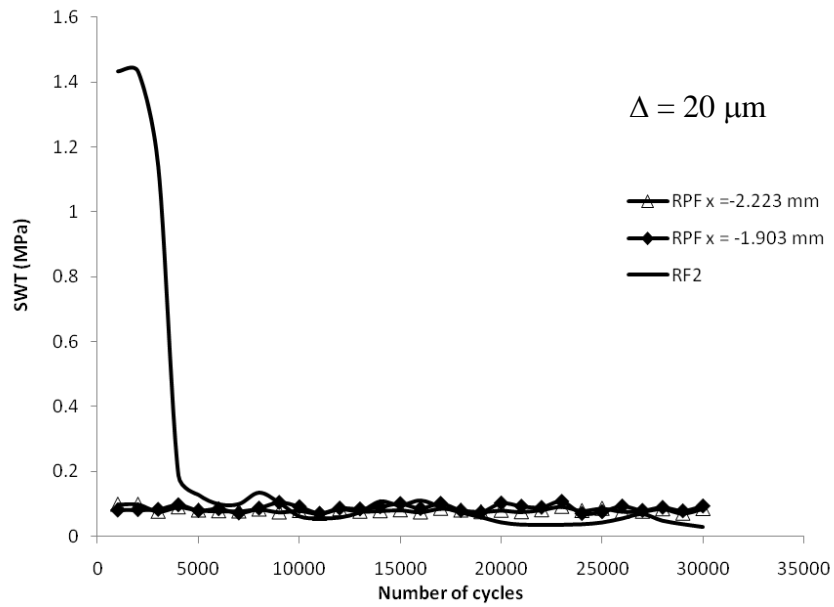
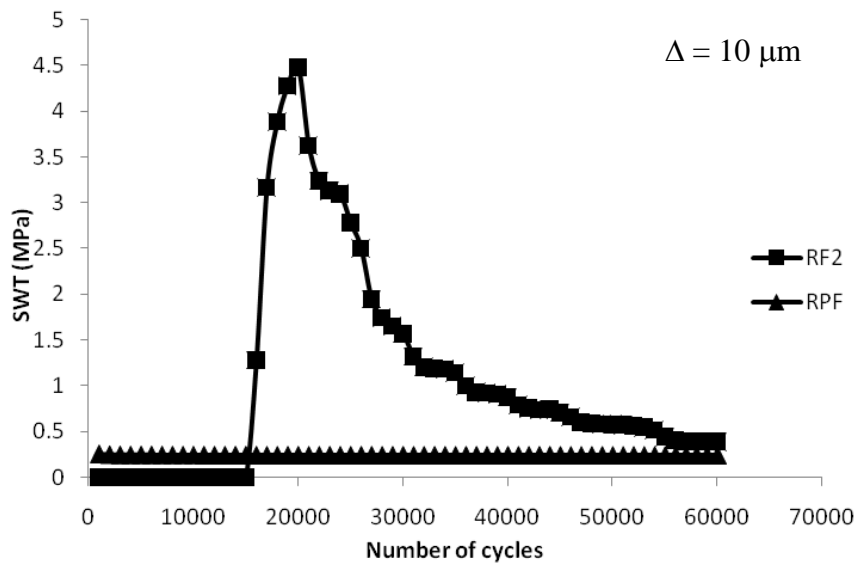


Fig. 5.23. Predicted evolution of critical-plane SWT with fretting cycles for: (a) RF2, 20 μm half-stroke (b) RF2, 10 μm half-stroke (c) RPF, 20 μm half-stroke and (d) RPF 10 μm half-stroke.



(a)



(b)

Fig. 5.24. Comparison of predicted crack nucleation performance of round on flat (RF2) and rounded punch on flat (RPF) in terms of critical-plane SWT evolution for: (a) 20 μm half-stroke, and (b) 10 μm half-stroke.

Fig. 5.23a and 5.23b illustrate the predicted evolutions of critical-plane *SWT* at the identified critical points along the contact surfaces of the round on flat, for the 20 μm and 10 μm half-strokes. The RF2 20 μm *SWT* value is seen to reduce dramatically (from the initial

high value) within the first 5000 cycles for the region $|x| < 0.5$ and remains low thereafter, whereas the 10 μm value starts low but increases dramatically and remains high for longer in the region $|x| < 0.25$. The RPF 20 μm *SWT* value follows a similar trend to the RF2 case but, as shown in Figure 5.24a, results in a very similar but slightly higher steady-state value than the RF2. Fig. 5.24b shows a comparison of the *SWT* evolution for RF2 and RPF at 10 μm half-strokes; the round on flat case is predicted to accrue significantly more fatigue damage over the first 60,000 cycles, even if the final steady-state values are somewhat similar.

5.3.7 Competition between ratchetting and fatigue

Table 5.8 presents a summary of the predicted numbers of cycles to 10 μm crack nucleation, both with and without the assumption of wear-induced material removal effects (since many studies still neglect wear effects in fatigue calculations) and also the predicted numbers of cycles to first ratchetting-induced cracking.

Table 5.8. Predicted life comparison between RF2 and RPF under the half-stroke of 20 μm , 14 μm and 10 μm

Geometry	Half-stroke (μm)	Life without wear	Life with wear	Ratchetting life
RF2	10 (PS)	2.5×10^7 (at $x = -0.40$ mm)	3.4×10^4 (at $x = -0.12$ mm)	$N_r = 4.8 \times 10^4$ (at $x = -0.06$ mm)
RPF	10 (PS)	1.6×10^{10} (at $x = -2.24$ mm)	2.0×10^{10} (at $x = -2.24$ mm)	n/a
RF2	14 (PS)	2.8×10^6 (at $x = -0.40$ mm)	7.0×10^3 (at $x = -0.10$ mm)	$N_r = 1.0 \times 10^4$ (at $x = -0.06$ mm)
RPF	14 (GS)	4.6×10^{11} (at $x = -2.24$ mm)	2.4×10^{13} (at $x = -0.17$ mm)	n/a
RF2	20 (GS)	2.3×10^6 (at $x = -0.40$ mm)	2.2×10^{13} (at $x = -0.36$ mm)	n/a
RPF	20 (GS)	1.8×10^{12} (at $x = -2.24$ mm)	3.0×10^{12} (at $x = -0.19$ mm)	n/a

Fig. 5.25 shows a graphical comparison of the effect of contact geometry and wear on predicted crack nucleation life as a function of half-stroke. The graph clearly displays a minimum nucleation life for the round on flat (RF2) when wear effects are incorporated, at 14 μm , which is very close to the Δ_{th} value of 15 μm . (As discussed before in detail, e.g. see Madge et al., (2007), these ‘with wear’ predictions are thus consistent with the experimentally-observed trend of a minimum fatigue life, corresponding broadly to the PS-GS threshold, as encapsulated also in the fretting maps of Vingsbo, (1988), whereas the ‘without wear’ predictions are thus inconsistent with respect to this aspect). For the round on flat, wear is predicted to have a significant detrimental effect of reducing life for $\Delta < \Delta_{\text{th}}$ (partial slip), from the HCF to the LCF domain, but a contrasting beneficial effect of increasing (HCF) life for $\Delta > \Delta_{\text{th}}$ (gross slip). The corresponding predictions for the rounded punch on flat are significantly different from these. Firstly, the predicted effect of wear is significantly less, the only noticeable effect being a predicted beneficial increase in (HCF) life for the $\Delta = 14 \mu\text{m}$ case (gross slip), from 4.6×10^{11} cycles to 2.4×10^{13} ; interestingly, for the $\Delta = 20 \mu\text{m}$ case, the EOC peaks are predicted to wear so fast that negligible fatigue damage accrues whereas, for the 10 μm case, there is no predicted effect of wear because no slip or wear occurs. Secondly, the effect of increasing stroke for the RPF is to increase life due to predicted decrease in EOC *SWT* value, whereas increasing stroke is predicted to decrease life for RF2 while $\Delta < \Delta_{\text{th}}$, and remain constant for $\Delta > \Delta_{\text{th}}$, consistent with previous ‘no wear’ predictions from (Madge et al., 2007), due to the increasing shear traction with increasing stroke for $\Delta < \Delta_{\text{th}}$, reaching saturation at Δ_{th} . Thirdly, the predicted RPF lives are significantly longer (all very high cycle fatigue), in general, than the predicted RF2 lives. The

one exception is the large stroke $\Delta = 20 \mu\text{m}$ case, where the ‘with wear’ predictions indicate that a slightly shorter RPF life, 3.0×10^{12} cycles, compared to 2.2×10^{13} cycles.

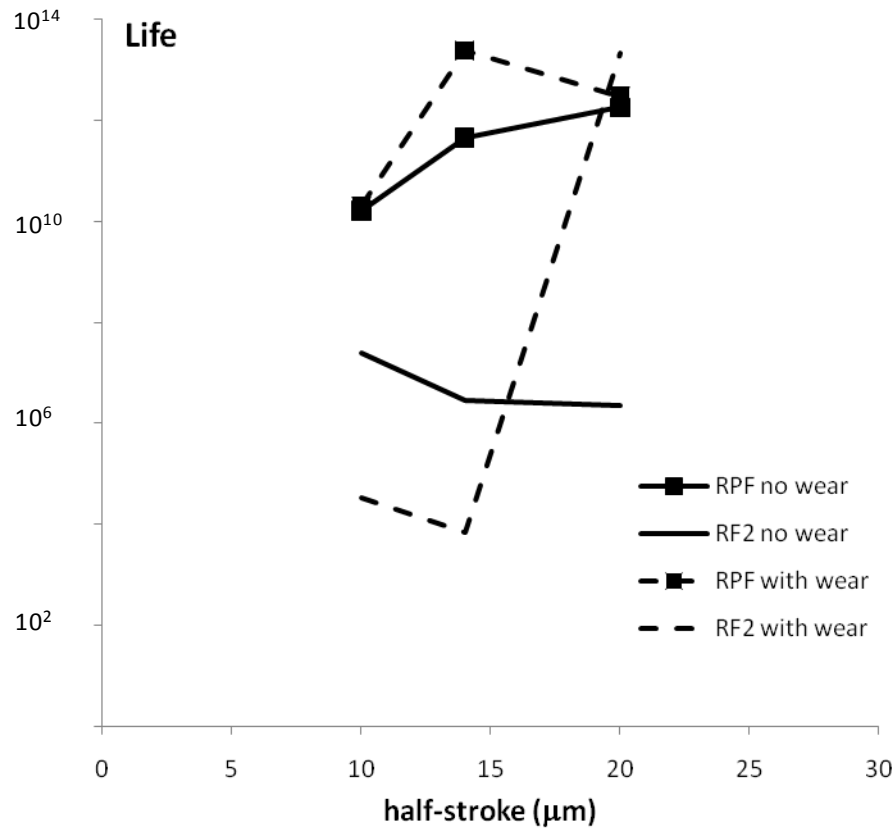


Fig. 5.25. Comparison of predicted crack nucleation performance of round on flat (RF2) against rounded punch on flat (RPF) as a function of half-stroke, for with wear and without wear assumptions.

Ratchetting failure is predicted to occur in the round on flat case for partial slip but not for gross slip, whereas no plasticity or ratchetting failure is predicted to occur in the rounded punch on flat. The numbers of cycles to predicted ratchetting failure are found to be competitive with those to fatigue crack nucleation, with the latter being slightly more conservative (see Fig. 5.26). For the RF2 partial slip cases, consistent with previous work

(Ding et al., 2009), crack nucleation is predicted at numerous locations across the slip zone. For $\Delta = 14 \mu\text{m}$, fatigue crack nucleation is predicted first at $x = -0.10 \text{ mm}$ after approximately 7000 cycles and next at $x = -0.06 \text{ mm}$ after approximately 9000 cycles, with ratchetting failure predicted at $x = -0.06 \text{ mm}$ at 10,000 cycles, assuming a monotonic critical value ϵ_c for Ti6Al4V of 12%. For $\Delta = 10 \mu\text{m}$, although first crack nucleation is predicted at $x = -0.12 \text{ mm}$ after 34,000 cycles, ratchetting failure is predicted after approximately 48,000 cycles at $x = -0.06 \text{ mm}$, just before predicted crack nucleation at that same location, at 49,000 cycles. Thus, from the present analyses, wear-induced ratchetting failure is predicted to be highly competitive with wear-induced fatigue crack nucleation for the round on flat under partial slip conditions.

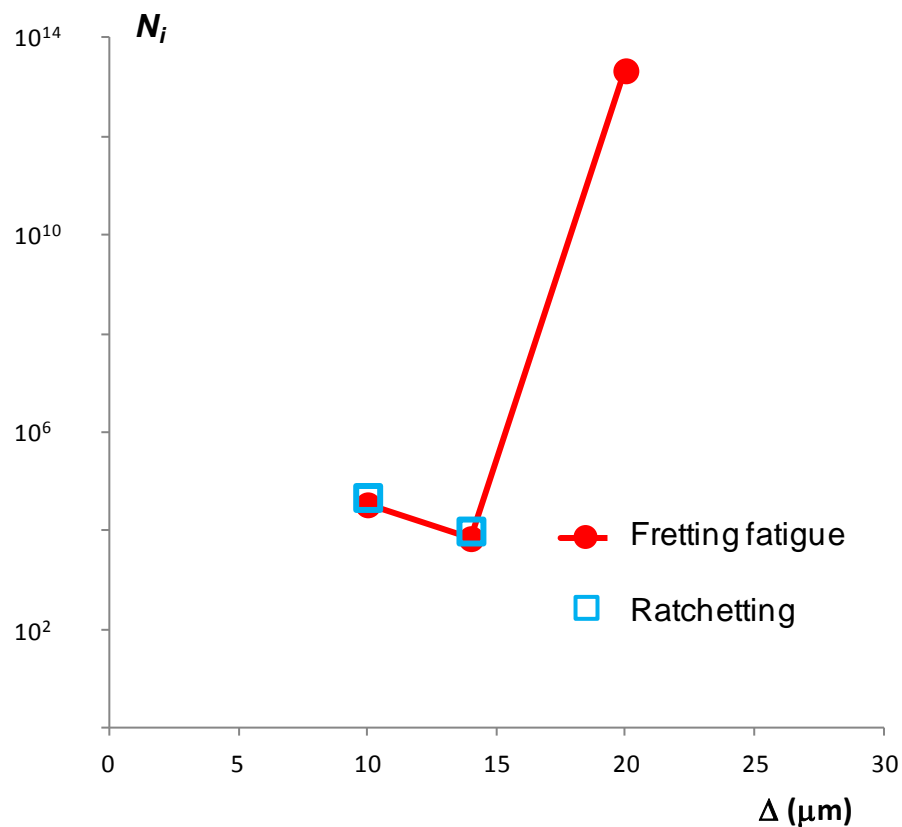


Fig. 5.25. Comparison of predicted crack nucleation performance between fretting fatigue model and plastic ratchetting failure model for round on flat (RF2).

It is important to note that although the comparison with a sample measured PS wear profile for RF1 suggests that the PS wear depth may be under-predicted by the energy-based wear approach, it is anticipated that improved wear depth correlation with test data would result in similar GS-PS trends for the RF1 and RF2 cases, except with lower predicted PS fatigue nucleation life.

5.4 Conclusions

A finite element based energy wear simulation method has been implemented for Ti6Al4V material. The method has been combined with (i) a critical-plane multiaxial fatigue prediction method for crack nucleation using the *SWT* fatigue parameter and (ii) non-linear kinematic hardening model for cyclic plasticity. Detailed FE models of two round on flat fretting configurations and a rounded punch on flat geometry have been developed for a comparative investigation on the effect of contact geometry on fretting wear, fatigue and cyclic plasticity (ratchetting) performance for a given normal load and space envelop and across a range of applied strokes. Validation against theoretical solutions for the round on flat and rounded punch on flat have shown the developed FE models to be in excellent agreement with the theoretical predictions of contact tractions and salient sub-surface stresses. Validation of the round on flat wear prediction against previously published test results for partial slip and gross slip have shown (i) that the gross slip predictions are in reasonable agreement with the sample measured profile, and (ii) that the partial slip predicted stick-zone and contact widths are in reasonable agreement but the partial slip predicted wear depth is about 10 times less than the measured value. Identification of the wear and friction coefficient for the comparison study was effected via previously published work from the

literature for the second round on flat geometry. However, it is worth to note that the great comparison shown here is only applicable for no substrate and thick substrate conditions. For those conditions methods would vary.

In terms of wear behaviour for the two fretting geometries, the following conclusions result:

- A significant predicted difference is that the round on flat geometry can sustain a stabilised partial slip solution with an associated wear pattern whereas the rounded punch on flat (incomplete) geometry is predicted to stick, resulting in no predicted wear, below the GSR threshold. The GSR threshold stroke is therefore shown to be a significant parameter for designing against wear in nearly complete contacts.
- Above the GSR threshold, the predicted wear scars in the rounded punch on flat is of uniform depth whereas the round on flat scar is more U-shaped, of larger maximum depth.
- The wear volume is larger for the rounded punch, particularly for the 14 μm case.

In terms of crack nucleation behaviour:

- The performances of the two geometries are significantly different, driven at least partly by the significantly lower stresses and initial fatigue damage parameter levels in the rounded punch case, despite the very localized edge of contact peaks. Specifically, in general, the rounded punch was predicted to have a significantly longer life to 10 μm crack nucleation (effectively infinite life), with the round on flat typically in the HCF regime (typically mega-cycle).

- The predicted effect of slip regime and associated wear on fatigue crack nucleation was much more significant for the round on flat than for the rounded punch; for the former, the predicted effect of wear was to (i) reduce the partial slip life from HCF to LCF and (ii) increase the gross slip life from HCF (mega-cycles) to very high cycle fatigue. For the rounded punch, the predicted effect was to slightly increase the life to nucleation (in the very high cycle regime) so that for 20 μm , life was predicted to be less than the round on flat value.
- There was a difference in predicted effect of stroke on fatigue for round on flat and for rounded punch. For the no-wear assumption, the predicted effect of increasing stroke in the round on flat was to reduce life whereas the predicted effect in rounded punch on flat was to increase life, due to the greater sensitivity of the rounded punch *SWT* value to relative movement as a result of the more localized edge of contact peak.
- For the round on flat, a significant effect of wear-induced cyclic plasticity was predicted in the partial slip regime, whereby ratchetting failure was predicted to occur within a similar number of cycles and at similar contact locations (stick-slip interfaces) to fatigue crack nucleation. Thus, it is proposed that many partial slip failures may be caused by wear-induced ratchetting, in addition to fatigue cracking. No ratchetting was predicted for the rounded punch or for the gross slip regime. The GSR threshold stroke was shown to be a significant parameter.

The presented findings have implications for the design of pressure armor layers in flexible risers and other complex contact geometries, as follows:

- The importance of modeling and predicting wear, especially for Hertzian contacts in partial and gross slip; not accounting for the effects of wear on stresses and fatigue damage can be non-conservative in the PSR and over-conservative in the GSR
- The importance of identification of slip regime for nearly complete geometries; for $\Delta < \Delta_{th}$, there is no need to model wear, whereas for the GSR, not modeling wear may lead to over-conservative lives.
- If there is freedom to choose the contact geometry, for a specified normal load, space envelop and known stroke, the nearly complete geometry is predicted to be superior in terms of fatigue life, provided the radius to nominal geometry ratio is akin to that used here; the nearly complete contact should give a significantly longer life, particularly in partial slip. On the other hand, the round on flat is predicted to be superior in terms of wear performance, particularly below the GSR threshold.

Chapter 6

Tribological Characterisation of Hip Implant Materials

6.1 Introduction

Design against wear is a major challenge for hip implants since the wear debris can cause problems such as local inflammatory reaction (Dumbleton et al., 2002). The methodology developed in this work is a key solution to this wear-fatigue design challenge. To carry out hip implant wear-fatigue analysis, the first step is to understand the materials. In this chapter, candidate materials for hip implants such as Co-28Cr-6Mo, Ti-6Al-4V alloys and 316L stainless steel are introduced. Representative tribological tests and profilometry analysis are carried out to investigate the tribological behaviour and wear resistance of the materials under realistic loading conditions. Coefficient of friction and energy-based wear coefficient are main target values from the tests, and are important inputs for FE fatigue-wear modelling of the hip taper-lock assembly.

6.2 Material properties

Stainless steels have been widely used for corrosion-resistant applications, including the offshore oil and gas industry, but also for prosthetic hip implants. A prosthetic hip implant normally contains a long stem implanted in the femur and a spherical femoral head that articulates with the acetabulum. The use of modular interlocking components is a popular design feature of the prosthetic hip joint implant (Hallab et al. 2004). Typically, for a modular head, a cylindrical taper-lock coupling is employed between the stem neck and the head. This coupling is susceptible to fretting wear (corrosion) and possibly fretting fatigue due to the potential for oscillatory small amplitude displacements under the combined effects

of the clamping pressure due to the taper-lock with superimposed ambulatory (cyclic) loading, exacerbated by the in-vivo environmental conditions.

Ti-6Al-4V (Ti64) and Co-28Cr-6Mo (CoCr) have been used for stem material and femoral head material, respectively. In terms of Ti64 material, traditionally forged Ti64 has been widely used. Rapid manufacturing techniques are beneficial for prosthesis production. Direct metal laser sintering (DMLS) is an evolving technique which can produce parts with complex geometries in a less costly and more rapid process, compared with conventional techniques (Gaard et al., 2006; Hänninen et al., 2001). The DMLS technology manufactures products from a computer-aided design (CAD) model in a layer-by-layer fashion (Gaard et al. 2006). The sintering of powder is achieved by the heat of a focused laser beam. However, the microstructure, phase composition as well as mechanical and tribological properties of the DMLS material may differ from these of the same material manufactured by conventional techniques.

Table 6.1 lists the elastic material properties for the three candidate materials evaluated here, namely 316L stainless steel, Ti-6Al-4V, and Co-28Cr-6Mo.

Table 6.1 Elastic material properties

Material	Young's Modulus (E) (GPa)	Possion ratio (ν)
Ti-6Al-4V	116	0.34
Co-28Cr-6Mo	240	0.34
Stainless Steel	200	0.30

6.3 Test method

6.3.1 Test description

Tests are carried out to evaluate the tribological performance of the biomaterials. A pin on disk reciprocating sliding test is proposed to investigate both tribological and wear

performance of the two contact arrangements: Co-28Cr-6Mo/forged Ti-6Al-4V and Co-28Cr-6Mo/DMLS Ti-6Al-4V. Fig. 6.1 shows the pin on disk arrangement, where a dead weight is applied on top of the arm which holds the CoCr pin, to push the pin and the Ti64 specimen in contact. A reciprocating tangential load is then applied to give a certain stroke to the arm. The pin is manufactured with a cylindrical surface and polished, as shown in Fig. 6.2. The test loading conditions are decided by performing a stress analysis at the stem-head contact. To reproduce the realistic stress conditions at the joint, 3D FE stress analysis of the taper-lock contact in the commercially available stem-head joint is carried out. Hertzian analytical calculation is then done to determine the design of the customized pin, e.g. the surface radius. Profilometry and SEM tests are carried out to measure the volume of the wear scars. Measurement of evolution of coefficient of friction (COF) and wear coefficient are the target outputs of the tests.

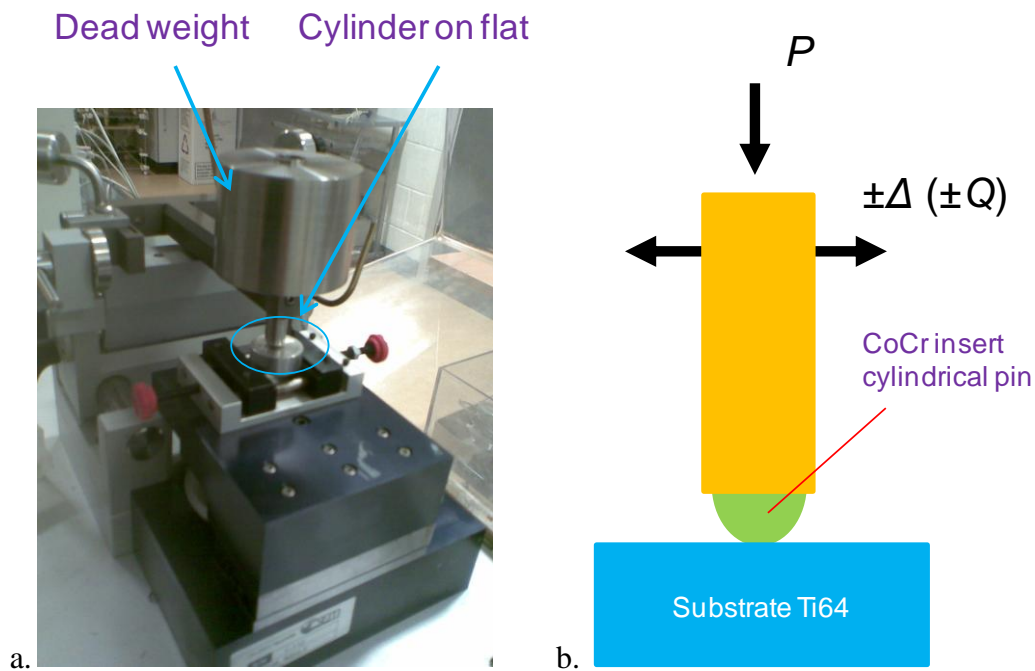


Fig. 6.1 (a) Picture of the pin on disk arrangement and (b) schematic of the pin on disk arrangement (where P is the normal load, Q is the tangential load and Δ is half stroke.)

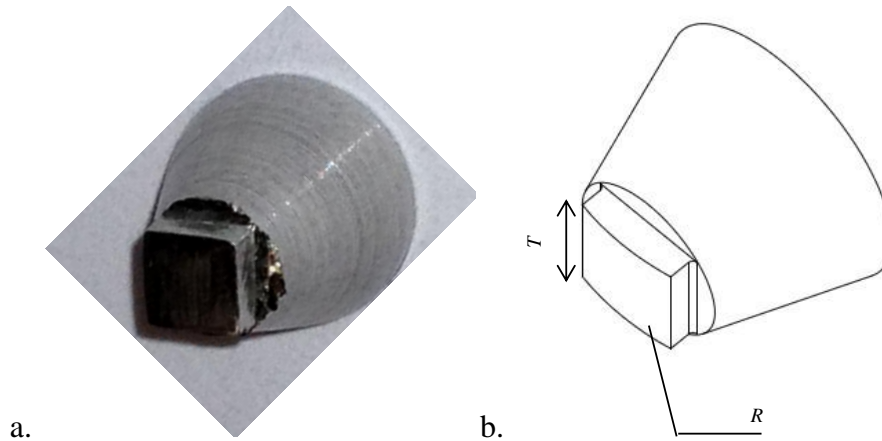


Fig. 6.2 (a) Picture of the Co-28Cr-6Mo pin and (b) schematic of the pin (where $T = 2$ mm is the contact length, $R = 6$ mm is the radius of the cylindrical surface)

6.3.2 3D stem neck-femoral head contact simulation

The general purpose, non-linear, 3D FE code Abaqus is used here to model the global stem-head contact using 4-node linear tetrahedron mesh. Fig. 6.3a shows the model of the taper-lock joint with applied loading conditions and constraints. Fig. 6.3b shows the meshed model where the element size in the contact region is about 1 mm. Fig. 6.3c illustrates the loading history of the model. Initially a press fit force of 1044 N is applied at the centre of the femoral head, representing the process whereby, the surgeon uses a hammer to introduce a press fit. Ideally, a 1 kg hammer of length of 0.5 m arm, swings of 0.03 s with an angle of 90° (0.785 m) resulting in 26.1 kg·m/s momentum. The impact is assumed to last for 2.5×10^{-4} s, therefore a load of 1044 N is calculated and applied. In the later steps, the peak body force of 2648.2 N is applied and released cyclically. For the axes shown in Fig. 6.3a, it can be divided into three directions, where $F_x = 558$ N, $F_y = -294$ N, $F_z = -2572$ N. This load is based on the work of Duda et al. (1997) to represent the maximum load in a gait cycle when a man (of 75 kg) is walking, in which F_z corresponds to a dynamic amplification of 3.5 times the body

weight and the values of F_x and F_y are taken when this maximum value of F_z occurs during a gait cycle.

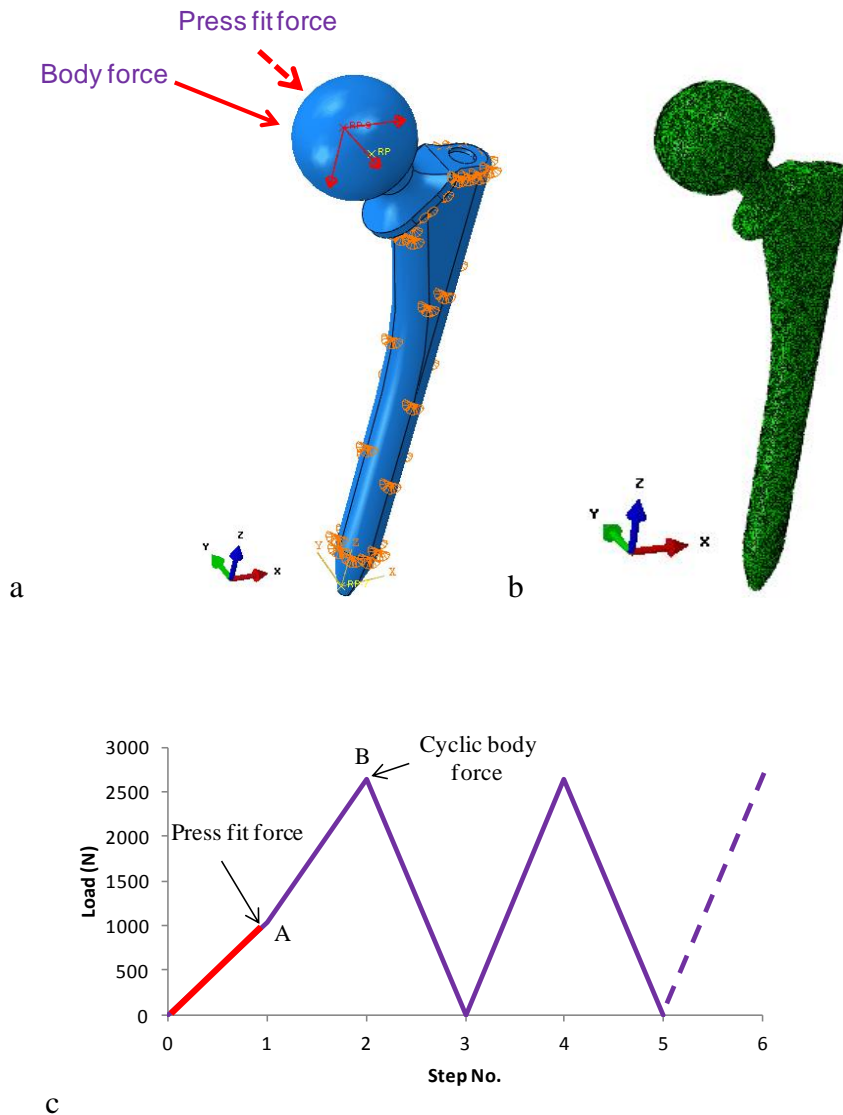


Fig. 6.3. (a) 3D FE model of stem-head contact (b) meshed model (c) loading history

6.3.3 Tibiological test

The pin on disk test is performed on a tribometer with linear movement. The stem-head contacting surface is relatively dry compared with the *in-vivo* environment since in the surgery, the surgeon normally would wipe the stem neck to avoid any tissue or particles

attaching to it. Besides, the taper-lock contact environment is generally locked from the moist conditions. Therefore here the tests are carried out in a dry sliding condition.

Different loading conditions and material arrangements are investigated in the tribological test, as shown in Table 6.2. The surface roughness of the specimen is polished to 0.28 μm for the first four tests while it is 1.50 μm in the last two tests. Rotation speed of the motor through all tests is selected as 1.8 cm/s, acquisition rate is set as 35 Hz to obtain a compromise with respect to number of data points in each hysteresis loop over a large number of cycles. The half-stroke of all tests is selected as 2 mm.

Table 6.2. Tribological tests arrangements (Half-stroke = 2 mm for all tests).

Test No.	Normal load (N)	Material arrangement	Surface roughness (Ra) (μm)	Number of cycles
1	10	CoCr / DMLS Ti64	0.28	18,000
2	10	CoCr / Forged Ti64	0.28	18,000
3	6	CoCr / DMLS Ti64	0.28	18,000
4	6	CoCr / Forged Ti64	0.28	18,000
5	8	CoCr / DMLS Ti64	1.50	21,000
6	8	CoCr / Forged Ti64	1.50	21,000

Key findings in the tribological tests will be COF and energy dissipated throughout the experiments. The energy dissipated can be explained by the energy wear approach, which can be represented by the following equation:

$$V = \alpha \sum E \quad (6.1)$$

where V is the wear volume, α is the energy wear coefficient and $\sum E$ is the accumulated dissipated energy through all the cycles. For a single cycle, the energy dissipated E is given as:

$$E = \int_{t=0}^t Q(x,t) dS(x,t) \quad (6.2)$$

where $Q(x,t)$ is the instantaneous shear loading and $dS(x,t)$ is the instantaneous incremental relative slip.

6.3.4 Profilometry test

Two types of analyses are carried out to investigate the wear volume of the worn specimens, namely the scanning electron microscope (SEM) method and a stylus profilometer (Taylor Hobson Surtronic 3+) method.

The SEM method is a non-contact approach which tilts and scans the specimen surface to generate a 3D image with numerical data points. To measure the wear volume, a bounding surface is needed to represent the unworn surface. There are different ways to define the bounding surface. Here a 'soap film' approach is selected and the reproduction of the unworn surface may follow the surrounding surface profile as a curved one. This method is also applied on the unworn surface as a datum. Subtraction of the unworn surface volume from the worn surface volume gives the final wear volume.

The profilometer method is a contact approach. During the test, the sensor needle of the profilometer is placed on top of the wear scar and slides through. Since the tribological tests are linear sliding tests, the wear scar is assumed as a cuboid. A number of tests are done in both wear scar length (sliding) direction and wear scar width (transverse) direction. The average wear area measured in the scar length direction multiplied by the wear scar width gives the wear volume; the average wear area measured in the scar width direction multiplied by the wear scar length is another way to calculate the wear volume. As for the SEM based

method, subtraction of the unworn surface volume from the worn surface volume compensates for the intrinsic error.

6.3.5 Wear coefficient and hardness test

The wear coefficient can be calculated according to Eq. 6.1. Rockwell hardness tests are carried out on the Co-28Cr-6Mo, forged Ti-6Al-4V and DMLS Ti-6Al-4V, using the Rockwell C type with 150 Kg force and diamond cone, as shown in Table 5.3.

Table 6.3. Hardness value (Rockwell C)

Material	Test 1 (HRC)	Test 2 (HRC)	Test 3 (HRC)	Averaged value (HRC)
Co-28Cr-6Mo	48	43	39	43.3
Forged Ti64	28	28	30.8	28.9
DMLS Ti64	28	31	32.5	30.5

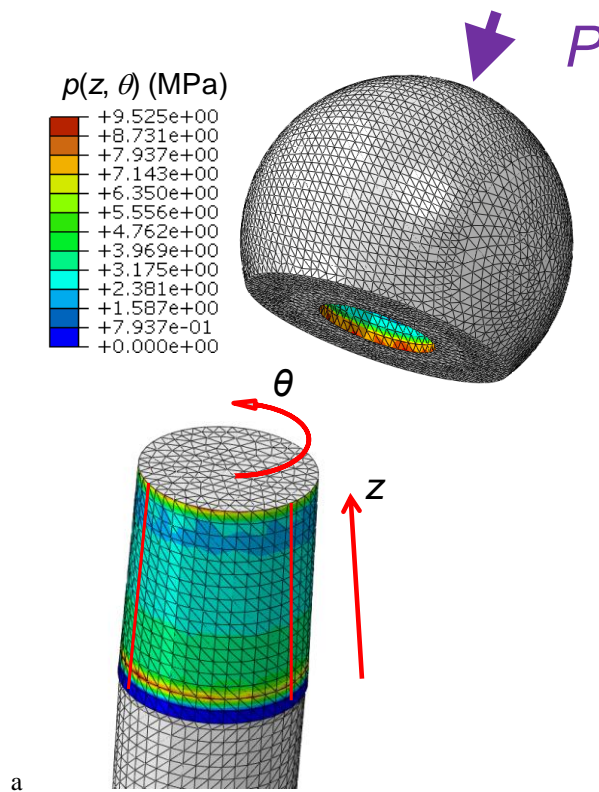
6.4 Results and discussion

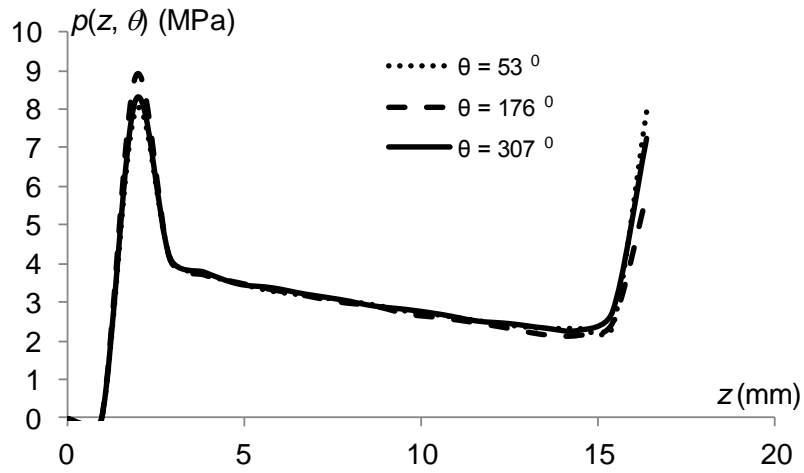
6.4.1 3D stem-head contact modelling results

Figs. 6.4a, b and c show the contact pressure distribution at the stem neck under clamping pressure (point A in Fig. 6.3b) and the relative slip distribution. The contact pressure is predicted to concentrate on the contact edges with a peak contact pressure of 9.5 MPa. This distribution is akin to that of a complete contact with sharp contact edges, e.g. punch on flat (Johnson, 1985). All contact nodes slip for around 3 to 4 μm due to the press fit force. The non-axisymmetric distribution of contact pressure and slip is attributed to the boundary conditions which are also non-axisymmetric.

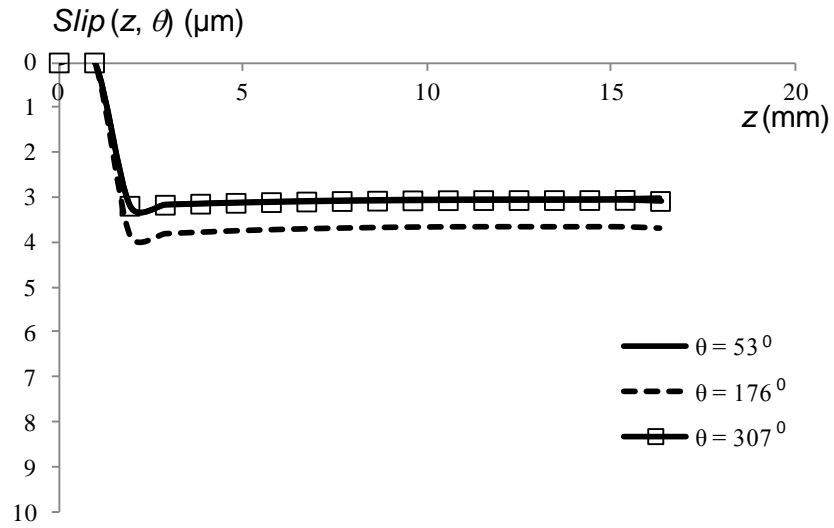
Figs. 6.5a to c show the contact pressure distribution at the stem neck under peak body force. Fig. 6.5a shows the contour plot of contact pressure distribution at the stem neck surface. Fig. 6.5b shows the contact pressure profile on three paths along the z axis direction

at different circumferential positions. Fig. 6.5c shows the circumferential contact pressure distribution at two z locations which are adjacent to the top and bottom contact edges. The contact pressure concentrates mainly at the contact edges at certain circumferential positions. The peak contact pressure is predicted to be 67.6 MPa. It is clear that along the top edge ($z = 16.4$ mm), the regions from $0^\circ \leq \theta \leq 100^\circ$ and $316^\circ \leq \theta \leq 360^\circ$ are out of contact and contact is concentrated on the $100^\circ \leq \theta \leq 316^\circ$. In contrast, along the bottom edge ($z = 1.9$ mm) contact extends over the regions $0^\circ \leq \theta \leq 123^\circ$ and $272^\circ \leq \theta \leq 360^\circ$ with no contact (gap) in $123^\circ \leq \theta \leq 272^\circ$. These distributions are akin to Hertzian round on flat (incomplete) distributions.



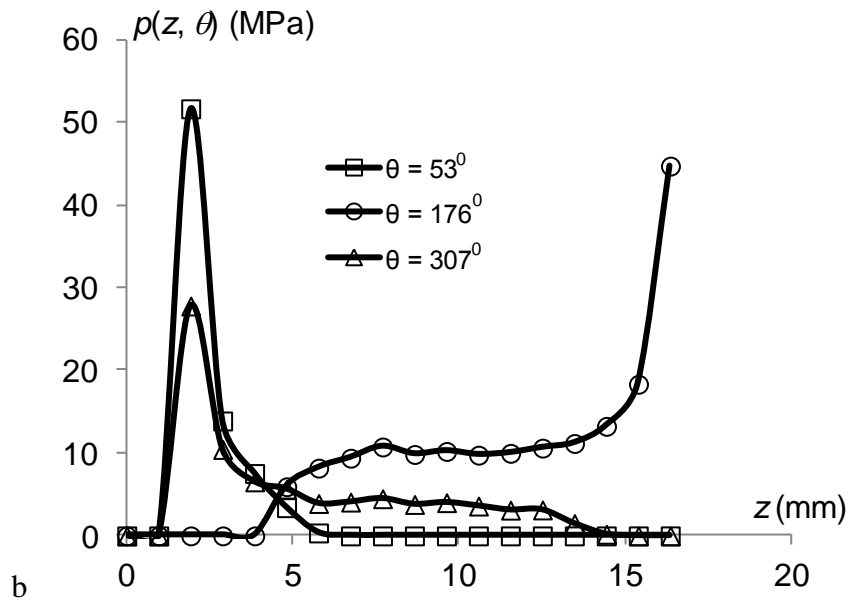
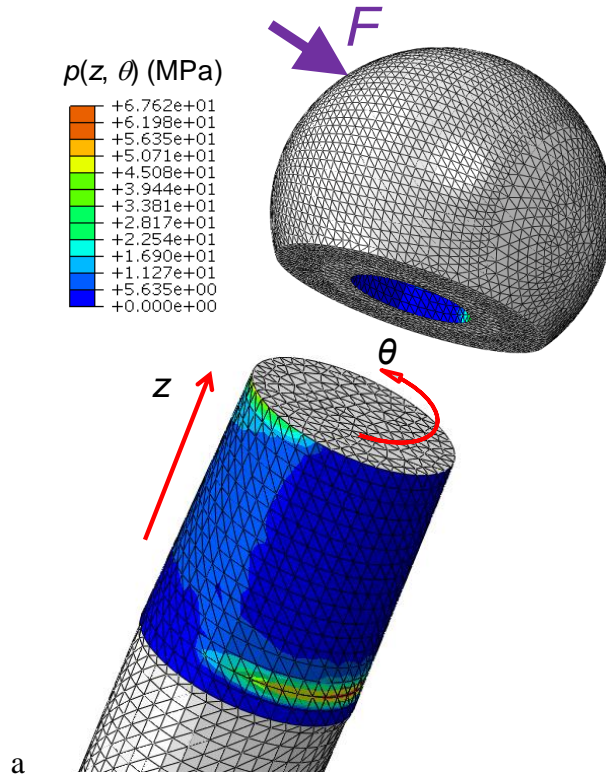


b



c

Fig. 6.4. (a) Contour plot of stem-head contact pressure under clamping pressure (b) Circumferential contact pressure distribution. (c) Axial relative slip distributions.



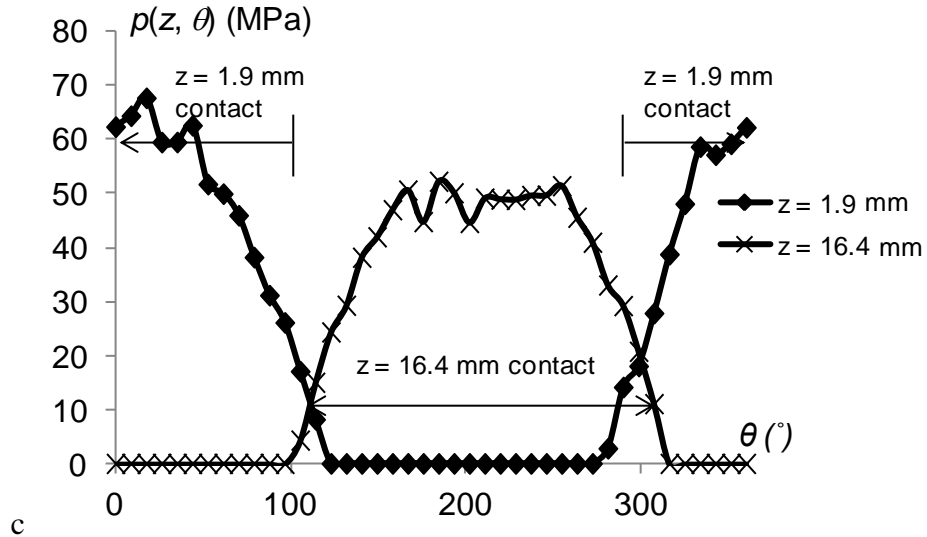


Fig. 6.5. (a) Contour plot of stem-head contact pressure under peak body force (b) Axial contact pressure distributions (c) Circumferential contact pressure distributions.

Figs. 6.6a and b show relative slip distributions in both axial (z) and circumferential directions. Gross slip is predicted while non-uniform slip profile is shown in the z direction. Around the bottom edge of the stem neck (small z location) it is seen to have more slip (maximum slip = $9.3 \mu\text{m}$) at certain circumferential locations, e.g. $0^\circ \leq \theta \leq 105^\circ$ and $280^\circ \leq \theta \leq 360^\circ$. The slip values are similar (between 3 and $4 \mu\text{m}$) around top edge of the stem neck (bigger z values). This shows that the taper-lock assembly experiences typical fretting slip amplitudes and distributions/ regime.

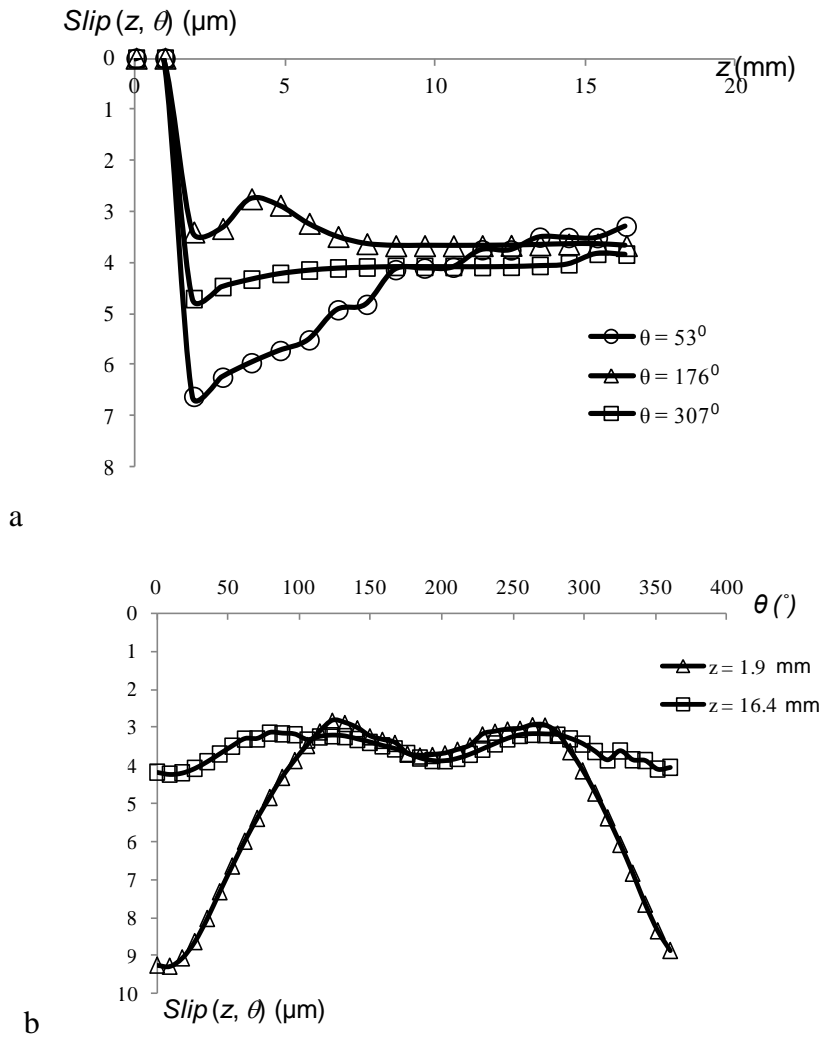


Fig. 6.6. (a) Axial relative slip distributions and (b) circumferential relative slip distributions

6.4.2 Pin design

The Co-28Cr-6Mo pin is designed and manufactured to represent the femoral head in the tribological tests. Due to machine holder limitations, a pin contact width T (as shown in Fig. 6.2b) is selected as 2 mm. Under a normal load of 8 N which is the medium level of the machine's loading capacity, Hertzian analyses (Johnson, 1985) can be carried out to help the design. As shown in Fig. 6.7, varying the pin radius from 3 mm to 20 mm reduces the peak Hertzian contact pressure from 95 MPa to 38 MPa. A 6 mm pin radius is selected as this

contact configuration gives a peak contact pressure of 68 MPa, which is close to the peak pressure level predicted in the 3D hip joint model for $z = 1.9$ mm (Fig. 5.5c).

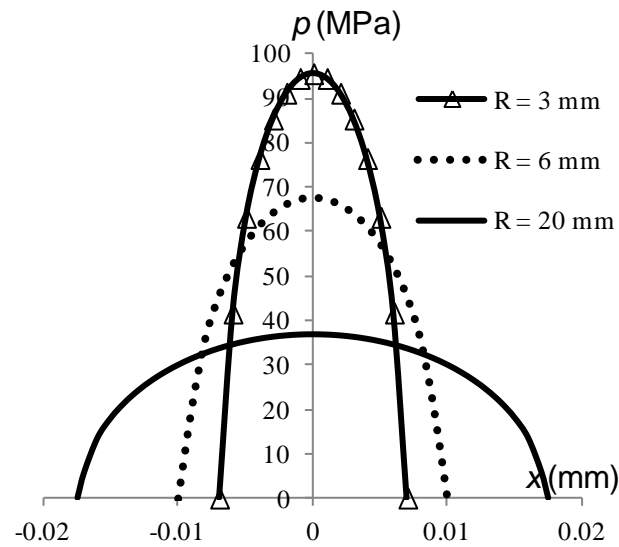
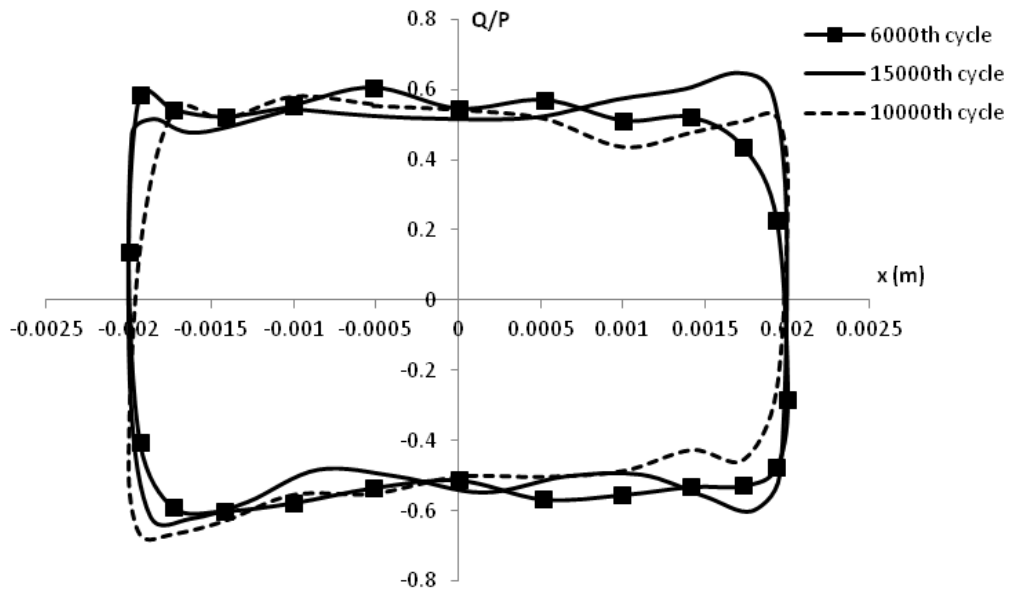


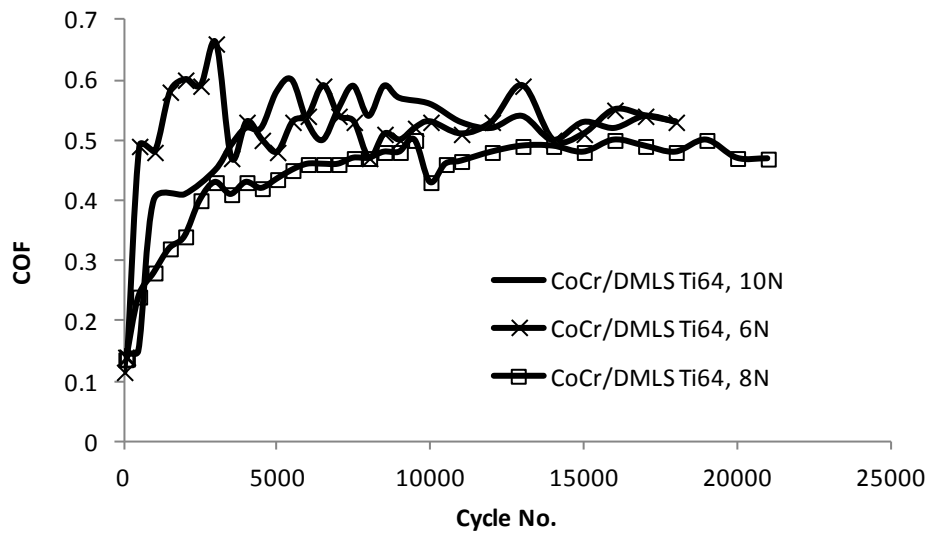
Fig. 6.7 Hertzian solution indicated contact pressure

6.4.3 Tribological tests results

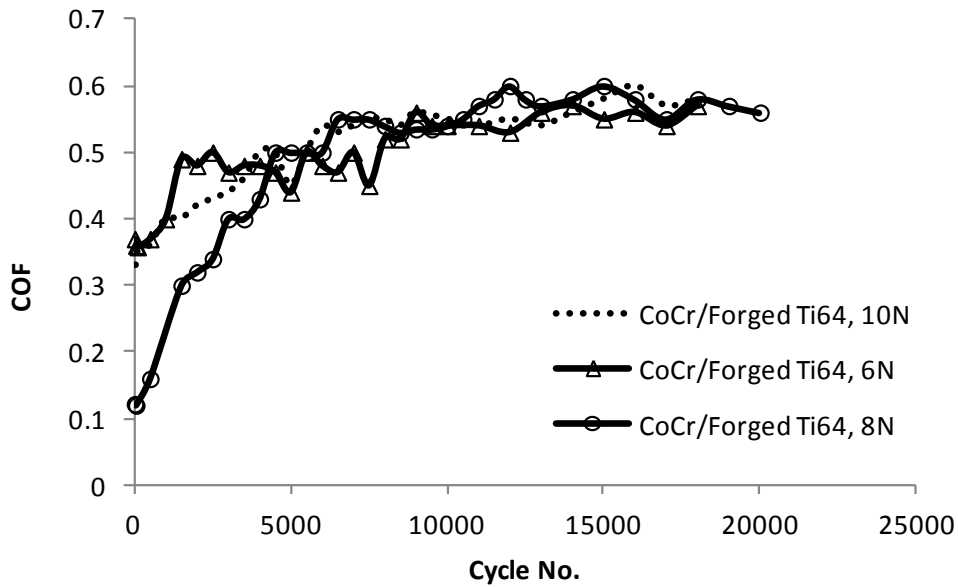
Table 6.2 shows the conditions for the series of tribological tests carried out. Fig. 6.8a shows examples of the hysteresis loops from test 3 for three sample cycles. The product of area within each hysteresis loop and the normal load gives the frictional energy dissipated. Table 6.5 shows the total accumulated energy through all cycles for each test. The averaged Q/P value during sliding (approximately horizontal parts) for each hysteresis loop represents the COF of each cycle. The evolution of COF for each test is determined. Fig. 6.8b and c show the COF evolution for the two material combinations. Typically, the COF increases rapidly during the first few thousands of cycles, then it fluctuates for several thousands of cycles, and finally levels off to an approximately steady-state (sliding) value. This is consistent with measured trends in fretting wear tests, e.g. see McColl et al. (2004).



a



b



c

Fig. 6.8 (a) Hysteresis loops, (b) COF evolution of CoCr/DMLS Ti64 and (c) COF evolution of CoCr/forged Ti64

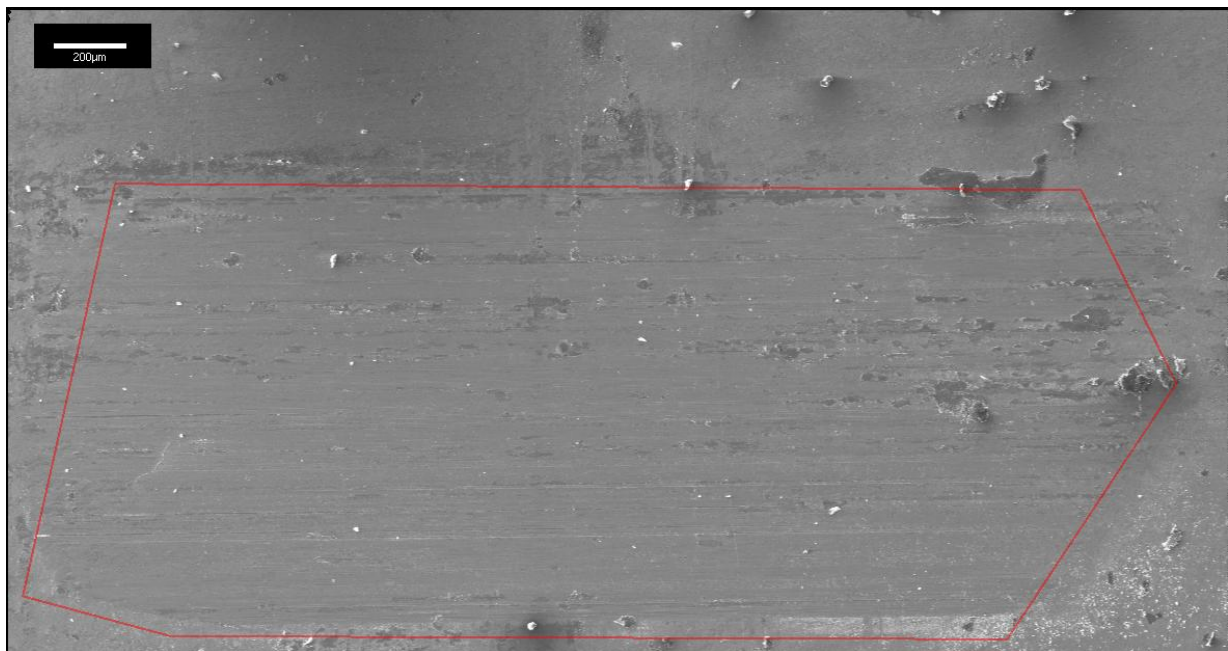
The measured steady-state COF and energy dissipated through all the cycles for each test are listed in Table 6.5. The COFs for the same material arrangement show similar values, i.e. for CoCr/DMLS Ti64 the measured COFs are in the range (0.50 - 0.53) for different loading conditions, surface roughness values and numbers of cycles; for the CoCr/Forged Ti64 the measured COFs are in the range (0.56 - 0.58). The frictional energy dissipated for each test follow the trend that larger normal load condition results in greater energy dissipation. For the same normal loading conditions, CoCr/Forged Ti64 dissipates more energy than CoCr/DMLS Ti64, since the former arrangement experiences a larger tangential force due to the higher COF.

Table 6.5. Tribological tests results (Half-stroke = 2 mm for all cases).

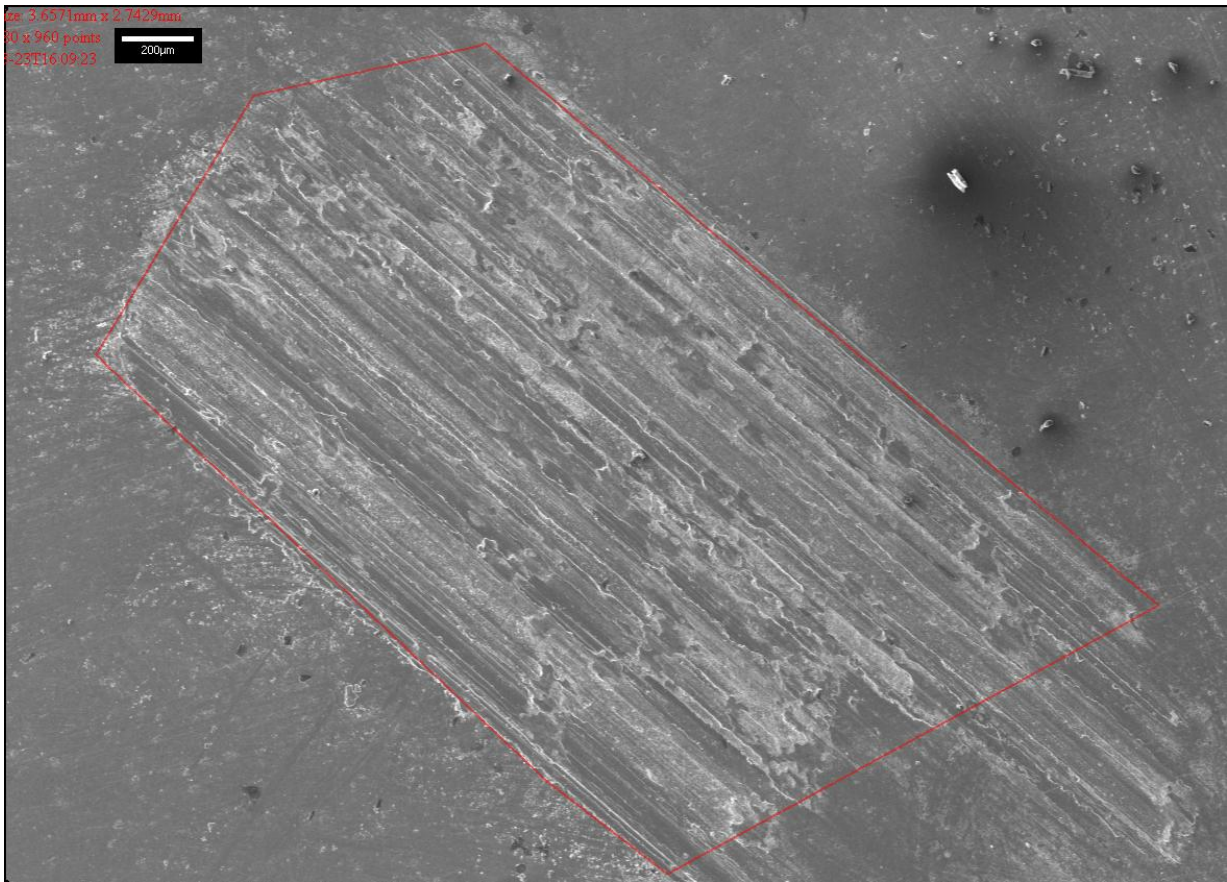
Test No.	Normal load (N)	Material arrangement	COF	Energy dissipated (Nmm)
1	10	CoCr / DMLS Ti64	0.52	7.02×10^5
2	10	CoCr / Forged Ti64	0.56	7.81×10^5
3	6	CoCr / DMLS Ti64	0.53	4.60×10^5
4	6	CoCr / Forged Ti64	0.57	4.81×10^5
5	8	CoCr / DMLS Ti64	0.50	6.26×10^5
6	8	CoCr / Forged Ti64	0.58	7.05×10^5

6.4.4 Profilometry tests results

Figs. 6.9a and b show sample SEM pictures taken from the worn specimens for Test 3 and 4. The highlighted frames indicate the wear scars. The DMLS Ti64 worn surfaces are seen to be more uniform than the forged Ti64 worn surfaces, which clearly have significantly more surface damage. This suggests that the DMLS manufacturing procedure improves material structure and damage resistance.



(a)



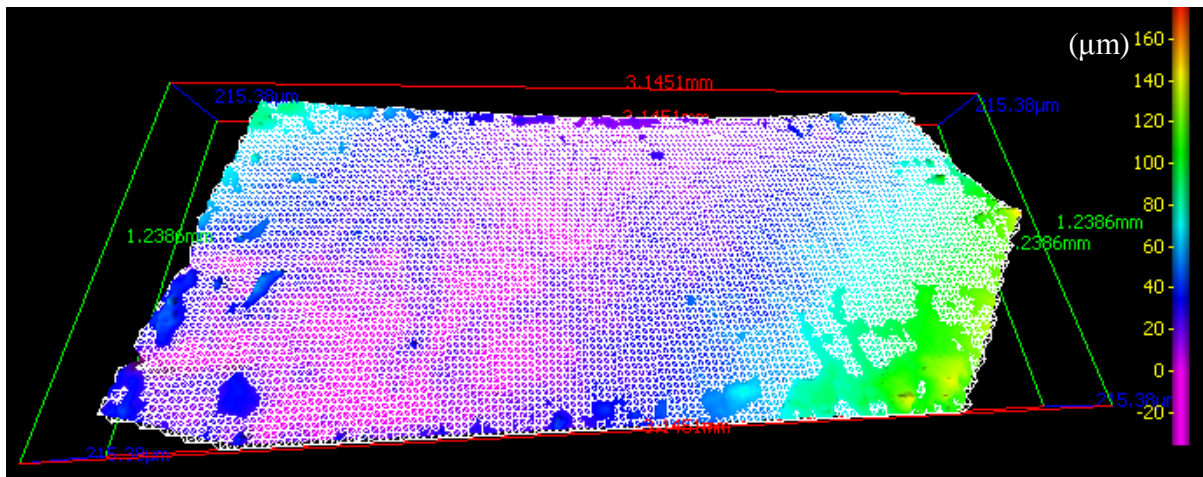
(b)

Fig. 6.9 SEM pictures of the wear scars for (a) Test 3, $P = 6$ N DMLS Ti64 and (b) Test 4, $P = 6$ N forged Ti64.

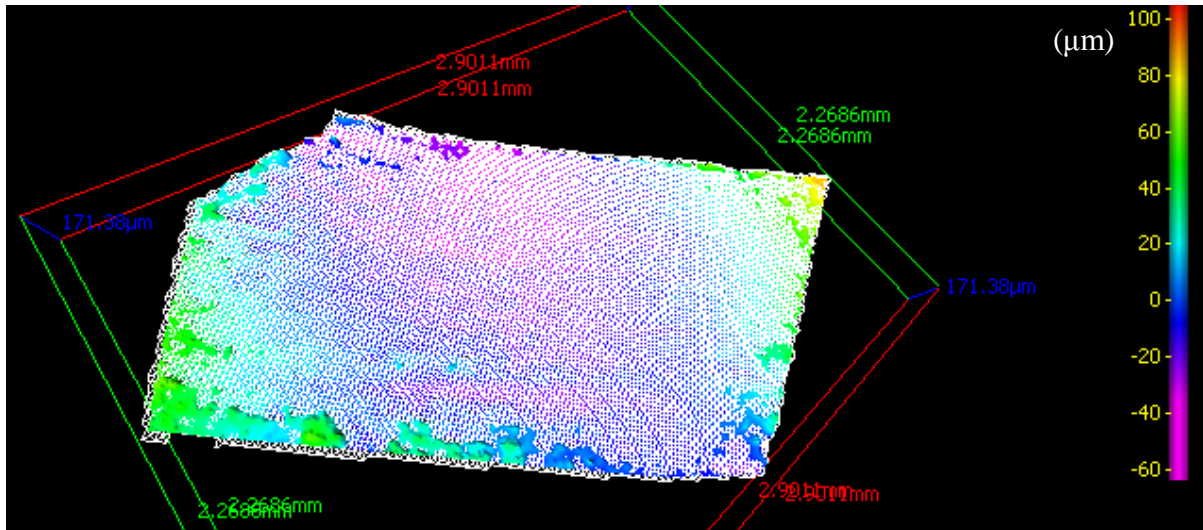
Figs. 6.10a and b show the computed 3D worn surface profile for Test 3 and 4. A film which represents the unworn surface is also manually generated for each case. The wear scar volume is then calculated using the space between the film and the generated worn surface.

Table 6.6 shows the results of the SEM wear analysis of the wear scars from Test 1 to 4. Wear profile analysis of Tests 5 and 6 using the SEM was not possible due to the large initial roughness. This indicates that polishing treatment is necessary before tribological tests in

order to obtain accurate wear scar profiles. The wear coefficient α , for each test is then calculated using Eq. 6.1, as shown in Table 6.6. The averaged wear coefficient for CoCr/DMLS Ti64 is $4.16 \times 10^{-8} \text{ MPa}^{-1}$ while it is $0.99 \times 10^{-7} \text{ MPa}^{-1}$ for CoCr/forged Ti64.



(a)



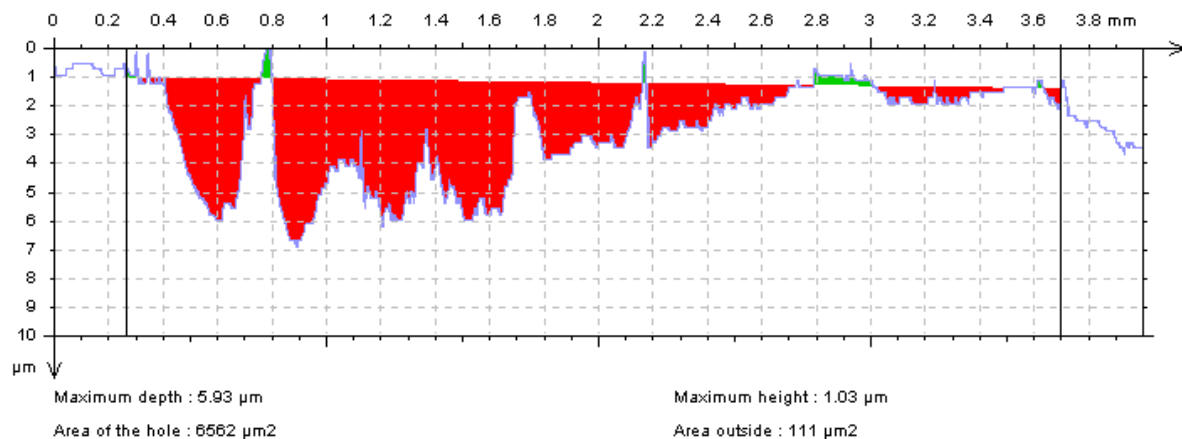
(b)

Fig. 6.10 Computed 3D worn surface profiles for (a) Test 3, $P = 6 \text{ N}$ DMLS Ti64 and (b) Test 4, $P = 6 \text{ N}$ forged Ti64.

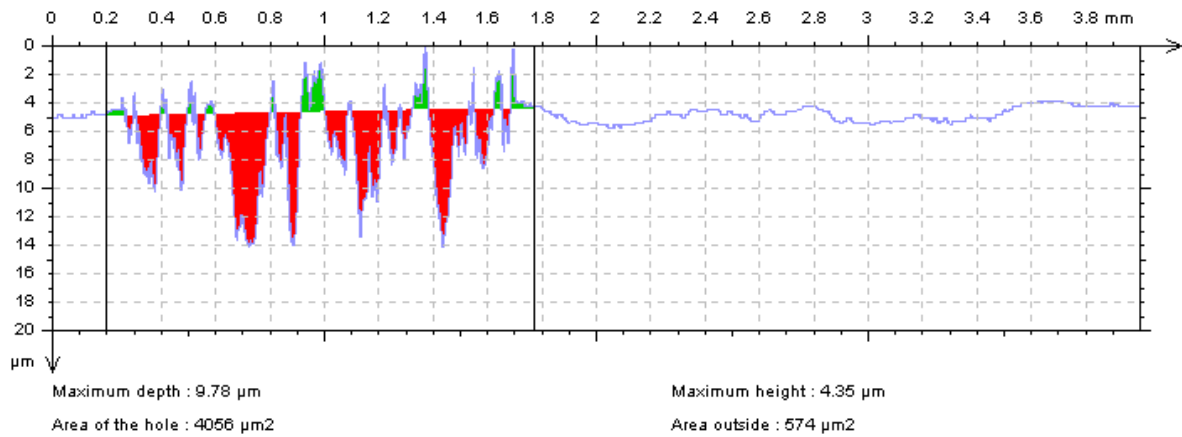
Table 6.6. Profilometry test results by SEM

Test No.	Normal load (N)	Material arrangement	Wear volume by SEM (mm ³)	Wear volume on free surface by SEM (mm ³)	Modified wear volume (mm ³)	Wear Coefficient, α (MPa ⁻¹)
1	10	CoCr / DMLS Ti64	0.0436	0.00613	0.03747	5.35×10^{-8}
2	10	CoCr / Forged Ti64	0.0960	0.01313	0.08287	1.06×10^{-7}
3	6	CoCr / DMLS Ti64	0.0198	0.00613	0.01367	2.97×10^{-8}
4	6	CoCr / Forged Ti64	0.0572	0.01313	0.04407	9.18×10^{-8}

Profilometry tests are also conducted using a single degree of freedom stylus profilometer. Figs. 6.11a and b show the sample wear scar profile along the stroke direction and normal to the stroke direction for Test 4. As mentioned earlier, the wear volume can be estimated using two methods, viz. product of average transverse wear scar area and length or product of average length wear scar area and width. Both methods are applied here to a sample of transverse and longitudinal profilometer trace data and the final wear volume is calculated by averaging the results of the two methods.



(a)



(b)

Fig. 6.11 Wear scar profile by profilometer for Test 4 $P = 6$ N Forged Ti64 (a) along the stroke direction (b) normal to the stroke direction.

The results of the profilometry-based wear analysis for Tests 1 to 4 are listed in Table 6.7. The averaged wear coefficient by profilometer for CoCr/DMLS Ti64 is 3.34×10^{-9} MPa^{-1} while it is 1.60×10^{-8} MPa^{-1} for CoCr/forged Ti64.

Table 6.7. Profilometry test results by profilometer.

Test No.	Normal load (N)	Material arrangement	Wear volume by profilometer (mm^3)	Wear volume on free surface by profilometer (mm^3)	Modified wear volume (mm^3)	Wear Coefficient, α (MPa^{-1})
1	10	CoCr / DMLS Ti64	0.0029	0.000163	0.00274	3.91×10^{-9}
2	10	CoCr / Forged Ti64	0.0106	0.000392	0.01021	1.31×10^{-8}
3	6	CoCr / DMLS Ti64	0.0015	0.000229	0.00127	2.76×10^{-9}
4	6	CoCr / Forged Ti64	0.0093	0.000280	0.00901	1.88×10^{-8}

The SEM-based data shows that the DMLS Ti64 is 2.4 times more wear resistant and the profilometer-based tests show that it is 4.8 times more wear resistant. The hardness tests

also report that DMLS Ti64 is slightly harder. Therefore, to reduce wear debris emission, it is recommended that DMLS Ti64 should be adopted for the hip joint stem-head coupling implemented here rather than the forged material. The wear coefficient of the forged Ti64 by SEM tests is about $1 \times 10^{-7} \text{ MPa}^{-1}$, which is around the same level reported in Magaziner et al. (2008). However, the wear coefficients tested by profilometer are significantly (nearly 10 times) smaller than the SEM results. This suggests single degree of freedom stylus profilometer is not as accurate as the 3D SEM-based methodology. The sensor needle slides along the specimen surface but without any control on the direction normal to the profilometer arm. Large compliance normally exists and the needle may change direction of motion in the normal to arm direction from time to time and hence not keep in a straight line. Therefore, the wear coefficients are chosen here from the SEM results and used as part of the input for the numerical simulations below.

6.6 Sample tribological tests for other materials

Sample tribological tests are carried out for other material combinations, as summarized in Table 6.8.

Table 6.8 Tribological test results for SS 316L and CoCr.

Test	Acquisition rate [Hz]:	Rotating speed [cm/s]:	Half stroke [mm]	Normal load [N]	Material	Cycle number	COF
i	30	0.4	2	6	316L(Sphere)/ Ti64	200	0.38
ii	30	5	2	10	316L Designed pin)/ CoCr	3000	0.21

Test i shows the 316L/Ti64 combination gives a similar early cycle COF compared with previous tests (CoCr/Ti64). Test ii shows that 316L/CoCr has a much lower COF after 3000 cycles, compared with previous tests.

6.7 Material grain size

The reason why DMLS Ti64 performs better in terms tribological and mechanical behaviour may be attributed to grain size that decided during manufacturing process. Instantaneous removal of heat and rapid material resolidification would occur with the laser sintering technique, which can help optimise grain size significantly.

6.8 Summary

Tribological and profilometry tests are carried out for two material combinations: Co-28Cr-6Mo/DMLS Ti-6Al-4V and Co-28Cr-6Mo/forged Ti-6Al-4V. The hardness and wear resistance of the DMLS Ti-6Al-4V are seen to be superior to those of forged Ti-6Al-4V.

- DMLS Ti64 is shown to have better wear resistance and lower coefficient of friction than forged Ti64 for contact pressure representing stem-head contact in modular hip implant.
- A 3D model of a stem-head taper-lock coupling in a modular hip implant is shown to predict complex contact variable distributions indicative of fretting regimes and is used to identify the contact pressure in the stem-head contact regions.

Chapter 7

Fretting Wear-Fatigue of Taper-Lock Coupling in a Prosthetic Hip Implant

7.1 Overview

Fretting of the stem-head joint in a prosthetic hip implant is investigated experimentally previously in Chapter 5. In this chapter a scientific approach for fretting wear-fatigue of a prosthetic hip implant is developed. The fretting wear-fatigue computational methodology has been presented in Chapter 4. On a macroscopic scale, the stem and cap surfaces are flat. However, on a microscopic scale, surface roughness undulations are employed to accentuate the frictional contact for an enhanced mechanical locking effect. Macroscopic (global) modelling for fretting wear-fatigue performance for two head/stem material combinations, namely Co-28Cr-6Mo against DMLS Ti-6Al-4V and Co-28Cr-6Mo against forged Ti-6Al-4V, are investigated. The significance of wear in a hip joint for 10 years of service in a normal weight person for moderately intense exercise is predicted for both material combinations. Microscale sub-model is developed to investigate the fretting wear-fatigue performance of the surface undulations and hence predict wear and fatigue micro-cracking.

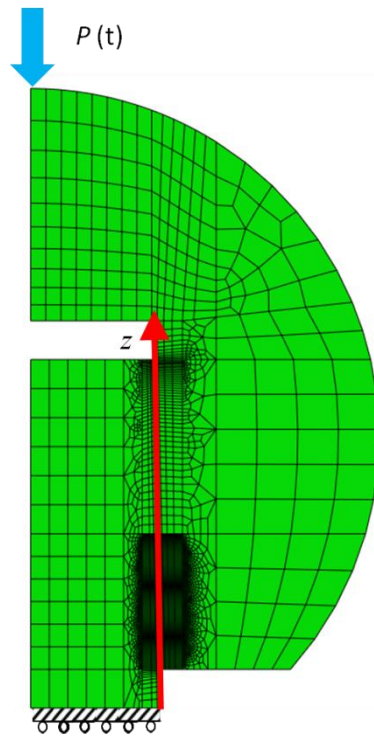
7.2 Numerical modelling of fretting wear and fatigue for hip implant

7.2.1 2D axisymmetric FE global model for fretting wear and fatigue in hip implants

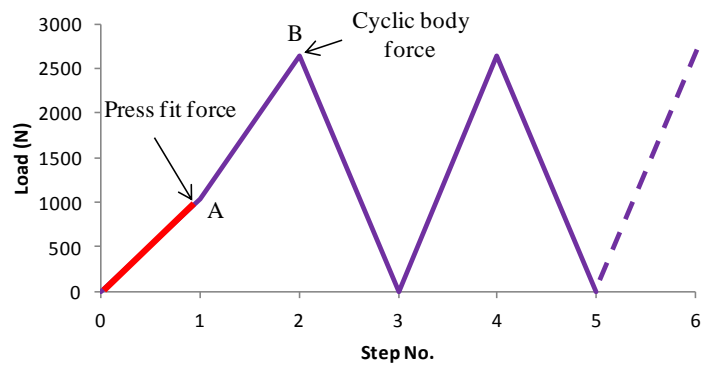
A 2D axisymmetric global model of the realistic commercially-available stem-head joint is developed for fretting wear and fatigue computation. The general purpose, non-linear,

FE code Abaqus is used here and 4-node bilinear axisymmetric quadrilateral elements are adopted. Fig. 7.1 shows the mesh and loading condition. A detailed mesh convergence study has been carried out. The mesh in the contact region is highly refined (10 μm width for the smallest element). It is predicted that the contact edges experience high contact pressure and large gradient of slip and fatigue indicator parameter (FIP); besides, locations where z is small (Fig. 7.1a) are predicted to experience relatively larger slip values thus potentially much more wear, therefore the mesh in these regions is made especially fine. The loading condition is similar to that of the 3D model in the previous section and the load magnitudes are the same as those in Fig. 7.1b. The difference here is the load direction. Here the peak body force of one gait cycle is applied in the axial direction; this is a more extreme wear condition that gives relatively more tangential motion between the stem neck and femoral head.

The contact surface interaction is defined via the finite sliding contact pair approach which adopts the master-slave algorithm in Abaqus. The maximum allowable penetration depth (*h-crit*) between the slave and master nodes during the iterative solution process is set to 1 μm . The minimum allowable distance between the initial coordinates of adjacent nodes on the mating contact surface (*ADJUST parameter*) is set to 0.001 μm . Coulomb friction is employed based on the Lagrange multiplier contact algorithm to ensure the exact stick condition when the shear stress is less than the critical shear value according to the Coulomb friction law. These contact parameters have been identified from previous studies, e.g. see Madge et al., (2007), Zhang et al., (2011).



(a)



(b)

Fig. 7.1 (a) 2D axisymmetric FE global model of stem-head contact. (b) Loading history

7.2.2 Material data

Co-28Cr-6Mo has a Young's modulus of 240 GPa and a Poisson's ratio of 0.34. Both Ti-6Al-4V alloys have a Young's modulus of 116 GPa and a Poisson's ratio of 0.34. Plasticity is only modelled for the Ti-6Al-4V alloys since it has been established in the previous section that Co-28Cr-6Mo is significantly harder.

A non-linear kinematic hardening (NLKH) model is employed here to model the *Bauschinger* effect in the titanium alloys. It has been presented in Chapter 4.

Fretting wear and fatigue methodologies have been described in Chapter 4 as well.

Hip implants can generally operate successfully for between 15 and 20 years. After a hip replacement, patients are advised to avoid high impact activities such as running and basketball. Here, attention is focused on the 10 year performance of a hip joint in a normal weight person (75 kg), for a medically recommended, moderately intense walking: 30 min per day and 50 gait cycles per minute. This results in 5.5×10^6 wear cycles. A cycle jump ΔN of 5×10^4 is used based on previous sensitivity studies and also due to a compromise with computational cost. Each simulated tangential fretting cycle is discretised into 100 equal increments. For simplicity, only the stem surface is assumed to wear since the head material in this work is much harder than the stem material.

7.2.3 2D FE submodel for fretting wear and fatigue in hip implants

On a macroscopic scale, the stem and cap surfaces are flat. However, on a microscopic scale, surface roughness undulations are employed to accentuate the frictional contact for an enhanced mechanical locking effect, as shown in Fig. 7.2.

A microscale sub-model of one segment (a nub-surface contact) of the repetitive undulations is developed for fretting wear and fatigue computation, with the nub-surface

contact assumed to be a Hertzian contact (see Fig. 7.3 with given boundary conditions). Previously Zografos et al. 2009 used submodelling technique in bolted connections. The geometry of the cylindrical surface in the model is based on the measurement in Fig. 7.2. 2D, four noded, quadrilateral, plane strain elements are adopted. Fig. 7.4 shows the mesh and loading condition. A detailed mesh convergence study has been carried out. The mesh in the contact region is highly refined (1 μm width for the smallest element). Forged Ti64 is adopted in this model.

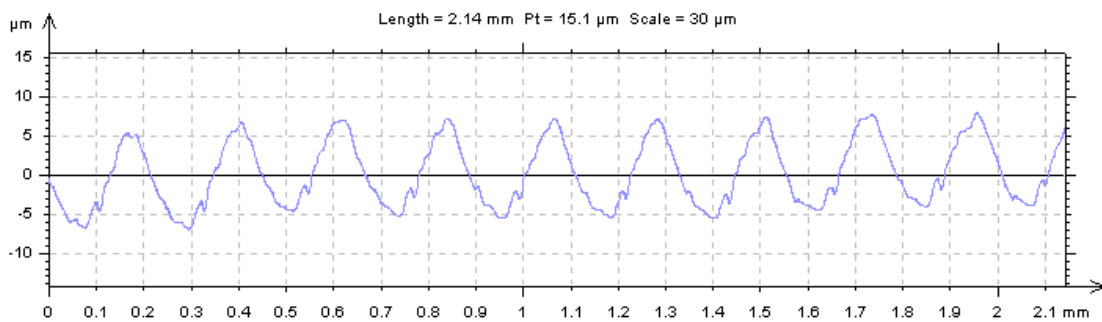


Fig. 7.2 Measured surface undulations on femoral cap inner contact surface.

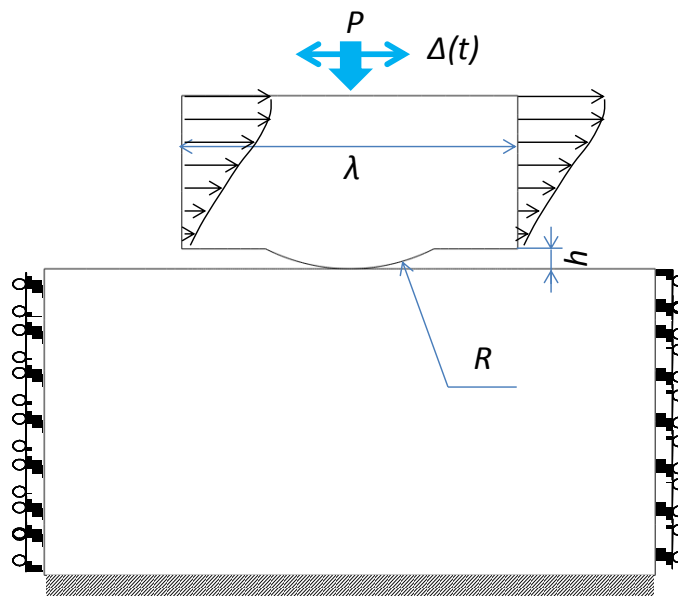
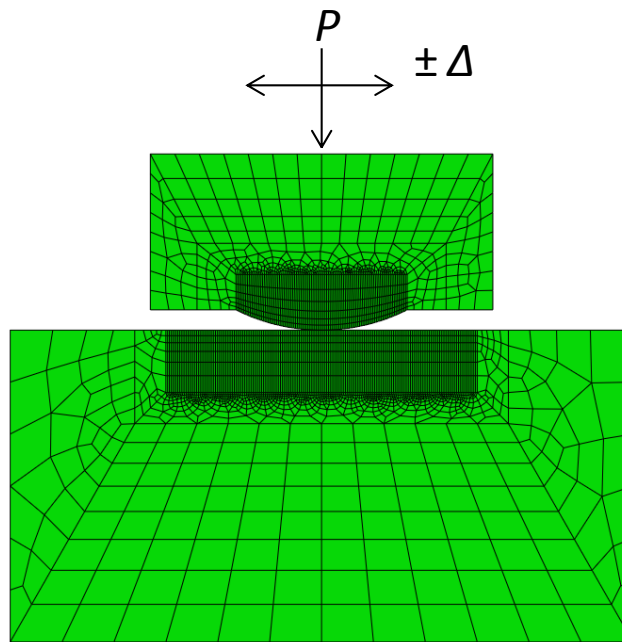
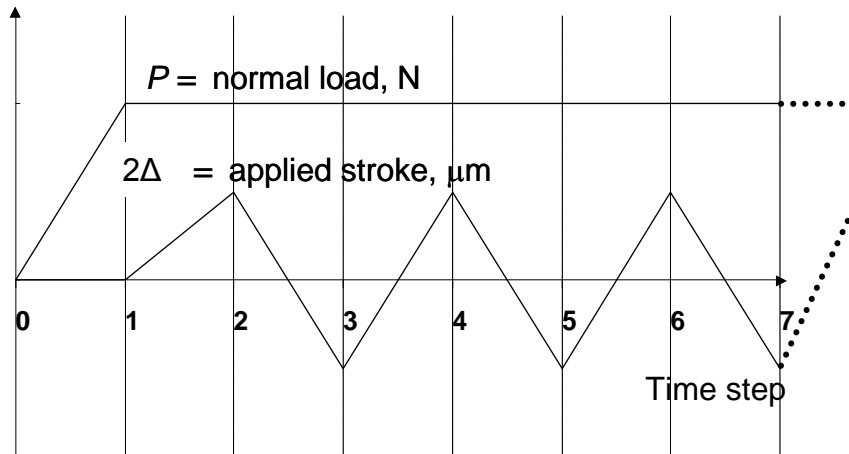


Fig. 7.3 Measured surface undulations on femoral cap contact surface. (Where the segment width $\lambda = 0.220$ mm, height of the nub $h = 0.013$ mm, radius of the cylindrical surface $R =$

0.123 mm) (Nodes on the side edges of cylindrical pad at the same vertical position are constraint to move the same in x direction)



(a)



(b)

Fig. 7.4 (a) 2D FE sub-model of stem-head contact (b) Loading history

Two sample locations which are most likely to be the hot spots (maximum SWT values) are selected for sub-modelling - the bottom contact edge ($z \approx 2$ mm) and the top contact edge ($z \approx 18$ mm) in Fig. 7.1a. The normal load can be calculated using the following equation (Ding et al., 2009):

$$P_{sub} = \lambda p(x) \quad (7.1)$$

where P_{sub} is the normal load applied for a certain submodel and $p(x)$ is the local contact pressure reported from the global model. The half-stroke Δ is adopted using the local slip amplitude $s(x)$ reported from the global model. Two sets of loading conditions representing the bottom contact edge ($z \approx 2$ mm) and the top contact edge ($z \approx 18$ mm) in Fig. 7.1a are adopted for submodelling. More details of the loading conditions are described in section 7.3.3.

The fretting wear-fatigue methodology used for submodelling is the same as described previously in this section, with the implementation of the modified wear-fatigue algorithm described in Section 4.4.2.

7.3 Results and discussion

7.3.1 Analytical validation of 2D axisymmetric model

When a press fit force is applied to the femoral head, an interference fit pressure is generated. The solution can be analytically calculated based on (Burr & Cheatham, 1995). As shown in Fig. 7.5, a tapered cylinder is pressed by Δh to give a prestress to the inner surface. The pressure p_f generated at the inner surface for a certain cross section x is expressed implicitly as

$$\frac{p_f n^3}{E_2(q^2 - n^2)} [1 - \nu_2 + (1 + \nu_2) \frac{q^2}{n^2}] + \frac{p_f n}{E_1} [1 - \nu_1] = \Delta h \tan \theta \quad (7.2)$$

where n , q and θ are geometrical parameters and ν_1 , ν_2 , E_1 and E_2 are material properties for the two contacting components.

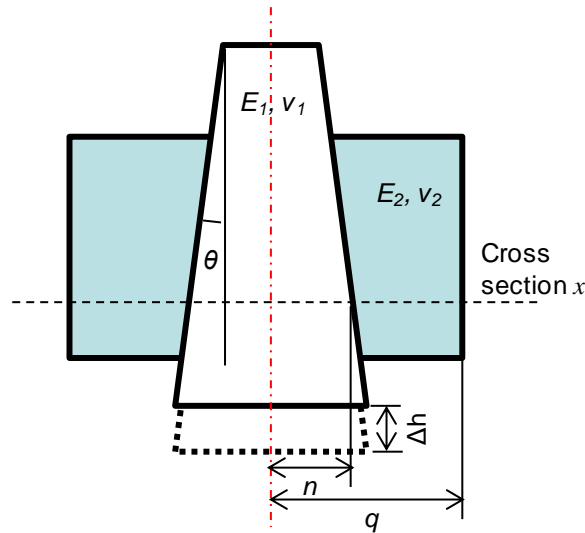


Fig. 7.5 Schematic of typical assembly with interference fit

Comparison of p_f is made between FE analysis and analytical calculation, as shown in Fig. 7.6. Good agreement is obtained for sample locations except for contact edges, where analytical solution is not capable of predicting the singularity effect.

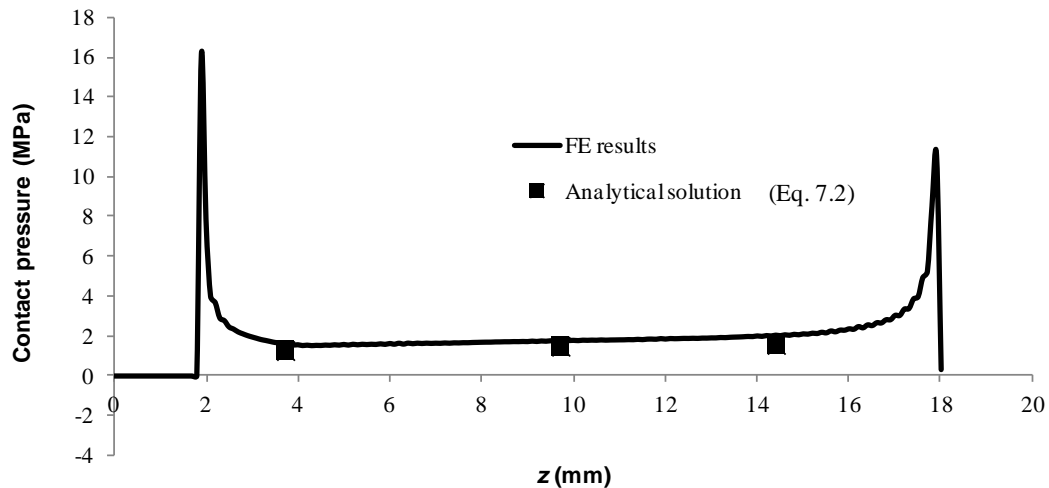
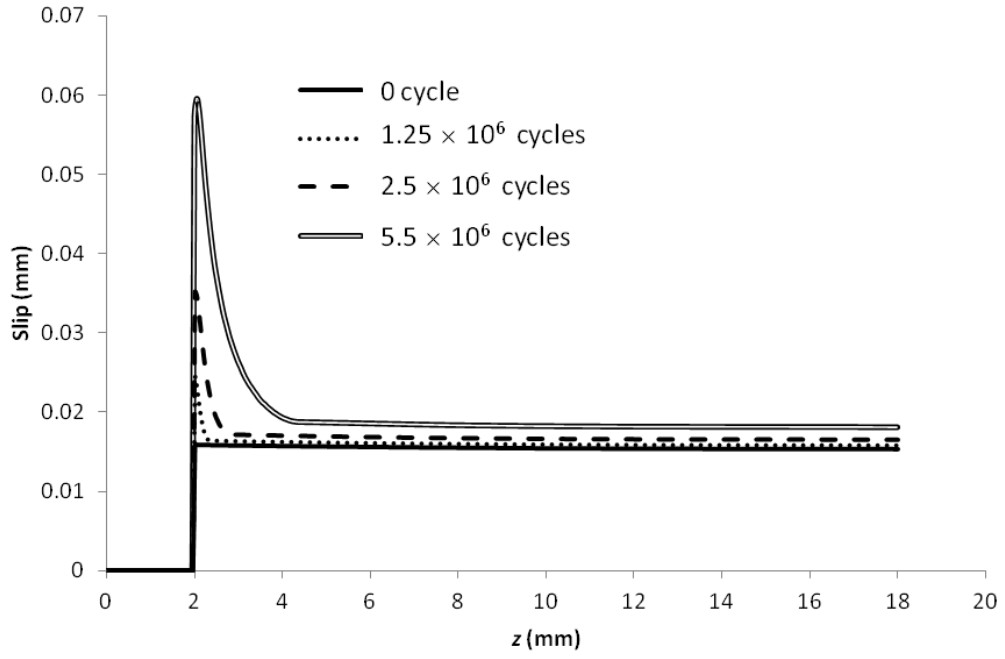


Fig. 7.6 Typical assembly with interference fit

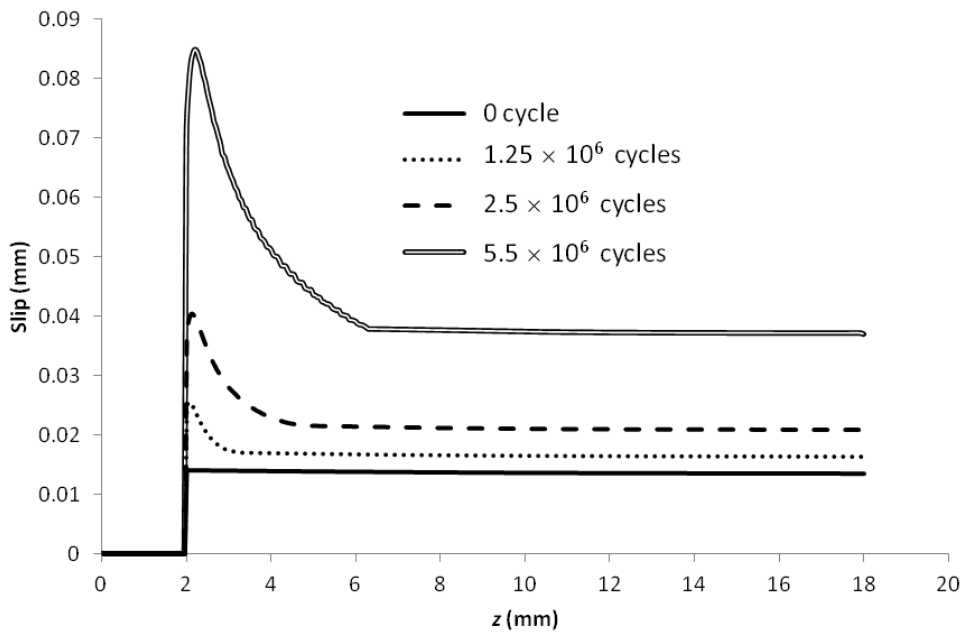
7.3.2 FE wear and fatigue results for global model

Ten years of operation of a prosthetic hip implant is simulated here for the FE model of Fig. 7.1a. Wear coefficients and COFs are adopted from the test (Chapter 5) results above: for CoCr/DMLS Ti64 the wear coefficient is $4.16 \times 10^{-8} \text{ MPa}^{-1}$ and the COF is 0.52; for CoCr/forged Ti64 the wear coefficient is $0.99 \times 10^{-7} \text{ MPa}^{-1}$ and the COF is 0.57.

Fig. 7.7a and b show relative slip evolution due to wear along the contact surface z direction shown in Fig. 7.1a. Significantly greater slip is predicted to occur on the root side of the stem surface (near $z = 2 \text{ mm}$) for both DMLS Ti64 and forged Ti64. A large gradient of slip occurs at ($2 \text{ mm} < z < 4 \text{ mm}$) for DMLS Ti64 and ($2 \text{ mm} < z < 6 \text{ mm}$) for the forged Ti64. Relative slip overall is predicted to increase due to wear and reach a peak value of $60 \mu\text{m}$ for DMLS Ti64 and $86 \mu\text{m}$ for forged Ti64 after 5.5×10^6 cycles.



(a)

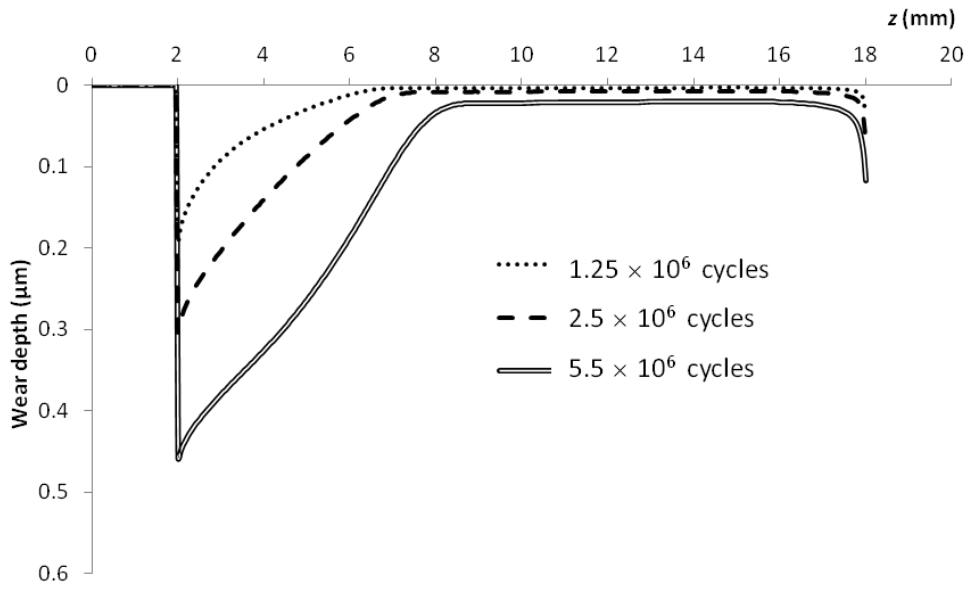


(b)

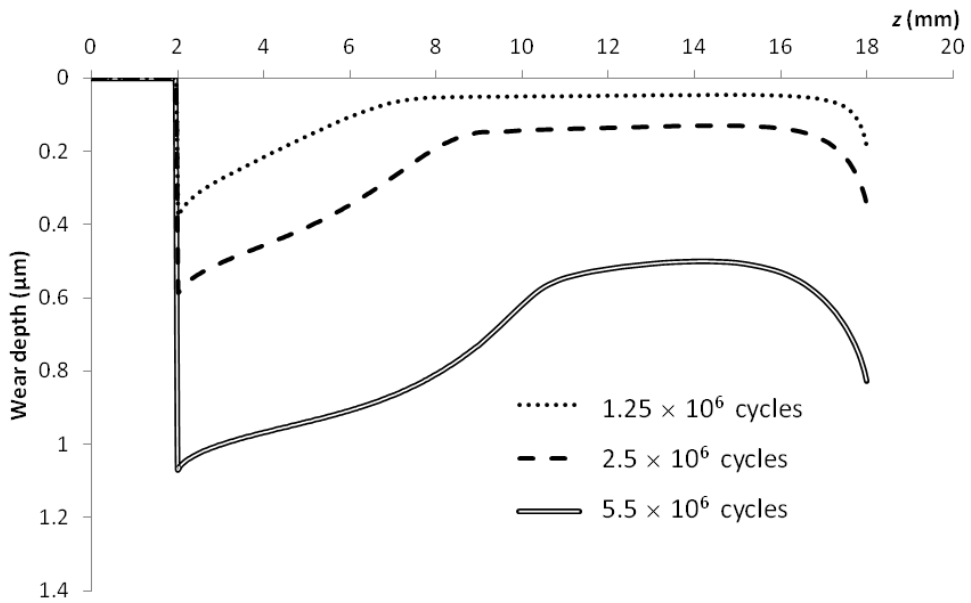
Fig. 7.7 Predicted slip evolution on stem neck surface from model of Fig. 7.1a for (a)

DMLS Ti64 and (b) Forged Ti64.

Figs. 7.8a and b show FE-predicted wear depth evolutions for the CoCr cup/DMLS Ti64 stem and the CoCr cup/forged Ti64 stem along the contact surface z direction. The maximum predicted wear depth the DMLS Ti64 is only $0.45 \mu\text{m}$ while it is $1.07 \mu\text{m}$ for the forged Ti64. The ratio of the two peak wear depth values is 2.37 which is consistent with the wear coefficient ratio for the two material combinations. The predicted depth for both materials is more severe on the root side of the stem (near $z = 2 \text{ mm}$) where higher relative slip is predicted relative to the top of the stem. The contact edges (near $z = 2 \text{ mm}$ and $z = 18 \text{ mm}$) are predicted to have higher wear than the central contact region ($8 \text{ mm} < z < 16 \text{ mm}$) since the edges experience higher contact pressure than the central contact region. The forged Ti64 is also predicted to evolve to a more uniform (deeper) wear scar along the stem surface, ostensibly due to the higher α and COF values. The DMLS Ti64 case is predicted to retain a slip regime quite close to that of partial slip with a significant gradient in slip and hence wear at approximately $2 \text{ mm} < z < 8 \text{ mm}$.



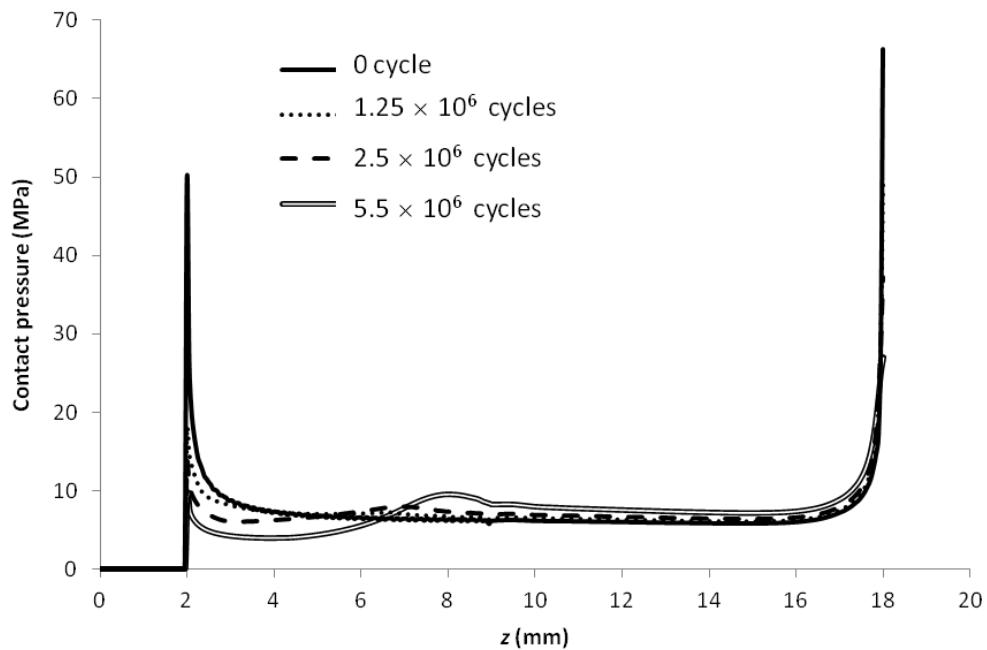
(a)



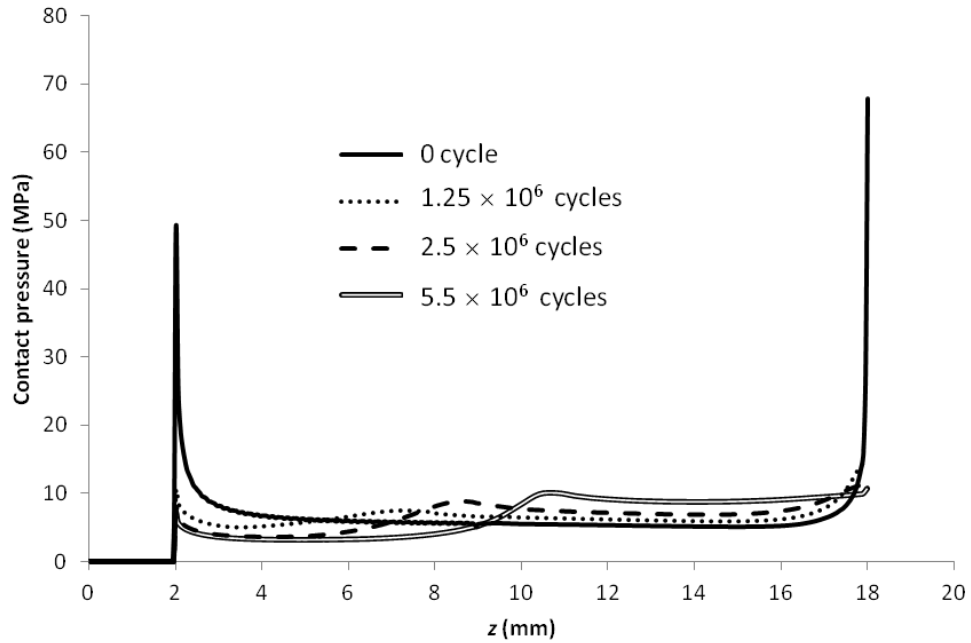
(b)

Fig. 7.8 Predicted wear depth evolution on stem neck surface from model of Fig. 7.1a for (a) DMLS Ti64 and (b) Forged Ti64.

Figs. 7.9a and b show the concomitant changes of contact pressure due to wear for CoCr cup/DMLS Ti64 stem and CoCr cup/forged Ti64 stem along the contact surface z direction. Peak contact pressures for both arrangements start from a value of 68 MPa at the top edge of the stem neck and drops to around 28 MPa for CoCr cup/DMLS Ti64 stem and 10 MPa for CoCr cup/forged Ti64 stem. Peak values of contact pressure drop significantly for other locations for both arrangements and new local peaks occur for each case near the centre of the contact length. Overall wear is beneficial in terms of fatigue loading in that it reduces the singularity effect of 'punch on flat' contact and eventually produce a much more uniform pressure distribution.



(a)



(b)

Fig. 7.9 Predicted contact pressure evolution on stem neck surface from model of Fig. 7.1a for (a) DMLS Ti64 and (b) Forged Ti64.

The predicted critical-plane SWT values are low for both CoCr/DMLS Ti64 and CoCr/forged Ti64. Fig. 7.10 shows the FE-predicted critical-plane SWT distributions for the early cycles for the forged Ti64 stem along the contacting sub surface of the stem neck. The peak SWT value here is predicted to be 0.0026 MPa which corresponds to a predicted N_i of $\gg 10^8$ cycles. The peak SWT value is predicted to level off and slight redistribution occurs due to wear. Therefore it is clear that fretting fatigue problems are not predicted to occur in this representative simulation, similarly for the CoCr cup/DMLS Ti64 stem arrangement. This also suggests that for simulations include the effect of wear or without wear, fatigue life predictions will give similar results. However, Fig. 7.10 also shows a significant gradient of SWT at the bottom contact edge (near $z = 2$ mm). This is due to the sharp edge configuration. To reduce the FIP gradient, it is recommended that rounded corners are adopted.

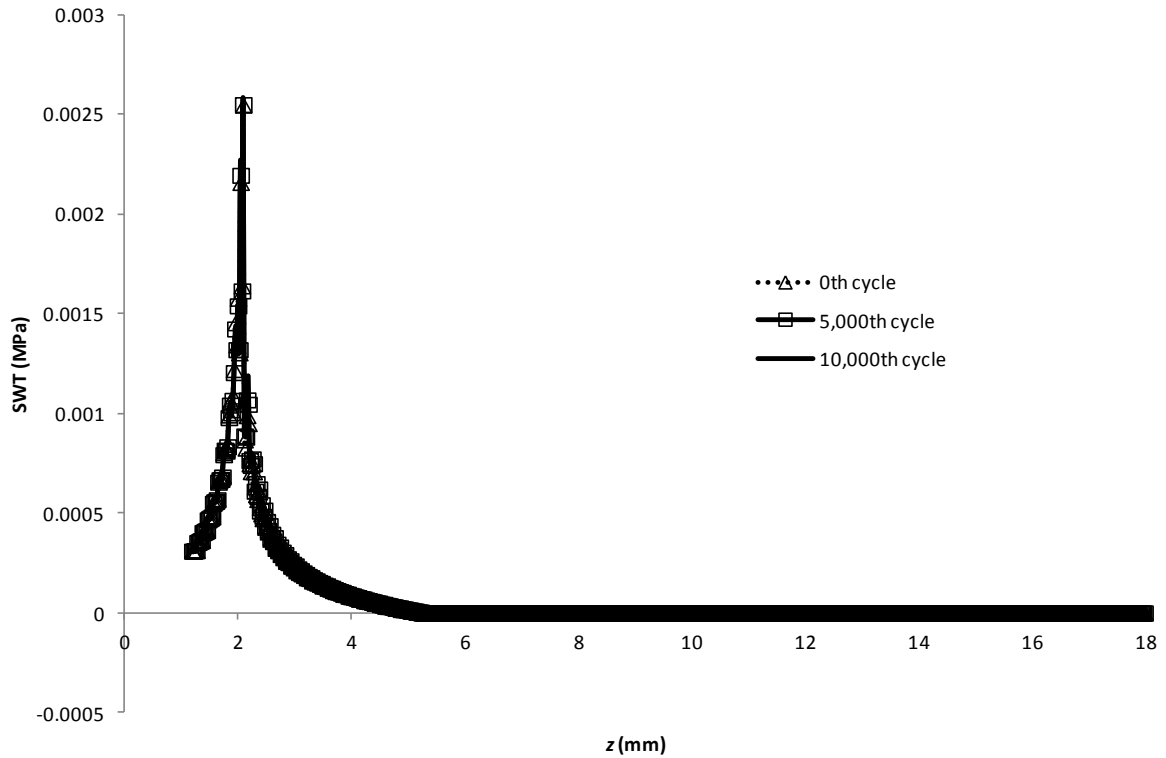


Fig. 7.10 Predicted SWT initial distribution for stem-head coupling along the contacting surface.

7.3.3 FE wear and fatigue results for submodel

Table 7.1 shows the two sets of loading conditions representing the bottom contact edge ($z \approx 2$ mm) and the top contact edge ($z \approx 18$ mm) in the global model. P_{sub} is the normal load applied for a certain submodel and based on the value of $p(x)$ which is reported from the global model (see Fig. 7.9). The half-stroke Δ is calculated based on the local slip amplitude $s(x)$ reported from the global model. Fig. 7.11 shows two slip distributions at the beginning of a cycle and after a quarter of a cycle, the difference is then sample Δs for submodels at each z location. Slip data is also collected for a half of a cycle, three quarters of a cycle and the end of a cycle. Averaged Δ is then given in Table 7.1.

Table 7.1 Submodel loading conditions

Contact Position	P_{sub} (N/mm)	Δ (μm)
Bottom contact edge ($z \approx 2$ mm)	10.73	0.27
Top contact edge ($z \approx 18$ mm)	14.93	0.02

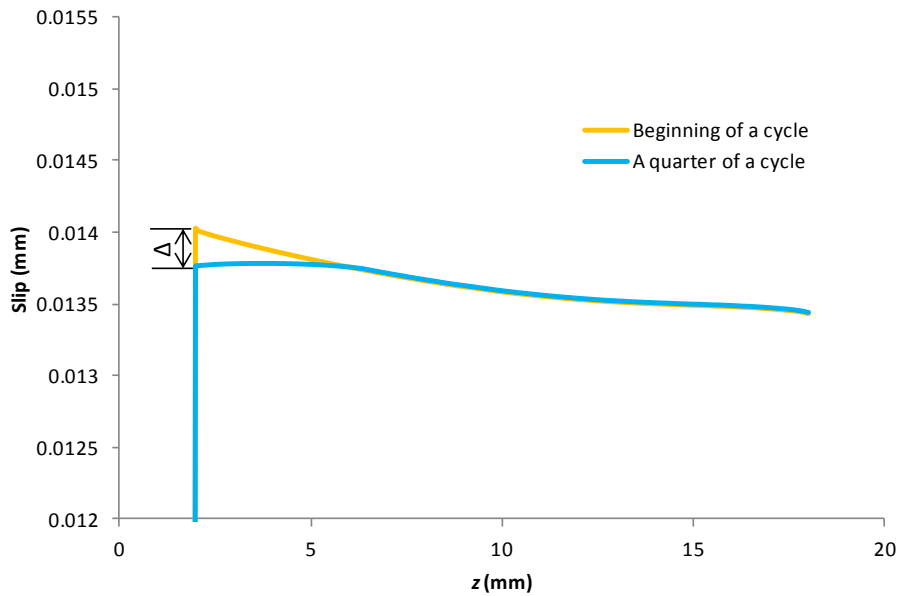
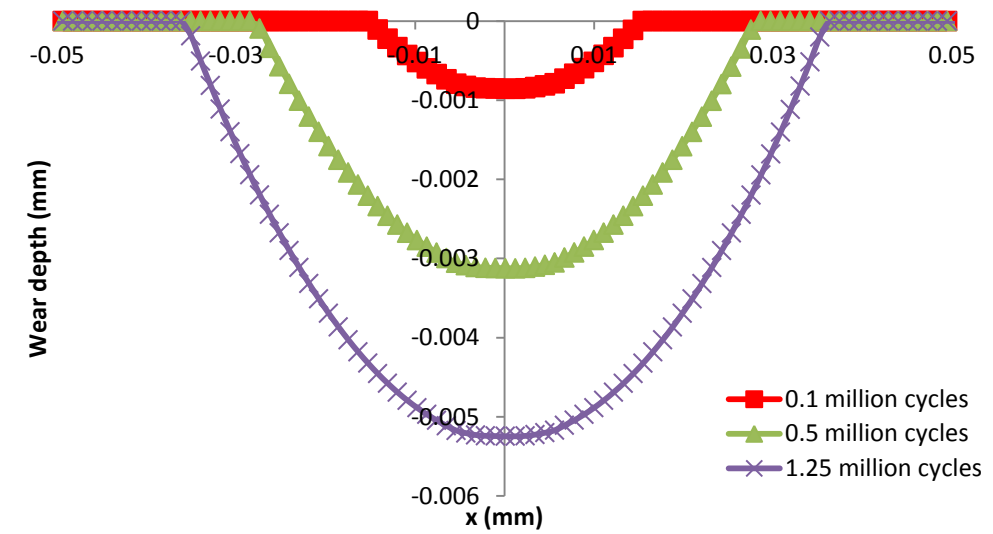


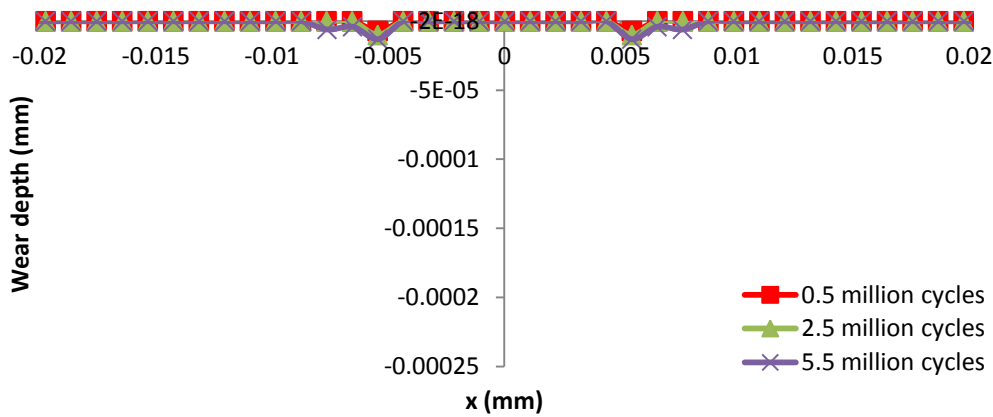
Fig. 7.11 Predicted slip distributions on stem neck surface from model of Fig. 7.1a at the beginning of a cycle and at a quarter of a cycle.

Fig. 7.12a and b show FE-predicted wear depth evolutions for the CoCr cup/forged Ti64 stem at two global contact locations - the bottom contact edge ($z \approx 2$ mm) and the top contact edge ($z \approx 18$ mm) in Fig. 7.1a, respectively. Fig. 7.12a shows that at the bottom contact edge it is a typical gross slip case. Wear in the submodel is significantly more compared to the global model - with maximum wear depth of $5.2 \mu\text{m}$ in the submodel and $0.4 \mu\text{m}$ in the global model after 1.25×10^6 cycles, for the bottom contact edge position. This may be attributed to the consideration of the micro undulations which cause more local pressure concentration and more frictional energy that helps material removal. Fig. 7.12b shows the wear evolution for the top contact edge in Fig. 7.1a. A typical partial slip

distribution is predicted. No significant wear is predicted since the relative slip in this location is initially very small ($0.02 \mu\text{m}$). Fig. 7.13 shows a comparison of wear depth profiles after 0.1 million cycles between two global contact locations ($z \approx 2 \text{ mm}$ and $z \approx 18 \text{ mm}$) using submodelling. Negligible wear is found at $z \approx 18 \text{ mm}$ compared with that at $z \approx 2 \text{ mm}$.



(a)



(b)

Fig. 7.12 Predicted wear depth evolution for two global contact locations in submodel: (a) the bottom contact edge ($z \approx 2 \text{ mm}$) and (b) the top contact edge ($z \approx 18 \text{ mm}$) in Fig. 7.1a.

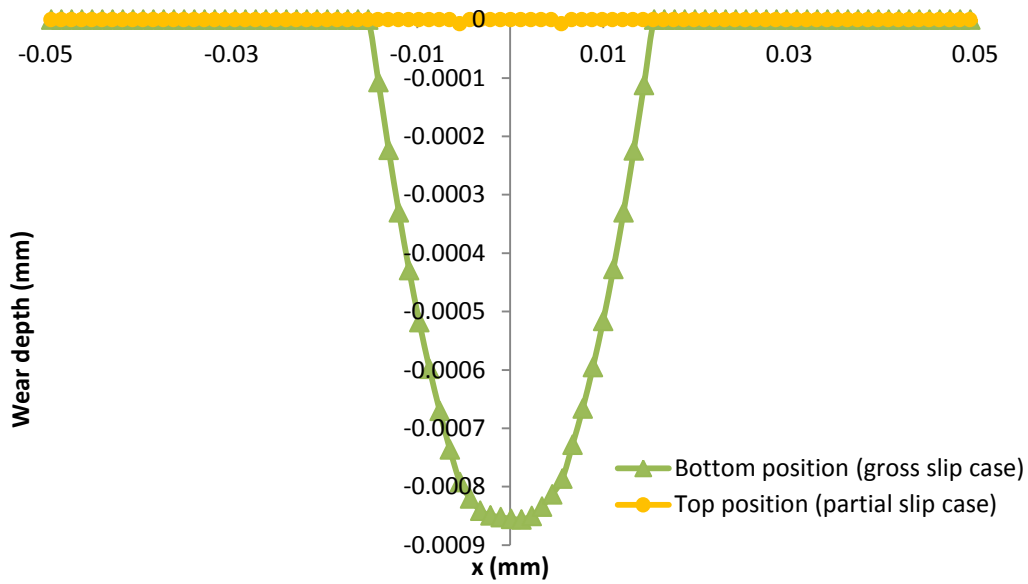
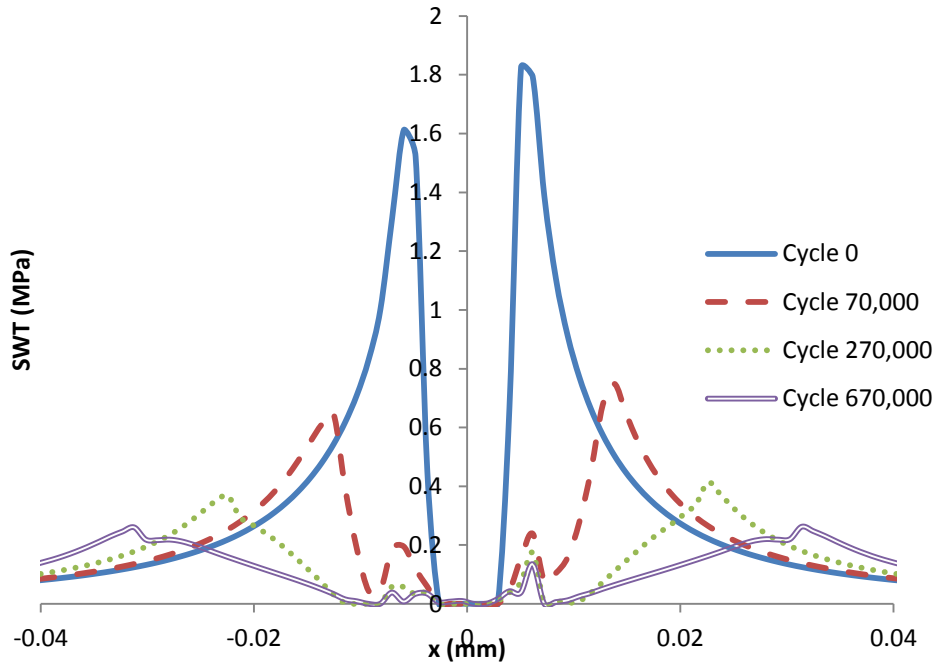
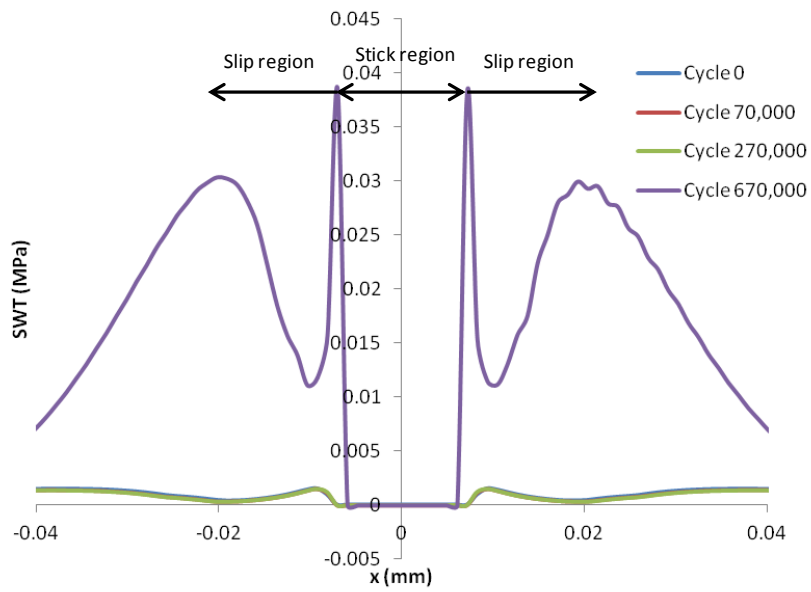


Fig. 7.13 Comparison of predicted wear depth after 0.1 million cycles for two global contact locations in submodel: (a) the bottom contact edge ($z \approx 2$ mm) and (b) the top contact edge ($z \approx 18$ mm).

SWT evolutions for the two contact locations are shown in Fig. 7.14. Fig. 7.14a shows that at the (global) bottom contact edge, peak SWT values is initially relatively high (≈ 1.83 MPa, corresponding to the micro cracking initiation to be 6.6×10^5 cycles) and drops significantly after 270,000 cycles. Fig. 7.14b shows the peak SWT values at the (global) top contact edge is low through all the 670,000 cycles. The submodelling shows the same trend with the global modelling that SWT values are high at the bottom contact edge region ($z \approx 2$ mm) and low at the top bottom contact edge region ($z \approx 18$ mm), with the submodelling magnifies SWT values in both region due to the consideration of micro undulations.



(a)



(b)

Fig. 7.14 Predicted SWT evolution for two global contact locations in submodel: (a) the bottom contact edge ($z \approx 2$ mm) and (b) the top contact edge ($z \approx 18$ mm) in Fig. 7.1a.

Fretting fatigue life distribution for case ($z \approx 2$ mm) is shown in Fig. 7.15. It shows that at the (global) bottom contact edge, lowest micro cracking initiation predicted is 8.9×10^7 cycles. This is due to the consideration of wear on fretting fatigue life, which redistributes the stresses and changes SWT values constantly (recall the micro cracking initiation is only 6.6×10^5 cycles without considering wear). For case ($z \approx 18$ mm), due to constant low SWT values all along the contact surface, micro cracking initiation is not predicted after 10^8 cycles.

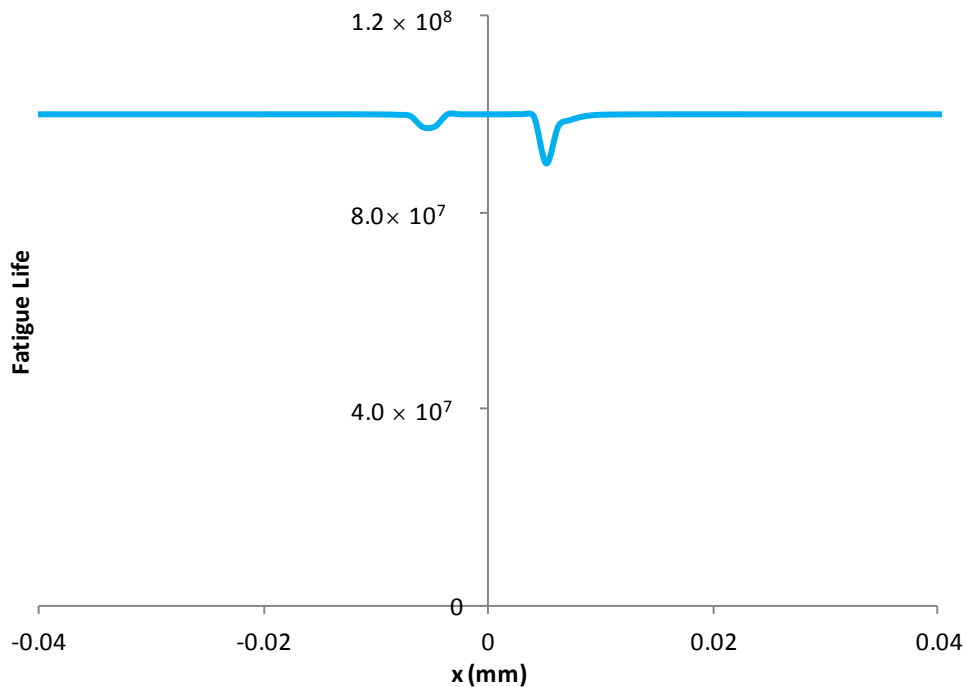


Fig. 7.15 Predicted fretting fatigue life along the contacting surface for two global contact locations in submodel at the bottom contact edge ($z \approx 2$ mm).

A comparison of the maximum wear depth and number of cycles to cracking initiation between the global model and submodel is shown in Table 7.2. The maximum wear depth of the submodel is estimated using the fit curve shown in Fig. 7.16. Wear in the submodel is predicted to be much more after 5.5 million cycles than in the global model. Cracking

initiation is predicted to be much greater than 10^8 cycles in the global model, with or without the effect of wear. Micro-cracking in the submodel is predicted to occur very early, after 6.6×10^5 cycles without wear, and after 8.9×10^7 cycles with wear.

Table 7.2 Comparison of maximum wear depth and cracking initiation between global model and submodels (forged Ti64 stem)

Models	Maximum wear depth (μm)	Cracking initiation cycles (no wear)	Cracking initiation cycles (with wear)
Global model	1.07	$\gg 10^8$	$\gg 10^8$
Submodel	7.56	6.6×10^5	8.9×10^7

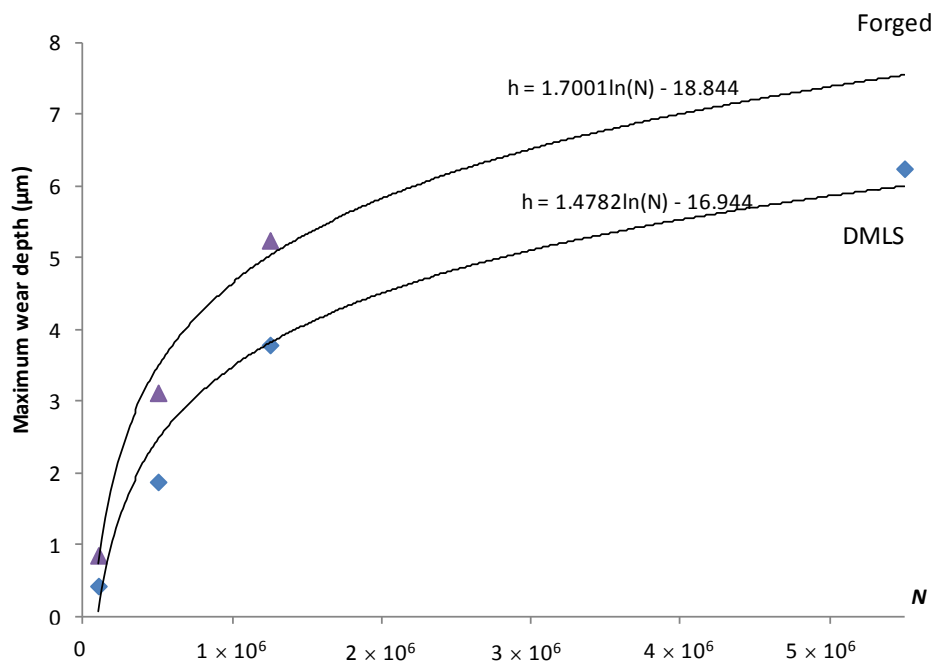


Fig. 7.16 Comparison of micro-scale predicted Ti64 maximum wear depth versus cycles.

7.3.4 Discussion

Fretting corrosion tests have very recently been reported by Hallab, (2011) on a modular hip implant which adopts a Co-alloy femoral head (Zimalloy™, Zimmer, Inc., Warsaw, IN). As shown in Fig. 7.17, no observable damage at low magnification is found on the femoral head inner surface, but at high magnification slight degradation (fretting

corrosion/abrasion) of some of the ridges within the taper is observed. Note that in the test (Hallab, 2011) observations are conducted after 5×10^6 cycles, and in the simulation here, micro crack initiation is predicted at the $\sim 10^7$ level (it also should be noted the loads used in the two are different (maximum load 2058 N in Hallab, 2011)).

As reported by National Health Service (UK), a modern artificial hip joint is designed to last for at least 15 years (N.H.S., 2012), which is about 8.25×10^6 cycles corresponding to a general moderately intense daily service for a normal weight person. The predicted cycles to crack initiation in this work 8.9×10^7 , which suggests that the type of hip implant modelled here satisfies the requirement recommended by NHS. However, in some extreme cases, e.g. overweight people or people who enjoy intense activities, a smaller number of cycles for crack initiation could be expected and could very well be a competitive number to the NHS recommendation.

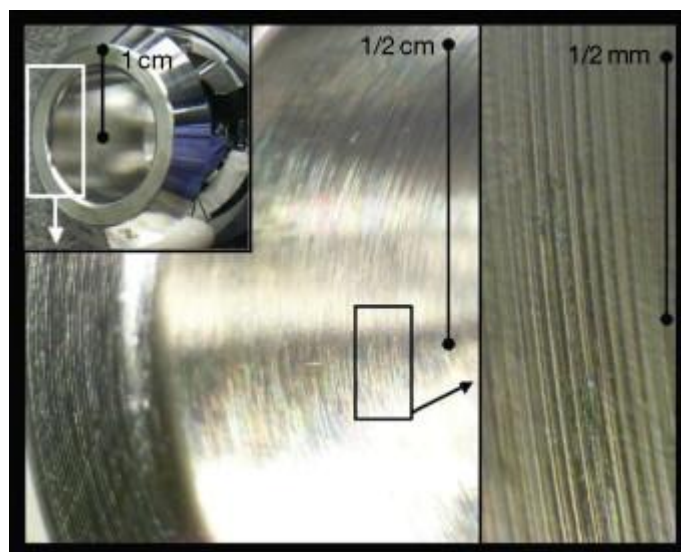


Fig. 7.17 Photographs showing the inside of the modular connection of a Co-alloy femoral head (Zimalloy™, Zimmer, Inc., Warsaw, IN) after fretting corrosion testing for 5×10^6 cycles (Hallab, 2011).

DMLS Ti64 stem is not simulated in submodels, but a better fretting wear and fatigue performance is expected since DMLS Ti64 has been proven to be harder, more wear resistant and has a smaller number of COF in previous studies.

7.4 Conclusions

A scientific approach using multi-scale models for fretting wear-fatigue prediction and design in a prosthetic hip implant is presented. Global modelling is carried out for two material combinations: Co-28Cr-6Mo/DMLS Ti-6Al-4V and Co-28Cr-6Mo/forged Ti-6Al-4V. The wear resistance of the DMLS Ti-6Al-4V is seen to be superior to that of forged Ti-6Al-4V. Submodelling is carried out to investigate the effect of micro-undulations on the femoral head inner surface.

- A fretting wear-fatigue global model is developed for the stem-head contact. The predicted wear depths for both DMLS and forged Ti64 for 10 years normal operation are about 1 μm with DMLS Ti64 giving superior predicted wear performance.
- For both material combinations the taper-lock assembly is predicted to have infinite ($> 10^8$ cycles) fretting fatigue life in the global model.
- For forged Ti64 stem surface, micro-cracking is predicted at the root side of the stem neck ($z \approx 2$ mm) in the submodel with consideration of micro undulations.
- Surface undulation is necessary to be simulated. Without considering the undulations, the effect of wear on crack initiation time is negligible and number of cycles to crack initiation is large ($\gg 10^8$) for forged Ti64 stem; however, when undulations are taken into consideration, wear is predicted to play an important role in micro-crack initiation life, e.g. without wear it is 6.6×10^5 cycles and with wear 8.9×10^7 cycles. This shows reasonable agreement to the work done by Hallab (2011). DMLS Ti64 is

expected to have better fretting wear and fatigue performance due to its larger hardness, smaller COF and wear coefficient.

Chapter 8

Conclusions and Future Work

8.1 Conclusions

This thesis has presented the development and validation of methodologies for fretting fatigue, wear and wear-fatigue interaction in simple and complex engineering contacts, with particular application to taper-lock assemblies in modular hip implants.

Two types of fatigue perspectives have been considered: one based on strain-life multiaxial fatigue relationships, namely the critical plane *SWT* approach, and the other on nonlinear continuum damage mechanics. The NLCD model has been applied to both plain (for unnotched and V-notched specimens) and fretting fatigue, and validated against experimental data (Military Handbook, 1998; Jin and Mall, 2004). It has been shown to be a robust and efficient numerical method in elastic, low wear conditions. Furthermore, a pick-up of fretting fatigue life for gross slip condition is predicted in the NLCD model, which shows that it has the capability of predicting the effect of slip amplitude on fretting fatigue lives even without including wear. Critical plane *SWT* approach has been compared with the NLCD model and good agreement is achieved. Since critical plane *SWT* approach is a post process which is not coupled with the FE simulation, it is significantly less computational costly. Therefore in chapters 4 to 7, critical plane *SWT* approach is adopted mainly for fretting fatigue calculations.

A finite element based energy wear simulation method has been developed and validated for Ti-6Al-4V material. The method has been combined with (i) a critical-plane

multiaxial fatigue prediction method for crack nucleation using the *SWT* fatigue parameter and (ii) non-linear kinematic hardening model for cyclic plasticity. Energy-based wear approach has been compared with Archard approach and validated against published experimental data (Ding et al., 2009). Similar results are shown for both wear approaches. Plastic ratchetting phenomenon is predicted and shown to be a powerful tool to estimate failure, since the lives predicted are competitive with those by fatigue models.

Two fretting configurations, a round on flat and a rounded punch on flat, have been developed for a comparative investigation on the effect of contact geometry on fretting wear, fatigue and cyclic plasticity (ratchetting) performance for a given normal load and space envelop and across a range of applied strokes. As for wear performance, under partial slip regime the round on flat geometry can sustain a stabilised partial slip solution with an associated wear pattern whereas the rounded punch on flat (incomplete) geometry is predicted to stick, resulting in no predicted wear; above gross slip threshold, the predicted wear scars in the rounded punch on flat is of uniform depth whereas the round on flat scar is more U-shaped, of larger maximum depth. The wear volume is larger for the rounded punch. As for fatigue performance, rounded punch on flat is overall superior. However, when stroke is above a certain value, the two may perform similarly. These suggest that when designing bearing, shaft-hubs and spline couplings, etc., RPF seems to be a safer choice generally in terms of fatigue life, but with more wear debris emission if it is a gross slip case.

Tribological and profilometry experimental tests are carried out on two combinations of biomedical materials for prosthetic hip implants - CoCr/DLMS Ti64 and CoCr/forged Ti64. The hardness and wear resistance of the DMLS Ti-6Al-4V are seen to be superior to those of forged Ti-6Al-4V. This suggests a material preference for medical device companies when choosing Ti64s.

Global and sub models are built for fretting wear-fatigue prediction in a prosthetic hip implant. It shows that CoCr/DMLS Ti64 combination performs much better in terms of wear than CoCr/forged Ti64 combination. The root side of the stem neck is normally more susceptible to fretting damage therefore attention should be paid to this region, e.g. introducing a further clamping force to minimize slip thus reduce wear. Surface undulations included in the submodels significantly reduce fretting fatigue lives, and suggests a more rapid wear rate than the flat surface assumption. Hallab (2011) also shows similar test results, where under a microscopic view some abrasion on the ridges (nub) between the machined grooves is observed after 5×10^6 cycles. The damaged ridges on contacting surfaces could potentially migrate into the other regions of the body cause infection or induce crack propagation. Therefore the consideration of surface undulations is conservative and safe for hip implant design.

8.2 Future work

8.2.1 Tribological parameter improvement

The fretting wear-fatigue methodology used in this work adopts a constant COF and a constant wear coefficient throughout the analysis. This is acceptable for materials whose tribological parameters perform stably for most of the fretting cycles (e.g. Fig.5.8). However, COF and wear coefficient may depends on parameters like contact pressure, slip amplitude and number of cycles. To be more accurate, more challenging experimental work needs to be carried out to determine the instantaneous local COF and wear coefficient, and input them to FE analysis as variables.

8.2.2 Simulation of real pressure armour layers in flexible risers

The effect of contact geometry has been studied by comparing a round on flat with a rounded punch on flat configuration and recommendations have been made. However, for complex geometries like pressure armour layers with spirally wounded surface profiles under multiaxial loading conditions like bending, compression and torsion, it is recommended that the realistic simulation could be carried out using the wear-fatigue methodology presented here.

8.2.3 Combining wear-fatigue methodology

The combination of NLCD model with wear simulation is a thrilling but challenging work. It will allow incremental wear and damage to be monitored instantaneously. However, numerical modifications need to be done to adjust the change of variables in the Lagrangian phase and Eulerian phase during adaptive meshing in UMESHMOTION. It has been mentioned that in fretting wear simulation, in adaptive meshing, mesh in the adaptive zone is incrementally swept and remeshed (Eulerian phase). Fig 8.1 shows the schematic of the process. In a certain increment, surface node A moves due to wear, then in the next increment, adaptive meshing scheme would try to minimize element distortion. It determines the weight function by computing a volume-weighted average of the element centers in the elements surrounding the node. For example, in Fig. 8.1 the new position of node B is determined by a volume-weighted average of the positions of the surrounding element centers. The volume weighting will tend to push the node away from point A, thus reducing element distortion. During this process, Abaqus/Standard applies an explicit method, based on the Lax-Wendroff method, to integrate the advection equation (ABAQUS user's and theory manuals, 1998). Advection of material quantities is found to cause the parameters such

as damage, mechanical properties, etc. to change constantly but wrongly. This results in a problem that the damage accumulation would be incorrect at all times.

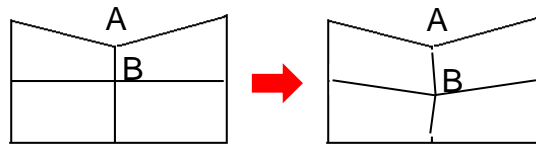


Fig. 8.1 Remeshing in adaptive meshing.

The author would recommend the future work in this field to investigate more about the flow rule in UMESHMOTION and develop a compensation algorithm for flowing of material quantities including damage.

8.2.4 Fretting wear-fatigue tests in hip implants

An FE based fretting wear-fatigue methodology for the taper-lock assembly in prosthetic implants has been developed. Cycles to micro-crack initiation here have been qualitatively compared to Hallab (2011) where CoCr is used and fretting corrosion is mainly concerned. One of the design recommendations here is to introduce extra grip in the bottom contact edge to minimize potential wear. Experimental tests on the real taper-lock assembly using CoCr/Ti64 materials would be helpful to study surface damage, micro crack initiation and propagation, etc.

The author would recommend the future work in this field to carry out fretting wear-fatigue experimental tests on taper-lock assembly for CoCr/forged Ti64 material combination, to validate the simulation results and investigate the potential locations which are susceptible to fretting damage under complex loading conditions.

Also to explicitly carry out submodelling analysis for surface undulations may be addressed.

8.2.5 Design of hip implants

This work has presented a fretting wear-fatigue methodology for taper-lock assemblies in modular hip implants. With respect to hip design, the method here can be applied for parametric feature modelling. For example, stem neck taper angle, upper and bottom radius, material combinations, loading conditions, contact width, etc. can all be evaluated as parameters which can affect wear-fatigue performance of the coupling.

Energy-based wear and critical plane SWT have been used to simulate the fretting wear-fatigue interaction. Due to the conclusion from this work that surface micro undulations play an important role in micro-crack initiation life predictions, future work can simulate this using nonlinear continuum damage mechanics based fretting wear methods which provide a framework of modelling microscopic progressive material degradation, e.g. micro-crack initiation and propagation.

Appendix A1 NLCD model derivations

Fatigue damage is a function of N :

$$D = f(N) \quad (\text{A1})$$

\dot{D} and \ddot{D} for the NLCD model are given by:

$$\dot{D} = [1 - (1 - D)^{\beta+1}]^\alpha \cdot \left[\frac{A_{II}}{M_0 (1 - 3b_2 \sigma_{H,mean}) (1 - D)} \right]^\beta \quad (\text{A2})$$

$$\ddot{D} = \left[\frac{A_{II}}{M_0 (1 - 3b_2 \sigma_{H,mean})} \right]^\beta \cdot \left[\alpha(\beta + 1)(1 - (1 - D)^{\beta+1})^{\alpha-1} + \beta(1 - (1 - D)^{\beta+1})^\alpha (1 - D)^{-(\beta+1)} \right] \cdot \dot{D} \quad (\text{A3})$$

Case 1: Central difference

For the central difference integration scheme, the incremental damage due to a ΔN increment in number of cycles from a damage state after N cycles is given by:

$$D^{(N+\Delta N)} = D^{(N)} + \Delta N \cdot \dot{D}^{(N+\Delta N/2)} \quad (\text{A4})$$

where

$$\dot{D}^{(N+\Delta N/2)} = \dot{D}^{(N-\Delta N/2)} + \Delta N \cdot \ddot{D}^{(N)} \quad (\text{A5})$$

where

$$\dot{D}^{(N-\Delta N/2)} = \frac{\dot{D}^{(N)} + \dot{D}^{(N-\Delta N)}}{2} \quad (\text{A6})$$

Hence

$$D^{(N+\Delta N)} = D^{(N)} + \Delta N \cdot \left[\frac{\dot{D}^{(N)} + \dot{D}^{(N-\Delta N)}}{2} + \Delta N \cdot \ddot{D}^{(N)} \right] \quad (\text{A7})$$

It can be seen that in the central difference scheme, it is necessary to know the present damage value at N and also the damage value from the previous step at $(N-\Delta N)$. The first derivatives (Eq. A2) at N and $(N-\Delta N)$ are necessary to know as well.

Case 2: Backward difference

Eq. 17 can be written as:

$$D^{(N+\Delta N)} - D^{(N)} = \left[1 - (1-D)^{\beta+1}\right]^{\alpha} \cdot \left[\frac{A_{II}}{M_0(1-3b_2\sigma_{H,mean})(1-D)}\right]^{\beta} \Delta N \quad (A8)$$

Rearranging Eq. A8 and letting $F(D^{N+\Delta N})$ be:

$$F(D^{(N+\Delta N)}) = D^{(N+\Delta N)} - D^{(N)} - \left[1 - (1-D)^{\beta+1}\right]^{\alpha} \cdot \left[\frac{A_{II}}{M_0(1-3b_2\sigma_{H,mean})(1-D)}\right]^{\beta} \Delta N \quad (A9)$$

For a converged value of $D^{N+\Delta N}$, we have $F(D^{N+\Delta N}) = 0$.

The derivative of $F(D^{N+\Delta N})$ is given by:

$$F'(D^{(N+\Delta N)}) = \frac{dF(D^{(N+\Delta N)})}{dD^{(N+\Delta N)}} = 1 - \Delta N \cdot \left(\frac{A_{II}}{M_0(1-3b_2\sigma_{H,mean})}\right)^{\beta} \cdot (\alpha(\beta+1) \cdot (1 - (1-D^{(N+\Delta N)})^{\beta+1})^{\alpha-1} + \beta(1 - (1-D^{(N+\Delta N)})^{\beta+1})^{\alpha} \cdot (1 - D^{(N+\Delta N)})^{-(\beta+1)}) \quad (A10)$$

Using the Newton-Raphson method, a converged answer of $D^{(N+\Delta N)}$ can be calculated by iteratively solving the following equation:

$$D_{k+1}^{(N+\Delta N)} = D_k^{(N+\Delta N)} - \frac{F(D_k^{(N+\Delta N)})}{F'(D_k^{(N+\Delta N)})} \quad (A11)$$

where k is the iteration number in Newton-Raphson method. This method is used incrementally in the backward difference integration scheme to calculate the damage value.

The code presented here is UMAT subroutine for coupled NLCD implementation to fretting fatigue analysis:

First the forward difference scheme:

```

*****
** UMAT FOR ABAQUS/STANDARD INCORPORATING ELASTIC BEHAVIOUR FOR PLANE **
** STRAIN AND AXI-SYMMETRIC ELEMENTS. **
*****
**
**
**
*USER SUBROUTINE
  SUBROUTINE UMAT(STRESS,STATEV,DDSDDE,SSE,SPD,SCD,
    1 RPL,DDSDDT,DRPLDE,DRPLDT,
    2 STRAN,DSTRAN,TIME,DTIME,TEMP,DTEMP,PREDEF,DPRED,CMNAME,
    3 NDI,NSHR,NTENS,NSTATV,PROPS,NPROPS,COORDS,DROT,PNEWDT,
    4 CELENT,DFGRD0,DFGRD1,NOEL,NPT,LAYER,KSPT,KSTEP,KINC)
  C
  INCLUDE 'ABA_PARAM.INC'
  C
  CHARACTER*80 CMNAME
  C
  C
  DIMENSION STRESS(NTENS),STATEV(NSTATV),
    1 DDSDDE(NTENS,NTENS),DDSDDT(NTENS),DRPLDE(NTENS),
    2 STRAN(NTENS),DSTRAN(NTENS),TIME(2),PREDEF(1),DPRED(1),
    3 PROPS(NPROPS),COORDS(3),DROT(3,3),DFGRD0(3,3),DFGRD1(3,3)
  C
  C
  Real   cyc, E0, Sdash,Nii,b, Nf, D, Smax, deltaD ,strmax
  Real   trSmax,strmin,trSmin,Sde11max, Sde11min
  Real   Sde22max,Sde22min,Sde33max,Sde33min,Sde12max
  Real   Sde13max,Sde13min,Sde23max,Sde23min,Svonmax,TRmax
  Real   TRmin,Sde12min
  Integer i,j,nmax
  PARAMETER (M=3,N=3,ID=3,ZERO=0.D0,ONE=1.D0,TWO=2.D0,THREE=3.D0,
+   SIX=6.D0, NINE=9.D0, TOLER=0.D-6)
  C
  DIMENSION DSTRESS(4), DDS(4,4)
  C
  C
  C
  C
  C-----
  C
  C SPECIFY MATERIAL PROPERTIES
  C
  C
  C Write output headings
  OPEN(unit=32,file='c:\damage1\sb50Elary.txt',status='unknown')

OPEN(unit=31,file='c:\damage1\sb50try.txt',status='unknown')

OPEN(unit=30,file='c:\damage1\sb50try1.txt',status='unknown')
  IF ((KSTEP == 1) .AND. (KINC == 1) .AND.
    & (NOEL == 6055) .AND. (NPT == 3))THEN

WRITE(32,*)'Step NO./Cycle NO./INC NO./Stress/D/Equivalent strain/'
endif

  C SPECIFY MATERIAL PROPERTIES

```

```

Sdash = 1817.2
b = -0.0978
  PROPS(1) = 116000.0
PROPS(2) = 0.34
PROPS(3) = 1040.0
E0 = PROPS(1)
XNUE = PROPS(2)
Su = PROPS(3)
SIO = 358.0
beta = 1.79
b1 = 0.00013
b2 = 0.00055
aM0beta = 1.79e-11
a = 0.6
c M0 = 859399.0
  M0 = (aM0beta/a)**(-1.0/beta)
C
C
  cyc = int((KSTEP-1)/4)+1

Nf = STATEV (1)
D = STATEV (2)

straeq = STATEV (3)
E = STATEV (4)
TRmean = STATEV (5)
strmean = STATEV (6)
strmax= STATEV (7)
strmin= STATEV (8)
trSmax= STATEV (9)
trSmin= STATEV (10)
Sde11max = STATEV (11)
Sde11min = STATEV (12)
Sde22max = STATEV (13)
Sde22min = STATEV (14)
Sde33max = STATEV (15)
Sde33min = STATEV (16)
Sde12max = STATEV (17)
Sde12min = STATEV (18)
Sde13max = STATEV (19)
Sde13min = STATEV (20)
Sde23max = STATEV (21)
Sde23min = STATEV (22)
Svonmax = STATEV (23)
  All = STATEV (24)
  Shmean = STATEV (25)
  Nii = STATEV (26)
  slope = STATEV (27)
  Allstar = STATEV (28)
  TRmax = STATEV (29)
  TRmin = STATEV (30)

trS = stress(1) + stress(2) + stress(3)
Sde11 = stress(1) - 1/3*trS
Sde22 = stress(2) - 1/3*trS
Sde33 = stress(3) - 1/3*trS
Sde12 = stress(4)
Sde13 = 0.0
Sde23 = 0.0

Svon = (1.0/sqrt(2.0))*sqrt((stress(1)-stress(2))**2+
& (stress(2)-stress(3))**2+(stress(3)-stress(1))**2+
&
6.0*((stress(4))**2+(0.0)**2+(0.0)**2))

```

C initialise parameters at the 1st increment of each cycle

```
if ((MOD((KSTEP-1),2)==0).AND.(KINC==1))then
trSmax = trS
trSmin = trS
Sde11max = Sde11
Sde11min = Sde11
Sde22max = Sde22
Sde22min = Sde22
Sde33max = Sde33
Sde33min = Sde33
Sde12max = Sde12
Sde12min = Sde12
Sde13max = Sde13
Sde13min = Sde13
Sde23max = Sde23
Sde23min = Sde23
```

```
Svonmax = Svon
else
```

c loop within cycles to maximise or minimise stresses

```
if (trS>trSmax)then
trSmax = trS
endif
if (trS<trSmin)then
trSmin = trS
endif
if (Sde11>Sde11max) Sde11max=Sde11
if (Sde11<Sde11min) Sde11min=Sde11
if (Sde22>Sde22max) Sde22max=Sde22
if (Sde22<Sde22min) Sde22min=Sde22
if (Sde33>Sde33max) Sde33max=Sde33
if (Sde33<Sde33min) Sde33min=Sde33
if (Sde12>Sde12max) Sde12max=Sde12
if (Sde12<Sde12min) Sde12min=Sde12
if (Sde13>Sde13max) Sde13max=Sde13
if (Sde13<Sde13min) Sde13min=Sde13
if (Sde23>Sde23max) Sde23max=Sde23
if (Sde23<Sde23min) Sde23min=Sde23
```

```
if (Svon>Svonmax) Svonmax=Svon
endif
```

c initialise E, D, Nf values at the 1st cycle

```
IF (KSTEP < 6)THEN
```

```
E = PROPS(1)
D = 0
Nf = 0
All = 0
Shmean = 0
Nii = 0.0
slope = 0
```

```
ELSEIF ((KSTEP == 6) .AND. (KINC < 50))THEN
```

```
E = PROPS(1)
D = 0
Nf = 0
All = 0
Shmean = 0
Nii = 0.0
```

```

slope = 0

c calculate Nf and damage at the end of each cycle

ELSEIF ((KSTEP ==6).AND.(KINC==50))THEN

Shmean = (trSmax+trSmin)/6.0
Allstar = S10*(1.0-3.0*b1*Shmean)
All = (1.0/2.0)*((3.0/2.0)*((Sde11max-Sde11min)**2+(Sde22max-
&
Sde22min)**2+(Sde33max-Sde33min)**2+2*(Sde12max-Sde12min)**2+
&
2*(Sde13max-Sde13min)**2+2*(Sde23max-Sde23min)**2)**(1.0/2.0)

    if((Su-Svonmax)<=0.0)then
Nf = 0.0

elseif((All-Allstar)<=0.0)then
Nf = 1.0e08
else
Nf = abs(1.0/(1.0+beta)*1.0/aM0beta*(Su-Svonmax)/(All-Allstar)*
& (All/(1-3.0*b2*Shmean))**(-beta))
endif
deltaD = 1.0/Nf
D = D + deltaD

E = E0 * (1-D)

Nii = 1.0
slope = 0
    ELSEIF ((KSTEP ==8).AND.(KINC==50))THEN

Shmean = (trSmax+trSmin)/6.0
Allstar = S10*(1.0-3.0*b1*Shmean)
All = (1.0/2.0)*((3.0/2.0)*((Sde11max-Sde11min)**2+(Sde22max-
&
Sde22min)**2+(Sde33max-Sde33min)**2+2*(Sde12max-Sde12min)**2+
&
2*0.0+2*0.0)**(1.0/2.0)

    if(((All-Allstar)/(Su-Svonmax))<=0.0)then
alfa = 1.0
else
alfa = 1.0 - a*(All-Allstar)/(Su-Svonmax)

endif

    deltaN = 1.0

c

deltaD = ((1.0 - (1.0 - D)**(beta+1.0))**alfa)*((All/M0/
& (1.0-3.0*b2*Shmean)/(1-D))**beta)*deltaN

D = D + deltaD

E = E0 * (1-D)

Nii = Nii+deltaN
slope = (D - Dlast)/deltaN

c ccc

```

```

ELSEIF((KSTEP<20).and.((MOD(KSTEP,2)==0).AND.(KINC==50)))THEN

Shmean = (trSmax+trSmin)/6.0
Allstar = S10*(1.0-3.0*b1*Shmean)
All = (1.0/2.0)*((3.0/2.0)*((Sde11max-Sde11min)**2+(Sde22max-
&
Sde22min)**2+(Sde33max-Sde33min)**2+2*(Sde12max-Sde12min)**2+
&
2*0.0+2*0.0)**(1.0/2.0)

    if(((All-Allstar)/(Su-Svonmax))<=0.0)then
    alfa = 1.0
    else
    alfa = 1.0 - a*(All-Allstar)/(Su-Svonmax)

endif

    deltaN = 1.0

c use nonlinear calculation starting from the 3rd cycle
c Newton-Raphson used to calculate DN1, next step D

deltaD = ((1.0 - (1.0 - D)**(beta+1.0))**alfa)*((All/M0/
& (1.0-3.0*b2*Shmean)/(1-D)**beta)*deltaN

D = D + deltaD

E = E0 * (1-D)

Nii = Nii+deltaN
slope = (D - Dlast)/deltaN

ELSEIF ((MOD(KSTEP,2)==0).AND.(KINC==50))THEN

Shmean = (trSmax+trSmin)/6.0
Allstar = S10*(1.0-3.0*b1*Shmean)
All = (1.0/2.0)*((3.0/2.0)*((Sde11max-Sde11min)**2+(Sde22max-
&
Sde22min)**2+(Sde33max-Sde33min)**2+2*(Sde12max-Sde12min)**2+
&
2*0.0+2*0.0)**(1.0/2.0)

    if(((All-Allstar)/(Su-Svonmax))<=0.0)then
    alfa = 1.0
    else
    alfa = 1.0 - a*(All-Allstar)/(Su-Svonmax)

endif

    deltaN = 2.5e03

c use nonlinear calculation starting from the 3rd cycle
c Newton-Raphson used to calculate DN1, next step D

deltaD = ((1.0 - (1.0 - D)**(beta+1.0))**alfa)*((All/M0/
& (1.0-3.0*b2*Shmean)/(1-D)**beta)*deltaN

D = D + deltaD

E = E0 * (1-D)

Nii = Nii+deltaN
slope = (D - Dlast)/deltaN

```

```

ENDIF
C

STATEV (1) = Nf
STATEV (2) = D
STATEV (3) = straeq
STATEV (4) = E
STATEV (5) = TRmean
STATEV (6) = strmean
STATEV (7) = strmax
STATEV (8) = strmin
STATEV (9) = trSmax
STATEV (10) = trSmin
STATEV (11) = Sde11max
STATEV (12) = Sde11min
STATEV (13) = Sde22max
STATEV (14) = Sde22min
STATEV (15) = Sde33max
STATEV (16) = Sde33min
STATEV (17) = Sde12max
STATEV (18) = Sde12min
STATEV (19) = Sde13max
STATEV (20) = Sde13min
STATEV (21) = Sde23max
STATEV (22) = Sde23min
STATEV (23) = Svonmax
STATEV (24) = All
STATEV (25) = Shmean
STATEV (26) = Nii
STATEV (27) = slope
STATEV (28) = Allstar
STATEV (29) = TRmax
STATEV (30) = TRmin
C
C
C SET UP ELASTICITY MATRIX
C
  EBULK3 = E/(ONE-TWO*XNUE)
  EG2 = E/(ONE+XNUE)
  EG = EG2/TWO
  ELAM = (EBULK3-EG2)/THREE
C
C
  DO K1 = 1, 3
    DO K2 = 1, 3
      DDS(K2,K1) = ELAM
    END DO
    DDS(K1,K1) = EG2 + ELAM
  END DO
C
  DDS(4,4) = EG
C
C
C DETERMINE STRESS INCREMENT
C
C
  TRVAL = DSTRAN(1)+DSTRAN(2)+DSTRAN(3)
  DO K=1,3
    DSTRESS(K) = 2*EG*DSTRAN(K)+ELAM*TRVAL
  END DO
  DSTRESS(4) = EG*DSTRAN(4)
C
C UPDATE STRESS
C
  DO K = 1,NTENS
    STRESS(K) = STRESS(K) + DSTRESS(K)

```

```

        END DO
C
C
C DETERMINE JACOBIAN
C
C
        DO I=1,3
        DO J=1,3
            DDSDE(I,J) = DDS(I,J)
        END DO
    END DO
    DDSDE(4,4) = DDS(4,4)
C
C
C
c   if ((mod(KSTEP,2) /= 0) .and. (KINC == 50))then
c   if ((KSTEP/10).eq.int(KSTEP/10))then
    if((NOEL==6055) .and. (NPT == 3).and.
    & (MOD(KSTEP,2)==0).and.(KINC == 50)) THEN

WRITE(32,1000)KSTEP, NOEL, slope, KINC, Nii,deltaN,Svonmax,D, Allstar

WRITE(31,3000)KSTEP, KINC, Nf, E, shmean, TRmean
    endif
    if ((NOEL == 6055) .and. (NPT == 3))then

WRITE(30,2000)KSTEP, KINC, cyc, E , trSmax, All, D
    endif
C
1000 FORMAT(2(1x,i4),1x,f15.13,1x,i4,2x,f11.0,2x,f7.0,1x,f11.3,1x,f11.7
    & ,1x,f5.1)
2000 FORMAT(2(1x,i4),1x,2(2x,f11.2),1x,f11.3,1x,f11.3,2x,f11.7)
3000 FORMAT(2(1x,i4),2x,f18.1,f12.1,2x,f11.3,2x,f6.3)
    RETURN
    END
**

```

Then central difference scheme:

```

*USER SUBROUTINE
  SUBROUTINE UMAT(STRESS,STATEV,DDSDDE,SSE,SPD,SCD,
  1 RPL,DDSDDT,DRPLDE,DRPLDT,
  2 STRAN,DSTRAN,TIME,DTIME,TEMP,DTEMP,PREDEF,DPRED,CMNAME,
  3 NDI,NSHR,NTENS,NSTATV,PROPS,NPROPS,COORDS,DROT,PNEWDT,
  4 CELENT,DFGRD0,DFGRD1,NOEL,NPT,LAYER,KSPT,KSTEP,KINC)
C
  INCLUDE 'ABA_PARAM.INC'
C
  CHARACTER*80 CMNAME
C
C
  DIMENSION STRESS(NTENS),STATEV(NSTATV),
  1 DDSDDE(NTENS,NTENS),DDSDDT(NTENS),DRPLDE(NTENS),
  2 STRAN(NTENS),DSTRAN(NTENS),TIME(2),PREDEF(1),DPRED(1),
  3 PROPS(NPROPS),COORDS(3),DROT(3,3),DFGRD0(3,3),DFGRD1(3,3)
C
C
  Real    cyc, E0, Sdash,Nii,b, Nf, D, Smax, deltaD ,strmax,strmin
  Integer::i,j,nmax
  PARAMETER (M=3,N=3,ID=3,ZERO=0.D0,ONE=1.D0,TWO=2.D0,THREE=3.D0,
+   SIX=6.D0, NINE=9.D0, TOLER=0.D-6)
C

```

```

C  DIMENSION DSTRESS(4), DDS(4,4)
C
C-----
C  Write output headings
  OPEN(unit=52,file='c:\dama\cRmd5s8005khis.txt',status='unknown')

OPEN(unit=51,file='c:\dama\cRmd5s8005ktry.txt',status='unknown')

OPEN(unit=50,file='c:\dama\cRmd5s8005ktry1.txt',status='unknown')
  IF ((KSTEP == 1) .AND. (KINC == 1) .AND.
    & (NOEL == 1) .AND. (NPT == 1))THEN

WRITE(52,*)'Step NO./Cycle NO./INC NO./Stress/D/Equivalent strain/'
  endif

C  SPECIFY MATERIAL PROPERTIES

  Sdash = 1817.2
  b = -0.0978
  PROPS(1) = 116000
  PROPS(2) = 0.34  PROPS(3) = 1040
  E0 = PROPS(1)
  XNUE = PROPS(2)
  Su = PROPS(3)
  S10 = 358
  beta = 1.79
  b1 = 0.0013
  b2 = 0.00055
  aM0beta = 1.79e-11
  a = 0.75
  M0 = 859399.0
C
C
  cyc = int((KSTEP-1)/4)+1

Nf = STATEV (1)
D = STATEV (2)

D0 = STATEV (3)
E = STATEV (4)
Dnm1 = STATEV (5)
strmean = STATEV (6)
strmax= STATEV (7)
strmin= STATEV (8)
trSmax= STATEV (9)
trSmin= STATEV (10)
Sde11max = STATEV (11)
Sde11min = STATEV (12)
Sde22max = STATEV (13)
Sde22min = STATEV (14)
Sde33max = STATEV (15)
Sde33min = STATEV (16)
Sde12max = STATEV (17)
Sde12min = STATEV (18)
Sde13max = STATEV (19)
Sde13min = STATEV (20)
Sde23max = STATEV (21)
Sde23min = STATEV (22)
Svonmax = STATEV (23)
  All = STATEV (24)
  Shmean = STATEV (25)
  Nii = STATEV (26)
  slope = STATEV (27)
  Allstar = STATEV (28)

trS = stress(1) + stress(2) + stress(3)

```

```

Sde11 = stress(1) - 1.0/3.0*trS
Sde22 = stress(2) - 1.0/3.0*trS
Sde33 = stress(3) - 1.0/3.0*trS
Sde12 = stress(4)
Sde13 = stress(5)
Sde23 = stress(6)

Svon = (1.0/sqrt(2.0))*sqrt((stress(1)-stress(2))**2+
& (stress(2)-stress(3))**2+(stress(3)-stress(1))**2+
&
6.0*((stress(4))**2+(stress(5))**2+(stress(6))**2))

C initialise parameters at the 1st increment of each cycle

if(KSTEP == 1)then

trSmax = -10000.0
trSmin = 10000.0
Sde11max = -10000.0
Sde11min = 10000.0
Sde22max = -10000.0
Sde22min = 10000.0
Sde33max = -10000.0
Sde33min = 10000.0
Sde12max = -10000.0
Sde12min = 10000.0
Sde13max = -10000.0
Sde13min = 10000.0
Sde23max = -10000.0
Sde23min = 10000.0
Svonmax = -10000.0
elseif ((MOD((KSTEP-1),4)==0).AND.(KINC==1))then
trSmax = trS
trSmin = trS
Sde11max = Sde11
Sde11min = Sde11
Sde22max = Sde22
Sde22min = Sde22
Sde33max = Sde33
Sde33min = Sde33
Sde12max = Sde12
Sde12min = Sde12
Sde13max = Sde13
Sde13min = Sde13
Sde23max = Sde23
Sde23min = Sde23

Svonmax = Svon
elseif (KSTEP/=1)then
c loop within cycles to maximise or minimise stresses

if (trS>trSmax)then
trSmax = trS
endif
if (trS<trSmin)then
trSmin = trS
endif
if (Sde11>Sde11max) Sde11max=Sde11
if (Sde11<Sde11min) Sde11min=Sde11
if (Sde22>Sde22max) Sde22max=Sde22
if (Sde22<Sde22min) Sde22min=Sde22
if (Sde33>Sde33max) Sde33max=Sde33
if (Sde33<Sde33min) Sde33min=Sde33
if (Sde12>Sde12max) Sde12max=Sde12
if (Sde12<Sde12min) Sde12min=Sde12
if (Sde13>Sde13max) Sde13max=Sde13

```

```

if (Sde13<Sde13min) Sde13min=Sde13
if (Sde23>Sde23max) Sde23max=Sde23
if (Sde23<Sde23min) Sde23min=Sde23

  if (Svon>Svonmax) Svonmax=Svon
endif

c initialise E, D, Nf values at the 1st cycle

  IF (KSTEP < 8)THEN

E = PROPS(1)
D = 0
Nf = 0
All = 0
Shmean = 0
Nii = 0.0
slope = 0

ELSEIF ((KSTEP == 8) .AND. (KINC < 50))THEN

E = PROPS(1)

D = 0
  Nf = 0
All = 0
Shmean = 0
Nii = 0.0
slope = 0

C
cccccccccccccccc
c calculate Nf and damage at the end of each cycle
c calculate the initial D using Miner's rule, to start the nonlinear calculation

ELSEIF ((KSTEP ==8).AND.(KINC==50))THEN

Shmean = (trSmax+trSmin)/6.0
Allstar = SIO*(1.0-3.0*b1*Shmean)
All = (1.0/2.0)*((3.0/2.0)*((Sde11max-Sde11min)**2+(Sde22max-
&
Sde22min)**2+(Sde33max-Sde33min)**2+2*(Sde12max-Sde12min)**2+
&
2*(Sde13max-Sde13min)**2+2*(Sde23max-Sde23min)**2))**(1.0/2.0)
Nf = abs(1.0/(1.0+beta)*1.0/aM0beta*(Su-Svonmax)/(All-Allstar)*
& (All/(1-3.0*b2*Shmean))**(-beta))
deltaD = 1.0/Nf
D = D + deltaD

Dnm1 = D/10.0
D0 = D

E = E0 * (1-D)

Nii = 1.0
slope = 0
c ccc
  ELSEIF ((KSTEP ==12).AND.(KINC==50))THEN

Shmean = (trSmax+trSmin)/6.0
Allstar = SIO*(1.0-3.0*b1*Shmean)
All = (1.0/2.0)*((3.0/2.0)*((Sde11max-Sde11min)**2+(Sde22max-
&
Sde22min)**2+(Sde33max-Sde33min)**2+2*(Sde12max-Sde12min)**2+
&
2*(Sde13max-Sde13min)**2+2*(Sde23max-Sde23min)**2))**(1.0/2.0)

```

alfa = 1.0 - a*(All-Allstar)/(Su-Svonmax)

- c use nonlinear calculation starting from the 3rd cycle
- c Newton-Raphson used to calculate DN1, next step D

```
deltaN=10.0
  D = D + deltaN*(((1.0-(1.0-D)**(beta+1.0))**alfa)/((1.0-D)
&
**beta)*((All/M0/(1.0-3.0*b2*Shmean))**beta)+
& ((1.0-(1.0-Dnm1)**(beta+1.0))**alfa)/((1.0-Dnm1)
&
**beta)*((All/M0/(1.0-3.0*b2*Shmean))**beta))/2.0+
& deltaN*(((All/M0/(1.0-3.0*b2*Shmean))**beta)*alfa*(beta+1.0)
& *((1.0-(1.0-D)**(beta+1.0))**(alfa-1.0))+ beta*((1.0
& -(1.0-D)**(beta+1.0))**alfa)*((1.0-D)**(-1.0-beta)))
& ((1.0-(1.0-D)**(beta+1.0))**alfa)/((1.0-D)
&
**beta)*((All/M0/(1.0-3.0*b2*Shmean))**beta))
```

Dnm1 = D0
D0 = D

E = E0 * (1-D)

Nii = Nii+deltaN
slope = (D - Dnm1)/deltaN

```
ELSEIF ((KSTEP <36).AND.(MOD(KSTEP,4)==0).AND.(KINC==50))THEN
Shmean = (trSmax+trSmin)/6.0
Allstar = S10*(1.0-3.0*b1*Shmean)
All = (1.0/2.0)*((3.0/2.0)*(Sde11max-Sde11min)**2+(Sde22max-
&
Sde22min)**2+(Sde33max-Sde33min)**2+2*(Sde12max-Sde12min)**2+
&
2*(Sde13max-Sde13min)**2+2*(Sde23max-Sde23min)**2)**(1.0/2.0)
```

alfa = 1.0 - a*(All-Allstar)/(Su-Svonmax)

- c use nonlinear calculation starting from the 3rd cycle
- c Newton-Raphson used to calculate DN1, next step D

```
nmax=1000

deltaN=100.0
  D = D + deltaN*(((1.0-(1.0-D)**(beta+1.0))**alfa)/((1.0-D)
&
**beta)*((All/M0/(1.0-3.0*b2*Shmean))**beta)+
& ((1.0-(1.0-Dnm1)**(beta+1.0))**alfa)/((1.0-Dnm1)
&
**beta)*((All/M0/(1.0-3.0*b2*Shmean))**beta))/2.0+
& deltaN*(((All/M0/(1.0-3.0*b2*Shmean))**beta)*alfa*(beta+1.0)
& *((1.0-(1.0-D)**(beta+1.0))**(alfa-1.0))+ beta*((1.0
& -(1.0-D)**(beta+1.0))**alfa)*((1.0-D)**(-1.0-beta)))
& ((1.0-(1.0-D)**(beta+1.0))**alfa)/((1.0-D)
&
**beta)*((All/M0/(1.0-3.0*b2*Shmean))**beta))
```

Dnm1 = D0

```

D0 = D

E = E0 * (1-D)

Nii = Nii+deltaN
slope = (D - Dnm1)/deltaN

c ccc

ELSEIF ((MOD(KSTEP,4)==0).AND.(KINC==50))THEN

Shmean = (trSmax+trSmin)/6.0
Allstar = S10*(1.0-3.0*b1*Shmean)
All = (1.0/2.0)*((3.0/2.0)*((Sde11max-Sde11min)**2+(Sde22max-
&
Sde22min)**2+(Sde33max-Sde33min)**2+2*(Sde12max-Sde12min)**2+
&
2*(Sde13max-Sde13min)**2+2*(Sde23max-Sde23min)**2)**(1.0/2.0)

alfa = 1.0 - a*(All-Allstar)/(Su-Svonmax)

c use nonlinear calculation starting from the 3rd cycle
c Newton-Raphson used to calculate DN1, next step D

if(slope>1.0e-4)then
deltaN=5000.0
c
elseif((slope>1.0e-8).and.(slope<=1.0e-6))then
c
deltaN=100.0
elseif((slope>1.0e-7).and.(slope<=1.0e-4))then
deltaN=5000.0
elseif(slope<=1.0e-7)then
deltaN=5000.0
endif

D = D + deltaN*(((1.0-(1.0-D)**(beta+1.0))**alfa)/(1.0-D)
&
**beta)*((All/M0/(1.0-3.0*b2*Shmean))**beta)+
& ((1.0-(1.0-Dnm1)**(beta+1.0))**alfa)/(1.0-Dnm1)
&
**beta)*((All/M0/(1.0-3.0*b2*Shmean))**beta))/2.0+
& deltaN*(((All/M0/(1.0-3.0*b2*Shmean))**beta)*(alfa*(beta+1.0)
& *((1.0-(1.0-D)**(beta+1.0))**alfa-1.0)+ beta*(1.0
& -(1.0-D)**(beta+1.0))**alfa*((1.0-D)**(-1.0-beta)))*)
& ((1.0-(1.0-D)**(beta+1.0))**alfa)/(1.0-D)
&
**beta)*((All/M0/(1.0-3.0*b2*Shmean))**beta)
Dnm1 = D0
D0 = D

E = E0 * (1-D)

Nii = Nii+deltaN
slope = (D - Dnm1)/deltaN
ENDIF
cccccccccccccc

STATEV (1) = Nf

```

```

STATEV (2) = D
D0
E
Dnm1
strmean
strmax
strmin
trSmax
= trSmin
= Sde11max
= Sde11min
= Sde22max
= Sde22min
= Sde33max
= Sde33min
= Sde12max
= Sde12min
= Sde13max
= Sde13min
= Sde23max
= Sde23min
= Svonmax
STATEV (24) = All
= Shmean
= Nii
= slope
= Allstar
C
C
C SET UP ELASTICITY MATRIX
C
EBULK3 = E/(ONE-TWO*XNUE)
EG2 = E/(ONE+XNUE)
EG = EG2/TWO
EG3 = THREE*EG
ELAM = (EBULK3-EG2)/THREE
C
C
CCCCCCCCCCCCCCCCCCCCCCCCCCCCCCCCCCCCCCCCCCCCCCCCCCCCCCCCCCCCCCCCCCCCCCCCCCCCCCCCCCCCCCCCCCCCCCCCCCCCCCCCCCCC
C ELASTIC STIFFNESS

```

```

STATEV (3) =
STATEV (4) =
STATEV (5) =
STATEV (6) =
STATEV (7) =
STATEV (8) =
STATEV (9) =
STATEV (10)
STATEV (11)
STATEV (12)
STATEV (13)
STATEV (14)
STATEV (15)
STATEV (16)
STATEV (17)
STATEV (18)
STATEV (19)
STATEV (20)
STATEV (21)
STATEV (22)
STATEV (23)
STATEV (25)
STATEV (26)
STATEV (27)
STATEV (28)

```



```

3 NDI,NSHR,NTENS,NSTATV,PROPS,NPROPS,COORDS,DROT,PNEWDT,
4 CELENT,DFGRD0,DFGRD1,NOEL,NPT,LAYER,KSPT,KSTEP,KINC)
C
INCLUDE 'ABA_PARAM.INC'
C
CHARACTER*80 CMNAME
C
C
DIMENSION STRESS(NTENS),STATEV(NSTATV),
1 DDSDE(NTENS,NTENS),DDSDDT(NTENS),DRPLDE(NTENS),
2 STRAN(NTENS),DSTRAN(NTENS),TIME(2),PREDEF(1),DPRED(1),
3 PROPS(NPROPS),COORDS(3),DROT(3,3),DFGRD0(3,3),DFGRD1(3,3)
C
C
Real    cyc, E0, Sdash,Nii,b, Nf, D, Smax, deltaD ,strmax,strmin
Integer:i,j,nmax
PARAMETER (M=3,N=3,LD=3,ZERO=0.D0,ONE=1.D0,TWO=2.D0,THREE=3.D0,
+        SIX=6.D0, NINE=9.D0, TOLER=0.D-6)
C
C DIMENSION DSTRESS(4), DDS(4,4)
C
C
C
C
C-----
C Write output headings
OPEN(unit=32,file='c:\dama\bRmd5s8005khis.txt',status='unknown')

OPEN(unit=31,file='c:\dama\bRmd5s8005ktry.txt',status='unknown')

OPEN(unit=30,file='c:\dama\bRmd5s8005ktry1.txt',status='unknown')
IF ((KSTEP == 1) .AND. (KINC == 1) .AND.
& (NOEL == 1) .AND. (NPT == 1))THEN

WRITE(32,*)'Step NO./Cycle NO./INC NO./Stress/D/Equivalent strain/'
endif

C SPECIFY MATERIAL PROPERTIES

Sdash = 1817.2
b = -0.0978
PROPS(1) = 116000
PROPS(2) = 0.34
PROPS(3) = 1040
E0 = PROPS(1)
XNUE = PROPS(2)
Su = PROPS(3)
SIO = 358
beta = 1.79
b1 = 0.0013
b2 = 0.00055
aM0beta = 1.79e-11
a = 0.75
MO = 859399.0
C
C
cyc = int((KSTEP-1)/4)+1

Nf = STATEV (1)
D = STATEV (2)

straeq = STATEV (3)
E = STATEV (4)
stra = STATEV (5)
strmean = STATEV (6)

```

```

strmax= STATEV (7)
strmin= STATEV (8)
trSmax= STATEV (9)
trSmin= STATEV (10)
Sde11max = STATEV (11)
Sde11min = STATEV (12)
Sde22max = STATEV (13)
Sde22min = STATEV (14)
Sde33max = STATEV (15)
Sde33min = STATEV (16)
Sde12max = STATEV (17)
Sde12min = STATEV (18)
Sde13max = STATEV (19)
Sde13min = STATEV (20)
Sde23max = STATEV (21)
Sde23min = STATEV (22)
Svonmax = STATEV (23)
  All = STATEV (24)
  Shmean = STATEV (25)
  Nii = STATEV (26)
  slope = STATEV (27)
  Allstar = STATEV (28)

trS = stress(1) + stress(2) + stress(3)
Sde11 = stress(1) - 1.0/3.0*trS
Sde22 = stress(2) - 1.0/3.0*trS
Sde33 = stress(3) - 1.0/3.0*trS
Sde12 = stress(4)
Sde13 = stress(5)
Sde23 = stress(6)

Svon = (1.0/sqrt(2.0))*sqrt((stress(1)-stress(2))**2+
& (stress(2)-stress(3))**2+(stress(3)-stress(1))**2+
&
6.0*((stress(4))**2+(stress(5))**2+(stress(6))**2))

C   initialise parameters at the 1st increment of each cycle

      if(KSTEP == 1)then

trSmax = -10000.0
trSmin = 10000.0
Sde11max = -10000.0
Sde11min = 10000.0
Sde22max = -10000.0
Sde22min = 10000.0
Sde33max = -10000.0
Sde33min = 10000.0
Sde12max = -10000.0
Sde12min = 10000.0
Sde13max = -10000.0
Sde13min = 10000.0
Sde23max = -10000.0
Sde23min = 10000.0
Svonmax = -10000.0
      elseif ((MOD((KSTEP-1),4)==0).AND.(KINC==1))then
trSmax = trS
trSmin = trS
Sde11max = Sde11
Sde11min = Sde11
Sde22max = Sde22
Sde22min = Sde22
Sde33max = Sde33
Sde33min = Sde33
Sde12max = Sde12
Sde12min = Sde12
Sde13max = Sde13

```

```

Sde13min = Sde13
Sde23max = Sde23
Sde23min = Sde23

Svonmax = Svon
  elseif (KSTEP/=1)then
c loop within cycles to maximise or minimise stresses

if (trS>trSmax)then
trSmax = trS
endif
if (trS<trSmin)then
trSmin = trS
endif
if (Sde11>Sde11max) Sde11max=Sde11
if (Sde11<Sde11min) Sde11min=Sde11
if (Sde22>Sde22max) Sde22max=Sde22
if (Sde22<Sde22min) Sde22min=Sde22
if (Sde33>Sde33max) Sde33max=Sde33
if (Sde33<Sde33min) Sde33min=Sde33
if (Sde12>Sde12max) Sde12max=Sde12
if (Sde12<Sde12min) Sde12min=Sde12
if (Sde13>Sde13max) Sde13max=Sde13
if (Sde13<Sde13min) Sde13min=Sde13
if (Sde23>Sde23max) Sde23max=Sde23
if (Sde23<Sde23min) Sde23min=Sde23

  if (Svon>Svonmax) Svonmax=Svon
endif

c initialise E, D, Nf values at the 1st cycle

  IF (KSTEP < 8)THEN

E = PROPS(1)
D = 0
Nf = 0
All = 0
Shmean = 0
Nii = 0.0
slope = 0

ELSEIF ((KSTEP == 8) .AND. (KINC < 50))THEN

E = PROPS(1)

D = 0
  Nf = 0
All = 0
Shmean = 0
Nii = 0.0
slope = 0

C
cccccccccccccccc
c calculate Nf and damage at the end of each cycle
c calculate the initial D using Miner's rule, to start the nonlinear calculation

ELSEIF ((KSTEP ==8).AND.(KINC==50))THEN

Shmean = (trSmax+trSmin)/6.0
Allstar = S10*(1.0-3.0*b1*Shmean)
All = (1.0/2.0)*((3.0/2.0)*((Sde11max-Sde11min)**2+(Sde22max-
&
Sde22min)**2+(Sde33max-Sde33min)**2+2*(Sde12max-Sde12min)**2+

```

```

&
2*(Sde13max-Sde13min)**2+2*(Sde23max-Sde23min)**2)**(1.0/2.0)
  Nf = abs(1.0/(1.0+beta)*1.0/aM0beta*(Su-Svonmax)/(All-Allstar)*
    & (All/(1-3.0*b2*Shmean))**(-beta))
  deltaD = 1.0/Nf
  D = D + deltaD

E = E0 * (1-D)

Nii = 1.0
slope = 0
c
  ELSEIF ((KSTEP ==12).AND.(KINC==50))THEN

  Shmean = (trSmax+trSmin)/6.0
  Allstar = S10*(1.0-3.0*b1*Shmean)
  All = (1.0/2.0)*((3.0/2.0)*((Sde11max-Sde11min)**2+(Sde22max-
    &
Sde22min)**2+(Sde33max-Sde33min)**2+2*(Sde12max-Sde12min)**2+
    &
2*(Sde13max-Sde13min)**2+2*(Sde23max-Sde23min)**2)**(1.0/2.0)

  alfa = 1.0 - a*(All-Allstar)/(Su-Svonmax)

c use nonlinear calculation starting from the 3rd cycle
c Newton-Raphson used to calculate DN1, next step D
  DN1k1=D/5.0
  j=0
  nmax=1000
  deltaN=10.0
  Dlast=D

do i = 1, nmax
  DN1k = DN1k1
  j = j+1
  f = -1.0*(1-DN1k)+1-D-(((1-(1-DN1k)**(beta+1.0))**alfa)/((1-DN1k)
    &
**beta)*(All/M0/(1.0-3.0*b2*Shmean))**beta)*deltaN

  ff = 1.0-deltaN*((All/M0/(1.0-3.0*b2*Shmean))**beta)*(alfa*(beta+1.0)
    &
*((1.0-(1.0-DN1k)**(beta+1.0))**alfa-1.0))+ beta*((1.0
    &
-(1.0-DN1k)**(beta+1.0))**alfa)*(1.0-DN1k)**(-1.0-beta)))
c
DN1k1=DN1k-f/ff

if(abs(DN1k1-DN1k)<1.0e-7)exit

enddo

D=DN1k1

E = E0 * (1-D)

Nii = Nii+deltaN
slope = (D - Dlast)/deltaN

c ccc

```

ccc

ELSEIF

((MOD(KSTEP,4)==0).AND.(KINC==50))THEN

```
Shmean = (trSmax+trSmin)/6.0
Allstar = S10*(1.0-3.0*b1*Shmean)
All = (1.0/2.0)*((3.0/2.0)*((Sde11max-Sde11min)**2+(Sde22max-
&
Sde22min)**2+(Sde33max-Sde33min)**2+2*(Sde12max-Sde12min)**2+
&
2*(Sde13max-Sde13min)**2+2*(Sde23max-Sde23min)**2))**(1.0/2.0)

alfa = 1.0 - a*(All-Allstar)/(Su-Svonmax)
```

c use nonlinear calculation starting from the 3rd cycle
c Newton-Raphson used to calculate DN1, next step D

```
if(slope>1.0e-4)then
  deltaN=1000.0
  DN1k1=D/10.0
  celseif((slope>1.0e-8).and.(slope<=1.0e-6))then
    c
    deltaN=100.0
    elseif((slope>1.0e-7).and.(slope<=1.0e-5))then
      deltaN=5000.0
      DN1k1=D/5.0
      elseif(slope<=1.0e-7)then
        deltaN=5000.0
        DN1k1=D*100.0
      endif

  j=0
  nmax=1000
```

Dlast=D

```
do i = 1, nmax
  DN1k = DN1k1
  j = j+1
  f = -1.0*(1-DN1k)+1-D-((1-(1-DN1k)**(beta+1.0))**alfa)/((1-DN1k)
  &
  **beta)*((All/M0)/(1.0-3.0*b2*Shmean))**beta)*deltaN

  ff = 1.0-deltaN*((All/M0)/(1.0-3.0*b2*Shmean))**beta*(alfa*(beta+1.0)
  &*((1.0-(1.0-DN1k)**(beta+1.0))**alfa-1.0))+ beta*((1.0
  & -(1.0-DN1k)**(beta+1.0))**alfa)*((1.0-DN1k)**(-1.0-beta)))
  c
```

DN1k1=DN1k-f/ff

if(abs(DN1k1-DN1k)<1.0e-7)exit

enddo

D=DN1k1

E = E0 * (1-D)

Nii = Nii+deltaN

Appendix A2 SWT Fortran program and wear-fatigue interpolation program

Cyclic SWT (due to wear) calculation:

```
implicit none
```

```
! Declare the variables
```

```
character :: line*120
```

```
integer      :: nelem,ncyc,ninc, nstep, nangle,dummy
```

```
integer      :: step1,i,flag1,cyc,step,inc,icelem,iangle
```

```
integer      :: elemt, flag2, flag3, ci, flags
```

```
real         :: pi,angle,x,y
```

```
real         :: s11t,s22t,s12t,xt,yt,e11t,e22t,e12t
```

```
real        :: x_elem(10000,10000), y_elem(10000,10000)
```

```
double precision h,fh,dfh,a,b,c,d,tmpswt,E,hf
```

```
integer, allocatable, dimension(:)      :: elem,swt_elem
```

```
real, allocatable, dimension(:)         :: swtmax,swt_angle,swt_x,swt_y
```

```
real, allocatable, dimension(:,:)       :: swt_con,SWTlife
```

```
real, allocatable, dimension(:,,:)      :: s11max,e11max,e11min
```

```
real, allocatable, dimension(:,,:)      :: swt, e_range
```

```
real, allocatable, dimension(:,,:,:)    :: s11_trans,e11_trans
```

```
pi = 4.0 * atan(1.0)
```

```
nstep = 2
```

```
nangle = 36
```

```
a=1817.2
```

```
b=-0.0978
```

```
c=-0.688
```

```
d=0.841
```

```
E=116000
```

```

h=2000
! Open the files to read and write
open(unit=30,file='roundonflat.dat',status='old')
open(unit=31,file='swt_cont.dat',status='unknown')
open(unit=32,file='swt_log.dat',status='unknown')
open(unit=33,file='stress.dat',status='unknown')
write(32,*)'Cyc ELEMENT SWT X-COORD Y-COORD ANGLE'

! Enter control information
! print *, 'Please input no. of elements to process'
! read *, nelem
! print *, "
! print *, 'Please input no. of fretting cycle to process'
! read *, ncy
! print *, "
! print *, 'Please input increment per step'
! read *, ninc
! print *, "
nelem=400
ncy=40
ninc=50

! Read in contact element and integration point data from stress.inp file
allocate(s11_trans(ncyc,nstep,ninc,nelem,nangle))
allocate(e11_trans(ncyc,nstep,ninc,nelem,nangle))
allocate(s11max(ncyc,nelem,nangle))
allocate(e11max(ncyc,nelem,nangle))
allocate(e11min(ncyc,nelem,nangle))
allocate(swt(ncyc,nelem,nangle))
allocate(e_range(ncyc,nelem,nangle))
allocate(swt_x(ncyc))
allocate(swt_y(ncyc))
allocate(SWTlife(ncyc,nelem))
allocate(swtmax(ncyc))
allocate(swt_elem(ncyc))
allocate(swt_angle(ncyc))
allocate(elem(nelem))
allocate(swt_con(ncyc,nelem))

! set initial value to zero

```

```

        do cyc=1, ncyc
            swtmax(cyc)=-1000
            do icelem=1,nelem
                swt_con(cyc,icelem) =-1000
                do iangle=1,36
                    s11max(cyc,icelem,iangle)=-2000.0
                    e11max(cyc,icelem,iangle)=-2000.0
                    e11min(cyc,icelem,iangle)=1000.0
                end do
            end do
        end do

cyc=1
step=0

! read in dat file until 'S T E P' found

1 continue
flag1=0
do while (flag1==0)
    read (30,'(a80)') line
!    print*, line
    if (line(25:29)=='S T E') then
        flag1=1 !flag1=1 when initial part of dat file has been read
    end if
end do

! ignore step 1 as it is normal load step not fretting cycle

!flag3=0
if (line(25:29)=='S T E') then

    read (line(38:39),'(i3)')step1 !read in step number
    if (step1==1) then
        go to 1
    end if

end if

```

3 continue

```
flag2=0 !flag2 do while reading file loop until 'increment' found
```

```
if (line(25:29)=='S T E') then
```

```
    step=step+1
```

```
print*,line
```

```
print*,'cycle==',cyc
```

```
print*,'step==',step
```

```
end if
```

```
do while (flag2==0)
```

```
    read (30,'(a80)') line
```

```
        if (line(33:36)=='INCR') then
```

```
            flag2=1
```

```
        end if
```

```
end do
```

```
! read data for current increment
```

2 continue

```
if (line(33:36)=='INCR') then
```

```
    read (line(46:47),'(i3)')inc
```

```
    if(inc.gt.ninc) then !greater than
```

```
        inc=ninc
```

```
    end if
```

```
end if
```

```
!!!!!!!!!!!!!!!!!!!!!!!!!!!!
```

```
flags=0 !flags do while reading file loop until 'target set' found
```

```
do while (flags==0)
```

```
    read (30,'(a80)') line
```

```
        if (line(4:9)=='SWTSET') then
```

```
            flags=1
```

```
        end if
```

```
end do
```

```
!!!!!!!!!!!!!!!!!!!!!!!!!!!!
```

```
do i=1,4
```

```
    read(30,*)
```

```
end do
```

```
do icelem=1,nelem
```

```

read(30,*)elemt,dummy,s11t,s22t,s12t,xt,yt,e11t,e22t,e12t
  if (elemt.eq. 15) then
!           write(33,3000)cyc, inc, elemt,s11t,s22t,s12t,e11t,e22t,e12t,xt,yt
  end if

          x_elem(cyc,icelem)=xt

          y_elem(cyc,icelem)=yt

          do iangle=1,36
            angle=iangle*pi/36

            elem(icelem)=elemt

            s11_trans(cyc,step,inc,icelem,iangle)=(s11t+s22t)/2+(s11t-
s22t)/2*cos(2*angle)+s12t*sin(2*angle)
            e11_trans(cyc,step,inc,icelem,iangle)=(e11t+e22t)/2+(e11t-
e22t)/2*cos(2*angle)+e12t*sin(2*angle)
            if (s11_trans(cyc,step,inc,icelem,iangle) > s11max(cyc,icelem,iangle)) then
              s11max(cyc,icelem,iangle) = s11_trans(cyc,step,inc,icelem,iangle)
            end if

            if (e11_trans(cyc,step,inc,icelem,iangle) > e11max(cyc,icelem,iangle)) then
              e11max(cyc,icelem,iangle) = e11_trans(cyc,step,inc,icelem,iangle)
            end if

            if (e11_trans(cyc,step,inc,icelem,iangle) < e11min(cyc,icelem,iangle)) then
              e11min(cyc,icelem,iangle) = e11_trans(cyc,step,inc,icelem,iangle)
            end if

            e_range(cyc,icelem,iangle)=      e11max(cyc,icelem,iangle) - e11min(cyc,icelem,iangle)
            swt(cyc,icelem,iangle)= s11max(cyc,icelem,iangle) * e_range(cyc,icelem,iangle)/2

            if (swt(cyc,icelem,iangle) > swtmax(cyc)) then
              swtmax(cyc) = swt(cyc,icelem,iangle)
              swt_elem(cyc) = elem(icelem)
              swt_angle(cyc) = angle
              swt_x(cyc)=xt
              swt_y(cyc)=yt
            end if

            if (swt(cyc,icelem,iangle) > swt_con(cyc,icelem)) then

```

```

                                swt_con(cyc,icelem) = swt(cyc,icelem,iangle)
                                end if
                                end do
                                end do
                                if (inc==ninc.and.step==2) then
                                write (32,2000)cyc,swt_elem(cyc),swtmax(cyc),swt_x(cyc),swt_y(cyc),swt_angle(cyc)*180.0/pi
                                end if
                                if (inc==ninc.and.step==2) then
                                do ci=1,nelem
                                tmpswt=swt_con(cyc,ci)
                                if(tmpswt.gt.0.8) then
                                h=1000
                                20          fh=(a**2/E)*(h**(2*b))+a*d*(h**(b+c))-tmpswt

                                dfh=(a**2/E)*(2*b)*(h**(2*b-1))+a*(d)*(b+c)*(h**(b+c-1))

                                hf = h - fh/dfh

                                if(abs(hf-h).lt.1.0e-1) then

                                goto 10
                                else
                                h = hf
                                end if

                                goto 20

                                10          continue

                                SWTlife(cyc,ci)=h/2

                                else
                                SWTlife(cyc,ci)=1e8
                                end if

                                write (31,4000)cyc, swt_con(cyc,ci), elem(ci), x_elem(cyc,ci),y_elem(cyc,ci),swtlife(cyc,ci)
                                end do
                                end if

                                flag3=0
                                do while (flag3==0)

```

```

        read (30,'(a80)',end=30) line
        if (line(33:36)=='INCR') then
            flag3=1

        else if (line(25:29)=='S T E') then
            flag3=1
        end if
    end do

        if (line(33:36)=='INCR') then
            go to 2
        end if

        if (line(25:29)=='S T E') then
            if (step==2) then
                step=0
            end if

            if (step==0) then
                cyc=cyc+1
            end if
            if (cyc.ge.ncyc) goto 30
            go to 3
        end if
30      continue
    print*,swtmax
    print*,swt_elem
    print*,swt_x
    print*,swt_y
    print*,swt_angle*180.0/pi
    close (unit=30)
    close (unit=31)
    close (unit=32)
! deallocate(s11_trans,e11_trans,s11max,e11max,e11min,swt,e_range)
! deallocate(swtmax,swt_elem,swt_angle,elem,swt_x,swt_y,SWTlife,swt_con)

2000    format(i3,i6,e15.6,e15.6,e15.6,e15.6,e15.6)
1000    format(e15.6)
3000    format(3(i8),8(f14.6, ", "))
4000    format(i8, f10.6, i8, 2(f10.6, " ,"), f20.1)
    end program swt_calculation

```

Interpolation scheme:

This program is to calculate the damage accumulation using material point mapping.

```
real::pt,swt,xco,yco,swt(4000),xco(4000),yco(4000),life(4000),da(4000)
!real, allocatable, dimension(:, :, :) :: xn, yn, Dn
real::xn(3,100,10),yn(3,100,10),Dn(3,100,10),Dnd(1,100,10),sum(100),sumo(100)
real::Dt(3,100,10),Dtin(3,100,10)
real::Nf(100),Nfo(100)
integer::i,ele(4000),cyc(4000),r,j,k,rn,jn,kn
open(unit=35,file='swt1.txt',status='old')
open(unit=36,file='swt2.txt',status='old')
open(unit=37,file='swt3.txt',status='old')
open(unit=39,file='cenaveraged.txt',status='unknown')
open(unit=59,file='cenaveragednointerpolation.txt',status='unknown')
```

```
rn=3 !layer of sets, normally 3
jn=100 !element number
kn=10 !cycle number
```

```
!allocate(xn(rn,jn,kn))
!allocate(yn(rn,jn,kn))
!allocate(Dn(rn,jn,kn))
```

```
deltaN=1000
```

```
cycck=kn*deltaN
```

```
! Firstly average all the variables such as SWT, coordinates, etc. at the centroid
do r=1,3
```

```
if(r==1)then
  do i=1,4000 !4000 is the element number * 4
```

```
read(35,*)cyc(i),swt(i),ele(i),xco(i),yco(i),life(i)
  da(i)=deltaN/life(i)
```

```
enddo
```

```
do i=1,4000
  if(mod(i,4)==0)then
    j=INT((i-400*(cyc(i)-1))/4)
    k=cyc(i)
    x=(xco(i)+xco(i-1)+xco(i-2)+xco(i-3))/4
    y=(yco(i)+yco(i-1)+yco(i-2)+yco(i-3))/4
    D=(da(i)+da(i-1)+da(i-2)+da(i-3))/4
```

```
    xn(r,j,k)=x
    yn(r,j,k)=y
    Dn(r,j,k)=D
```

```
! write(39,*)r,j,k,xn(r,j,k),yn(r,j,k),Dn(r,j,k)
  endif
enddo
endif
```

```
if(r==2)then
  do i=1,4000
```

```
read(36,*)cyc(i),swt(i),ele(i),xco(i),yco(i),life(i)
```

```

da(i)=deltaN/life(i)

enddo

do i=1,4000
if(mod(i,4)=0)then

!relationship between j and line number; k and line number, as follows
j=INT((i-400*(cyc(i)-1))/4)
k=cyc(i)
x=(xco(i)+xco(i-1)+xco(i-2)+xco(i-3))/4
y=(yco(i)+yco(i-1)+yco(i-2)+yco(i-3))/4
D=(da(i)+da(i-1)+da(i-2)+da(i-3))/4

xn(r,j,k)=x
yn(r,j,k)=y
Dn(r,j,k)=D
! write(39,*)r,j,k,xn(r,j,k),yn(r,j,k),Dn(r,j,k)
endif
enddo
endif

if(r==3)then
do i=1,4000

read(37,*)cyc(i),swt(i),ele(i),xco(i),yco(i),life(i)
da(i)=deltaN/life(i)

```

```

enddo

do i=1,4000
if(mod(i,4)=0)then

j=INT((i-400*(cyc(i)-1))/4)
k=cyc(i)
x=(xco(i)+xco(i-1)+xco(i-2)+xco(i-3))/4
y=(yco(i)+yco(i-1)+yco(i-2)+yco(i-3))/4
D=(da(i)+da(i-1)+da(i-2)+da(i-3))/4

xn(r,j,k)=x
yn(r,j,k)=y
Dn(r,j,k)=D
! write(39,*)r,j,k,xn(r,j,k),yn(r,j,k),Dn(r,j,k),ele(i)
endif
enddo
endif

enddo

do j=1,jn
sum(j)=0.0
sumo(j)=0.0
Nf(j)=0.0
Nfo(j)=0.0
enddo

cyccc=5.0
cyccco=5.0
position1=5
position2=5
!do j=1,jn
!do k=1,kn
! show=3
! show=Dnd(1,j,k)

```

```

! sum1=sum(j)
! sumo1=sumo(j)
! lsum(j)=sum(j)+Dnd(1,j,k)
! lsumo(j)=sumo(j)+Dn(1,j,k)

do r=1,rn
do j=1,jn
do k=1,kn
Dt(r,j,k)=0.0
enddo
enddo
enddo

do r=1,rn
do j=1,jn
do k=1,kn
Dtin(r,j,k)=0.0
enddo
enddo
enddo
do r=1,rn
do j=1,jn
do k=1,kn
if(k==1)then
Dt(r,j,k)=Dn(r,j,k)
endif
if(k>1)then
Dt(r,j,k)=Dt(r,j,k-1)+Dn(r,j,k)
endif
enddo
enddo
enddo

do k=1,kn
do j=1,jn
do r=1,rn-1
! write(39,*)yn(1,j,k), yn(r,j,1), yn(r+1,j,1)
! Find where the deformed point sits and interpolate.
if((yn(1,j,k)>=yn(r+1,j,1)).and.(yn(1,j,k)<=yn(r,j,1)))then
! Dnd(1,j,k)=(Dn(r,j,k)-Dn(r+1,j,k))/(yn(r,j,1)-yn(r+1,j,1))* &
! & yn(1,j,k)+Dn(r,j,k)-(Dn(r,j,k)-Dn(r+1,j,k))/(yn(r,j,1)-yn(r+1,j,1))*yn(r,j,1)
Dtin(1,j,k)=(Dt(r,j,k)-Dt(r+1,j,k))/(yn(r,j,1)-yn(r+1,j,1))* &
& yn(1,j,k)+Dt(r,j,k)-(Dt(r,j,k)-Dt(r+1,j,k))/(yn(r,j,1)-yn(r+1,j,1))*yn(r,j,1)

endif
! Due to round off error, y coordinates may even be greater in the later cycles than the orininal when no wear occurs, so
if((yn(1,j,k)>=yn(1,j,1)))then
Dtin(1,j,k)=Dt(1,j,k)
endif

enddo
enddo
enddo

! if cracking occurs in the one of the cycle, stop looping time k, go directly report life and damage.

do k=1,kn
do j=1,jn

if(Dtin(1,j,k)>=1.0)then
cyccc=(k-1)*DeltaN+(1-Dtin(1,j,k-1))/Dn(1,j,k-1)*DeltaN
position1=xn(1,j,k)
position2=yn(1,j,k)
damagee=Dtin(1,j,k)
go to 1

```

```

endif

! if(sumo(j)>=1.0)then
! cyccco=(k-1)*DeltaN+(1-sumo1)/Dn(1,j,k-1)*DeltaN
! position1=xn(1,j,k)
! position2=yn(1,j,k)
! damagee=sumo(j)
! go to 1
! endif
!if it reaches the max cycle number but still not cracking, estimate life.

if(k==kn)then
Nf(j)=(1-Dtin(1,j,k))/Dn(1,j,k)*deltaN+k*DeltaN
Nfo(j)=(1-Dt(1,j,k))/Dn(1,j,k)*deltaN+k*DeltaN
endif
enddo
enddo

1 do j=1, jn
write(39,*)xn(1,j,1),yn(1,j,1),Dtin(1,j,kn),Nf(j)
write(59,*)xn(1,j,1),yn(1,j,1),Dt(1,j,kn),Nfo(j)
enddo

write(39,*)position1, position2,cyccc,damagee
!write(59,*)position1, position2, cyccco, damagee

stop
end

```

Appendix A3 Abaqus subroutine for energy wear

approach

The code presented here is UMESHMOTION subroutine for energy-based wear approach implementation to fretting fatigue analysis:

```
C USER INPUT FOR ADAPTIVE MESH CONSTRAINT
C debris interfact is controlled by a function of stress, thickness
c and so on.
C
  SUBROUTINE UMESHMOTION(UREF,ULOCAL,NODE,NNDOF,
    $ LNODETYPE,ALOCAL,NDIM,TIME,DTIME,PNEWDT,
    $ KSTEP,KINC,KMESHSWEEP,JMATYP,JGVBLOCK)
C
  include 'ABA_PARAM.INC'
C
C USER DEFINED DIMENSION STATEMENTS
C
C The dimensions of the variables ARRAY
C must be set equal to or greater than 15
C
  DIMENSION ARRAY(15)
  DIMENSION ULOCAL(NDIM)
  DIMENSION UGLOBAL(NDIM)
  DIMENSION JGVBLOCK(100000),JMATYP(100000)
  DIMENSION ALOCAL(NDIM,100000)
  PARAMETER (NELEMMAX=100000)
  DIMENSION JELEMLIST(NELEMMAX),JELEMTYPE(NELEMMAX)
C
C
  INTEGER flag1, cnt1
  INTEGER master
  REAL CPRESS,CSHEAR,CSLIP,COPEN,XCOORD,YCOORD,ZCOORD,INCSLIP
  REAL CSHEAR1,CSHEAR2,CSLIP1, CSLIP2,INCSLIP1, INCSLIP2
  REAL*8 Weardepth1, sign11
  PARAMETER (Nslavenode=183)
  PARAMETER (Nmasternode=103)
  INTEGER slavenode(Nslavenode), masternode(Nmasternode)
  INTEGER dbr(Nslavenode)
    character line*120
  DIMENSION WVLOCAL(3),WVGLOBAL(3)
C
C
  common /wear/
  & inctol,
  & tempslip(10000),
  & tempress(10000),
  & temphear(10000), !add
  & tempAvshear(10000), !add
  & tempincslip(10000),
  & totwdp(10000),
  & totwdp1(10000),
  & xpos(10000),
  & ypos(10000)
  data masternode/
  &5,
  &6,
  &1641/
```

```

data slavenode/

C 81

C Initialise database
C
master=0
cnt1=1
isgn=-1
flag1=0
Weardepth1=0.0
NELEMS = NELEMMAX
OPEN(unit=31,file='c:\hipwears\slavedn5e4.txt',status='unknown')
OPEN(unit=32,file='c:\hipwears\slave1dn5e4.txt',status='unknown')
C
C
C
JRCD=0
JTYP=0
CALL GETNODETOELEMCONN(NODE,NELEMS,JELEMLIST,JELEMTYPE,
$ JRCD,JGVBLOCK)
c
IF(NODE==slavenode(1))THEN

WRITE(31,*)'LOADSTEP',KSTEP,'INCREMENT ',KINC

WRITE(31,*)NODE, isclock-1, ilastnode
WRITE(31, 2000)'NODE CPRESS CSHEAR CSLIP
& Weardepth1 Weardepth2 XCOORD
& YCOORD ZCOORD'
WRITE(32,*)'LOADSTEP',KSTEP,'INCREMENT ',KINC

WRITE(32,*)NODE, isclock-1, ilastnode
WRITE(32, 2000)'NODE CPRESS CSHEAR CSLIP
& Weardepth1 Weardepth2 XCOORD
& YCOORD ZCOORD'
c
inctol=inctol+1
END IF

C

C

CALL GETVRN(NODE,'COORD',ARRAY,JRCD,JGVBLOCK,LTRN)

XCOORD=ARRAY(1)
YCOORD=ARRAY(2)

Do cnt1=1, Nslavenode
IF(NODE == slavenode(cnt1)) THEN
flag1=1
CALL GETVRMAVGATNODE(NODE,JTYP,'CSTRESS',ARRAY,JRCD,
$ JELEMLIST,NELEMS,JMATYP,JGVBLOCK)
CPRESS = ARRAY(1)
CSHEAR= ARRAY(2)
CALL GETVRMAVGATNODE(NODE,JTYP,'CDISP',ARRAY,JRCD,
$ JELEMLIST,NELEMS,JMATYP,JGVBLOCK)
CSLIP = ARRAY(2)
COPEN = ARRAY(1)

tempress(NODE)=CPRESS

INCSLIP=CSLIP-tempslip(NODE)
AvSHEAR=0.5*(CSHEAR+tempsshear(NODE))

tempslip(NODE)=CSLIP

```

```

        tempincslip(NODE)=INCSLIP
        tempsshear(NODE)=CSHEAR
        tempAvshear(NODE)=AvSHEAR
        if ((KSTEP == 6) .or. (KSTEP == 7))THEN

Weardepth1=-abs(INCSLIP*AvSHEAR*0.962E-7)
        ELSE

Weardepth1=-abs(INCSLIP*AvSHEAR*0.962*1.0E-3)
        endif

totwdp(NODE)= Weardepth1+totwdp(NODE)

xpos(NODE)=XCOORD

ypos(NODE)=YCOORD
        end if
        end do
        c
        Do cnt1=1, Nslavenode
        IF(NODE == masternode(cnt1)) THEN

flag1=3

nod1=slavenode(cnt1)
        CPRESS = tempress(nod1)
        cslip = tempslip(nod1)
        AvSHEAR = tempAvshear(nod1)
        INCSLIP= tempincslip(nod1)
        sign11=7.1216e-4
        Weardepth1=-INCSLIP*AvSHEAR*sign11*0.0000000

totwdp1(NODE)= Weardepth1+totwdp1(NODE)
        end if
        end do
WVGLOBAL(1)=0

WVGLOBAL(2)=Weardepth1
WVGLOBAL(3)=0
        C Transformation to the local directions
        do k2=1,NDIM
        WVLOCAL(k2)=0
        do k3=1,NDIM
        WVLOCAL(k2)=WVLOCAL(k2)+WVGLOBAL(k3)*ALOCAL(k3,k2)
        end do
        end do
        do k2 = 1,NDIM
        ULOCAL(k2) = ULOCAL(k2) + WVLOCAL(k2)
        end do
        c
        if ((KINC/25.0).eq.int(KINC/25.0)) then
        if (flag1.eq.1) then
        WRITE(31,1000),NODE, CPRESS,CSHEAR,CSLIP,
        & Weardepth1,XCOORD,
        & YCOORD, ZCOORD, INCSLIP,totwdp(NODE)
        else if (flag1.eq.3) then
        WRITE(32,1000),NODE, CPRESS,CSHEAR,CSLIP,
        & Weardepth1,XCOORD,
        & YCOORD, ZCOORD, tempslip(NODE),totwdp1(NODE)
        end if
        end if
        1000 FORMAT(i6,3(1x,f11.6),1x,f14.10,5(1x,f11.6))
        2000 FORMAT(a150)
        3000 FORMAT(a120)
        c
        RETURN
        END

```

References

- ABAQUS user's and theory manuals, Version 6.9. RI, US: HKS Inc.; 1998.
- Ambrico J.M., Begley M.R., 2000 "Plasticity in fretting contact", *J MECH PHYS*, 48(11), 2000, pp. 2391-2417
- Appenzeller, T., 2004 'The End of Cheap Oil'. *National Geographic*. June 2004.
- Araújo, J.A. , Castro, F.C., A comparative analysis between multiaxial stress and ΔK -based short crack arrest models in fretting fatigue, *Engineering Fracture Mechanics*, Volume 93, October 2012, Pages 34-47.
- Araújo, J. A., Susmel, L., Taylor, D., Ferro, J. C. T. & Mamiya, E. N. 2007 On the use of the Theory of Critical Distances and the Modified Wöhler Curve Method to estimate fretting fatigue strength of cylindrical contacts. *International Journal of Fatigue* 29, 95–107 (2007).
- Araujo, J.A.& Nowell, D. 2002 The effect of rapidly varying contact stress fields on fretting fatigue. *International Journal of Fatigue* 24, 763-775 (2002).
- Archard JF. 1953 Contact and rubbing of flat surfaces. *J Appl Phys* 1953; 24: 981-8.
- Archard J F and Hirst W, 1956 The Wear of Materials under unlubricated Conditions, *Proc. Roy. Soc. Lond.* 236A, 397-410, 1956
- Attia, M. H. 1992 Standardization of Fretting Fatigue Test Methods and Equipment. (*Astm Intl*: 1992).

- Barrack, R. L. 1994 Modularity of Prosthetic Implants. *J Am Acad Orthop Surg* 2, 16–25 (1994).
- Basquin, O. H., 1910 The Exponential Law of Endurance Tests, *Proceedings, American Society for Testing and Materials, ASTEA*, Vol. 10, 1910, pp. 625- 630.
- Benedetti, M. & Fontanari, V. 2004 The effect of bi-modal and lamellar microstructures of Ti-6Al-4V on the behaviour of fatigue cracks emanating from edge-notches. *Fatigue & Fracture of Engineering Materials & Structures* 27, 1073-1089 (2004).
- Bhushan, B. & Gupta, B. K. 1991 *Handbook of Tribology: Materials, Coatings and Surface Treatments* (McGraw–Hill, New York, 1991).
- Brand, R. A., Pedersen, D. R. and Friederich, J. A. (1986) The sensitivity of muscle force predictions to changes in physiological crosssectional area. *Journal of Biomechanics* 19, 589-596.
- Bramhall, Studies in fretting fatigue. DPhil Thesis, University of Oxford; 1973.
- Brown M.W. and Miller K.J., 1973 A theory for fatigue failure under multiaxial stress-strain conditions, *Proc Instn Mech Engrs*, Vol. 187, pp. 745-755, 1973.
- Burr, A. H. & Cheatham, J. B. 1995 *Mechanical Analysis and Design*. (Prentice Hall: 1995).
- Cattaneo C. 1938 Sul contatto di due corpi elastici: distribuzione locale degli sforzi, *Rendiconti dell'Accademia Nazionale dei Lincei*, 27 (1938), pp. 342–348
- Chaboche, J.L. & Lesne, P.M. 1988 A Non-linear Continuous Fatigue Damage Model. *Fatigue & Fracture of Engineering Materials & Structures* 11, 1-17 (1988).

- Ciavarella M, Hills D.A, Monno G., 1998 The influence of rounded edges on indentation by flat punch, *Proceedings of the Institution of Mechanical Engineers Part C-Journal of Mechanical Engineering Science* 212 (4) (1998) 319-328.
- Ciavarella M, Macina G, 2003 New results for the fretting-induced stress concentration on Hertzian and flat rounded contacts, *International Journal of Mechanical Sciences*, 45 (3) (2003) 449-467.
- Clements, R. A. & Tan, Z. 2008 Flexible Pipe Having Pressure Armour Layer. at <<http://www.google.com/patents/US20110030831>>
- Collier, J. P. et al. 1992 Mechanisms of failure of modular prostheses. *Clin. Orthop. Relat. Res.* 129–139 (1992).
- Collins JA, Marco SM. 1964 The effect of stress direction during fretting on subsequent fatigue life. In: *Proceedings of the American Society for testing and materials*, Vol 64 pp. 547-560.
- Cruzado, A., Hartelt, M., Wäsche, R., Urchegui, 2011 M. A. & Gómez, X. Fretting wear of thin steel wires. Part 2: Influence of crossing angle. *Wear* 273, 60–69 (2011).
- Dick, T. & Cailletaud, G. 2006 Fretting modelling with a crystal plasticity model of Ti6Al4V. *Computational Materials Science* 38, 113–125 (2006).
- Dini, D. and D. Nowell, 2004 "Flat and rounded fretting contact problems incorporating elastic layers", *Int. J. Mech. Sci.*, 46(11), (2004), p. 1635-1657.
- Dini, D. and D.A. Hills, 2004 "A consideration of the effects of the slip displacement on fretting fatigue behaviour", *J. Strain Anal. Eng.*, 39(4), (2004), p. 397-407.

- Dini, D., A. Sackfield, and D.A. Hills, 2005 "Comprehensive bounded asymptotic solutions for incomplete contacts in partial slip", *J. Mech. Phys. Solids*, 53(2), (2005), p. 437-454.
- Dini, D., D. Nowell, and I.N. Dyson, 2006 "The use of notch and short crack approaches to fretting fatigue threshold prediction: Theory and experimental validation", *Tribol. Int.*, 39(10), (2006), p. 1158-1165.
- Ding, J., Leen, S.B. & McColl, I.R. 2004 The effect of slip regime on fretting wear-induced stress evolution. *International Journal of Fatigue* 26, 521-531 (2004).
- Ding, J., Leen, S. B., Williams, E. J. & Shipway, P. H. 2009 A multi-scale model for fretting wear with oxidation-debris effects. *Proceedings of the Institution of Mechanical Engineers, Part J: Journal of Engineering Tribology* 223, 1019–1031 (2009).
- Ding, J., Houghton, D., Williams, E. J. & Leen, S. B. 2011 Simple parameters to predict effect of surface damage on fretting fatigue. *International Journal of Fatigue* 33, 332–342 (2011).
- Dobromirski, J. M. 1992 Variables in the fretting process: are there 50 of them? Standardisation of fretting fatigue test methods and equipment. R. B. Waterhouse and M. H. Attia, ASTM: 60-66.
- Donahue, R. J., Clark, H. M., Atanmo, P., Kumble, R. and McEvily, A. J., 1972 Crack opening displacement and the rate of fatigue crack growth. *International Journal of Fracture Mechanics*. 8: 209-219.
- Duda, G. N., Schneider, E. & Chao, E. Y. 1997 Internal forces and moments in the femur during walking. *J Biomech* 30, 933–941 (1997).

- Dudley, D. W. 1957 How to design involute splines. *Product Engineering*, Oct 28 1957, pp 75-80.
- Duisabeau, L., Combrade, P. & Forest, B. Environmental effect on fretting of metallic materials for orthopaedic implants. *Wear* 256, 805–816 (2004).
- Dumbleton, J. H., Manley, M. T. & Edidin, A. A. 2002 A literature review of the association between wear rate and osteolysis in total hip arthroplasty. *The Journal of Arthroplasty* 17, 649–661 (2002).
- Ebramzadeh, E. et al. 2005 Simulation of fretting wear at orthopaedic implant interfaces. *J Biomech Eng* 127, 357–363 (2005).
- Ekberg, A. 2004 Fretting fatigue of railway axles—a Review of predictive methods and an outline of a finite element model. *Proceedings of the Institution of Mechanical Engineers, Part F: Journal of Rail and Rapid Transit* 218, 299–316 (2004).
- Erdogan, E. 2000 Fracture Mechanics, *International Journal of Solids and Structures*, 37, pp. 171–183.
- Fatemi A. and Socie D.F., 1988 “A critical plane approach to multiaxial fatigue damage including out-of-phase loading”, *Fatigue & Fracture of Eng Materials and Structures*, Vol. 11(3), pp. 149-165, 1988
- Fatemi A. and Stephens R. I., 1989 "Biaxial Fatigue of 1045 Steel Under In-Phase and 90 Degree Out-of-Phase Loading Conditions," *Multiaxial Fatigue: Analysis and Experiment, Chapter 9, SAE AE14*, pp. 121-137, 1989.
- Forman RG, Kearney VE and Engle RM. 1967, Numerical analysis of crack propagation in cyclic-loaded structures. *Trans. ASME, Journal of Basic Engineering*. 1967; 89:459-464.

- Forsyth, P. J. E., 1969 *The Physical Basis of Metal Fatigue*, p. 90, *American Elsevier Pub. Company, Inc.*, New York, 1969.
- Fouvry, S., Liskiewicz, T., Kapsa, P., Hannel, S. & Sauger, E. 2003 An energy description of wear mechanisms and its applications to oscillating sliding contacts. *Wear* 255, 287-298 (2003).
- Feret, J.J. & Bournazel, C.L. 1987 Calculation of Stresses and Slip in Structural Layers of Unbonded Flexible Pipes. *J. Offshore Mech. Arct. Eng.* 109, 263-269 (1987).
- Fitch, E. C. 1992 Proactive Maintenance for Mechanical Systems: An Activity Conducted to Detect and Correct Root Cause Aberrations of Failure. (*Elsevier Advanced Technology*: 1992).
- Fridrici, V., Fouvry, S. & Kapsa, P. 2001 Effect of shot peening on the fretting wear of Ti-6Al-4V. *Wear* 250, 642-649 (2001).
- Fridrici, V., Fouvry, S., Kapsa, P. & Perruchaut, P. 2004 Prediction of cracking in Ti-6Al-4V alloy under fretting-wear: use of the SWT criterion. *Wear* 259, 300–308
- Fridrici, V., Fouvry, S., Kapsa, P. & Perruchaut, P. 2005 Prediction of cracking in Ti-6Al-4V alloy under fretting-wear: use of the SWT criterion. *Wear* 259, 300-308 (2005).
- Gåård, A., Krakhmalev, P. & Bergström, J. 2006 Microstructural characterization and wear behavior of (Fe,Ni)-TiC MMC prepared by DMLS. *Journal of Alloys and Compounds* 421, 166–171 (2006).
- Garud, Y. S., 1981 "Multiaxial Fatigue: A Survey of the State of the Art," *Journal of Testing and Evaluation*, Vol. 9, 1981, pp. 165-178.

- Glaeser, W. A. 1981 *Tribology, the Science of Combatting Wear*. (Battelle, Columbus Division: 1981).
- Godet M., 1984 “The Third-Body Approach: A Mechanical View of Wear”, *Wear*, Vol. 100, pp. 437-452, 1984.
- Goh, C.-H., Neu, R. W. & McDowell, D. L. 2003 Crystallographic plasticity in fretting of Ti-6AL-4V. *International Journal of Plasticity* 19, 1627–1650 (2003).
- Goodman, J. E., 1899. *Mechanics Applied to Engineering, Longman, Green & Company, London*, 1899
- Goodman, L. E., 1962. Contact stress analysis of normally loaded rough spheres. *Trans. ASME E, J. Appl. Mech.* 29 (3), 515--522.
- Hallab, N. J., Messina, C., Skipor, A. & Jacobs, J. J. 2004 Differences in the fretting corrosion of metal–metal and ceramic–metal modular junctions of total hip replacements. *Journal of Orthopaedic Research* 22, 250–259 (2004).
- Hallab, N. J. 2011 Fretting Corrosion of Orthopedic Implants. *Comprehensive Biomaterials* 89–96 (2011).
- Hamilton, G. M., Goodman, L. E., 1966. The stress field created by a circular sliding contact. *Journal of Applied Mechanics* 33 (2), 371--&.
- Hamilton, G. M., Dec. 1983. Explicit equations for the stresses beneath a sliding spherical contact. *Proceedings of the Institution of Mechanical Engineers C: Journal of Mechanical Engineering Science* 197 (1983), 53--59.
- Hänninen, J. 2001 DMLS moves from rapid tooling to rapid manufacturing. *Metal Powder Report* 56, 24–29 (2001).

- Harris, S. J., Waterhouse, R. B. & McColl, I. R. 1993 Fretting damage in locked coil steel ropes. *Wear* 170, 63–70 (1993).
- Hattori, T., Nakamura, M. & Watanabe, T. 2003 Simulation of fretting-fatigue life by using stress-singularity parameters and fracture mechanics. *Tribology International* 36, 87–97 (2003).
- Hills, D.A. and D. Dini, 2006 "A new method for the quantification of nucleation of fretting fatigue cracks using asymptotic contact solutions", *Tribol. Int.*, 39(10), (2006), p. 1114-1122.
- Hills, D. A. & Nowell, 1994 D. *Mechanics of Fretting Fatigue*. (Springer: 1994).
- Hills, D. A., Nowell, D. & O'Connor, J. J. 1988 *On the mechanics of fretting fatigue*. *Wear* 125, 129–146 (1988).
- Hills D.A., Nowell D., Sackfield A., 1993 *Mechanics of Elastic Contacts*, Butterworth-Heinemann Ltd., Oxford, UK, 1993
- Hills, D.A., Thaitirarot, A., Barber, J.R., and Dini, D., 2012 "Correlation of Fretting Fatigue Experimental Results Using an Asymptotic Approach", *International Journal of Fatigue*, 43, (2012), p. 62–75.
- Hirsch, M. R. & Neu, R. W. 2011 Fretting damage in thin sheets: Analysis of an experimental configuration. *Tribology International* 44, 1503–1510 (2011).
- Hop, J. D. et al. 1997 The Frank Stinchfield Award. Contribution of cable debris generation to accelerated polyethylene wear. *Clin. Orthop. Relat. Res.* 20–32 (1997).
- Hutchins, I. 1992 *Tribology, Friction and Wear of Engineering Materials*. (Elsevier Limited: 1992).

- Irwin, G. 1957, Analysis of stresses and strains near the end of a crack traversing a plate, *Journal of Applied Mechanics* 24, 361–364.
- Jäger, J. 2002 New analytical and numerical results for two-dimensional contact profiles. *International Journal of Solids and Structures* 39, 959-972 (2002).
- Jin, O. & Mall, S. Influence of contact configuration on fretting fatigue behaviour of Ti-6Al-4V under independent pad displacement condition. *International Journal of Fatigue* 24, 1243-1253 (2002).
- Jin, O. & Mall, S. Effects of slip on fretting behaviour: experiments and analyses. *Wear* 256, 671-684 (2004).
- Johnson, K. L., 2002 Contact Mechanics, Cambridge *University Press, Cambridge*, 1985.
- Kanazawa K., Miller K. J. and Brown M. W., 1977, Low cycle fatigue under out-of-phase loading conditions. *J. Eng. Mater. Technol. (ASME)*, 99, 222–228.
- Kallmeyer A.R., Krgo A., Kurath P., 2002 “Evaluation of multiaxial fatigue life prediction methodologies for Ti-6Al-4V”, *Journal of Engineering Materials and Technology*, Vol. 124, pp. 229-237, April 2002.
- Kennedy A.J., 1963 Processes of Creep and Fatigue in Metals, *John Wiley & Sons, Inc., New York*, 1963
- Kim, T.-W., Kang, D.-H., Yeom, J.-T. & Park, N.-K. 2007 Continuum damage mechanics-based creep–fatigue-interacted life prediction of nickel-based superalloy at high temperature. *Scripta Materialia* 57, 1149-1152 (2007).
- Kitagawa, H. and Takai-Iasi-II, S. (1976) Applicability of fracture mechanics to very small cracks or the cracks in the early stage, *Proc. 2nd Int. Conf. Meek*.

- Klesnil, M. and Lukas, P. 1972. Influence of strength and stress history on growth and stabilisation of fatigue cracks. *Engineering Fracture Mechanics* 4, 77–92.
- Klesnil M. and Lukas P., 1992 “Fatigue of Metallic Materials”, *Elsevier*, 1992.
- Koji Kato, 2000 Wear in relation to friction — a review, *Wear*, 241, 2000. 151–157.
- Korsunsky, A.M., D. Dini, F.P.E. Dunne, and M.J. Walsh, "Comparative assessment of dissipated energy and other fatigue criteria", *Int. J. Fatigue*, 29(9-11), (2007), p. 1990-1995.
- Leen, S. B., Hyde, T. H., Ratsimba, C. H. H., Williams, E. J. and McColl, I. R. (2002) 'An investigation of the fatigue and fretting performance of a representative aeroengine splined coupling'. *Journal of Strain Analysis, Special Issue: Fretting Fatigue*, 37 (6):565-583.
- Leen, S. B., McColl, I. R., Ratsimba, C. H. H. & Williams, E. J. 2003 Fatigue life prediction for a barrelled spline coupling under torque overload. *Proceedings of the Institution of Mechanical Engineers, Part G: Journal of Aerospace Engineering* 217, 123–142 (2003).
- Lemaitre, J. and Chaboche, J.L. (1990) *Mechanics of Solid Materials*.: Cambridge University Press, Cambridge.
- Liskiewicz, T. & Fouvry, S. 2005 Development of a friction energy capacity approach to predict the surface coating endurance under complex oscillating sliding conditions. *Tribology International* 38, 69–79 (2005).
- Madge, J. J. 2008. Numerical modelling of the effect of fretting wear on fretting fatigue. PhD Thesis, University of Nottingham, United Kingdom.
- Madge, J., Leen, S. B., McColl, I. & Shipway, P. 2007 Contact-evolution based prediction of fretting fatigue life: Effect of slip amplitude. *Wear* 262, 1159-1170 (2007).

- Madge, J., Leen, S. B. & Shipway, P. 2007 The critical role of fretting wear in the analysis of fretting fatigue. *Wear* 263, 542-551 (2007).
- Madge, J., Leen, S. & Shipway, P. 2008 A combined wear and crack nucleation-propagation methodology for fretting fatigue prediction. *International Journal of Fatigue* 30, 1509-1528 (2008).
- Magaziner, R., Jin, O., Mall, S., 2004, Slip regime explanation of observed size effects in fretting, *Wear* 257, pp. 190–197.
- Magaziner, R., Jain, V. & Mall, S. 2008 Wear characterization of Ti-6Al-4V under fretting-reciprocating sliding conditions. *Wear* 264, 1002-1014 (2008).
- Marmi, A.K., Habraken, A.M. & Duchene, L., 2009 Multiaxial fatigue damage modelling at macro scale of Ti-6Al-4V alloy. *International Journal of Fatigue* 31, 2031-2040 (November, 2009).
- Marco, S.M. and Starkey, W.L. (1954) "A Concept of Fatigue Damage," *Trans. ASME*, Vol. 76, No. 4, pp. 627-632.
- McColl I.R., Waterhouse R.B., Harris S. J. 1995 Lubricated fretting wear of a high-strength eutectoid steel rope wire. *Wear* 1995; 185(1–2): 203–12.
- McColl, I.R., Ding, J. & Leen, S.B. 2004 Finite element simulation and experimental validation of fretting wear. *Wear* 256, 1114-1127 (2004).
- McDowell, D. L. & Dunne, F. P. E. Microstructure-sensitive computational modeling of fatigue crack formation. *International Journal of Fatigue* 32, 1521–1542 (2010).

- McFarlane C., Hyde T. H., Williams E. J.. 1999 Comparison of spline boundary element analysis with experimental measurements. *In IMechE Seminar on Couplings and Shaft Technology for Aerospace Transmissions*, June
- McKellop, H. A., Rostlund, T., Ebramzadeh, E., and Sarmiento, A., 2001 'Wear of Titanium 6-4 Alloy in Laboratory Tests and in Retrieved Human Joint Replacements', *in Titanium in Medicine*, D. M. Brunette et al., eds. Springer, Berlin, pp. 747-770, 2001
- Military Handbook 1998 - MIL-HDBK-5H: Metallic Materials and Elements for Aerospace Vehicle Structures (Knovel Interactive Edition).. *U.S. Department of Defense*. (1998)
- Mindlin R.D. 1949 Compliance of elastic bodies in contact, *Journal of Applied Mechanics*, 16 (1949), pp. 259–268
- Miner, M. A. (1945) Cumulative damage in fatigue, *Trans. ASEM, J. Appl. Mech*, Vol. 67, 1945, pp. A159—A164.
- Mirzajanzadeh, M., Chakherlou, T. N. & Vogwell, J. 2011 The effect of interference-fit on fretting fatigue crack initiation and ΔK of a single pinned plate in 7075 Al-alloy. *Engineering Fracture Mechanics* 78, 1233–1246 (2011).
- Moës, Nicolas; Dolbow, John; Belytschko, Ted (1999). "A finite element method for crack growth without remeshing". *International Journal for Numerical Methods in Engineering* 46 (1): 131–150.
- Mohd Tobi, A., Ding, J., Bandak, G., Leen, S. B. & Shipway, P. 2009 A study on the interaction between fretting wear and cyclic plasticity for Ti-6Al-4V. *Wear* 267, 270-282 (2009).

- Nesládek, M. , Španiel, M., Jurenka, J., Růžička, J., Kuželka, J., 2012 Fretting fatigue - Experimental and numerical approaches (Review), *International Journal of Fatigue*, Volume 44, November 2012, Pages 61-73.
- Neu, R.W., Pape, J.A., and Swalla, D.R. 2000 “Methodologies for Linking Nucleation and Propagation Approaches for Predicting Life Under Fretting Fatigue”, Fretting Fatigue: Current Technology and Practices, ASTM STP 1367, D.W. Hoepfner, V. Chandrasekaran and C.B. Elliott, Eds., *American Society for Testing and Materials*, 2000
- Neuber H. 1958 Theory of notch stresses. Berlin: Springer, 1958.
- N. H. S., 2012 Choices, N. H. S. Hip replacement - NHS Choices. (2012). at <<http://www.nhs.uk/conditions/Hip-replacement/Pages/Introduction.aspx>>
- Nicholas T. 1999 Critical issues in high cycle fatigue. *Int J Fatigue* 1999;21(S):221–31.
- Nowell, D., D. Dini, and D.A. Hills, 2006 "Recent developments in the understanding of fretting fatigue", *Eng. Fract. Mech.*, 73(2), (2006), p. 207-222.
- Nowell D. 1988 An analysis of fretting fatigue, D.Phil Thesis, University of Oxford; 1988.
- Palmgren A. G., 1924 *Die Lebensdauer von Kugellagern* (Life Length of Roller Bearings. In German). *Zeitschrift des Vereines Deutscher Ingenieure (VDI Zeitschrift)*, ISSN 0341-7258, Vol 68, No 14, April 1924, pp 339–341.
- Papanikos, P., Meguid, S. . & Stjepanovic, Z.1998 Three-dimensional nonlinear finite element analysis of dovetail joints in aeroengine discs. *Finite Elements in Analysis and Design* 29, 173–186 (1998).

- Paris, P. and Erdogan, F., 1963, A critical analysis of crack propagation laws, *Journal of Basic Engineering, Transactions of the American Society of Mechanical Engineers*, December 1963, pp.528-534.
- Patriarco, A. G., Mann, R. W., Simon, S. R. and Mansours, J.M. (1981) An evaluation of the approaches of optimization models in the prediction of muscle forces during human gait. *Journal of Biomechanics* 14, 513-525.
- Penner, J. E., D. H. Lister, D. J. Griggs, D. J. 2000 Dokken and M. McFarland (2000). Aviation and the Global Atmosphere, *Intergovernmental Panel on Climate Change*.
- Peterson RE. 1959 Notch sensitivity. In: Sines G, Waisman JL, editors. *Metal fatigue*. McGraw-Hill, 1959:293-306.
- Rooke, D.P. and Cartwright, D.J., 1976. Compendium of stress intensity factors. HMSO Ministry of Defence. *Procurement Executive*.
- Ruiz, C., Boddington, P.H.B., and Chen, K.C., 1984 "An Investigation of Fatigue and Fretting in Dovetail Joint", *Experimental Mechanics*, Vol. 24(3), pp. 208-217, 1984
- Sabelkin, V. & Mall, S. 2005 Investigation into relative slip during fretting fatigue under partial slip contact condition. *Fatigue & Fracture of Engineering Materials & Structures* 28, 809-824 (2005).
- Sabelkin, V. & Mall, S. 2006 Relative Slip on Contact Surface under Partial Slip Fretting Fatigue Condition. *Strain* 42, 11–20 (2006).
- Sackfield, A.; Hills, D. A., 1983, "Some useful results in the classical Hertz contact problem". *Journal of Strain Analysis*, London, v. 18, n. 2, pp. 101-105.
- Schütz, W. 1996 A history of fatigue. *Engineering Fracture Mechanics* 54, 263–300 (1996).

- Sih, G. C., Paris, P. C. and Erdogan, F. 1962, Crack-tip stress intensity factors for the plane extension and plate bending problem, *Journal of Applied Mechanics*, 29: 306--312.
- Sines. G, 1959 Behavior of metals under complex static and alternating stresses, G. Sines, J.L. Waisman, Editors , *Metal fatigue, McGraw Hill, New York* pp., 145–169. (1959).
- Smith JO, Liu CK. 1953 Stresses due to tangential and normal loads on an elastic solid. *Trans ASME, Series E, J Appl Mech* (1953); 20: 157-66.
- Smith KN, Watson P, Topper TH. 1970 A stress-strain function for the fatigue of metals. *J Mater*, (1970) 15, 767-78.
- Socie D., 1987 “Multiaxial fatigue damage models”, *J. Eng Materials & Technology, Trans ASME*, Vol. 109, pp. 293-298, 1987
- Stephens, R. I., Fatemi, A., Stephens, R. R. & Fuchs, H. O. 2000 *Metal Fatigue in Engineering*. (John Wiley & Sons: 2000).
- Stieler, M. 1954 Untersuchungen über die Dauerzähigkeit metallischer Bauteile ein Raumtemperatur. Thesis of Dr Ingr., *Technische Hochschule Stuttgart*, 1954.
- Sum, W.S., Williams, E.J. & Leen, S.B. 2005 Finite element, critical-plane, fatigue life prediction of simple and complex contact configurations. *International Journal of Fatigue* 27, 403-416 (2005).
- Szolwinski MP, Farris TN. 1996 Mechanics of fretting fatigue crack formation. *Wear* 1996 Oct;198(1-2):93-107.
- Szolwinski, M.P., Harish, G., McVeigh, P.A. and Farris, T.N., 2000 “Experimental Study of Fretting Crack Nucleation in Aerospace Alloys with Emphasis on Life Prediction,” *ASTM*

- STP 1367, *Fretting Fatigue: Current Technologies and Practices*, D.W. Hoepfner, V. Chandrasekaran and C.B. Elliot, Eds, pp 267-281 (2000).
- Taylor, D. 2007 *The Theory of Critical Distances: A New Perspective in Fracture Mechanics*. (Elsevier Science, 2007).
- The Freedonia Group, 2012 *Orthopedic Implants (US industry forecasts for 2012 & 2017)*, August, 2012
- Vadiraj, A. & Kamaraj, M. 2007 Effect of surface treatments on fretting fatigue damage of biomedical titanium alloys. *Tribology International* 40, 82–88 (2007).
- Varenberg, M., Etsion, I. & Halperin, G. 2004 Slip Index: A New Unified Approach to Fretting. *Tribology Letters* 17, 569–573 (2004).
- Varenberg, M., Etsion, I. & Halperin, G. 2005 Nanoscale fretting wear study by scanning probe microscopy. *Tribology Letters* 18, 493–498 (2005).
- Vidner, J. & Leidich, E. 2007 Enhanced Ruiz criterion for the evaluation of crack initiation in contact subjected to fretting fatigue. *International Journal of Fatigue* 29, 2040–2049 (2007).
- Vingsbo O, Soderberg S. On fretting maps. 1988 *Wear* 1988 Sep;126(2):131-147.
- Wang, D., Zhang, D. & Ge, S. 2012 Effect of displacement amplitude on fretting fatigue behavior of hoisting rope wires in low cycle fatigue. *Tribology International* 52, 178–189 (2012).
- Wang, Y. & Hadfield, M. 2003 A mechanism for nucleating secondary fractures near a pre-existing flaw subjected to contact loading. *Wear* 254, 597–605 (2003).
- Waterhouse, R. B. 1992 Fretting fatigue. *International Materials Reviews* 37, 77–98 (1992).

- Waterhouse R. B., 1971 Taylor DE. Fretting fatigue in steel ropes. *Lubrication Engineering* 1971; 27(4): 123-127.
- Wittkowsky, B.U., Birch, P.R., Dominguez, J. & Suresh, S. 1999 An apparatus for quantitative fretting testing. *Fatigue & Fracture of Engineering Materials & Structures* 22, 307–320 (1999).
- Wöhler A., 1858 Bericht über die Versuche, welche auf der königl. Niederschlesisch-märkischen eisenbahn mit Apparaten zum Messen der Biegung und Verdehnung von Eisenbahnwagenachsen während der Fahrt angestellt wurden. *Zeitschrift für Bauwesen*, VIII (1858), pp. 641–652
- Wöhler A., 1860 Versuche zur Ermittlung der auf die Eisenbahnwagenachsen einwirkenden Kräfte und die Widerstandsfähigkeit der Wagen-Achsen. *Zeitschrift für Bauwesen.*, X (1860), pp. 583–616
- Wöhler A. 1870 Über die Festigkeitsversuche mit Eisen und Stahl. Auf Anordnung des Ministers für Handel, Gewerbe u. öffentl. Arbeiten, Grafen Itzenblitz, angestellt. *Ernst und Korn, Berlin* (1870)
- Yan, W.Y. , Busso, E.P. , O'Dowd, N.P., 2000 A micromechanics investigation of sliding wear in coated components, *Proceedings of the Royal Society of London A* 456 (2000) 2387 - 2407.
- Yuan, H. & Xu, Y. Fracture mechanics assessment of stress concentrations in incomplete fretting contacts. *Engineering Fracture Mechanics* 76, 2344–2358 (2009).
- Zahavi E. and Torbilo V., 1996 “Fatigue design: Life expectancy of machine parts”, *CRC Press Inc.*, 1996.

- Zamrik, Y. S. and Frishmuth, R. E., 1973 "The Effects of Out-of-Phase Biaxial Strain Cycling on Low- Cycle Fatigue," *Experimental Mechanics*, Vol. 13, 1973, pp. 204-208.
- Zhang, M., Neu, R. W. & McDowell, D. L. Microstructure-sensitive modeling: Application to fretting contacts. *International Journal of Fatigue* 31, 1397–1406 (2009).
- Zografos, A. & Dini, D. 2009 A combined BEM/Contact Asymptotics (BEM-CA) semi-analytical formulation for the assessment of fretting damage in bolted joints. *Procedia Engineering* 1, 201–204 (2009).
- Zografos, A., D. Dini, and A.V. Olver, "Fretting fatigue and wear in bolted connections: A multi-level formulation for the computation of local contact stresses", *Tribol. Int.*, 42(11-12), (2009), p. 1663-1675.